

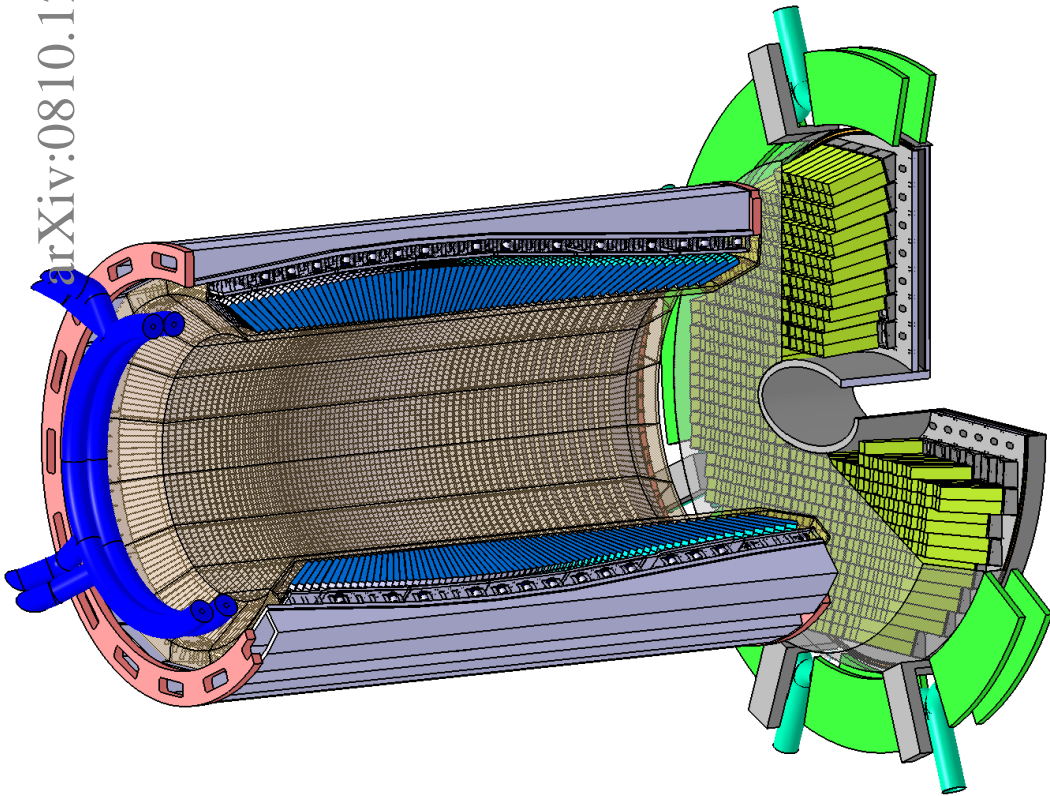
arXiv:0810.1216v1 [physics.ins-det] 7 Oct 2008

Technical Design Report for:  
 $\bar{P}$ ANDA  
Electromagnetic Calorimeter (EMC)

(AntiProton Annihilations at Darmstadt)

Strong Interaction Studies with Antiprotons

$\bar{P}$ ANDA Collaboration



**Cover:** The figure shows the barrel (left) and forward endcap part (right) of the electromagnetic calorimeter. The parts of the barrel calorimeter are cut to get a better view to the inside. Displayed are the PWO crystals with the carbon fiber alveole packs, the support feet connecting to the support beam, held by the support rings at front and back. On the right side the forward endcap crystals inside the carbon fiber packs are shown along with the insulation (shown transparent) and the eight supporting structures on the outside.

# The PANDA Collaboration

Universität **Basel**, Switzerland

W. Erni, I. Keshelashvili, B. Krusche, M. Steinacher

Institute of High Energy Physics, Chinese Academy of Sciences, **Beijing**, China

Y. Heng, Z. Liu, H. Liu, X. Shen, O. Wang, H. Xu

Universität **Bochum**, I. Institut für Experimentalphysik, Germany

F.-H. Heinsius, T. Held, H. Koch, B. Kopf, M. Pelizäus, M. Steinke, U. Wiedner, J. Zhong

Università di Brescia, **Brescia**, Italy

A. Bianconi

Institutul National de C&D pentru Fizica si Inginerie Nucleara "Horia Hulubei", **Bukarest-Magurele**, Romania

M. Bragadireanu, P. Dan, T. Preda, A. Tudorache

Dipartimento di Fisica e Astronomia dell'Università di **Catania** and INFN, Sezione di Catania, Italy

M. De Napoli, F. Giacoppo, G. Raciti, E. Rapisarda

IFJ, Institute of Nuclear Physics PAN, **Cracow**, Poland

E. Bialkowski, A. Budzanowski, B. Czech, S. Kliczewski, A. Kozela, P. Kulessa, K. Malgorzata, K. Pysz, W. Schäfer, R. Siudak, A. Szczurek

Instytut Fizyki, Uniwersytet Jagiellonski, **Cracow**, Poland

W. Bardan, P. Brandys, T. Czyżewski, W. Czyżewski, M. Domagala, G. Filo, D. Gil, P. Hawranek, B. Kamys, P. Kazmierczak, St. Kistryn, K. Korcyl, M. Krawczyk, W. Krzemień, E. Lisowski, A. Magiera, P. Moskal, J. Pietraszek, Z. Rudy, P. Salabura, J. Smyrski, L. Wojnar, A. Wrońska

Gesellschaft für Schwerionenforschung mbH, **Darmstadt**, Germany

M. Al-Turany, I. Augustin, H. Deppe, H. Flemming, J. Gerl, K. Götzen, G. Hohler, D. Lehmann, B. Lewandowski, J. Lühning, F. Maas, D. Mishra, H. Orth, K. Peters, T. Saito, G. Schepers, L. Schmitt, C. Schwarz, C. Sfienti, P. Wieczorek, A. Wilms

Technische Universität **Dresden**, Germany

K.-T. Brinkmann, H. Freiesleben, R. Jäkel, R. Kliemt, T. Würschig, H.-G. Zaunick

Veksler-Baldin Laboratory of High Energies (VBLHE), Joint Institute for Nuclear Research. **Dubna**, Russia

V.M. Abazov, G. Alexeev, A. Arefiev, V.I. Astakhov, M.Yu. Barabanov, B.V. Batyunya, Yu.I. Davydov, V.Kh. Dodokhov, A.A. Efremov, A.G. Fedunov, A.A. Feshchenko, A.S. Galoyan, S. Grigoryan, A. Karmokov, E.K. Koshurnikov, V.Ch. Kudaev, V.I. Lobanov, Yu.Yu. Lobanov, A.F. Makarov, L.V. Malinina, V.L. Malyshev, G.A. Mustafaev, A. Olshevski, M.A.. Pasyuk, E.A. Perevalova, A.A. Piskun, T.A. Pocheptsov, G. Pontecorvo, V.K. Rodionov, Yu.N. Rogov, R.A. Salmin, A.G. Samartsev, M.G. Sapozhnikov, A. Shabratova, G.S. Shabratova, A.N. Skachkova, N.B. Skachkov, E.A. Strokovsky, M.K. Suleimanov, R.Sh. Teshev, V.V. Tokmenin, V.V. Uzhinsky A.S. Vodopianov, S.A. Zaporozhets, N.I. Zhuravlev, A.G. Zorin

University of **Edinburgh**, United Kingdom

D. Branford, K. Föhl, D. Glazier, D. Watts, P. Woods

Friedrich Alexander Universität **Erlangen-Nürnberg**, Germany

W. Eyrich, A. Lehmann, A. Teufel

Northwestern University, **Evanston**, U.S.A.

S. Dobbs, Z. Metreveli, K. Seth, B. Tann, A. Tomaradze

Università di **Ferrara** and INFN, Sezione di Ferrara, Italy

D. Bettoni, V. Carassiti, A. Cecchi, P. Dalpiaz, E. Fioravanti, M. Negrini, M. Savriè, G. Stancari

INFN-Laboratori Nazionali di **Frascati**, Italy

B. Dulach, P. Gianotti, C. Guaraldo, V. Lucherini, E. Pace

INFN, Sezione di **Genova**, Italy

A. Bersani, M. Macri, M. Marinelli, R.F. Parodi

Justus Liebig-Universität **Gießen**, II. Physikalisches Institut, Germany

W. Döring, P. Drexler, M. Düren, Z. Gagyi-Palffy, A. Hayrapetyan, M. Kotulla, W. Kühn, S. Lange,  
M. Liu, V. Metag, M. Nanova, R. Novotny, C. Salz, J. Schneider, P. Schönmeier, R. Schubert,  
S. Spataro, H. Stenzel, C. Strackbein, M. Thiel, U. Thöring, S. Yang,

University of **Glasgow**, United Kingdom

T. Clarkson, E. Downie, M. Hoek, D. Ireland, R. Kaiser, J. Kellie, I. Lehmann, K. Livingston,  
S. Lumsden, D. MacGregor, B. McKinnon, M. Murray, D. Protopopescu, G. Rosner, B. Seitz, G. Yang

Kernfysisch Versneller Instituut, University of **Groningen**, Netherlands

M. Babai, A.K. Biegun, A. Bubak, E. Guliyev, V.S. Jothi, M. Kavatsyuk, H. Löhner, J. Messchendorp,  
H. Smit, J.C. van der Weele

Helsinki Institute of Physics, **Helsinki**, Finland

F. Garcia, D.-O. Riska

Forschungszentrum Jülich, Institut für Kernphysik, **Jülich**, Germany

M. Büscher, R. Dossdall, A. Gillitzer, F. Goldenbaum, F. Hügging, M. Mertens, T. Randriamalala,  
J. Ritman, S. Schadmand, A. Sokolov, T. Stockmanns, P. Wintz

University of Silesia, **Katowice**, Poland

J. Kisiel

Chinese Academy of Science, Institute of Modern Physics, **Lanzhou**, China

S. Li, Z. Li, Z. Sun, H. Xu

Lunds Universitet, Department of Physics, **Lund**, Sweden

S. Fissum, K. Hansen, L. Isaksson, M. Lundin, B. Schröder

Johannes Gutenberg-Universität, Institut für Kernphysik, **Mainz**, Germany

P. Achenbach, M.C. Mora Espi, J. Pochodzalla, S. Sanchez, A. Sanchez-Lorente

Research Institute for Nuclear Problems, Belarus State University, **Minsk**, Belarus

V.I. Dormenev, A.A. Fedorov, M.V. Korzhik, O.V. Missevitch

Institute for Theoretical and Experimental Physics, **Moscow**, Russia

V. Balanutsa, V. Chernetsky, A. Demekhin, A. Dolgolenko, P. Fedorets, A. Gerasimov, V. Goryachev

Moscow Power Engineering Institute, **Moscow**, Russia

A. Boukharov, O. Malyshev, I. Marishev, A. Semenov

Technische Universität **München**, Germany

C. Höppner, B. Ketzer, I. Konorov, A. Mann, S. Neubert, S. Paul, Q. Weitzel

Westfälische Wilhelms-Universität **Münster**, Germany

A. Khoukaz, T. Rausmann, A. Täschner, J. Wessels

IIT Bombay, Department of Physics, **Mumbai**, India

R. Varma

Budker Institute of Nuclear Physics, **Novosibirsk**, Russia

E. Baldin, K. Kotov, S. Peleganchuk, Yu. Tikhonov

Institut de Physique Nucléaire, **Orsay**, France

J. Boucher, T. Hennino, R. Kunne, S. Ong, J. Pouthas, B. Ramstein, P. Rosier, M. Sudol,

J. Van de Wiele, T. Zerguerras

Warsaw University of Technology, Institute of Atomic Energy, **Otwock-Swierk**, Poland

K. Dmowski, R. Korzeniewski, D. Przemyslaw, B. Slowinski

Dipartimento di Fisica Nucleare e Teorica, Università di Pavia, INFN, Sezione di Pavia, **Pavia**, Italy

G. Boca, A. Braghieri, S. Costanza, A. Fontana, P. Genova, L. Lavezzi, P. Montagna, A. Rotondi

Institute for High Energy Physics, **Protvino**, Russia

N.I. Belikov, A.M. Davidenko, A.A. Derevschikov, Y.M. Goncharenko, V.N. Grishin, V.A. Kachanov,  
D.A. Konstantinov, V.A. Kormilitsin, V.I. Kravtsov, Y.A. Matulenko, Y.M. Melnik A.P. Meschanin,  
N.G. Minaev, V.V. Mochalov, D.A. Morozov, L.V. Nogach, S.B. Nurushev, A.V. Ryazantsev,  
P.A. Semenov, L.F. Soloviev, A.V. Uzunian, A.N. Vasiliev, A.E. Yakutin

Kungliga Tekniska Högskolan, **Stockholm**, Sweden

T. Bäck, B. Cederwall

Stockholms Universitet, **Stockholm**, Sweden

C. Bargholtz, L. Gerén, P.E. Tegnér

Petersburg Nuclear Physics Institute of Academy of Science, Gatchina, **St. Petersburg**, Russia

S. Belostotski, G. Gavrilov, A. Itzotov, A. Kisselev, P. Kravchenko, S. Manaenkov, O. Miklukho,  
Y. Naryshkin, D. Veretennikov, V. Vikhrov, A. Zhadanov

Università del Piemonte Orientale Alessandria and INFN, Sezione di Torino, **Torino**, Italy

L. Fava, D. Panzieri

Università di Torino and INFN, Sezione di Torino, **Torino**, Italy

D. Alberto, A. Amoroso, M. Anselmino, E. Botta, T. Bressani, M.P. Bussa, L. Busso, F. De Mori,  
L. Ferrero, A. Grasso, M. Greco, T. Kugathasan, M. Maggiora, S. Marcello, C. Mulatera,  
G.C. Serbanut, S. Sosio

INFN, Sezione di Torino, **Torino**, Italy

R. Bertini, D. Calvo, S. Coli, P. De Remigis, A. Feliciello, A. Filippi, G. Girauda, G. Mazza, A. Rivetti,  
K. Szymanska, F. Tosello, R. Wheadon

INAF-IFSI and INFN, Sezione di Torino, **Torino**, Italy

O. Morra

Politecnico di Torino and INFN, Sezione di Torino, **Torino**, Italy

M. Agnello, F. Iazzi, K. Szymanska

Università di Trieste and INFN, Sezione di Trieste, **Trieste**, Italy

R. Birsa, F. Bradamante, A. Bressan, A. Martin

Universität Tübingen, **Tübingen**, Germany

H. Clement

The Svedberg Laboratory, **Uppsala**, Sweden

C. Ekström

Uppsala Universitet, Institutionen för Strålningsvetenskap, **Uppsala**, Sweden

H. Calén, S. Grape, B. Höistad, T. Johansson, A. Kupsc, P. Marciniowski, E. Thomé, J. Zlomanczuk

Universitat de Valencia, Dpto. de Física Atómica, Molecular y Nuclear, **Valencia**, Spain

J. Díaz, A. Ortiz

Soltan Institute for Nuclear Studies, **Warsaw**, Poland

S. Borsuk, A. Chlopik, Z. Guzik, J. Kopec, T. Kozlowski, D. Melnychuk, M. Plominski, J. Szewinski,  
K. Traczyk, B. Zwieglinski

Österreichische Akademie der Wissenschaften, Stefan Meyer Institut für Subatomare Physik, **Wien**,  
Austria

P. Bühler, A. Gruber, P. Kienle, J. Marton, E. Widmann, J. Zmeskal

Editors:	Fritz-Herbert Heinsius	Email: heinsius@ep1.rub.de
	Bertram Kopf	Email: bertram@ep1.rub.de
	Bernd Lewandowski	Email: b.lewandowski@gsi.de
	Herbert Löhner	Email: h.loehner@kvi.nl
	Rainer Novotny	Email: rainer.novotny@exp2.physik.uni-giessen.de
	Klaus Peters	Email: k.peters@gsi.de
	Philippe Rosier	Email: rosierph@ipno.in2p3.fr
	Lars Schmitt	Email: l.schmitt@gsi.de
	Alexander Vasiliev	Email: alexander.vasiliev@ihep.ru
Technical Coordinator:	Lars Schmitt	Email: l.schmitt@gsi.de
Deputy:	Bernd Lewandowski	Email: b.lewandowski@gsi.de
Spokesperson:	Ulrich Wiedner	Email: ulrich.wiedner@ts1.uu.se
Deputy:	Paola Gianotti	Email: paola.gianotti@lnf.infn.it

---

## **Preface**

This document presents the technical layout and the envisaged performance of the Electromagnetic Calorimeter (EMC) for the PANDA target spectrometer. The EMC has been designed to meet the physics goals of the PANDA experiment. The performance figures are based on extensive prototype tests and radiation hardness studies. The document shows that the EMC is ready for construction up to the front-end electronics interface.

---

The use of registered names, trademarks, *etc.* in this publication does not imply, even in the absence of specific statement, that such names are exempt from the relevant laws and regulations and therefore free for general use.

# Contents

---

<b>Preface</b>	<b>vii</b>	3.3.1 Production Schemes . . . . .	37
<b>1 Executive Summary</b>	<b>1</b>	3.3.2 Assembly Schemes . . . . .	37
1.1 The PANDA Experiment . . . . .	1	3.4 Conclusion . . . . .	37
1.2 The $\bar{\text{P}}\text{ANDA}$ Electromagnetic Calorimeter . . . . .	3	<b>4 Scintillator Material</b>	<b>39</b>
1.2.1 PWO-II Scintillator Material . . . . .	3	4.1 Inorganic Scintillators . . . . .	39
1.2.2 APD and VPT Photo Detectors . . . . .	5	4.1.1 Specific Requirements for the target spectrometer EMC . . . . .	40
1.2.3 Electronics . . . . .	5	4.1.2 Hit Rates and Absorbed Energy Dose in Single Crystals . . . . .	40
1.2.4 Mechanics and Integration . . . . .	7	4.2 Lead Tungstate PWO . . . . .	42
1.2.5 Calibration and Monitoring . . . . .	8	4.2.1 General Aspects . . . . .	42
1.2.6 Simulation . . . . .	8	4.2.2 Basic Properties of $\text{PbWO}_4$ and the Scintillation Mechanism . . . . .	42
1.2.7 Performance . . . . .	10	4.2.3 The Improved Properties of PWO-II . . . . .	44
1.3 Conclusion . . . . .	11	4.3 Radiation Induced Absorption in PWO-II Crystals . . . . .	46
<b>2 Overview of the PANDA Experiment</b>	<b>13</b>	4.3.1 The Irradiation Facility at IHEP, Protvino . . . . .	46
2.1 The Physics Case . . . . .	13	4.3.2 The Irradiation Facility at the Justus-Liebig-University Giessen . . . . .	48
2.2 The High Energy Storage Ring . . . . .	15	4.3.3 The Irradiation Facilities at INP (Minsk) and BTCP . . . . .	49
2.2.1 Overview of the HESR . . . . .	15	4.3.4 Irradiation Studies with Neutrons, Protons and High Energy $\gamma$ -rays . . . . .	50
2.2.2 Beam Cooling . . . . .	15	4.4 The PWO-II Crystals for $\bar{\text{P}}\text{ANDA}$ . . . . .	50
2.2.3 Luminosity Estimates . . . . .	15	4.4.1 Light Yield and Decay Kinetics . . . . .	51
2.3 The $\bar{\text{P}}\text{ANDA}$ Detector . . . . .	17	4.4.2 Radiation Hardness of PWO-II . . . . .	51
2.3.1 Target Spectrometer . . . . .	18	4.4.3 Radiation Hardness Required for PANDA . . . . .	54
2.3.2 Forward Spectrometer . . . . .	25	4.4.4 Pre-Production Run of PWO-II Crystals . . . . .	57
2.3.3 Luminosity monitor . . . . .	26	4.5 Quality Requirements and Control . . . . .	59
2.3.4 Data Acquisition . . . . .	27	4.5.1 Measurements of the Light Yield and the Light Yield Non-uniformity . . . . .	60
2.3.5 Infrastructure . . . . .	28	4.5.2 Inspection of the Optical Properties . . . . .	61
References . . . . .	29	4.5.3 Measurement of the Geometrical Dimensions . . . . .	61
<b>3 Design Considerations</b>	<b>31</b>	4.5.4 Analysis and Documentation . . . . .	61
3.1 Electromagnetic Particle Reconstruction . . . . .	31		
3.1.1 Coverage Requirements . . . . .	31		
3.1.2 Resolution Requirements . . . . .	33		
3.2 Environment . . . . .	34		
3.2.1 Surrounding Detectors . . . . .	34		
3.2.2 Count-rate and Occupancy . . . . .	35		
3.2.3 Operational Aspects . . . . .	37		
3.3 Production and Assembly . . . . .	37		

4.5.5	Control Measurements of Production Stability . . . . .	62	6.7.3	Cable Performance and Specifications for barrel EMC and forward endcap EMC . . . . .	100
4.5.6	Manufacturer for the Final Production . . . . .	62	6.7.4	Circuit Description . . . . .	100
	References . . . . .	64	6.7.5	Manufacturing, Operation, and Safety . . . . .	100
<b>5</b>	<b>Photo Detectors</b>	<b>67</b>	6.7.6	Alternatives . . . . .	100
5.1	Avalanche Photodiodes (APD) . . . . .	67	6.8	Detector Control System . . . . .	100
5.1.1	Introduction . . . . .	67	6.8.1	Goals . . . . .	100
5.1.2	Characteristics . . . . .	68	6.8.2	Process Control . . . . .	102
5.1.3	Radiation Damage due to Different Kinds of Radiation . . . . .	72	6.8.3	Detector Control and Monitoring	103
5.1.4	APD Screening Procedure . . . . .	78	6.9	Production and Assembly . . . . .	103
5.1.5	Mounting Procedure . . . . .	78	6.9.1	ASIC preamplifier . . . . .	103
5.2	Vacuum Phototriodes (VPT) . . . . .	79	6.9.2	Discrete preamplifier . . . . .	105
5.2.1	Introduction . . . . .	79		References . . . . .	105
5.2.2	Available Types . . . . .	79	<b>7</b>	<b>Mechanics and Integration</b>	<b>107</b>
5.2.3	Characteristics and Requirements	80	7.1	The Barrel Calorimeter . . . . .	107
5.2.4	Testing . . . . .	81	7.1.1	The crystal geometry and housing	107
5.2.5	Screening Procedure . . . . .	83	7.1.2	Mechanics around Crystals - Slice Definition . . . . .	112
	References . . . . .	83	7.1.3	Electronics Integration . . . . .	112
<b>6</b>	<b>Electronics</b>	<b>85</b>	7.1.4	Thermal Cooling . . . . .	114
6.1	General EMC Readout Scheme . . . . .	85	7.1.5	Integration in the $\bar{P}$ ANDA Target Spectrometer . . . . .	119
6.2	Preamplifier and Shaper for barrel EMC APD-readout . . . . .	86	7.1.6	Construction of the Slices and Assembly of the Barrel . . . . .	120
6.2.1	Requirements and Specifications . . . . .	87	7.2	Forward Endcap . . . . .	121
6.2.2	Integrated Circuit Development . . . . .	88	7.2.1	Requirements . . . . .	121
6.3	Preamplifier and Shaper for forward endcap EMC VPT-readout . . . . .	92	7.2.2	Crystal shape . . . . .	122
6.3.1	Requirements and Specifications . . . . .	92	7.2.3	Subunit Structure . . . . .	122
6.3.2	Circuit Description . . . . .	94	7.3	Backward Endcap of the Calorimeter	128
6.3.3	Performance Parameters . . . . .	95		References . . . . .	129
6.3.4	SPICE Simulations . . . . .	96	<b>8</b>	<b>Calibration and Monitoring</b>	<b>131</b>
6.4	APD Timing Performance with FADC Readout . . . . .	97	8.1	Calibration . . . . .	131
6.5	Digitizer Module . . . . .	97	8.1.1	Calibration with Physics Events . . . . .	131
6.6	Data Multiplexer . . . . .	98	8.1.2	Precalibration with Cosmic Muons and at Test Beams . . . . .	131
6.7	Signal Routing and Cabling . . . . .	99	8.1.3	Online Calibration . . . . .	132
6.7.1	Requirements . . . . .	99	8.2	Monitoring . . . . .	132
6.7.2	Cable Performance and Specifications for Proto60 Assembly . . . . .	99	8.2.1	Concept of a Light Source and Light Distribution System . . . . .	133

8.2.2	Concept of the Light Monitoring System . . . . .	133	11.2.1	Mechanics . . . . .	172
8.2.3	Light Pulser Prototype Studies . . . . .	133	11.2.2	Electrical Equipment and Cooling	173
8.2.4	Light Monitoring System for $\bar{P}$ ANDA Calorimeter . . . . .	136	11.2.3	Radiation Aspects . . . . .	173
References	. . . . .	139	11.3	Schedule . . . . .	173
<b>9</b>	<b>Simulations</b>	<b>141</b>	<b>Acknowledgments</b>		<b>177</b>
9.1	Offline Software . . . . .	141	<b>List of Acronyms</b>		<b>179</b>
9.1.1	Photon Reconstruction . . . . .	141	<b>List of Figures</b>		<b>181</b>
9.1.2	Electron Identification . . . . .	144	<b>List of Tables</b>		<b>187</b>
9.2	Material Budget in front of the EMC	146			
9.2.1	DIRC Preshower . . . . .	147			
9.3	Benchmark Studies . . . . .	148			
9.3.1	$h_c$ Detection with the $h_c \rightarrow \eta_c \gamma$ Decay and the Role of low Energy $\gamma$ -ray Threshold . . . . .	148			
9.3.2	$Y(4260)$ in Formation . . . . .	150			
9.3.3	Charmonium Hybrid in Production	151			
9.3.4	Time-like Electromagnetic Form-Factors . . . . .	152			
References	. . . . .	154			
<b>10</b>	<b>Performance</b>	<b>157</b>			
10.1	Results from Prototype Tests . . . . .	158			
10.1.1	Energy Resolution of PWO arrays	158			
10.1.2	Position Resolution . . . . .	164			
10.1.3	Particle Identification . . . . .	165			
10.1.4	Construction and Basic Performance of the Barrel Prototype Comprising 60 Modules . . . . .	165			
10.2	Expected performance of the EMC . . . . .	167			
References	. . . . .	169			
<b>11</b>	<b>Organisation</b>	<b>171</b>			
11.1	Quality Control and Assembly . . . . .	171			
11.1.1	Production Logistics . . . . .	171			
11.1.2	The PWO-II Crystals . . . . .	171			
11.1.3	Detector Module Assembly . . . . .	171			
11.1.4	Final Assembly, Pre-calibration and Implementation into $\bar{P}$ ANDA	172			
11.1.5	Other Calorimeter Components . . . . .	172			
11.1.6	Integration in PANDA . . . . .	172			
11.2	Safety . . . . .	172			



# 1 Executive Summary

---

## 1.1 The PANDA Experiment

$\bar{\text{P}}\text{ANDA}$  is a next generation hadron physics detector planned to be operated at the future Facility for Antiproton and Ion Research (FAIR) at Darmstadt, Germany. It will use cooled antiproton beams with a momentum between  $1.5 \text{ GeV}/c$  and  $15 \text{ GeV}/c$  interacting with various internal targets.

At FAIR the antiprotons will be injected into HESR, a slow ramping synchrotron and storage ring with excellent beam energy definition by means of stochastic and electron cooling. This allows to measure masses and widths of hadronic resonances with an accuracy of  $50\text{--}100 \text{ keV}$ , which is 10 to 100 times better than achieved in any  $e^+e^-$ -collider experiment. In addition states of all quantum numbers can be directly formed in antiproton-proton annihilations whereas in  $e^+e^-$ -collisions states with quantum numbers other than  $J^{PC} = 1^{--}$  of a virtual photon can only be accessed by higher order processes with corresponding lower cross section or production reactions with much worse mass resolution. In the  $\bar{\text{P}}\text{ANDA}$  experiment, the antiprotons will interact with an internal target, either a hydrogen cluster jet or a high frequency frozen hydrogen pellet target, to reach a peak luminosity of up to  $2 \cdot 10^{32} \text{ cm}^{-2} \text{ s}^{-1}$ . For reactions with heavy nuclear targets thin wires or foils are inserted in the beam halo.

The experiment is focusing on hadron spectroscopy, in particular the search for exotic states in the charmonium mass region, on the interaction of charmed hadrons with the nuclear medium, on double-hypernuclei to investigate the nuclear potential and hyperon-hyperon interactions as well as on electromagnetic processes to study various aspects of nucleon structure.

From these goals a list of physics benchmarks can be derived defining the requirements for the  $\bar{\text{P}}\text{ANDA}$  detector system. For precision spectroscopy of charmonium states and exotic hadrons in the charmonium region, full acceptance is required to perform a proper partial wave analysis. Final states with many photons can occur, leading to a low photon threshold as a central requirement for the electromagnetic calorimeters. To reconstruct charmed mesons, a vertex detector and the identification of kaons is necessary.

Further requirements result from other signals of

interest: final states with muons occur in  $J/\psi$  decays, semi-leptonic charm meson decays and the Drell-Yan process. Measuring wide angle Compton scattering requires detection of high energy photons. Investigating hypernuclei requires the detection of hyperon cascades. The measurement of proton formfactors relies on an efficient  $e^\pm$  identification and discrimination against pions.

For the reconstruction of invariant masses a good momentum resolution in the order of  $\delta p/p \sim 1\%$  is desirable. Low cross-section processes and precision measurements lead to a high rate operation at up to 20 million interactions per second. To perform several measurements in parallel an efficient event selection is needed.

**General Setup.** To achieve almost  $4\pi$  acceptance and good momentum resolution over a large range, a solenoid magnet for high  $p_T$  tracks (*target spectrometer*) and a dipole magnet for the forward-going reaction products (*forward spectrometer*) are foreseen (Fig. 1.1). The solenoid magnet is superconducting, provides a field strength of 2 T and has a coil opening of 1.89 m and a coil length of 2.75 m. The target spectrometer is arranged in a barrel part for angles larger than  $22^\circ$  and an endcap part for the forward range down to  $5^\circ$  in the vertical and  $10^\circ$  in the horizontal plane.

The dipole magnet has a field integral of up to 2 Tm with a 1.4 m wide and 70 cm high opening. The forward spectrometer covers the very forward angles.

Both spectrometer parts are equipped with tracking, charged particle identification, electromagnetic calorimetry and muon identification.

To operate the experiment at high rate and with different parallel physical topologies a self-triggering readout scheme was adopted. The frontend electronics continuously digitizes the detector data and autonomously finds valid hits. Physical signatures like energy clusters, tracklets or ringlets are extracted on the fly. Compute nodes make a fast first selection of interesting time slices which then is refined with further data in subsequent levels. Data logging happens only after online reconstruction. This allows full flexibility in applying selection algorithms based on any physics signatures detectable by the spectrometer. In addition physics topics with identical target and beam settings can be treated in parallel.

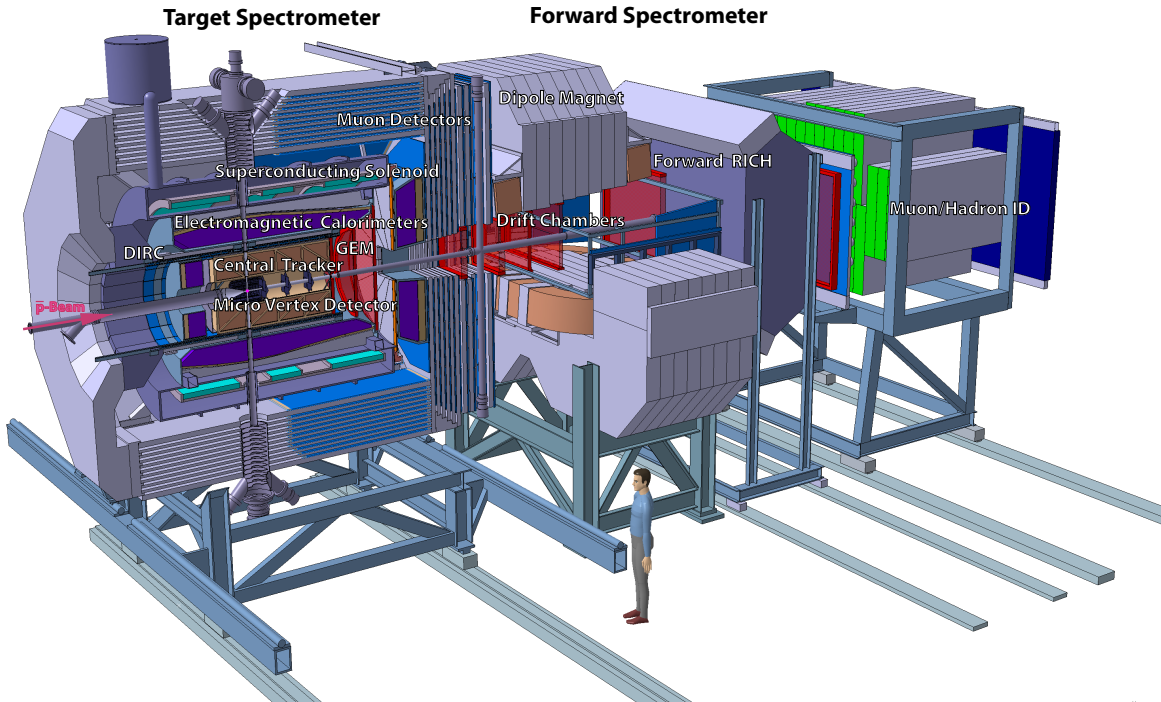


Figure 1.1: Overview of the PANDA spectrometer.

**Tracking detectors.** The silicon vertex detector consists of two inner layers of hybrid pixel detectors and two outer layers with silicon strip detectors. The pixel layers consist of a silicon sensor coupled to a custom-made self-triggering readout ASIC realized in  $0.13\ \mu\text{m}$  CMOS with  $100 \times 100\ \mu\text{m}^2$  pixel size and cover  $0.15\ \text{m}^2$  with 13 million channels. The strip part is based on double-sided silicon strips read by a self-triggering 128-channel ASIC with discriminator and analog readout and covers  $0.5\ \text{m}^2$  with 70 000 channels.

For the tracking in the solenoid field low-mass straw tubes arranged in straight and skewed configuration are foreseen. The straws have a diameter of 1 cm and a length of 150 cm and are operated with  $\text{Ar}/\text{CO}_2$  at 1 bar overpressure giving them rigidity without heavy support frames.

Alternatively an ungated time projection chamber based on GEM foils as readout stage is being developed. The GEM foils suppress the ion backflow into the drift volume, minimizing the space charge build-up. As detector gas  $\text{Ne}/\text{CO}_2$  is used. The readout plane consists of 100 000 pads of  $2 \times 2\ \text{mm}^2$ . With 500 hits per track and more than  $50\ \mu\text{s}$  drift time 500 events are overlapping, leading to a very high data rate which has to be handled online.

Tracks at small polar angles ( $5^\circ < \theta < 22^\circ$ ) are

measured by large planar GEM detectors. Further downstream, in the forward spectrometer, straw tube chambers with a tube diameter of 1 cm will be employed.

**Particle Identification.** Charged particle identification is required over a large momentum range from 200  $\text{MeV}/c$  up to almost 10  $\text{GeV}/c$ . Different physical processes are employed.

The main part of charged particles is identified by various Cherenkov detectors. In the target spectrometer two detectors based on the detection of internally reflected Cherenkov light (DIRC) are under design, one consisting of quartz rods for the barrel region, the other one in shape of a disc for the forward endcap. Novel readout techniques are under study to achieve correction or compensation of dispersion in the radiator material. In the forward spectrometer a ring imaging Cherenkov detector with aerogel and  $\text{C}_4\text{F}_{10}$  as radiators is planned.

Time of flight can be partly exploited in PANDA. Although no dedicated start detector is available, a scintillator wall after the dipole magnet can measure the relative timing of charged particles with very good time resolution in the order of 100 ps.

The energy loss within the trackers will be employed as well for particle identification below  $1\ \text{GeV}/c$

since the individual charge is obtained by analog readout or time-over-threshold measurement. Here the TPC option would provide best performance.

The detection system is complemented by muon detectors based on drift tubes located inside the segmented magnet yoke, between the spectrometer magnets and at the end of the spectrometer. Muon detection is implemented as a range system with interleaved absorbing material and detectors to best distinguish muons from pions in the low momentum range of PANDA.

**Calorimetry.** In the target spectrometer high precision electromagnetic calorimetry is required over a large energy range from a few MeV up to several GeV. Lead-tungstate is chosen for the calorimeters in the target spectrometer due to its good energy resolution, fast response and high density, allowing a compact setup.

Good identification and reconstruction of multi-photon and lepton-pair channels are of utmost importance for the success of the PANDA experiment. Low energy thresholds and good energy and spatial resolution are important assets to achieve high yield and good background rejection. Due to the high luminosity, fast response and radiation hardness are additional requirements which have to be fulfilled. Table 1.1 shows the detailed list of requirements for the EMC.

To achieve the required very low energy threshold, the light yield has to be maximized. Therefore improved lead-tungstate crystals are employed with a light output twice as high as used in CMS. These crystals are operated at  $-25\text{ }^{\circ}\text{C}$  which increases the light output by another factor of four. In addition, large area APDs are used for readout, providing high quantum efficiency and an active area four times larger than used in CMS.

The largest sub-detector is the barrel calorimeter with 11360 crystals of 200 mm length. In the backward direction 592 crystals provide hermeticity at worse resolution due to the presence of readout and supply lines of other detectors. The 3600 crystals in the forward direction face a much higher range of particle rates across the acceptance of the calorimeter in the forward endcap. A readout with vacuum phototriodes is foreseen to be able to safely operate at the higher particle rates and correspondingly higher radiation load.

The crystal calorimeter is complemented in the forward spectrometer with a shashlik type sampling calorimeter consisting of 1404 modules of  $55 \times 55\text{ mm}^2$  cell size covering  $2.97 \times 1.43\text{ m}^2$ .

This document presents the details of the technical design of the electromagnetic crystal calorimeter of the PANDA target spectrometer.

## 1.2 The PANDA Electromagnetic Calorimeter

### 1.2.1 PWO-II Scintillator Material

The concept of PANDA places the target spectrometer EMC inside the super-conducting coil of the solenoid. Therefore, the basic requirements of the appropriate scintillator material are compactness to minimize the radial thickness of the calorimeter layer, fast response to cope with high interaction rates, sufficient energy resolution and efficiency over the wide dynamic range of photon energies given by the physics program, and finally an adequate radiation hardness. In order to fulfill these requirements, even a compact geometrical design must provide a high granularity leading to a large quantity of crystal elements. Their fabrication relies on existing proven technology for mass production to guarantee the necessary homogeneity of the whole calorimeter. Presently and even in the near future there is no alternative material besides lead tungstate available.

The intrinsic parameters of  $\text{PbWO}_4$  (PWO) as developed for CMS/ECAL are meeting all requirements, except for the light output. Therefore, an extended R&D program was initiated to improve the luminescence combined with an operation at low temperatures such as  $T=-25\text{ }^{\circ}\text{C}$ . Several successful steps have been taken, which have lead to a significantly improved material labelled as PWO-II. The research was aiming at an increase of the structural perfection of the crystal and the optimized activation with luminescent impurity centers, which have a large cross section to capture electrons from the conduction band, combined with a sufficiently short delay of radiative recombination. Beyond the improvement of the crystal quality, the reduction of the thermal quenching of the luminescence process by cooling the crystals leads to an additional increase of the light yield without any considerable distortion of the scintillation kinetics. Operating at a temperature of  $T=-25\text{ }^{\circ}\text{C}$  provides an overall gain factor of about 4 compared to  $T=+25\text{ }^{\circ}\text{C}$ . As a result, full size crystals with 200 mm length deliver a light yield of 17-20 photoelectrons per MeV (phe/MeV) at  $18\text{ }^{\circ}\text{C}$  measured with a photomultiplier with bi-alkali photocathode (quantum efficiency  $\sim 20\%$ ).

	Required performance value		
Common properties			
energy resolution $\sigma_E/E$	$\leq 1\% \oplus \frac{\leq 2\%}{\sqrt{E/\text{GeV}}}$		
energy threshold (photons) $E_{thres}$	10 MeV (20 MeV tolerable)		
energy threshold (single crystal) $E_{xtl}$	3 MeV		
rms noise (energy equiv.) $\sigma_{E,noise}$	1 MeV		
angular coverage % $4\pi$	99 %		
mean-time-between-failures $t_{mtbf}$ (for individual channel)	2000 y		
Subdetector specific properties			
	backward ( $\geq 140^\circ$ )	barrel ( $\geq 22^\circ$ )	forward ( $\geq 5^\circ$ )
energy range from $E_{thres}$ to	0.7 GeV	7.3 GeV	14.6 GeV
angular equivalent of crystal size $\theta$		4°	1°
spatial resolution $\sigma_\theta$	0.5°	0.3°	0.1°
maximum signal load $f_\gamma$ ( $E_\gamma > E_{xtl}$ )		60 kHz	500 kHz
(p $\bar{p}$ -events) maximum signal load $f_\gamma$ ( $E_\gamma > E_{xtl}$ )		100 kHz	500 kHz
(all events) shaping time $t_s$		400 ns	100 ns
radiation hardness	0.15 Gy	7 Gy	125 Gy
(maximum annual dose p $\bar{p}$ -events)			
radiation hardness		10 Gy	125 Gy
(maximum annual dose from all events)			

**Table 1.1:** Main requirements for the PANDA EMC. Rates and doses are based on a luminosity of  $L = 2 \cdot 10^{32} \text{ cm}^{-2} \text{ s}^{-1}$ .

The radiation level will be well below typical LHC values by at least two orders of magnitude even at the most forward direction and be much lower at larger angles. The radiation hardness and the effective loss of light yield as a function of dose rate and accumulated total dose are well known from the studies for CMS but investigated at room temperature. The effective deterioration of the optical transmission during the experiment is caused by the interplay of damaging and recovering mechanisms. The latter are fast at room temperature and keep the loss of light yield moderate. As shown by detailed investigations, at temperatures well below 0°C the relaxation times of color centers become extremely slow, reaching values well above 200 hours. As a consequence, there is a continuous and asymptotic reduction of the scintillation output. However, the present quality of PWO-II has reached induced absorption values well below the limits of the CMS crystals. A saturation is reached after an integral dose of 30-50 Gy, leading to a maximum loss of light yield of 30%. To emphasize, these effects have to be considered only in the very forward region of the forward endcap EMC. Taking the radiation-damage effects in forward-angle detectors into account, the proposed operation of the calorimeter at T=-25°C can be based on a net increase of the light yield by

a factor of 3 compared to room temperature operation in addition to the improvement due to crystal quality and a more effective arrangement of the photosensors. A detector being back at room temperature will recover from radiation damage within 1-2 weeks.

The performance parameters are based on a large quantity of full size crystal samples and the experience of a pre-production run of 710 crystals comprising all geometrical shapes to complete one slice of the barrel. Detailed specifications as well as a quality control program have been elaborated, taking into account the experience of the CMS/ECAL collaboration.

The requested crystal quality can be provided at the moment by the Russian manufacturer BTCP. The only alternative producer SICCAS in China has not yet delivered full size samples of comparable quality.

Based on the ongoing developments of PWO-II crystals, a detailed program has been worked out for the quality assurance of the crystals. This includes the preparation of various facilities for irradiation studies. The quality control is planned to be performed at CERN, taking advantage of the existing infrastructure and experience developed for CMS. One of the two ACCOS machines, semi-automatic

robots, is presently getting modified for the different specification limits and geometrical dimensions of the PANDA crystals.

### 1.2.2 APD and VPT Photo Detectors

The low energy threshold of 10 MeV for the PANDA EMC requires the usage of excellent photo detectors. The magnetic field of about 2 T precludes the use of conventional photomultipliers. On the other hand the signal generated by ionization in a PIN photodiode by a traversing charged particle is too large for our applications. To solve these problems a photosensor insensitive to magnetic fields and with a small response to ionizing radiation has to be used.

Since lead tungstate has a relatively low light yield, the photosensor is required to have an internal gain in addition. Due to the envisaged operation temperature of  $T = -25^{\circ}\text{C}$  for the EMC, not only the PWO-II crystals but also the used photo detectors have to be radiation hard in this temperature region, which implies detailed studies concerning possibly occurring radiation damages.

For the barrel EMC an Avalanche Photodiode (APD) which has an internal signal amplification (gain) in the silicon structure is chosen as photo detector. To maximize the light yield the coverage of the readout surface of the crystals has to be as large as possible, leading to the development of Large Area APDs (LAAPD) with an active area of  $10 \times 10 \text{ mm}^2$ . Their characterisation has been focused on the given requirements.

Several prototypes of LAAPDs have been studied for their characteristics, especially for their radiation hardness: These devices have been exposed to proton, photon and neutron radiation, while their dark currents have been monitored to analyse the damage of the surface and of the bulk structure.

The response to hadrons was investigated and will provide complementary information to the particle tracking or even identification of muons based on the energy deposition or different cluster multiplicity of trespassing hadrons.

In addition to several screenings done using monochromatic light, certain properties of the diodes could only be determined by scanning the complete spectrum of visible light. The latter procedure is not only used for studying the quantum efficiency but also to detect effects on the structure of an LAAPD after irradiation. These studies enable us to identify the best structure of the APDs

fulfilling the requirements of the PANDA EMC.

The operation of an LAAPD requires the correct knowledge about its gain factor. Since this condition changes with the operation temperature, the screening of this photo detector is being done at room temperature as well as at the operating temperature of  $T = -25^{\circ}\text{C}$  to study its gain-voltage dependence. During the screening process the knowledge about this voltage dependence will be used for grouping LAAPDs in the detector to enable the usage of one HV line for one block of sensors. Again we take advantage of the CMS experience for the screening of the photo sensors.

During the development of the readout system for the EMC the typical size of the crystal readout surface of  $27 \times 27 \text{ mm}^2$  lead to the development of an LAAPD with a rectangular shape (active area:  $14 \times 6.8 \text{ mm}^2$ ) to cover a maximum of this space with two neighboring photo detectors. The new geometry allows to fit two sensors on each crystal irrespectively of its individual shape.

In contrast to the barrel EMC, the forward endcap EMC has to deal with rates up to 500 kHz per crystal and magnetic fields up to 1.2 T. Therefore vacuum phototriodes (VPTs) have been chosen for the photo detection in this EMC part due to the following reasons: rate capability, radiation hardness, absence of nuclear counter effect and absence of temperature dependence. Standard photomultipliers are excluded due to the magnetic field environment. Different to the barrel region, the magnetic field is oriented in the axial direction of the VPTs and thus makes it feasible to use them for the endcap readout. Vacuum phototriodes are essentially a photomultiplier tube with only one dynode and weak field dependence. Tests and the parameters presented are based on VPTs produced for the CMS experiment. A new VPT with a significantly higher quantum efficiency combined with a larger internal gain is under development and will be produced by the company Photonis and will be tested as soon as it becomes available to us.

The operation of these photo detectors at different angles relative to the orientation of a magnetic field as well as the high rate capability are being studied. These studies are being done both at room temperature as well as at the envisaged EMC operation temperature of  $T = -25^{\circ}\text{C}$ .

### 1.2.3 Electronics

The PANDA Electromagnetic Calorimeter (EMC) will provide an almost full coverage of the final

state phase space for photons and electrons. The low-energy photon threshold will be around 10 MeV, while the threshold for individual detectors can be as low as 3 MeV with correspondingly low noise levels of 1 MeV. Such settings allow the precision spectroscopy of charmonium states and transitions. With a dynamic range of 12000 for the readout electronics, a maximum photon energy deposition of 12 GeV per crystal can be detected which allows the study of neutral decays of charmed mesons at the maximum beam energy of the HESR. Typical event rates of 10 kHz and maximum 100 kHz are expected for the barrel part of the calorimeter and up to 500 kHz in the forward endcap. Two different photo detectors, LAAPD and vacuum photo triodes (VPTs) will be used. The photo sensors are directly attached to the end faces of the individual crystals and the preamplifier is placed as close as possible inside the calorimeter volume for optimum performance and minimum space requirements. Since every barrel EMC crystal is equipped with two APDs, not only redundancy is achieved but also a significantly (max.  $\sqrt{2}$ ) improved signal to noise ratio and a lower effective threshold level.

The readout of small and compact subarrays of crystals requires very small preamplifier geometries. The low-temperature environment of the EMC will improve the noise performance of the analogue circuits. For efficient cooling and stable temperature behavior, low power consumption electronics has been developed in combination with extremely low-noise performance.

Two complementary low-noise and low-power (LNP) charge-sensitive preamplifier-shaper (LNP-P) circuits have been developed. The LNP design based on discrete components utilizes a low-noise J-FET transistor. The circuit achieves a very good noise performance using signal shaping with a peaking time of 650 ns. This preamplifier will be used for the readout of the forward endcap EMC for which we expect a single-channel rate up to 500 kHz. Such an approach minimizes the overall power consumption and keeps the probability for pileup events at a moderate level well below 1%. The noise floor of the LNP-P at  $-25^\circ\text{C}$ , loaded with an input capacitance of 22 pF, has a typical equivalent noise charge (ENC) of  $235\text{ e}^-$  (rms) using signal shaping with a peaking-time of 650 ns. Because the VPT has almost no dark current, the noise is not increased due to the leakage current of that photo detector. By applying the quantum efficiency and the internal gain of the VPT, the ENC of  $235\text{ e}^-$  (rms) corresponds to an energy noise level of 0.8 MeV (rms).

The second circuit for the LAAPD readout is

a state-of-the-art CMOS ASIC (APFEL), which achieves a similar noise performance with a shorter peaking time of 250 ns. The advantage of the CMOS ASIC is the very low power consumption. The noise floor of the APFEL ASIC at  $-20^\circ\text{C}$ , loaded with an input capacitance of 270 pF, has a typical equivalent noise charge (ENC) of  $4150\text{ e}^-$  (rms). Based on measurements of PWO-II light production and the amplification characteristics of the photon sensor, this corresponds to an energy noise level of 0.9 MeV (rms). This is about the same level as achieved in the forward endcap EMC with the VPT readout. Both systems will allow an energy threshold of 3 MeV and thus fulfill the requirements. The ASIC was designed in a 350 nm CMOS technology. The power consumption at  $-20^\circ\text{C}$  is 52 mW per channel. Prototypes have been produced on Multi Project Wafer (MPW) runs of the EURO PRACTICE IC prototyping program. For the instrumentation of the electromagnetic calorimeter about 23000 pieces of the preamplifier are needed for the barrel EMC. These amounts of ASICs can no longer be produced cost effectively with MPW runs, thus a chip production campaign has to be started in due time.

The readout of the electromagnetic calorimeter is based on the digitization of the amplified signal-shape response of LAAPD and VPT photo sensors to the light output of PWO-II crystals. The digitizer modules are located at a distance of 20–30 cm and 90–100 cm for the barrel EMC and the forward endcap EMC, respectively, away from the analogue circuits and outside the cold volume. Signal transfer from the front-end over short distances is achieved by flat cables with low thermal budget. The digitizers consist of high-frequency, low-power pipelined ADC chips, which continuously sample the amplified and shaped signals. With an 80 MHz sampling ADC a time resolution better than 1 ns has been achieved at energy deposits above 60 MeV and 150 ps at energies above 500 MeV. At the lower energies the time resolution is limited by APD- and preamplifier-noise. This time resolution is sufficient for maintaining a good event correlation and rejecting background hits or random noise. The sampling is followed by the digital logic, which processes time-discrete digital values, detects hits and forwards hit-related information to the multiplexer module via optical fibers. The multiplexer modules will be located in the DAQ hut and they perform advanced signal processing to extract amplitude and signal-time information.

The front-end electronics of the barrel EMC is located inside the solenoid magnet where any access

for maintenance or repair is limited to shutdown periods of the HESR, expected to occur once a year. Redundancy in the system architecture is achieved by arranging the digitization of the two APDs of every crystal in two blocks, respectively, and providing interconnections at the level of FPGA using high-speed links. A prototype ADC module has been developed containing 32 channels of 12 bit 65 MSPS ADCs. The total power consumption of the module is 15 W.

The EMC and its subcomponents will be embedded in the general Detector Control System (DCS) structure of the complete  $\bar{P}$ ANDA detector. The aim of a DCS is to ensure the correct and stable operation of an experiment, so that the data taken by the detector are of high quality. The scope of the DCS is therefore very wide and includes all subsystems and other individual elements involved in the control and monitoring of the detector.

### 1.2.4 Mechanics and Integration

The calorimeter design in the target region is in full accordance with the constraints imposed by a fixed target experiment with the strong focusing of the momenta in forward direction. A nearly full coverage of  $\sim 99\%$  solid angle in the center-of-mass system is guaranteed in combination with the forward electromagnetic calorimeter, which is located downstream beyond the dipole magnet. The granularity is adapted to the tolerable maximum count rate of the individual modules and the optimum shower distribution for energy and position reconstruction by minimizing energy losses due to dead material. The front sizes of the crystal elements cover a nearly identical laboratory solid angle and have absolute cross sections close to the Molière radius.

The mechanical design is composed of three parts: the barrel part for a length of 2.5 m and 0.57 m of inner radius; the forward endcap for a diameter of 2 m located at 2.1 m downstream from the target; and the backward endcap of 0.8 m in diameter located at 1 m upstream from the target. The conceptual design of these elements is equivalent. The basic PWO crystal shape is a truncated pyramid of 200 mm length and this principle is based on the “flat-pack” configuration used in the CMS calorimeter. Right angle corners are introduced in order to simplify the CAD design and the mechanical manufacturing process to reduce machining costs. The presented geometry foresees that the crystals are not pointing toward the target position. A tilt of a few degrees is added on the focal axis to reduce the

dead zone effect and to ensure that particles entering between crystals will always cross a significant part of a crystal. The crystals are wrapped in a foil of a high reflectivity (98 %) and inserted in carbon fiber alveoles to hold them by the back. This helps also to avoid any piling-up stress and any heavy material in front of the crystals. The nominal distance between crystals is around  $600\ \mu\text{m}$  taking into account the thickness of the reflector ( $2 \times 65\ \mu\text{m}$ ), carbon fiber alveoles ( $2 \times 200\ \mu\text{m}$ ) and mechanical free gaps.

All crystals have a common length of 200 mm corresponding to 22 radiation lengths, which allows optimum shower containment up to 15 GeV photon energy and limits the nuclear counter effect in the subsequent photo sensor to a tolerable level.

The necessary thermal shield for the low-temperature operation of the EMC is made of panels using either thin components with high thermal resistivity and low material budget (in terms of  $X_0$ ) in front of the crystals or thicker standard foam in the other areas. The cooling circuit is composed of carbon fiber or copper thermal screens depending on the position. Silicone oil, Syltherm XLT has been chosen as cooling liquid for its low viscosity and high thermal efficiency. To avoid any moisture or ice, dry nitrogen gas is flowing through the detector which therefore has to be made airtight. All these elements, crystals, front-end electronics and thermal screens are sustained by a metallic support structure at room temperature connected to the mainframe of the  $\bar{P}$ ANDA magnet or yoke, for the barrel or the endcaps, respectively. On these structures boards and various services are implemented as the digitizing, optical fibers for calibration and data transfer, or cables for the supply of electrical power and sensors for the detector control system. The electronics itself consists of a low-noise and low-power consumption charge sensitive preamplifier connected to the digitizer part by flat cables to reduce the heat transfer.

The mechanical designs of the barrel and the endcaps differ in some details. The barrel is divided in 16 slices of 710 crystals each and 11 different shapes of crystals are necessary to fill the volume. The average crystal has approximately a square front face of 21.3 mm and a square rear face (readout) of 27.3 mm for an average mass of 0.98 kg. Each slice is divided in 6 modules for an easier construction and assembled to a stainless steel support beam. Two rings connect all these slices to make a compact cylindrical calorimeter inserted into the magnet by special tools. All the barrel services are going

through the yoke on its backward side.

The endcaps are designed as a wall structure with quadrant symmetry. Each quarter is composed of subunit structures composed of 16 crystals each inserted in carbon fiber alveoles and screwed through an interface insert to a thick aluminum back plate. Contrary to the barrel, only one shape of crystal is necessary for the endcaps and the average dimensions are for the front face 24.4 mm and for the rear face 26 mm.

The feasibility of the construction of such devices has been validated by the construction of several prototypes. The last one and the most representative is a 60-crystal prototype which uses some crystals from the barrel and integrates all the different elements described above. It permits to check the mechanical design and to focus on the result of the temperature stability which shows a promising result of  $\pm 0.05^\circ\text{C}$ . In a next iteration, a mechanical prototype with 200 crystals is presently under construction. This device is primarily meant for studying stable operation and cooling by simulating two adjacent detector slices of the barrel section of the EMC.

### 1.2.5 Calibration and Monitoring

The ultimate performance of the EMC can only be reached with a precise calibration of the individual crystal channels. The energy resolution of less than 2% at energies above 1 GeV demands a precision at the sub-percent level. To reach this goal, three methods are combined: A pre calibration with cosmic muons, in situ calibration with physics events and continuous monitoring with a light-pulser system.

Before the start up of the experiment all crystals will be calibrated in situ with cosmic muons at a level of 10% accuracy. The correspondence between the light output of a muon and a photon will be determined with test beams. The position reconstruction algorithm will also be optimized at test beams.

The final calibration will be performed with physics events during data taking. Events with three to four  $\pi^0$  or  $\eta$  mesons in the final state serve as an input to apply the calibration by constraining the energy measurements to the invariant mass of the meson. A dedicated software trigger will select the events based on total energy and multiplicity at a rate of about 4 kHz. An integrated luminosity of  $8 \text{ pb}^{-1}$ , accumulated in less than a day will be enough to perform a full calibration. With the hardware-

trigger free concept of  $\overline{\text{P}}\text{ANDA}$  the full event selection relies on the online trigger system. An efficient operation requires a quick calibration of the EMC. This will be achieved by combining the calibration constants from the previous day with the information from the light-pulser system.

The amount of collected light per MeV may change slightly due to radiation damage. Radiation damage affects only the optical transmission and can thus be corrected for by measuring the effect with the light-pulser system. With a light-pulser system operating at several wavelengths (455 nm, 530 nm and 660 nm) the effects from radiation damage can be disentangled from other effects such as changes of gain in the photodetectors and preamplifiers. The wavelength at 455 nm is close to the emission wavelength at 420 nm. A dominant defect center due to Molybdenum is at 530 nm and far in the red spectral region one does not expect any radiation damage so that one can control separately the readout chain including the photo sensor.

Ultra-bright LEDs driven by electronic circuits reproducing the time dependence of the PWO scintillation light will serve as the light source. The light will be distributed to the crystal back face by radiation hard silica/silica fibers. The normalizations of the pulses are done with temperature stabilized Si PIN photodiodes. A test system showed stabilities of 0.1 to 0.2% over a day, which is enough to follow the variations of the light output up to the next full calibration.

A first prototype of the light-pulser system is already implemented into the PROTO60 array and operating.

### 1.2.6 Simulation

The simulation studies are focused on the expected performance of the planned EMC with respect to the energy and spatial resolution of reconstructed photons, on the capability of an electron hadron separation, and also on the feasibility of the planned physics program of  $\overline{\text{P}}\text{ANDA}$ .

The software follows an object oriented approach, and most of the code is written in C++. Several proven software tools and packages from other HEP experiments have been adapted to the  $\overline{\text{P}}\text{ANDA}$  needs and are in use. It contains event generators with proper decay models for all particles and resonances involved in the individual physics channels, particle tracking through the complete  $\overline{\text{P}}\text{ANDA}$  detector by using the GEANT4 transport code, a digitization which models the signals and the signal

processing in the front-end electronics of the individual detectors, the reconstruction of charged and neutral particles as well as user friendly high-level analysis tools.

The digitization of the EMC has been realized with realistic properties of PWO crystals at the operational temperature at  $-25^{\circ}\text{C}$ . A Gaussian distribution of  $\sigma = 1\text{ MeV}$  has been used for the constant electronics noise. The statistical fluctuations were estimated by 80 phe/MeV produced in the LAAPD with an excess noise factor of 1.38. This results in a photo statistic noise term of  $0.41\% / \sqrt{E}$ . A comparison with a 3x3 crystal array test measurement demonstrates that this digitization gives sufficiently realistic results. The simulated line shape at discrete photon energies as well as the energy resolution as a function of the incident photon energy are in good agreement with the measurements.

Different EMC detector scenarios have been investigated in terms of energy and spatial resolutions. While the variation of the crystal length (15 cm, 17 cm and 20 cm) show nearly the same results for photons below 300 MeV, the performance gets significantly better for higher energetic photons for longer crystals. The 20 cm setup yields an energy resolution of 1.5% for 1 GeV photons, and even  $< 1\%$  for photons above 3 GeV. Another important aspect is the choice of the individual crystal reconstruction threshold, which is driven by the electronics noise term. Comparisons of the achievable resolution for the most realistic scenario with a noise term of  $\sigma = 1\text{ MeV}$  and a individual crystal reconstruction threshold of  $E_{xtl} = 3\text{ MeV}$  and a worse case ( $\sigma = 3\text{ MeV}$ ,  $E_{xtl} = 9\text{ MeV}$ ) show that the degradation increases by more than a factor of 2 for the lowest photon energies. This result demonstrates clearly that the single crystal threshold has a strong influence on the energy resolution.

The high granularity of the planned EMC provides an excellent position resolution for photons. Based on a standard cluster finding and bump splitting algorithm a  $\sigma$ -resolution of less than 3 mm can be obtained for energies above 1 GeV. This corresponds to roughly 10% of the crystal size.

Apart from accurate measurements of photons, the EMC is also the most powerful detector for the identification of electrons. Suitable properties for the distinction to hadrons and muons are the ratio of the energy deposit in the calorimeter to the reconstructed track momentum ( $E/p$ ) and shower shape variables derived from the cluster. Good electron identification can be achieved with a Multilayer Perceptron. For momenta above 1 GeV/c an electron efficiency of greater than 98% can be obtained while

the contamination by other particles is substantially less than 1%.

The reconstruction efficiency of the EMC is affected by the interaction of particles with material in front of the calorimeter. The largest contribution to the material budget comes from the Cherenkov detectors, which consist of quartz radiators of 1-2 cm. This corresponds to a radiation length between 17% and 50%, depending on the polar angle.

Four different benchmark channels relevant to the EMC have been investigated in order to demonstrate the feasibility of the planned physics program of  $\bar{\text{P}}\text{ANDA}$ . The studies cover charmonium spectroscopy, the search of charmed hybrids as well as the measurement of the time-like electromagnetic formfactors of the proton. All channels have in common that the particle detection with the electromagnetic calorimeter plays an essential role.

The first charmonium channel is the production of  $h_c$  in the formation mode. One of the main decay channels of this singlet P wave state ( $1^1P_1$ ) is the electromagnetic transition to the ground state  $\eta_c$  ( $\bar{\text{p}}\text{p} \rightarrow h_c \rightarrow \eta_c \gamma$ ). The analysis is based on the  $\eta_c \rightarrow \phi\phi$  decay mode with  $\phi \rightarrow K^+K^-$ . The three background channels  $\bar{\text{p}}\text{p} \rightarrow K^+K^-K^+K^-\pi^0$ ,  $\bar{\text{p}}\text{p} \rightarrow \phi K^+K^-\pi^0$  and  $\bar{\text{p}}\text{p} \rightarrow \phi\phi\pi^0$  are considered as the main contributors, having a few orders of magnitude higher cross sections. With one  $\gamma$ -ray from a  $\pi^0$  decay left undetected, these reactions have the same list of decay products as the studied  $h_c$  decay, and thus the  $\gamma$  reconstruction threshold plays an essential role for the background suppression. A signal to background ratio of better than 3 can be obtained with a reasonable photon reconstruction threshold of 10 MeV. With a 30 MeV threshold instead the signal to background ratio decreases by 20% to 40%.

The second charmonium channel is the formation of the recently discovered vector-state  $Y(4260)$  in the reaction  $\bar{\text{p}}\text{p} \rightarrow Y(4260) \rightarrow J/\psi\pi^0\pi^0$ . The challenge of this channel is to achieve an efficient and clean electron identification for the reconstruction of  $J/\psi \rightarrow e^+e^-$ , and also an accurate measurement of the final state photons originating from the  $\pi^0$  decays. After an event selection by applying kinematical and vertex fits, the reconstruction efficiency is found to be 14%, whereas the suppression rate for the background channels  $\bar{\text{p}}\text{p} \rightarrow J/\psi\eta\eta$  and  $\bar{\text{p}}\text{p} \rightarrow J/\psi\eta\pi^0$  is better than  $10^4$ . Another source of background which has been investigated are non-resonant  $\bar{\text{p}}\text{p} \rightarrow \pi^+\pi^-\pi^0\pi^0$  events. Due to the expected high cross section of this channel a suppression of at least  $10^7$  is required. With the currently available amount of MC events a suppres-

sion better than  $10^7$  is obtained.

Closely connected with charmonium spectroscopy is the search for charmonium hybrids. The ground state  $\psi_g$  is generally expected to be a spin-exotic  $J^{PC} = 1^{-+}$  state within the mass range of  $4.1 \text{ GeV}/c^2$  and  $4.4 \text{ GeV}/c^2$ . In  $\bar{p}p$  annihilations this state can be produced only in association with one or more recoil particles. In the study, the decay of the charmonium hybrid to  $\chi_{c1}\pi^0\pi^0$  with the subsequent radiative  $\chi_{c1} \rightarrow J/\psi\gamma$  decay is considered. The recoiling meson is reconstructed from the decay  $\eta \rightarrow \gamma\gamma$ . The reconstruction efficiency after all selection criteria is 4% and 6% for events with  $J/\psi \rightarrow e^+e^-$  and  $J/\psi \rightarrow \mu^+\mu^-$  decays, respectively. One major background source are events with hidden charm, in particular events including a  $J/\psi$  meson. The suppression is found to be  $7 \cdot 10^3$  for the channel  $\bar{p}p \rightarrow \chi_{c0}\pi^0\pi^0\eta$ ,  $3 \cdot 10^4$  for  $\bar{p}p \rightarrow \chi_{c1}\pi^0\eta\eta$  and  $1 \cdot 10^5$  for  $\bar{p}p \rightarrow \chi_{c1}\pi^0\pi^0\pi^0\eta$  and thus low contamination of the  $\psi_g$  signal from these background reactions is expected for the foreseen PANDA EMC.

The 4th channel is related to the measurement of the time-like electromagnetic formfactors of the proton. The electric ( $G_E$ ) and magnetic ( $G_M$ ) form factors can be described by analytic functions of the four momentum transfer  $q^2$  ranging from  $q^2 = -\infty$  to  $q^2 = +\infty$ . The  $\bar{p}p$  annihilation process allows to access positive  $q^2$  (time like) starting from the threshold of  $q^2 = 4m_p^2$ . In this region  $G_E$  and  $G_M$  become complex functions and their determination for low to intermediate momentum transfers is an open question. At PANDA the region between  $5 \text{ (GeV}/c)^2$  and  $22 \text{ (GeV}/c)^2$  can be accessed. The factors  $|G_E|$  and  $|G_M|$  can be derived from the angular distribution of  $\bar{p}p \rightarrow e^+e^-$  events. For a precise determination of the form factors a suppression better than  $10^8$  of the dominant background from  $\bar{p}p \rightarrow \pi^+\pi^-$  is required. With the currently available amount of MC events the background rejection of  $\bar{p}p \rightarrow \pi^+\pi^-$  is found to be better than  $10^8$ . Furthermore it was shown that the angular distributions can be obtained with a sufficient accuracy for the determination of  $G_E$  and  $G_M$ .

### 1.2.7 Performance

To prove the concept for the EMC, test experiments have concentrated on the response to photons and charged particles at energies below 1 GeV since those results are dominated by the photon statistics of the scintillator, the sensitivity and efficiency of the photo sensor and the noise contributions of the front-end electronics. The conclusions

are drawn based on crystal arrays comprising up to 25 modules. The individual crystals have a length of 200 mm and a rectangular shape with a cross section of  $20 \times 20 \text{ mm}^2$ . Only the most recently assembled array PROTO60 consists of 60 crystals in PANDA geometry. The tapered shape will improve the light collection due to the focusing effect of the geometry as known from detailed simulations at CMS/ECAL.

The performance tests completed up to now have been aiming at two complementary aspects. On one hand, the quality of full size PWO-II crystals has to be verified in in-beam measurements with energy-tagged photons covering the most critical energy range up to 1 GeV. Therefore, the scintillator modules were read out with standard photomultiplier tubes (Philips XP1911) with a bi-alkali photocathode, which covers  $\sim 35\%$  of the crystal endface with a typical quantum efficiency QE=18%. The noise contribution of the sensor can be neglected and the fast response allows an estimate of the time response. The achieved resolution deduced at various operating temperatures can be considered as benchmark limits for further studies including simulations and electronics development. The achieved resolution represent excellent lower limits of the performance to be expected. Operation at T=-25°C using a photomultiplier readout delivers an energy resolution of  $\sigma/E = 0.95\%/\sqrt{E/\text{GeV}} + 0.91\%$  for a  $3 \times 3$  sub-array accompanied with time resolutions below  $\sigma=130$  ps.

From the experimental tests one can extrapolate and confirm an energy resolution at an operating temperature of T= -25°C, which will be well below 2.5% at 1 GeV photon energy. The resolution of 13% at the lowest investigated shower energy of 20 MeV reflects the excellent statistical term. A threshold of 3 MeV is expected for an individual detector channel in the final setup. Relevant for the efficient detection and reconstruction of multi-photon events, an effective energy threshold of 10 MeV can be considered for the whole calorimeter as a starting value for cluster identification, which will enable us to disentangle from the measured data even physics channels with extremely low cross section.

The second R&D activity intended to come close to the final readout concept with large area avalanche photodiodes (LAAPD), which are mandatory for the operation within the magnetic field. All the reported results are obtained by collecting and converting the scintillation light only with a single quadratic LAAPD of  $10 \times 10 \text{ mm}^2$  active area with a quantum efficiency above 60% using newly developed low-noise preamplifiers but commercial electronics for the digitization. Not even taking ad-

vantage of an operation at the lowest temperature, an energy resolution of  $\sigma/E = 1.86\%/\sqrt{E/\text{GeV}} + 0.65\%$  has been achieved at  $T=0^\circ\text{C}$  for a  $3\times 3$  sub-array, which would come very close to a measurement using photomultiplier readout under similar conditions. In addition timing information can be expected with an accuracy well below 1 ns for energy depositions in a single crystal above 100 MeV. The present data document experimentally only the lower limit of the envisaged performance.

As mentioned above, radiation damage might reduce asymptotically the light output at the most forward angles, since relaxation processes become very slow at low temperatures. However, due to the further improved radiation hardness of the crystals, the loss of light yield will stay below 30%. Combining all improvements including the foreseen sensor concept the target spectrometer EMC can rely on a factor of 15-20 higher light yield compared to CMS/ECAL.

In order to study the operation of large arrays, the mechanical support structures, cooling and temperature stabilization concepts and long term stabilities, a large prototype comprising 60 tapered crystals in PANDA-geometry has been designed and brought into operation. First in-beam tests are scheduled for summer 2008.

### 1.3 Conclusion

The intrinsic performance parameters of the present quality of PWO-II, such as luminescence yield, decay kinetics and radiation hardness and the additional gain in light yield due to cooling down to  $T=-25^\circ\text{C}$  fulfill the basic requirements for the electromagnetic calorimeter. The general applicability of PWO for calorimetry in High-Energy Physics has been promoted and finally proven by the successful realization of the CMS/ECAL detector as well as the photon spectrometer ALICE/PHOS, both installed at LHC. The necessary mass production of high-quality crystals has been achieved at least at BTCP in Russia.

The operation at low temperatures imposes a technological challenge on the mechanical design, the cooling concept and thermal insulation under the constraints of a minimum material budget of dead material. Detailed simulations and prototyping have confirmed the concept and high accuracy has been achieved in temperature stabilization taking into account also realistic scenarios of the power consumption of the front-end electronics.

Concepts for the photon sensors and the readout

electronics have been tested. As the most sensitive element, a prototype of a custom designed ASIC implementing pre-amplification and shaping stages has been successfully brought into operation and will provide a large dynamic range of 12,000 with a typical noise level corresponding to  $\sim 1$  MeV.

The overall performance of the calorimeter will be controlled by injecting light from LED-sources distributed via optical fibers at the rear face of the crystal.

Based on the ongoing developments of PWO-II crystals and LAAPDs, respectively, a detailed program has been elaborated for quality assurance of the crystals and screening of the photo sensors.

The general layout of the mechanical structure is completed including first estimates of the integration into the PANDA detector. The concepts for signal- and HV-cables, cooling, slow control, monitoring as well as the stepwise assembly are worked out to guarantee that the crystal geometries could be finalized. Prototypes of the individual crystal containers, based on carbon fiber alveoles, have been fabricated and tested and are already implemented in the PROTO60 device.

The experimental data together with the elaborate design concepts and simulations show that the ambitious physics program of PANDA can be fully explored based on the measurement of electromagnetic probes, such as photons, electrons/positrons or the reconstruction of the invariant mass of neutral mesons.



## 2 Overview of the PANDA Experiment

---

$\bar{\text{P}}\text{ANDA}$  represents the efforts of the world-wide hadron physics community to attack the most fundamental and burning problems in the strong interaction. Given the complexity of the strong interaction in the non-perturbative regime this requires studies of rather diverse topics. The  $\bar{\text{P}}\text{ANDA}$  experiment should complement the new antiproton accelerator complex at the FAIR facility in Darmstadt. The high-energy storage ring HESR will deliver antiproton beams of unprecedented precision and intensity. It is a definite challenge for experimentalists to build an experiment which on one side covers an “as broad as possible” range of physics topics and on the other side has to go beyond the precision reached in the past with specialized setups. The proposed detector clearly has to be as modern and versatile as possible to fulfill the physics needs without jeopardizing quality.

The concept of  $\bar{\text{P}}\text{ANDA}$  is based on the experience from previous experiments in the field like the Crystal Barrel and OBELIX detectors at LEAR, the E835 experiment at Fermilab, the running FINUDA experiment at Frascati, and takes into account the concepts, which have been developed and implemented for the most modern LHC experiments.  $\bar{\text{P}}\text{ANDA}$  is a hermetic detector for charged and neutral particles in the energy range of 10 MeV up to 10 GeV. Precise micro-vertex tracking is mandatory as is good particle identification. The possibility to combine all these elements of information simultaneously for each given event gives the  $\bar{\text{P}}\text{ANDA}$  detector its unprecedented power, both in the ability to establish (rather than just suggest) new unexpected phenomena and in the redundant identification of interesting processes predicted by present models. Since the ratio of interesting events to backgrounds is often rather small we shall need all the capability that we can provide.

Clearly the design choices for a detector represent a well-thought balance between physics needs and the available resources. The hadron physics community will not have a second detector besides  $\bar{\text{P}}\text{ANDA}$  for this physics available and hence the detector has to be sufficiently robust, redundant and resistant to radiation damage for an operation over many years. Superb calibration and monitoring capabilities must be present for all subsystems. The data rate of  $2 \cdot 10^7$  antiproton annihilations per second poses not only a challenge for the individual detectors but also for the data acquisition system and

the online data selection.

In the cost/performance optimization one has to distinguish between items that at a later stage could be improved by upgrades if the need arises and items where scope reductions remain forever. To the latter belong in our opinion the choice of magnets and expensive items like calorimeters and the overall performance of a central tracker. Even though savings could be achieved by reducing even their parameters, we believe that going below the levels proposed in this document would lead to unacceptable technical and performance degradation. The current report should justify the parameter choices in view of the physics that should be achieved.

### 2.1 The Physics Case

One of the most challenging and fascinating goals of modern physics is the achievement of a fully quantitative understanding of the strong interaction, which is the subject of hadron physics. Significant progress has been achieved over the past few years thanks to considerable advances in experiment and theory. New experimental results have stimulated a very intense theoretical activity and a refinement of the theoretical tools.

Still there are many fundamental questions which remain basically unanswered. Phenomena such as the confinement of quarks, the existence of glueballs and hybrids, the origin of the masses of hadrons in the context of the breaking of chiral symmetry are long-standing puzzles and represent the intellectual challenge in our attempt to understand the nature of the strong interaction and of hadronic matter.

Experimentally, studies of hadron structure can be performed with different probes such as electrons, pions, kaons, protons or antiprotons. In antiproton-proton annihilation particles with gluonic degrees of freedom as well as particle-antiparticle pairs are copiously produced, allowing spectroscopic studies with very high statistics and precision. Therefore, antiprotons are an excellent tool to address the open problems.

The recently approved FAIR facility (Facility for Antiproton and Ion Research), which will be built as a major upgrade of the existing GSI laboratory in Germany, will provide antiproton beams of the

highest quality in terms of intensity and resolution, which will provide an excellent tool to answer the aforementioned fundamental questions.

The PANDA experiment (Pbar ANnihilations at DArmstadt) will use the antiproton beam from the High-Energy Storage Ring (HESR) colliding with an internal proton target at a CMS energy between 2.2 GeV and 5.5 GeV within a general purpose spectrometer to carry out a rich and diversified hadron physics program.

The experiment is being designed to fully exploit the extraordinary physics potential arising from the availability of high-intensity, cooled antiproton beams. The aim of the rich experimental program is to improve our knowledge of the strong interaction and of hadron structure. Significant progress beyond the present understanding of the field is expected thanks to improvements in statistics and precision of the data.

Many measurements are foreseen in PANDA, part of which can be carried out in parallel. In the following the main topics of the PANDA physics program are outlined.

**Charmonium spectroscopy.** The  $c\bar{c}$  spectrum can be computed within the framework of non-relativistic potential models and, more recently, in Lattice QCD. A precise measurement of all states below and above open charm threshold is of fundamental importance for a better understanding of QCD. All charmonium states can be formed directly in  $\bar{p}p$  annihilation.

At full luminosity PANDA will be able to collect several thousand  $c\bar{c}$  states per day. By means of fine scans it will be possible to measure masses with accuracies of the order of 100 keV and widths to 10% or better. The entire energy region below and above open charm threshold will be explored.

**Search for gluonic excitations (hybrids and glueballs).** One of the main challenges of hadron physics is the search for gluonic excitations, i.e. hadrons in which the gluons can act as principal components. These gluonic hadrons fall into two main categories: glueballs, i.e. states of pure glue, and hybrids, which consist of a  $q\bar{q}$  pair and excited glue. The additional degrees of freedom carried by gluons allow these hybrids and glueballs to have  $J^{PC}$  exotic quantum numbers: in this case mixing effects with nearby  $q\bar{q}$  states are excluded and this makes their experimental identification easier. The properties of glueballs and hybrids are determined by the long-distance features of QCD and

their study will yield fundamental insight into the structure of the QCD vacuum. Antiproton-proton annihilations provide a very favourable environment to search for gluonic hadrons.

**Study of hadrons in nuclear matter.** The study of medium modifications of hadrons embedded in hadronic matter is aimed at understanding the origin of hadron masses in the context of spontaneous chiral symmetry breaking in QCD and its partial restoration in a hadronic environment. So far experiments have been focused on the light quark sector. The high-intensity  $\bar{p}$  beam of up to 15 GeV/c will allow an extension of this program to the charm sector both for hadrons with hidden and open charm. The in-medium masses of these states are expected to be affected primarily by the gluon condensate.

Another study which can be carried out in PANDA is the measurement of  $J/\psi$  and D meson production cross sections in  $\bar{p}$  annihilation on a series of nuclear targets. The comparison of the resonant  $J/\psi$  yield obtained from  $\bar{p}$  annihilation on protons and different nuclear targets allows to deduce the  $J/\psi$ -nucleus dissociation cross section, a fundamental parameter to understand  $J/\psi$  suppression in relativistic heavy ion collisions interpreted as a signal for quark-gluon plasma formation.

**Open charm spectroscopy.** The HESR running at full luminosity and at  $\bar{p}$  momenta larger than 6.4 GeV/c would produce a large number of D meson pairs. The high yield (e.g. 100 charm pairs per second around the  $\psi(4040)$ ) and the well defined production kinematics of D meson pairs would allow to carry out a significant charmed meson spectroscopy program which would include, for example, the rich D and  $D_s$  meson spectra.

**Hypernuclear physics.** Hypernuclei are systems in which up or down quarks are replaced by strange quarks. In this way a new quantum number, strangeness, is introduced into the nucleus. Although single and double  $\Lambda$ -hypernuclei were discovered many decades ago, only 6 events of double  $\Lambda$ -hypernuclei were observed up to now. The availability of  $\bar{p}$  beams at FAIR will allow efficient production of hypernuclei with more than one strange hadron, making PANDA competitive with planned dedicated facilities. This will open new perspectives for nuclear structure spectroscopy and for studying the forces between hyperons and nucleons.

**Electromagnetic Processes.** In addition to the spectroscopic studies described above, PANDA will be able to investigate the structure of the nucleon using electromagnetic processes, such as Wide Angle Compton Scattering (WACS) and the process  $\bar{p}p \rightarrow e^+e^-$ , which will allow the determination of the electromagnetic form factors of the proton in the timelike region over an extended  $q^2$  region.

## 2.2 The High Energy Storage Ring

The FAIR facility at Darmstadt, Germany will provide anti-proton beams with very high quality. A 30 GeV/c proton beam is used to produce anti-protons which subsequently are accumulated and cooled at a momentum of 3.7 GeV/c. A derandomized bunch of anti-protons is then fed into the High Energy Storage Ring (HESR) which serves as slow synchrotron to bring the anti-protons to the desired energy and then as storage ring for internal target experiments. HESR will have both stochastic and electron cooling to deliver high quality beams.

### 2.2.1 Overview of the HESR

An important feature of the new anti-proton facility is the combination of phase-space cooled beams and dense internal targets, comprising challenging beam parameter in two operation modes: high-luminosity mode (HL) with beam intensities up to  $10^{11}$ , and high-resolution mode (HR) with a momentum spread down to a few times  $10^{-5}$ , respectively. Powerful electron and stochastic cooling systems are necessary to meet the experimental requirements.

The HESR lattice is designed as a racetrack shaped ring, consisting of two  $180^\circ$  arc sections connected by two long straight sections. One straight section will mainly be occupied by the electron cooler. The other section will host the experimental installation with internal  $H_2$  pellet target, RF cavities, injection kickers and septa (see Fig. 2.1). For stochastic cooling pickup and kicker tanks are also located in the straight sections, opposite to each other. To improve longitudinal stochastic cooling a third pickup location in the arc is presently being investigated. Special requirements for the lattice are dispersion free straight sections and small betatron amplitudes in the range of a few meters at the internal interaction point. In addition the betatron amplitudes at the electron cooler are adjustable within a large range.

Table 2.2.1 summarizes the specified injection parameters, experimental requirements and operation modes.

### 2.2.2 Beam Cooling

Beam equilibrium is of major concern for the high-resolution mode. Calculations of beam equilibria for beam cooling, intra-beam scattering and beam-target interaction are being performed utilizing different simulation codes like BETACOOOL (JINR, Dubna), MOCAC (ITEP, Moscow), and PTARGET (GSI, Darmstadt). Cooled beam equilibria calculations including special features of pellet targets have been carried out with a simulation code based on PTARGET.

An electron cooler is realized by an electron beam with up to 1 A current, accelerated in special accelerator columns to energies in the range of 0.4 to 4.5 MeV for the HESR. The 22 m long solenoidal field in the cooler section has a field range from 0.2 to 0.5 T with a magnetic field straightness in the order of  $10^{-5}$  [1]. This arrangement allows beam cooling for beam momenta between 1.5 GeV/c and 8.9 GeV/c.

In the HR mode RMS relative momentum spreads of less than  $4 \cdot 10^{-5}$  can be achieved with electron cooling.

The main stochastic cooling parameters were determined for a cooling system utilizing quarter-wave loop pickups and kickers with a band-width of 2 to 4 GHz. Stochastic cooling is presently specified above 3.8 GeV/c [2]. Applying stochastic cooling one can achieve an RMS relative momentum spread of 3 to  $4 \cdot 10^{-5}$  for the HR mode. In the HL mode an RMS relative momentum spread slightly below  $10^{-4}$  can be expected. Transverse stochastic cooling can be adjusted independently to ensure sufficient beam-target overlap.

### 2.2.3 Luminosity Estimates

Beam losses are the main restriction for high luminosities, since the antiproton production rate is limited. Three dominating contributions of beam-target interaction have been identified: Hadronic interaction, single Coulomb scattering and energy straggling of the circulating beam in the target. In addition, single intra-beam scattering due to the Touschek effect has also to be considered for beam lifetime estimates. Beam losses due to residual gas scattering can be neglected compared to beam-target interaction, if the vacuum is better than

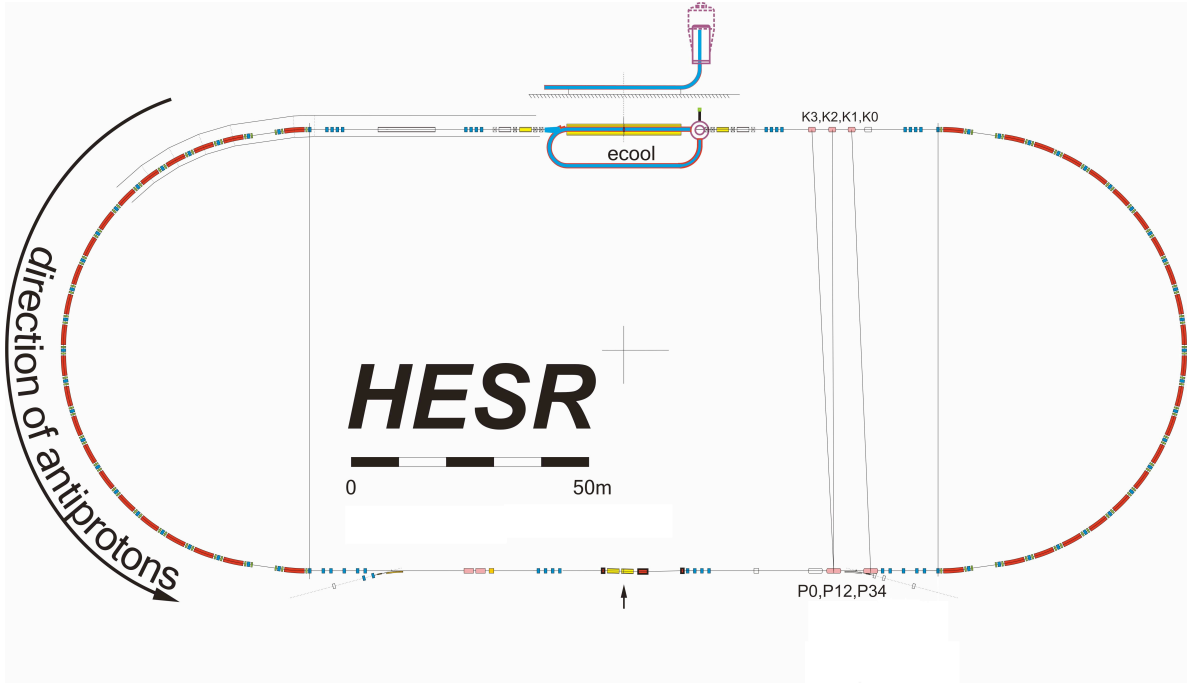


**Figure 2.1:** Schematic view of the HESR. Tentative positions for injection, cooling devices and experimental installations are indicated.

<b>Injection Parameters</b>	
Transverse emittance	1 mm · mrad (normalized, RMS) for $3.5 \cdot 10^{10}$ particles, scaling with number of accumulated particles: $\varepsilon_{\perp} \sim N^{4/5}$
Relative momentum spread	$1 \cdot 10^{-3}$ (normalized, RMS) for $3.5 \cdot 10^{10}$ particles, scaling with number of accumulated particles: $\sigma_p/p \sim N^{2/5}$
Bunch length	Below 200 m
Injection Momentum	3.8 GeV/c
Injection	Kicker injection using multi-harmonic RF cavities
<b>Experimental Requirements</b>	
Ion species	Antiprotons
$\bar{p}$ production rate	$2 \cdot 10^7$ /s ( $1.2 \cdot 10^{10}$ per 10 min)
Momentum / Kinetic energy range	1.5 to 15 GeV/c / 0.83 to 14.1 GeV
Number of particles stored in HESR	$10^{10}$ to $10^{11}$
Target thickness	$4 \cdot 10^{15}$ atoms/cm <sup>2</sup>
Transverse emittance	< 1 mm · mrad
Betatron amplitude E-Cooler	25–200 m
Betatron amplitude at IP	1–15 m
<b>Operation Modes</b>	
High resolution (HR)	Luminosity of $2 \cdot 10^{31}$ cm <sup>-2</sup> s <sup>-1</sup> for $10^{10}$ $\bar{p}$ RMS momentum spread $\sigma_p/p \leq 4 \cdot 10^{-5}$ , 1.5 to 9 GeV/c, electron cooling up to 9 GeV/c
High luminosity (HL)	Luminosity of $2 \cdot 10^{32}$ cm <sup>-2</sup> s <sup>-1</sup> for $10^{11}$ $\bar{p}$ RMS momentum spread $\sigma_p/p \sim 10^{-4}$ , 1.5 to 15 GeV/c, stochastic cooling above 3.8 GeV/c

**Table 2.1:** Injection parameters, experimental requirements and operation modes.

$10^{-9}$  mbar. A detailed analysis of all beam loss processes can be found in [3, 4].

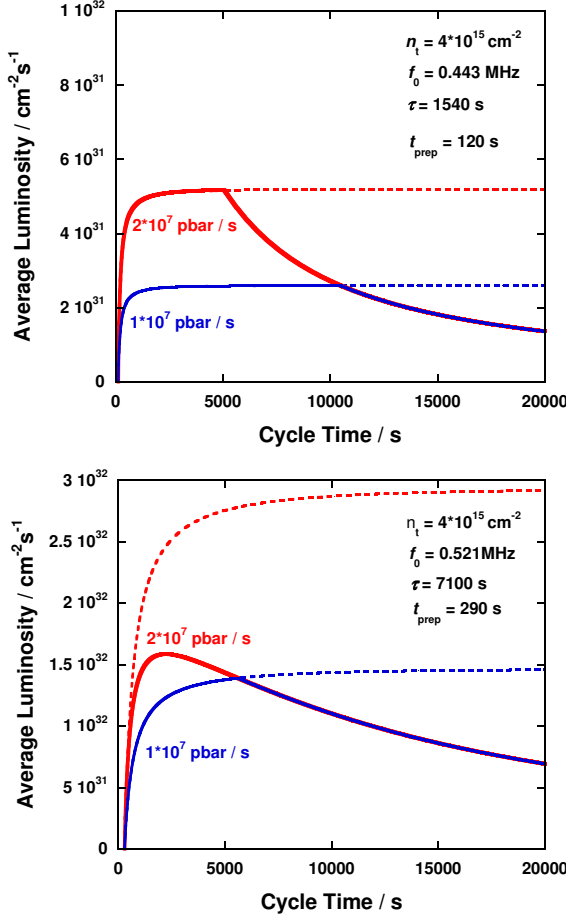


**Figure 2.2:** Average luminosity vs. cycle time at 1.5 (top) and 15 GeV/c (bottom). The maximum number of particles is limited to  $10^{11}$  (solid line), and unlimited (dashed lines).

The maximum luminosity depends on the antiproton production rate  $dN_{\bar{p}}/dt = 2 \cdot 10^7 / \text{s}$  and loss rate

$$L_{\text{max}} = \frac{dN_{\bar{p}}/dt}{\sigma_{\text{tot}}} \quad (2.1)$$

and ranges from  $0.8 \cdot 10^{32} \text{ cm}^{-2}\text{s}^{-1}$  at 1.5 GeV/c to  $3.9 \cdot 10^{32} \text{ cm}^{-2}\text{s}^{-1}$  at 15 GeV/c.

To calculate the average luminosity, machine cycles and beam preparation times have to be specified. After injection, the beam is pre-cooled to equilibrium (with target off) at 3.8 GeV/c. The beam is then ac-/decelerated to the desired beam momentum. A maximum ramp rate for the superconducting dipole magnets of 25 mT/s is specified. After reaching the final momentum beam steering and focusing in the target and beam cooler region takes

place. Total beam preparation time  $t_{\text{prep}}$  ranges from 120 s for 1.5 GeV/c to 290 s for 15 GeV/c.

In the high-luminosity mode, particles should be re-used in the next cycle. Therefore the used beam is transferred back to the injection momentum and merged with the newly injected beam. A bucket scheme utilizing broad-band cavities is foreseen for beam injection and the refill procedure. During acceleration 1% and during deceleration 5% beam losses are assumed. The average luminosity reads

$$\bar{L} = f_0 N_{i,0} n_t \frac{\tau [1 - e^{-t_{\text{exp}}/\tau}]}{t_{\text{exp}} + t_{\text{prep}}} \quad (2.2)$$

where  $\tau$  is the  $1/e$  beam lifetime,  $t_{\text{exp}}$  the experimental time (beam on target time), and  $t_{\text{cycle}}$  the total time of the cycle, with  $t_{\text{cycle}} = t_{\text{exp}} + t_{\text{prep}}$ . The dependence of the average luminosity on the cycle time is shown for different antiproton production rates in Fig. 2.2.

With limited number of antiprotons of  $10^{11}$ , as specified for the high-luminosity mode, average luminosities of up to  $1.6 \cdot 10^{32} \text{ cm}^{-2}\text{s}^{-1}$  can be achieved at 15 GeV/c for cycle times of less than one beam lifetime. If one does not restrict the number of available particles, cycle times should be longer to reach maximum average luminosities close to  $3 \cdot 10^{32} \text{ cm}^{-2}\text{s}^{-1}$ . This is a theoretical upper limit, since the larger momentum spread of the injected beam would lead to higher beam losses during injection due to the limited longitudinal ring acceptance. For the lowest momentum, more than  $10^{11}$  particles can not be provided in average, due to very short beam lifetimes. As expected, average luminosities are below  $10^{32} \text{ cm}^{-2}\text{s}^{-1}$ .

In the operation cycle of HESR the time for re-injection and acceleration of a bunch of anti-protons can be used by the experiment to do pulser calibrations and tests required to monitor noise and signal quality.

## 2.3 The PANDA Detector

The main objectives of the design of the PANDA experiment pictured in Fig. 2.3 are to achieve  $4\pi$  acceptance, high resolution for tracking, particle identification and calorimetry, high rate capabilities and a versatile readout and event selection. To obtain a good momentum resolution the detector is split into a *target spectrometer* based on a superconducting solenoid magnet surrounding the interaction point and measuring at high angles and a *forward spectrometer* based on a dipole magnet for small angle

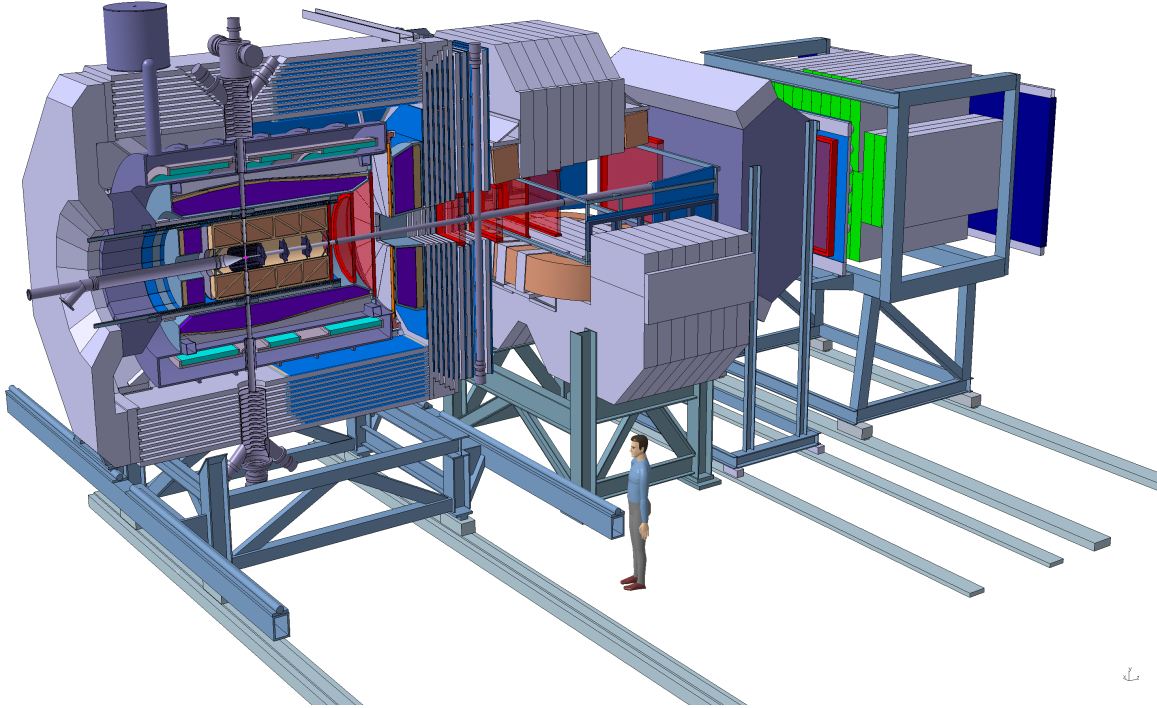


**Figure 2.3:** Artistic view of the  $\bar{P}$ ANDA Detector.

tracks. A silicon vertex detector surrounds the interaction point. In both spectrometer parts tracking, charged particle identification, electromagnetic calorimetry and muon identification are available to allow to detect the complete spectrum of final states relevant for the  $\bar{P}$ ANDA physics objectives.

In the following paragraphs the components of all detector subsystems are briefly explained.

### 2.3.1 Target Spectrometer

The target spectrometer surrounds the interaction point and measures charged tracks in a solenoidal field of 2 T. In the manner of a collider detector it contains detectors in an onion shell like configuration. Pipes for the injection of target material have to cross the spectrometer perpendicular to the beam pipe.

The target spectrometer is arranged in a barrel part for angles larger than  $22^\circ$  and an endcap part for the forward range down to  $5^\circ$  in the vertical and  $10^\circ$  in the horizontal plane. The target spectrometer is given in a side view in Fig. 2.4.

A main design requirement is compactness to avoid a too large and a too costly magnet and crystal

calorimeter.

#### 2.3.1.1 Target

The compact geometry of the detector layers nested inside the solenoidal magnetic field combined with the request of minimal distance from the interaction point to the vertex tracker leaves very restricted space for the target installations. The situation is displayed in Fig. 2.5, showing the intersection between the antiproton beam pipe and the target pipe being gauged to the available space. In order to reach the design luminosity of  $2 \cdot 10^{32} \text{ s}^{-1} \text{ cm}^{-2}$  a target thickness of about  $4 \cdot 10^{15}$  hydrogen atoms per  $\text{cm}^2$  is required assuming  $10^{11}$  stored anti-protons in the HESR ring.

These are conditions posing a real challenge for an internal target inside a storage ring. At present, two different, complementary techniques for the internal target are developed further: the cluster-jet target and the pellet target. Both techniques are capable of providing sufficient densities for hydrogen at the interaction point, but exhibit different properties concerning their effect on the beam quality and the definition of the interaction point. In addition, internal targets also of heavier gases, like deuterium,

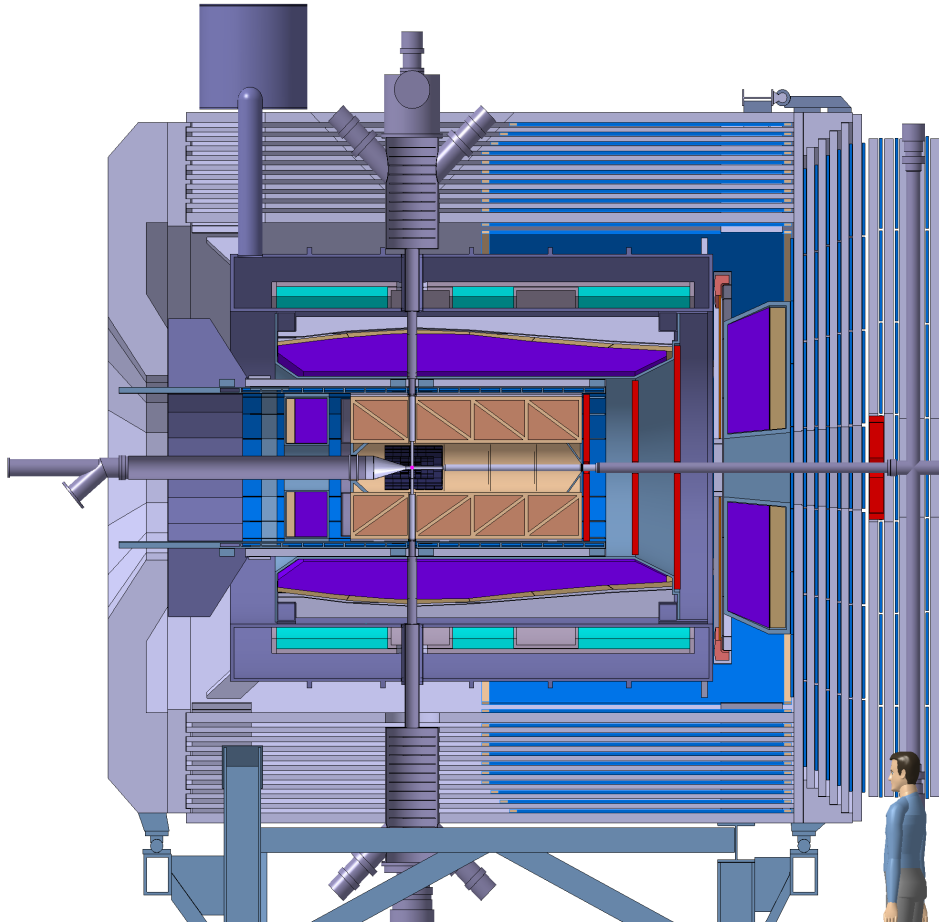


**Figure 2.4:** Side view of the target spectrometer.

nitrogen or argon can be made available.

For non-gaseous nuclear targets the situation is different in particular in case of the planned hyper-nuclear experiment. In these studies the whole upstream end cap and part of the inner detector geometry will be modified.

**Cluster-Jet Target** The expansion of pressurized cold hydrogen gas into vacuum through a Laval-type nozzle leads to a condensation of hydrogen molecules forming a narrow jet of hydrogen clusters. The cluster size varies from  $\cdot 10^3$  to  $\cdot 10^6$  hydrogen molecules tending to become larger at higher inlet pressure and lower nozzle temperatures. Such a cluster-jet with density of  $\cdot 10^{15}$  atoms/cm<sup>3</sup> acts as a very diluted target since it may be seen as a localized and homogeneous monolayer of hydrogen atoms being passed by the antiprotons once per revolution.

Fulfilling the luminosity demand for  $\bar{P}$ ANDA still re-

quires a density increase compared to current applications. Additionally, due to detector constraints, the distance between the cluster-jet nozzle and the target will be larger. The size of the target region will be given by the lateral spread of hydrogen clusters. This width should stay smaller than 10 mm when optimized with skimmers and collimators both for maximum cluster flux as well as for minimum gas load in the adjacent beam pipes. The great advantage of cluster targets is the homogeneous density profile and the possibility to focus the antiproton beam at highest phase space density. Hence, the interaction point is defined transversely but has to be reconstructed longitudinally in beam direction. In addition the low  $\beta$ -function of the antiproton beam keeps the transverse beam target heating effects at the minimum. The possibility of adjusting the target density along with the gradual consumption of antiprotons for running at constant luminosity will be an important feature.

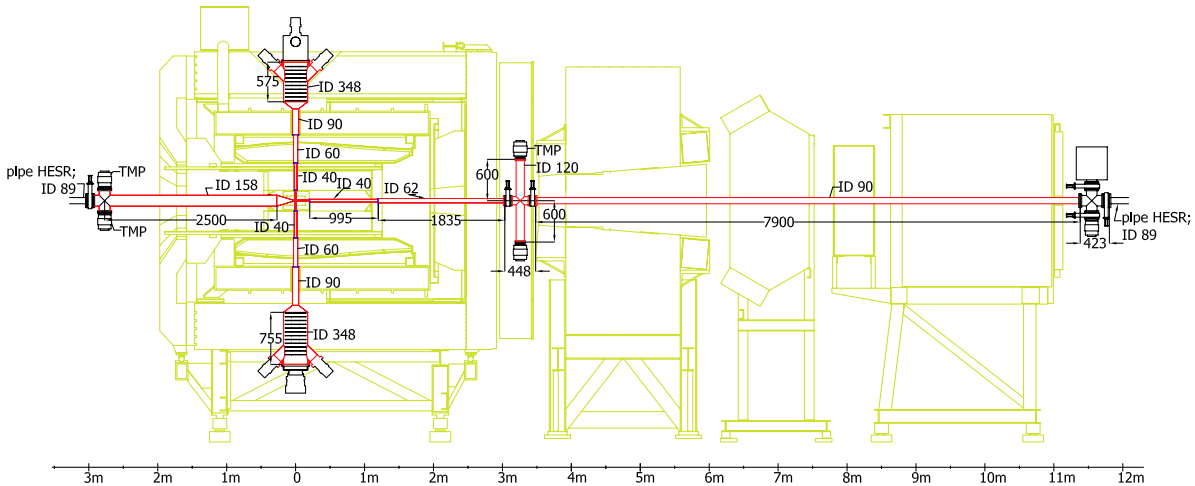


Figure 2.5: Schematic of the target and beam pipe setup with pumps.

**Pellet Target** The pellet target features a stream of frozen hydrogen micro-spheres, called pellets, traversing the antiproton beam perpendicularly. A pellet target presently is in use at the Wasa at COSY experiment. Typical parameters for pellets at the interaction point are the rate of  $1.0 - 1.5 \cdot 10^4 \text{ s}^{-1}$ , the pellet size of 25 - 40  $\mu\text{m}$ , and the velocity of about 60 m/s. At the interaction point the pellet train has a lateral spread of  $\sigma \approx 1 \text{ mm}$  and an interspacing of pellets that varies between 0.5 to 5 mm. With proper adjustment of the  $\beta$ -function of the coasting antiproton beam at the target position, the design luminosity for  $\bar{\text{PANDA}}$  can be reached in time average. The present R&D is concentrating on minimizing the luminosity variations such that the instantaneous interaction rate does not exceed the acceptance of the detector systems. Since a single pellet becomes the vertex for more than hundred nuclear interactions with antiprotons during the time a pellet traverses the beam, it will be possible to determine the position of individual pellets with the resolution of the micro-vertex detector averaged over many events. R&D is going on to devise an optical pellet tracking system. Such a device could determine the vertex position to about 50  $\mu\text{m}$  precision for each individual event independently of the detector. It remains to be seen if this device can later be implemented in  $\bar{\text{PANDA}}$ .

The production of deuterium pellets is also well established, the use of other gases as pellet target material does not pose problems.

**Other Targets** are under consideration for the hyper-nuclear studies where a separate target station upstream will comprise primary and secondary

target and detectors. Moreover, current R&D is undertaken for the development of a liquid helium target and a polarized  $^3\text{He}$  target. A wire target may be employed to study antiproton-nucleus interactions.

### 2.3.1.2 Solenoid Magnet

The magnetic field in the target spectrometer is provided by a superconducting solenoid coil with an inner radius of 90 cm and a length of 2.8 m. The maximum magnetic field is 2 T. The field homogeneity is foreseen to be better than 2 % over the volume of the vertex detector and central tracker. In addition the transverse component of the solenoid field should be as small as possible, in order to allow a uniform drift of charges in the time projection chamber. This is expressed by a limit of  $\int B_r/B_z dz < 2 \text{ mm}$  for the normalized integral of the radial field component.

In order to minimize the amount of material in front of the electromagnetic calorimeter, the latter is placed inside the magnetic coil. The tracking devices in the solenoid cover angles down to  $5^\circ/10^\circ$  where momentum resolution is still acceptable. The dipole magnet with a gap height of 1.4 m provides a continuation of the angular coverage to smaller polar angles.

The cryostat for the solenoid coils has two warm bores of 100 mm diameter, one above and one below the target position, to allow for insertion of internal targets.

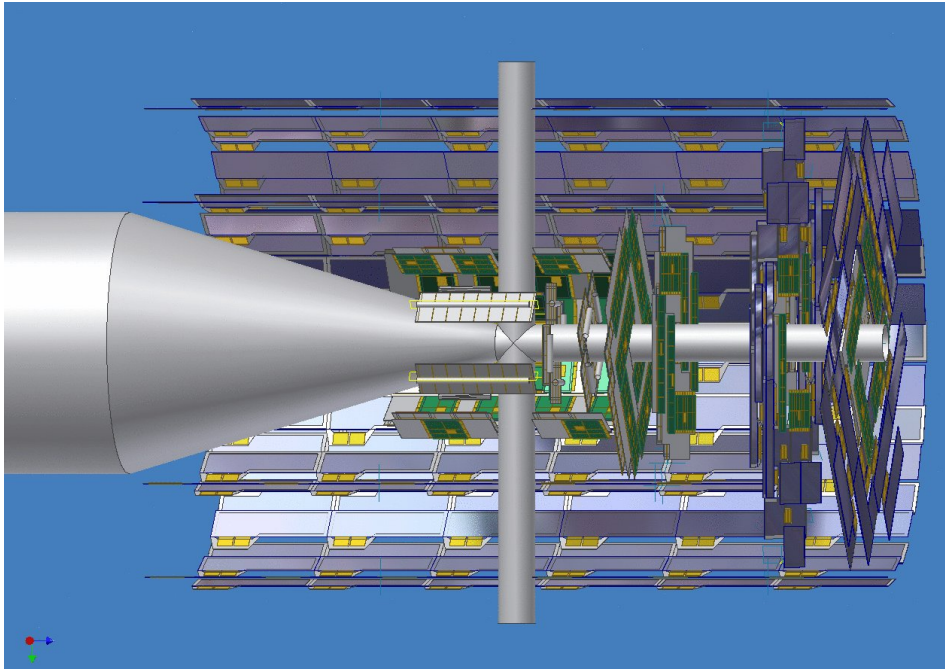


**Figure 2.6:** The Microvertex detector of  $\bar{\text{P}}\text{ANDA}$

### 2.3.1.3 Microvertex Detector

The design of the micro-vertex detector (MVD) for the target spectrometer is optimized for the detection of secondary vertices from  $D$  and hyperon decays and maximum acceptance close to the interaction point. It will also strongly improve the transverse momentum resolution. The setup is depicted in Fig. 2.6.

The concept of the MVD is based on radiation hard silicon pixel detectors with fast individual pixel readout circuits and silicon strip detectors. The layout foresees a four layer barrel detector with an inner radius of 2.5 cm and an outer radius of 13 cm. The two innermost layers will consist of pixel detectors while the outer two layers are considered to consist of double sided silicon strip detectors.

Eight detector wheels arranged perpendicular to the beam will achieve the best acceptance for the forward part of the particle spectrum. Here again, the inner two layers are made entirely of pixel detectors, the following four are a combination of strip detectors on the outer radius and pixel detectors closer to the beam pipe. Finally the last two wheels, made entirely of silicon strip detectors, are placed further downstream to achieve a better acceptance of hyperon cascades.

The present design of the pixel detectors comprises detector wafers which are 200  $\mu\text{m}$  thick (0.25%  $X_0$ ).

The readout via bump-bonded wafers with ASICs as it is used in ATLAS and CMS [5, 6] is foreseen as the default solution. It is highly parallelized and allows zero suppression as well as the transfer of analog information at the same time. The readout wafer has a thickness of 300  $\mu\text{m}$  (0.37%  $X_0$ ). A pixel readout chip based on a 0.13  $\mu\text{m}$  CMOS technology is under development for  $\bar{\text{P}}\text{ANDA}$ . This chip allows smaller pixels, lower power consumption and a continuously sampling readout without external trigger.

Another important R&D activity concerns the minimisation of the material budget. Here strategies like the thinning of silicon wafers and the use of ultra-light materials for the construction are investigated.

### 2.3.1.4 Central Tracker

The charged particle tracking devices must handle the high particle fluxes that are anticipated for a luminosity of up to several  $10^{32} \text{ cm}^{-2} \text{ s}^{-1}$ . The momentum resolution  $\delta p/p$  has to be on the percent level. The detectors should have good detection efficiency for secondary vertices which can occur outside the inner vertex detector (e.g.  $K_S^0$  or  $\Lambda$ ). This is achieved by the combination of the silicon vertex detectors close to the interaction point (MVD) with two outer systems. One system is covering a

large area and is designed as a barrel around the MVD. This will be either a stack of straw tubes (STT) or a time-projection chamber (TPC). The forward angles will be covered using three sets of GEM trackers similar to those developed for the COMPASS experiment at CERN. The two options for the central tracker are explained briefly in the following.

**Straw Tube Tracker (STT)** This detector consists of aluminized mylar tubes called *straws*, which are self supporting by the operation at 1 bar overpressure. The straws are arranged in planar layers which are mounted in a hexagonal shape around the MVD as shown in Fig. 2.7. In total there are 24 layers of which the 8 central ones are tilted to achieve an acceptable resolution of 3 mm also in  $z$  (parallel to the beam). The gap to the surrounding detectors is filled with further individual straws. In total there are 4200 straws around the beam pipe at radial distances between 15 cm and 42 cm with an overall length of 150 cm. All straws have a diameter of 10 mm. A thin and light space frame will hold the straws in place, the force of the wire however is kept solely by the straw itself. The mylar foil is 30  $\mu\text{m}$  thick, the wire is made of 20  $\mu\text{m}$  thick gold plated tungsten. This design results in a material budget of 1.3 % of a radiation length.

The gas mixture used will be Argon based with  $\text{CO}_2$  as quencher. It is foreseen to have a gas gain no greater than  $10^5$  in order to warrant long term operation. With these parameters, a resolution in  $x$  and  $y$  coordinates of about 150  $\mu\text{m}$  is expected.

**Time Projection Chamber (TPC)** A challenging but advantageous alternative to the STT is a TPC, which would combine superior track resolution with a low material budget and additional particle identification capabilities through energy loss measurements.

The TPC depicted in a schematic view in Fig. 2.8 consists of two large gas-filled half-cylinders enclosing the target and beam pipe and surrounding the MVD. An electric field along the cylinder axis separates positive gas ions from electrons created by ionizing particles traversing the gas volume. The electrons drift with constant velocity towards the anode at the upstream end face and create an avalanche detected by a pad readout plane yielding information on two coordinates. The third coordinate of the track comes from the measurement of the drift time of each primary electron cluster. In common TPCs the amplification stage typically occurs in multi-wire proportional chambers. These are gated by

an external trigger to avoid a continuous backflow of ions in the drift volume which would distort the electric drift field and jeopardize the principle of operation.

In  $\bar{P}$ ANDA the interaction rate is too high and there is no fast external trigger to allow such an operation. Therefore a novel readout scheme is employed which is based on GEM foils as amplification stage. These foils have a strong suppression of ion backflow, since the ions produced in the avalanches within the holes are mostly caught on the backside of the foil. Nevertheless about two ions per primary electron are drifting back into the ionisation volume even at moderate gains. The deformation of the drift field can be measured by a laser calibration system and the resulting drift can be corrected accordingly. In addition a very good homogeneity of the solenoid field with a low radial component is required.

A further challenge is the large number of tracks accumulating in the drift volume because of the high rate and slow drift. While the TPC is capable of storing a lot of tracks at the same time, their assignment to specific interactions has to be done by time correlations with other detectors in the target spectrometer. To achieve this, first a tracklet reconstruction has to take place. The tracklets are then matched against other detector signals or are pointed to the interaction. This requires either high computing power close to the readout electronics or a very high bandwidth at the full interaction rate.

**Forward GEM Detectors** Particles emitted at angles below  $22^\circ$  which are not covered fully by the Straw Tube Tracker or TPC will be tracked by three stations of GEM detectors placed 1.1 m, 1.4 m and 1.9 m downstream of the target. The chambers have to sustain a high counting rate of particles peaked at the most forward angles due to the relativistic boost of the reaction products as well as due to the small angle  $\bar{p}p$  elastic scattering. With the envisaged luminosity, the expected particle flux in the first chamber in the vicinity of the 5 cm diameter beam pipe is about  $3 \cdot 10^4 \text{ cm}^{-2} \text{ s}^{-1}$ . In addition it is required that the chambers work in the 2 T magnetic field produced by the solenoid. Drift chambers cannot fulfill the requirements here since they would suffer from aging and the occupancy would be too high. Therefore gaseous micropattern detectors based on GEM foils as amplification stages are chosen. These detectors have rate capabilities three orders of magnitude higher than drift chambers.

In the current layout there are three double planes with two projections per plane. The readout plane

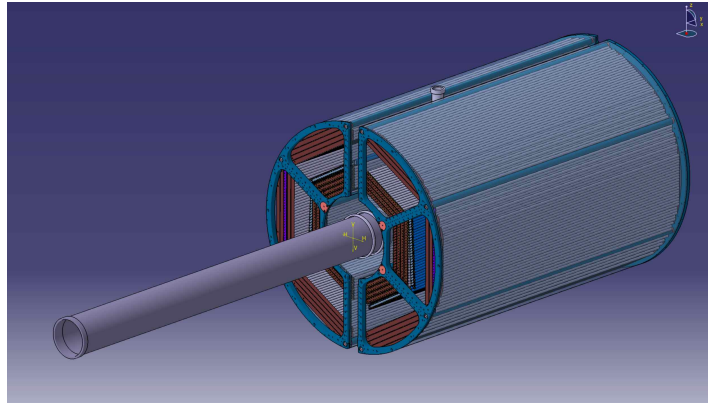


**Figure 2.7:** Straw Tube Tracker in the Target Spectrometer.

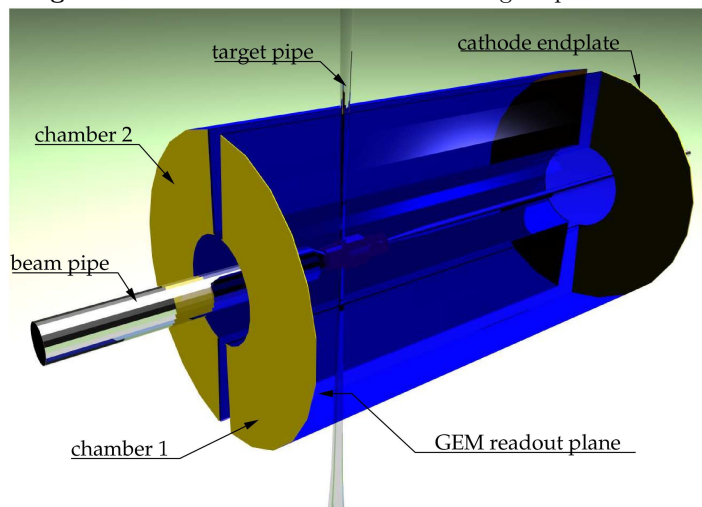


**Figure 2.8:** GEM Time Projection Chamber in the Target Spectrometer.

is subdivided in an outer ring with longer and an inner ring with shorter strips. The strips are arranged in two orthogonal projections per readout plane. Owing to the charge sharing between strip layers a strong correlation between the orthogonal strips can be found giving an almost 2D information rather than just two projections.

The readout is performed by the same frontend chips as are used for the silicon microstrips. The first chamber has a diameter of 90 cm, the last one of 150 cm. The readout boards carrying the ASICs are placed at the outer rim of the detectors.

### 2.3.1.5 Cherenkov Detectors and Time-of-Flight

Charged particle identification of hadrons and leptons over a large range of angles and momenta is an essential requirement for meeting the physics

objectives of  $\bar{P}$ ANDA. There will be several dedicated systems which, complementary to the other detectors, will provide means to identify particles. The main part of the momentum spectrum above 1 GeV/c will be covered by Cherenkov detectors. Below the Cherenkov threshold of kaons several other processes have to be employed for particle identification: The tracking detectors are able to provide energy loss measurements. Here in particular the TPC with its large number of measurements along each track excels. In addition a time-of-flight barrel can identify slow particles.

**Barrel DIRC** Charged particles in a medium with index of refraction  $n$ , propagating with velocity  $\beta c < 1/n$ , emit radiation at an angle  $\Theta_C = \arccos(1/n\beta)$ . Thus, the mass of the detected particle can be determined by combining the velocity information determined from  $\Theta_C$  with the momentum information from the tracking detectors.

A very good choice as radiator material for these detectors is fused silica (i.e. artificial quartz) with a refractive index of 1.47. This provides pion-kaon-separation from rather low momenta of 800 MeV/ $c$  up to about 5 GeV/ $c$  and fits well to the compact design of the target spectrometer. In this way the loss of photons converting in the radiator material can be reduced by placing the conversion point as close as possible to the electromagnetic calorimeter.

At polar angles between  $22^\circ$  and  $140^\circ$ , particle identification will be performed by the detection of internally reflected Cherenkov (DIRC) light as realized in the BaBar detector [7]. It will consist of 1.7 cm thick quartz slabs surrounding the beam line at a radial distance of 45 - 54 cm. At BaBar the light was imaged across a large stand-off volume filled with water onto 11 000 photomultiplier tubes. At  $\bar{\text{P}}\text{ANDA}$ , it is intended to focus the images by lenses onto micro-channel plate photomultiplier tubes (MCP PMTs) which are insensitive to magnet fields. This fast light detector type allows a more compact design and the readout of two spatial coordinates. In addition MCP PMTs provide good time resolution to measure the time of light propagation for dispersion correction and background suppression.

The DIRC design with its compact radiator mounted close to the EMC minimises the conversions. Part of these conversions can be recovered with information from the DIRC detector, as was shown by BaBar[8].

**Forward Endcap DIRC** A similar concept can be employed in the forward direction for particles between  $5^\circ$  and  $22^\circ$ . The same radiator, fused silica, is to be employed however in shape of a disk. At the rim around the disk focusing will be done by mirroring quartz elements reflecting onto MCP PMTs. Once again two spatial coordinates plus the propagation time for corrections will be read. The disk will be 2 cm thick and will have a radius of 110 cm. It will be placed directly upstream of the forward endcap calorimeter.

**Barrel Time-of-Flight** For slow particles at large polar angles particle identification shall be provided by a time-of-flight detector. In the target spectrometer the flight path is only in the order of 50 - 100 cm. Therefore the detector must have a very good time resolution between 50 and 100 ps.

Implementing an additional start detector would introduce too much material close to the interaction point deteriorating considerably the resolution of

the electromagnetic crystal calorimeter. In the absence of a start-detector relative timing of a minimum of two particles has to be employed.

As detector candidates scintillator bars and strips or pads of multi-gap resistive plate chambers are considered. In both cases a compromise between time resolution and material budget has to be found. The detectors will cover angles between  $22^\circ$  and  $140^\circ$  using a barrel arrangement around the STT/TPC at 42 - 45 cm radial distance.

### 2.3.1.6 Electromagnetic Calorimeters

Expected high count rates and a geometrically compact design of the target spectrometer require a fast scintillator material with a short radiation length and Molière radius for the construction of the electromagnetic calorimeter (EMC). Lead tungstate ( $\text{PbWO}_4$ ) is a high density inorganic scintillator with sufficient energy and time resolution for photon, electron, and hadron detection even at intermediate energies [9, 10, 11]. For high energy physics  $\text{PbWO}_4$  has been chosen by the CMS and ALICE collaborations at CERN [12, 13] and optimized for large scale production. Apart from a short decay time of less than 10 ns good radiation hardness has been achieved [14]. Recent developments indicate a significant increase of light yield due to crystal perfection and appropriate doping to enable photon detection down to a few MeV with sufficient resolution. The light yield can be increased by a factor of about 4 compared to room temperature by cooling the crystals down to  $-25^\circ\text{C}$ .

The crystals will be 20 cm long, i.e. approximately  $22 X_0$ , in order to achieve an energy resolution below 2% at 1 GeV [9, 10, 11] at a tolerable energy loss due to longitudinal leakage of the shower. Tapered crystals with a front size of  $2.1 \times 2.1 \text{ cm}^2$  will be mounted with an inner radius of 57 cm. This implies 11360 crystals for the barrel part of the calorimeter. The forward endcap calorimeter will have 3600 tapered crystals, the backward endcap calorimeter 592. The readout of the crystals will be accomplished by large area avalanche photo diodes in the barrel and vacuum phototriodes in the forward and backward endcaps.

The EMC allows to achieve an  $e/\pi$  ratio of  $10^3$  for momenta above 0.5 GeV/ $c$ . Therefore,  $e$ - $\pi$ -separation does not require an additional gas Cherenkov detector in favor of a very compact geometry of the EMC.

### 2.3.1.7 Muon Detectors

Muons are an important probe for, among others,  $J/\psi$  decays, semi-leptonic  $D$ -meson decays and the Drell-Yan process. The strongest background are pions and their decay daughter muons. However at the low momenta of  $\bar{P}$ ANDA the signature is less clean than in high energy physics experiments. To allow nevertheless a proper separation of primary muons from pions and decay muons a range tracking system will be implemented in the yoke of the solenoid magnet. Here a fine segmentation of the yoke as absorber with interleaved tracking detectors allows the distinction of energy loss processes of muons and pions and kinks from pion decays. Only in this way a high separation of primary muons from the background can be achieved.

In the barrel region the yoke is segmented in a first layer of 6 cm iron followed by 12 layers of 3 cm thickness. The gaps for the detectors are 3 cm wide. This is enough material for the absorption of pions in the momentum range in  $\bar{P}$ ANDA at these angles. In the forward endcap more material is needed. Since the downstream door of the return yoke has to fulfill constraints for space and accessibility, the muon system is split in several layers. Six detection layers are placed around five iron layers of 6 cm each within the door, and a removable muon filter with additional five layers of 6 cm iron is located in the space between the solenoid and the dipole. This filter has to provide cut-outs for forward detectors and pump lines and has to be built in a way that it can be removed with few crane operations to allow easy access to these parts.

As detector within the absorber layers rectangular aluminum drift tubes are used as they were constructed for the COMPASS muon detection system. They are essentially drift tubes with additional capacitively coupled strips read out on both ends to obtain the longitudinal coordinate.

### 2.3.1.8 Hypernuclear Detector

The hypernuclei study will make use of the modular structure of  $\bar{P}$ ANDA. Removing the backward endcap calorimeter will allow to add a dedicated nuclear target station and the required additional detectors for  $\gamma$  spectroscopy close to the entrance of  $\bar{P}$ ANDA. While the detection of anti-hyperons and low momentum  $K^+$  can be ensured by the universal detector and its PID system, a specific target system and a  $\gamma$ -detector are additional components required for the hypernuclear studies.

**Active Secondary Target** The production of hypernuclei proceeds as a two-stage process. First hyperons, in particular  $\Xi\bar{\Xi}$ , are produced on a nuclear target. In some cases the  $\Xi$  will be slow enough to be captured in a secondary target, where it reacts in a nucleus to form a double hypernucleus.

The geometry of this secondary target is determined by the short mean life of the  $\Xi^-$  of only 0.164 ns. This limits the required thickness of the active secondary target to about 25–30 mm. It will consist of a compact sandwich structure of silicon micro strip detectors and absorbing material. In this way the weak decay cascade of the hypernucleus can be detected in the sandwich structure.

**Germanium Array** An existing germanium-array with refurbished readout will be used for the  $\gamma$ -spectroscopy of the nuclear decay cascades of hypernuclei. The main limitation will be the load due to neutral or charged particles traversing the germanium detectors. Therefore, readout schemes and tracking algorithms are presently being developed which will enable high resolution  $\gamma$ -spectroscopy in an environment of high particle flux.

## 2.3.2 Forward Spectrometer

### 2.3.2.1 Dipole Magnet

A dipole magnet with a window frame, a 1 m gap, and more than 2 m aperture will be used for the momentum analysis of charged particles in the forward spectrometer. In the current planning, the magnet yoke will occupy about 2.5 m in beam direction starting from 3.5 m downstream of the target. Thus, it covers the entire angular acceptance of the target spectrometer of  $\pm 10^\circ$  and  $\pm 5^\circ$  in the horizontal and in the vertical direction, respectively. The maximum bending power of the magnet will be 2 Tm and the resulting deflection of the antiproton beam at the maximum momentum of 15 GeV/c will be  $2.2^\circ$ . The design acceptance for charged particles covers a dynamic range of a factor 15 with the detectors downstream of the magnet. For particles with lower momenta, detectors will be placed inside the yoke opening. The beam deflection will be compensated by two correcting dipole magnets, placed around the PANDA detection system.

### 2.3.2.2 Forward Trackers

The deflection of particle trajectories in the field of the dipole magnet will be measured with a set of wire chambers (either small cell size drift chambers

or straw tubes), two placed in front, two within and two behind the dipole magnet. This will allow to track particles with highest momenta as well as very low momentum particles where tracks will curl up inside the magnetic field.

The chambers will contain drift cells of 1 cm width. Each chamber will contain three pairs of detection planes, one pair with vertical wires and two pairs with wires inclined by  $+10^\circ$  and  $-10^\circ$ . This configuration will allow to reconstruct tracks in each chamber separately, also in case of multi-track events. The beam pipe will pass through central holes in the chambers. The most central wires will be separately mounted on insulating rings surrounding the beam pipe. The expected momentum resolution of the system for 3 GeV/c protons is  $\delta p/p = 0.2\%$  and is limited by the small angle scattering on the chamber wires and gas.

### 2.3.2.3 Forward Particle Identification

**RICH Detector** To enable the  $\pi/K$  and  $K/p$  separation also at the very highest momenta a RICH detector is proposed. The favored design is a dual radiator RICH detector similar to the one used at Hermes [15]. Using two radiators, silica aerogel and  $\text{C}_4\text{F}_{10}$  gas, provides  $\pi/K/p$  separation in a broad momentum range from 2–15 GeV/c. The two different indices of refraction are 1.0304 and 1.00137, respectively. The total thickness of the detector is reduced to the freon gas radiator (5%  $X_0$ ), the aerogel radiator (2.8%  $X_0$ ), and the aluminum window (3%  $X_0$ ) by using a lightweight mirror focusing the Cherenkov light on an array of phototubes placed outside the active volume. It has been studied to reuse components of the HERMES RICH.

**Time-of-Flight Wall** A wall of slabs made of plastic scintillator and read out on both ends by fast phototubes will serve as time-of-flight stop counter placed at about 7 m from the target. In addition, similar detectors will be placed inside the dipole magnet opening, to detect low momentum particles which do not exit the dipole magnet. The relative time of flight between two charged tracks reaching any of the time-of-flight detectors in the experiment will be measured. The wall in front of the forward spectrometer EMC will consist of vertical strips varying in width from 5 to 10 cm to account for the differences in count rate. With the expected time resolution of  $\sigma = 50$  ps  $\pi$ - $K$  and  $K/p$  separation on a  $3\sigma$  level will be possible up to momenta of 2.8 GeV/c and 4.7 GeV/c, respectively.

### 2.3.2.4 Forward Electromagnetic Calorimeter

For the detection of photons and electrons a Shashlyk-type calorimeter with high resolution and efficiency will be employed. The detection is based on lead-scintillator sandwiches read out with wavelength shifting fibers passing through the block and coupled to photomultipliers. The technique has already been successfully used in the E865 experiment [16]. It has been adopted for various other experiments [17, 18, 19, 20, 21, 22]. An energy resolution of  $4\%/\sqrt{E}$  [20] has been achieved. To cover the forward acceptance, 26 rows and 54 columns are required with a cell size of 55 mm, i.e. 1404 modules in total, which will be placed at a distance of 7–8 m from the target.

### 2.3.2.5 Forward Muon Detectors

For the very forward part of the muon spectrum a further range tracking system consisting of interleaved absorber layers and rectangular aluminium drift-tubes is being designed, similar to the muon system of the target spectrometer, but laid out for higher momenta. The system allows discrimination of pions from muons, detection of pion decays and, with moderate resolution, also the energy determination of neutrons and anti-neutrons.

## 2.3.3 Luminosity monitor

In order to determine the cross section for physical processes, it is essential to determine the time integrated luminosity  $L$  for reactions at the  $\bar{\text{P}}\text{ANDA}$  interaction point that was available while collecting a given data sample. Typically the precision for a relative measurement is higher than for an absolute measurement. For many observables connected to narrow resonance scans a relative measurement might be sufficient for  $\bar{\text{P}}\text{ANDA}$ , but for other observables an absolute determination of  $L$  is required. The absolute cross section can be determined from the measured count rate of a specific process with known cross section. In the following we concentrate on elastic antiproton-proton scattering as the reference channel. For most other hadronic processes that will be measured concurrently in  $\bar{\text{P}}\text{ANDA}$  the precision with which the cross section is known is poor.

The optical theorem connects the forward elastic scattering amplitude to the total cross section. The total reaction rate and the differential elastic reac-

tion rate as a function of the 4-momentum transfer  $t$  can be used to determine the total cross section.

The differential cross section  $d\sigma_{el}/dt$  becomes dominated by Coulomb scattering at very low values of  $t$ . Since the electromagnetic amplitude can be precisely calculated, Coulomb elastic scattering allows both the luminosity and total cross section to be determined without measuring the inelastic rate [23].

Due to the 2 T solenoid field and the existence of the MVD it appears most feasible to measure the forward going antiproton in  $\bar{\text{PANDA}}$ . The Coulomb-nuclear interference region corresponds to 4-momentum transfers of  $-t \approx 0.001 \text{ GeV}^2$  at the beam momentum range of interest to  $\bar{\text{PANDA}}$ . At a beam momentum of 6 GeV/ $c$  this momentum transfer corresponds to a scattering angle of the antiproton of about 5 mrad.

The basic concept of the luminosity monitor is to reconstruct the angle (and thus  $t$ ) of the scattered antiprotons in the polar angle range of 3-8 mrad with respect to the beam axis. Due to the large transverse dimensions of the interaction region when using the pellet target, there is only a weak correlation of the position of the antiproton at e.g.  $z=+10.0 \text{ m}$  to the recoil angle. Therefore, it is necessary to reconstruct the angle of the antiproton at the luminosity monitor. As a result the luminosity monitor will consist of a sequence of four planes of double-sided silicon strip detectors located as far downstream and as close to the beam axis as possible. The planes are separated by 20 cm along the beam direction. Each plane consists of 4 wafers (e.g. 2 cm  $\times$  5 cm  $\times$  200  $\mu\text{m}$ , with 50  $\mu\text{m}$  pitch) arranged radially to the beam axis. Four planes are required for sufficient redundancy and background suppression. The use of 4 wafers (up, down, right, left) in each plane allows systematic errors to be strongly suppressed.

The silicon wafers are located inside a vacuum chamber to minimize scattering of the antiprotons before traversing the 4 tracking planes. The acceptance for the antiproton beam in the HESR is  $\pm 3 \text{ mrad}$ , corresponding to the 89 mm inner diameter of the beam pipe at the quadrupoles located at about 15 m downstream of the interaction point. The luminosity monitor can be located in the space between the downstream side of the forward spectrometer hadronic calorimeter and the HESR dipole needed to redirect the antiproton beam out of the  $\bar{\text{PANDA}}$  chicane back into the direction of the HESR straight stretch (i.e. between  $z=+10.0 \text{ m}$  and  $z=+12.0 \text{ m}$  downstream of the target). At this distance from the target the luminosity moni-

tor needs to measure particles at a radial distance of between 3 and 8 cm from the beam axis.

As pilot simulations show, at a beam momentum of 6.2 GeV/ $c$  the proposed detector measures antiprotons elastically scattered in the range  $0.0006(\text{GeV})^2 < -t < 0.0035 (\text{GeV})^2$ , which spans the Coulomb-nuclear interference region. Based upon the granularity of the readout the resolution of  $t$  could reach  $\sigma_t \approx 0.0001 (\text{GeV})^2$ . In reality this value is expected to degrade to  $\sigma_t \approx 0.0005 (\text{GeV})^2$  when taking small-angle scattering into account. At the nominal  $\bar{\text{PANDA}}$  interaction rate of  $2 \cdot 10^7/\text{s}$  there will be an average of 10 kHz/cm<sup>2</sup> in the sensors. In comparison with other experiments an absolute precision of about 3% is considered feasible for this detector concept at  $\bar{\text{PANDA}}$ , which will be verified by more detailed simulations.

### 2.3.4 Data Acquisition

In many contemporary experiments the trigger and data acquisition (DAQ) system is based on a two layer hierarchical approach. A subset of specially instrumented detectors is used to evaluate a first level trigger condition. For the accepted events, the full information of all detectors is then transported to the next higher trigger level or to storage. The available time for the first level decision is usually limited by the buffering capabilities of the front-end electronics. Furthermore, the hard-wired detector connectivity severely constrains both the complexity and the flexibility of the possible trigger schemes.

In  $\bar{\text{PANDA}}$ , a data acquisition concept is being developed which is better matched to the high data rates, to the complexity of the experiment and the diversity of physics objectives and the rate capability of at least  $2 \cdot 10^7 \text{ events/s}$ .

In our approach, every sub-detector system is a self-triggering entity. Signals are detected autonomously by the sub-systems and are preprocessed. Only the physically relevant information is extracted and transmitted. This requires hit-detection, noise-suppression and clusterisation at the readout level. The data related to a particle hit, with a substantially reduced rate in the preprocessing step, is marked by a precise time stamp and buffered for further processing. The trigger selection finally occurs in computing nodes which access the buffers via a high-bandwidth network fabric. The new concept provides a high degree of flexibility in the choice of trigger algorithms. It makes trigger conditions available which are outside the capabilities of the standard approach. One obvious

example is displaced vertex triggering.

In this scheme, sub-detectors can contribute to the trigger decision on the same footing without restrictions due to hard-wired connectivity. Different physics can be accessed either in parallel or via software reconfiguration of the system.

High speed serial (10 Gb/s per link and beyond) and high-density FPGA (field programmable gate arrays) with large numbers of programmable gates as well as more advanced embedded features are key technologies to be exploited within the DAQ framework.

The basic building blocks of the hardware infrastructure which can be combined in a flexible way to cope with varying demands, are the following:

- Intelligent front-end modules capable of autonomous hit detection and data preprocessing (e.g. clustering, hit time reconstruction, and pattern recognition) are needed.
- A precise time distribution system is mandatory to provide a clock norm from which all time stamps can be derived. Without this, data from subsystems cannot be correlated.
- Data concentrators provide point-to-point communication, typically via optical links, buffering and online data manipulation.
- Compute nodes aggregate large amounts of computing power in a specialized architecture rather than through commodity PC hardware. They may employ fast FPGAs (fast programmable gate arrays), DSPs (digital signal processors), or other computing units. The nodes have to deal with feature extraction, association of data fragments to events, and, finally, event selection.

A major component providing the link for all building blocks is the network fabric. Here, special emphasis is put on embedded switches which can be cascaded and reconfigured to reroute traffic for different physics selection topologies. Alternatively, with an even higher aggregate bandwidth of the network, which according to projections of network speed evolution will be available by the time the experiment will start, a flat network topology where all data is transferred directly to processing nodes may be feasible as well. This requires a higher total bandwidth but would have a simpler architecture and allow event selection in a single environment. The bandwidth required in this case would be at least 200 GB/s. After event selection in the order of 100-200 MB/s will be saved to mass storage.

An important requirement for this scheme is that all detectors perform a continuous online calibration with data. The normal data taking is interleaved with special calibration runs. For the monitoring of the quality of data, calibration constants and event selection a small fraction of unfiltered raw data is transmitted to mass storage.

To facilitate the association of data fragments to events the beam structure of the accelerator is exploited: Every 1.8  $\mu$ s there is a gap of about 400 ns needed for the compensation of energy loss with a bucket barrier cavity. This gap provides a clean division between consistent data blocks which can be processed coherently by one processing unit.

### 2.3.5 Infrastructure

The target for antiproton physics is located in the straight section at the east side of the HESR. At this location an experimental hall of 43 m  $\times$  29 m floor space and 14.5 m height is planned (see Fig. 2.9). A concrete radiation shield of 2 m thickness on both sides along the beam line is covered by concrete bars of 1 m thickness to suppress the neutron sky shine. Within the elongated concrete cave the  $\bar{P}$ PANDA detector together with auxiliary equipment, beam steering, and focusing elements will be housed. The roof of the cave can be opened and heavy components hoisted by crane.

The shielded beam line area for the  $\bar{P}$ PANDA experiment including dipoles and focusing elements is foreseen to have 37 m  $\times$  9.4 m floor space and a height of 8.5 m with the beam line at a height of 3.5 m. The general floor level of the HESR is 2 m higher. This level will be kept for a length of 4 m in the north of the hall (right part in Fig. 2.9), to facilitate transport of heavy equipment into the HESR tunnel.

The target spectrometer with electronics and supplies will be mounted on rails which makes it retractable to a parking position outside the HESR beam line (i.e. into the lower part of the hall in Fig. 2.9). The experimental hall provides additional space for delivery of components and assembly of the detector parts. In the south corner of the hall, a counting house complex with five floors is foreseen. The lowest floor will contain various supplies for power, high voltage, cooling water, gases etc. The next level is planned for readout electronics including data concentrators. The third level will house the online computing farm. The fourth floor is at level with the surrounding ground and will house the control room, a meeting room and social rooms for the shift crew. Above this floor, hall electricity



- [5] Technical report, ATLAS Technical Design Report 11, CERN/LHCC 98-13.
- [6] Technical report, CMS Technical Design Report 5, CERN/LHCC 98-6.
- [7] H. Staengle et al., Nucl. Instrum. Meth. **A397**, 261 (1997).
- [8] A. Adametz, "Preshower Measurement with the Cherenkov Detector of the BABAR Experiment Aleksandra Adametz", Diploma thesis, Master's thesis, University Heidelberg, 2005.
- [9] K. Mengel et al., IEEE Trans. Nucl. Sci. **45**, 681 (1998).
- [10] R. Novotny et al., IEEE Trans. Nucl. Sci. **47**, 1499 (2000).
- [11] M. Hoek et al., Nucl. Instrum. Meth. **A486**, 136 (2002).
- [12] Technical Proposal, CERN/LHC 9.71.
- [13] Technical Proposal, 1994, CERN/LHCC 94-38, LHCC/P1.
- [14] E. Auffray et al., Moscow, 1999.
- [15] N. Akopov et al., Nucl. Instrum. Meth. **A479**, 511 (2002).
- [16] G. S. Atoyan et al., Nucl. Instrum. Meth. **A320**, 144 (1992).
- [17] G. David et al., Performance of the PHENIX EM calorimeter, Technical report, PHENIX Tech. Note 236, 1996.
- [18] A. Golutvin, (1994), HERA-B Tech. Note 94-073.
- [19] LHCb Technical Proposal CERN LHCC 98-4, LHCC/P4, 1998.
- [20] I.-H. Chiang et al., (1999), KOPIO Proposal.
- [21] H. Morii, (2004), Talk at NP04 Workshop at J-PARC.
- [22] G. Atoyan et al., Test beam study of the KOPIO Shashlyk calorimeter prototype, in *Proceedings of "CALOR 2004"*, 2004.
- [23] T. A. Armstrong et al., Phys. Lett. **B385**, 479 (1996).

## 3 Design Considerations

The  $\bar{\text{P}}\text{ANDA}$  experiment aims at various physics topics related to the very nature of large distance strong binding. Although the details and observables turn out to be different, most channels share one important feature - many photons and/or electrons/positrons in the final state. Examples are hidden charm decays of charmonium hybrids with neutral recoils and low-mass isoscalar S-waves (appearing in  $\pi^0\pi^0$ ), radiative charm decays and the nucleon structure physics. This puts special emphasis on the electromagnetic calorimeter, and its basic performance parameters have to be tuned to accomplish the effective detection of these channels in order to succeed in the basic programme of  $\bar{\text{P}}\text{ANDA}$ .

The basic function of an electromagnetic calorimeter is the efficient reconstruction of electrons, positrons and photons with high efficiency and low background. This is performed by measuring the deposited energy ( $E$ ) and the direction via the point of impact. ( $\theta$  and  $\phi$ ). High resolution is mandatory for a sufficient resolving power for final states with multiple electrons, positrons and photons.

Photons in the final state can originate from various sources. The most abundant sources are  $\pi^0$  and  $\eta$  mesons. Important probes are radiative charmonium decays (like  $\chi_{c1} \rightarrow J/\psi\gamma$ ), which are suppressed by the charm production yield or direct photons from rare electromagnetic processes. To distinguish radiatively decaying charmonium and direct photons from background with undetected photons (from  $\pi^0$  and  $\eta$  rich states) it is of utmost importance to identify very efficiently  $\pi^0$  and  $\eta$  by reducing the number of undetected photons due to solid angle or energy threshold.

The EMC may also provide timing information. This is needed to accomplish a proper distinction among different events. The annihilation rate goes up to several  $\cdot 10^7/\text{s}$  leading to  $\sigma_t \approx 10$  ns. Thus a fast scintillator is required for operation.

$\bar{\text{P}}\text{ANDA}$  will not have a threshold Cherenkov detector to discriminate pions from electrons and positrons. Therefore, the EMC has to add complementary information to the basic  $E/p$  information. Lateral shower shape information is needed to discriminate  $e^\pm$  from background. These informations are deduced from the difference of lateral shower shapes. Hadronic showers ( $K_L$ ,  $n$ , charged hadrons) in an electromagnetic calorimeter differ significantly due to the difference in energy loss per

interaction and the elementary statistics of these processes. The quality of this discrimination does not (to first order) depend on the actual choice of crystal geometry and readout, as long as the front face size of the crystal is matched to the Molière radius. Therefore, this does not place a strong requirement on the calorimeter design. Nevertheless, the final design process must incorporate an optimization of the electron-pion separation power.

One basic aspect of the  $\bar{\text{P}}\text{ANDA}$  EMC is the requirement on compactness to reduce cost. The price of the scintillator and the surrounding magnet scales with the cube of their dimension thus, e.g., leading to a 50% increase in price for  $\approx 15\%$  increase in radius.

### 3.1 Electromagnetic Particle Reconstruction

#### 3.1.1 Coverage Requirements

##### 3.1.1.1 Energy Threshold

Apart from energy resolution the minimum photon energy  $E_{thres}$  being accessible with the EMC is an important issue since it determines the very acceptance of low energy photons.

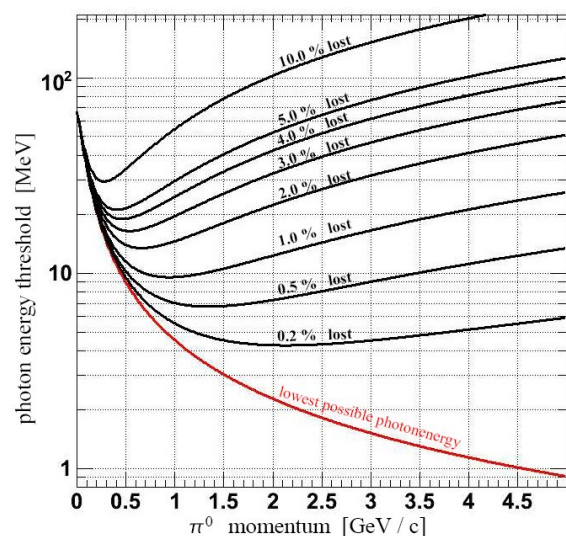


**Figure 3.1:** Percentage of  $\pi^0$  loss as a function of energy threshold.

It is easily shown that the bare photon and  $\pi^0$  loss rate is not very large even for energy thresholds higher than 20 MeV as long as a limit below 50 MeV is maintained (e.g.  $\pi^0$  loss in Fig. 3.1). Also the number of events dropped due to the energy threshold within the limits just mentioned is not dramatic. What is really driving the limit is the fact, that the physics being performed with PANDA requires an effective background rejection to distinguish radiative charmonium decays (as a tag for exotic charmonia) and other electromagnetic probes from background events with at least one undetected photon. So even small losses result in an unacceptable drop of the signal-to-background ratio.

How the energy threshold affects the sensitivity for physics with PANDA can be exemplified by the hybrid production channel  $p\bar{p} \rightarrow \eta_{c1}\eta$  with the charmonium hybrid  $\eta_{c1}$  decaying to  $\chi_{c1}\pi^0\pi^0$  leading to the final state  $J/\psi\gamma\pi^0\pi^0\eta$ . The production ratio between potential background and signal is expected to have the same order of magnitude. We consider only background with  $c\bar{c}$  content - e.g.  $J/\psi 3\pi^0\eta$ , since generic light quark background disappears to an undetectable level after the electron-id and charmonium cuts. However the decay branching ratios suppress the signal by one or two orders of magnitude compared to the background. Therefore, every effect of background leaking into the selection has to be minimized. Simulations show that the signal-to-background ratio depends almost quadratically on the minimum photon energy.

This is due to the fact that, if the energies of the undetected photons are small enough, the residual particles may be recognized as an exclusive event and may contribute to the background of a channel with one photon less. Due to imperfect energy resolution, there is a certain probability, that the reduced set of particles of the background event fulfill all selection criteria of the signal channel and even survive a kinematic fit with high probability.

From this discussion it is clear, that the lowest achievable value of  $E_{thres}$  is necessary to get the optimum in terms of photon detection. Although  $E_{thres} = 10$  MeV would be ideal in that context, technical limitations like noise or a reasonable coverage of a low energy shower may increase this value, but at least  $E_{thres} \leq 20$  MeV should be achieved to reach the physics goals of PANDA. More details are given in the simulation part of the report (Sec. 9).

### 3.1.1.2 Geometrical Coverage

The acceptance due to geometrical cuts is to 1<sup>st</sup> order proportional to  $(\Omega/4\pi)^n$  ( $n$  being the number of  $e^\pm, \gamma$ ). This is illustrated by the example of 6 photons and 90% solid angle coverage where the geometrical acceptance drops to 1/2. Since final states with many electrons, positrons and/or photons are one of the prime signals, these put, therefore, strong requirements on the angular coverage. As demonstrated in Sec. 3.1.1.1, undetected photons are an important source of background effects and the loss due to the solid angle coverage should be minimized to the mechanical limit. In the backward region the beampipe is the limiting factor, but a maximum opening of  $\approx 10^\circ - 15^\circ$  should be reached. In the forward direction a dipole bends all charged particles. In particular the  $\bar{p}$ -beam is inclined by  $2^\circ$ , which allows for  $0^\circ$  calorimetry to maximize performance. Additional holes for mechanics, support, pipes and cables have to be considered. Nevertheless, the angular coverage should be maximized and the aim is 99%  $4\pi$  coverage in the center-of-mass system. In addition to the target spectrometer EMC the forward part down to  $0^\circ$  will be covered by a shashlyk detector. The actual partitioning between forward endcap EMC and forward shashlyk is optimized to allow high momentum tracks to enter the spectrometer dipole.

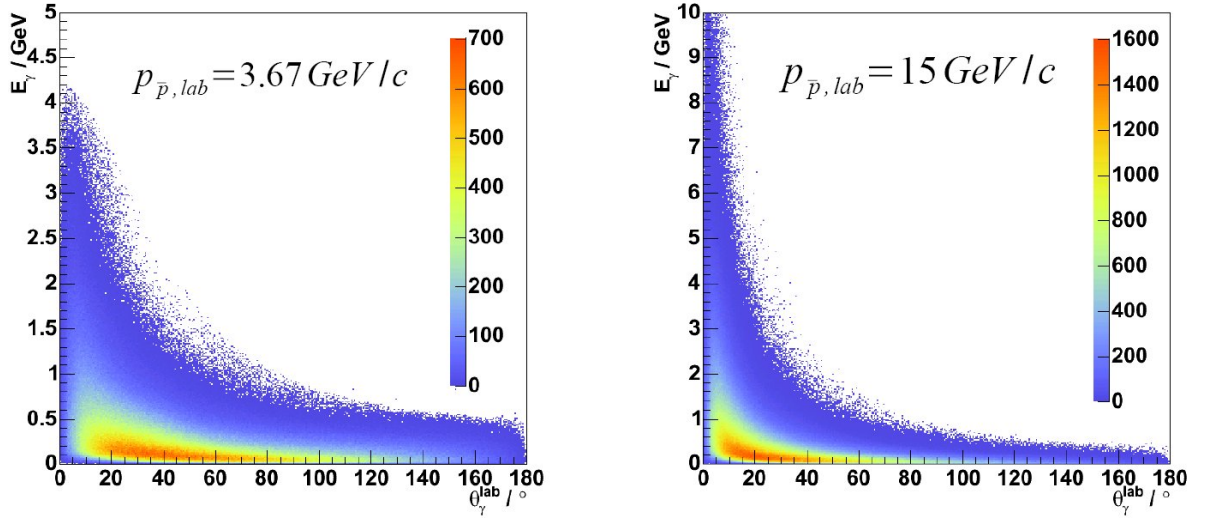
### 3.1.1.3 Dynamical Energy Range

Fig. 3.2 shows the range of energies from the DPM generator for two different momentum settings for the antiproton beam. The highest energies are in forward direction, while backward particles are relatively low in energy. Since low energy capabilities are mandatory for all regions of the calorimeter the dynamic range is mainly driven by the highest energy possible. The dynamic range for the various detector parts should at least cover in

- backward endcap EMC: 10(20) MeV- 0.7 GeV,
- barrel EMC: 10(20) MeV- 7.3 GeV, and
- forward endcap EMC: 10(20) MeV- 14.6 GeV.

### 3.1.1.4 Vertex Distribution

The primary vertex distribution is dictated by the overlap of beam and target stream. The worst case appears for a cluster-jet target with a spread in the order of a cm. In order to ensure that no photon escapes in the dead area between neighbouring crystals, a non-pointing geometry is needed. Ideally, the



**Figure 3.2:** Photon energy distribution vs. lab. angle for two momentum settings.

distance of closest approach of the pointer normal to the frontface of the crystal to the primary vertex should be at least 4 cm. Thus the focus of the endcap is off the average vertex position in  $z$  by at least 10 cm. In the barrel part a tilt of  $4^\circ$  is needed to fulfill the same requirement.

### 3.1.2 Resolution Requirements

#### 3.1.2.1 Energy Resolution

Apart from obtaining the best resolution to ensure the exclusiveness of events, the choice of the appropriate energy resolution has various additional aspects:

- Precise measurement of electron and positron energies for
  - very accurate  $E/p$  determination, and
  - optimum  $J/\psi$  mass resolution
- Efficient recognition of light mesons (e.g.  $\pi^0$  and  $\eta$ ) to reduce potential background.

Precise  $E/p$  measurement is an important asset to positively identify electrons and positrons against pions. This is achieved if the error on the electron energy is negligible compared to the momentum error from the tracking detectors ( $\approx 1\%$ ). This puts a limit on the resolution  $\frac{\sigma_E}{E} \leq 1.0\%$  at high energies.

Another effect of bad energy resolution is the bad mass determination of  $\pi^0$  and  $\eta$  mesons. At low energies this is due to the  $1/\sqrt{E}$  dependence of

the energy resolution, while at high energies this is dominated by the constant term. Experiments like Crystal Barrel, CLEO, BaBar and BES, with similarities in the topology and composition of final states have proven, that a  $\pi^0$  width of less than 8 MeV and  $\eta$  width of less than 30 MeV is necessary for reasonable final state decomposition. Assuming an energy dependence of the energy resolution of the form

$$\frac{\sigma_E}{E} = a \oplus \frac{b}{\sqrt{E/\text{GeV}}} \quad (3.1)$$

leads to the requirement  $a \leq 1\%$  and  $b \leq 2\%$ . This balance of values also ensures a  $J/\psi$  resolution which is well matched with the resolution of the typical light recoil mesons (like  $\eta$  and  $\omega$ ).

#### 3.1.2.2 Single Crystal Threshold

Energy threshold and energy resolution place a requirement on the required minimum single crystal energy  $E_{xtl}$ .

As a consequence this threshold puts a limit on the single crystal noise, since the single crystal cut (several MeV) should be high enough to exclude a random assignment of photons. This requirement can be relaxed by demanding a higher single-crystal energy to identify a bump, i.e. a local maximum in energy deposition (e.g. 10 MeV). Starting with those seeds, additional crystals are only collected in the vicinity of this central crystal. With typically 10 neighbours and not more than 10 particles the probability of less or equal of one random crystal hit per event for a single crystal cut of

$E_{xtl} = 3\sigma_{noise}$ . Fig. 3.3 shows that a single crystal threshold of  $E_{xtl} = 3$  MeV is needed to obtain the required energy resolution. Also the containment of low energy photons in more than the central crystal can only be achieved for  $E_{xtl} \leq 3$  MeV. From this consideration we deduce a limit for the total noise of  $\sigma_{E,noise} = 1$  MeV.

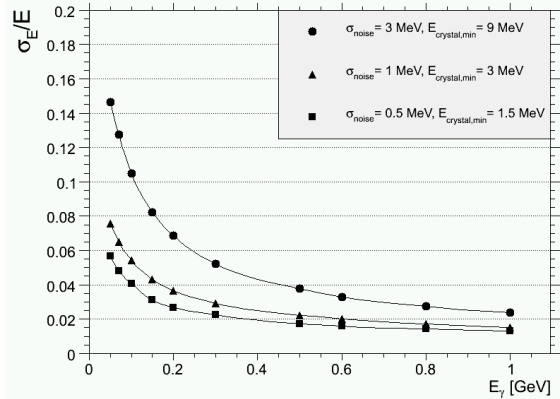


**Figure 3.3:** Comparison of the energy resolutions for three different single crystal reconstruction thresholds. The most realistic scenario with a noise term of  $\sigma = 1$  MeV and a single crystal threshold of  $E_{xtl} = 3$  MeV is illustrated by triangles, a worse case ( $\sigma = 3$  MeV,  $E_{xtl} = 9$  MeV) by circles and the better case ( $\sigma = 0.5$  MeV,  $E_{xtl} = 1.5$  MeV) by rectangles.

### 3.1.2.3 Spatial Resolution

The spatial resolution is mainly governed by the granularity. The reconstruction of the point of impact is achieved by weighted averaging of hits in adjacent crystals. In addition, to identify overlapping photons (e.g. due to  $\pi^0$  with small opening angles) it is mandatory to efficiently split crystal clusters into individual photons. This requires, that the central hits of the involved photons are separated by at least two crystal widths to assure two local maxima in energy deposition. If this can not be achieved, a cluster moment analysis has to be performed to identify  $\pi^0$  without identifying individual photons. This is possible down to a spatial separation of one crystal.

Fig. 3.4 shows the energy distribution of  $\pi^0$  and  $\eta$  for a cocktail of events with many photons for the three detector regions. The average (maximum)  $\pi^0/\eta$  momenta for the three detector parts are  $< 1$  GeV ( $< 1$  GeV),  $\approx 2$  GeV ( $\approx 7$  GeV) and  $\approx 5$  GeV ( $\approx 14$  GeV) for backward endcap EMC, barrel EMC and forward endcap EMC, respectively, for the highest incident antiproton momentum of

15 GeV/c. Fig. 3.5 shows the minimum opening angle for various  $\pi^0$  momenta. The angular coverage of a crystal should be tuned to the smallest  $\pi^0$  opening angle possible for this subdetector and should not exceed  $10^\circ$ ,  $2^\circ$  and  $0.5^\circ$ , respectively, to fully resolve the photons. These angles may be a factor 2 larger when taking cluster moment analysis into account.

The required spatial resolution is mainly governed by the required width of the  $\pi^0$  invariant mass peak in order to assure proper final-state decomposition. Fig. 3.6 shows the effect on the  $\pi^0$  mass resolution as a function of momentum for various spatial resolution values. Taking into account the average  $\pi^0$  energies a narrow  $\pi^0$  width below 8 MeV is maintained for a  $\cos\theta$  dependent spatial resolution of  $\leq 0.5^\circ$ ,  $\leq 0.3^\circ$  and  $\leq 0.1^\circ$  for backward endcap EMC, barrel EMC and forward endcap EMC, respectively. These resolutions are in accordance with the granularity requirement. They can be achieved by an asymmetric geometry where compactness is still maintained for the radial component, while it extends more to the forward direction.

## 3.2 Environment

### 3.2.1 Surrounding Detectors

#### 3.2.1.1 Magnet System

The EMC will be operated in a high solenoidal magnetic field (2 T). Therefore the sensors perpendicular (barrel part) to the field have to be field insensitive. In the endcaps the requirements due to the magnetic field are relaxed since the sensors would be differently oriented.

Backscattering in the magnet may take place. These effects are accounted for in the detector simulations in subsequent chapters.

#### 3.2.1.2 DIRC

Detectors of Internally Reflected Cherenkov Light (DIRC) are placed in the barrel part and in the forward endcap for particle identification. They are located near the front face of the scintillator and add substantially to the material budget before the EMC. It has been shown, that the preshower information of the Cherenkov light of the shower electrons of such a detector can be used to repair the distorted calorimeter information.

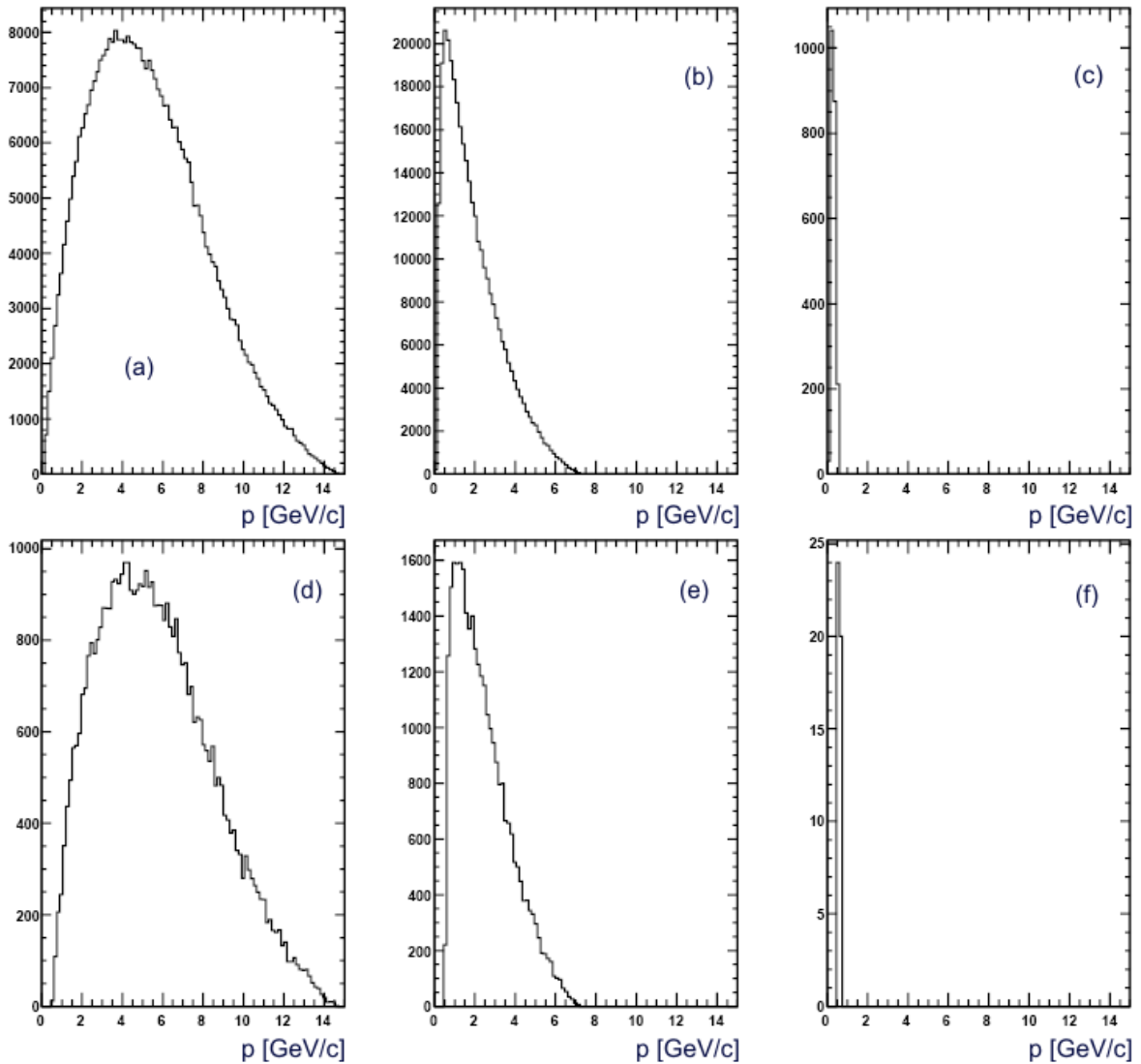


**Figure 3.4:**  $\pi^0$  and  $\eta$  energy spectrum (scale in GeV) for  $p_{\bar{p}} = 15 \text{ GeV}/c$  for the forward endcap EMC (left), barrel EMC (middle) and backward endcap EMC (right), for  $\pi^0$  (top) and  $\eta$  (bottom).

### 3.2.1.3 Other Systems

Various different target systems are foreseen for the PANDA experiment. Gas-Jet and Pellet targets require a target pipe perpendicular to the beam pipe. Since pumps have to be placed outside of the detector, the target pipes extend to the end of the magnet, thus crossing the EMC. Mechanical cutouts for these pipes have to be foreseen.

## 3.2.2 Count-rate and Occupancy

### 3.2.2.1 Signal Load

Fig. 3.7 and 3.8 show the hit rates ( $E_\gamma > 1 \text{ MeV}$ , DPM background generator) for a geometrical setup which fulfills the spatial requirements already mentioned. The rates are for the barrel part and the forward endcap, respectively. The detector has to be able to digest the maximum hit rate which happens for the highest beam momenta. The maximum rates per crystal are  $\approx 60 \text{ kHz}$  and  $\approx 500 \text{ kHz}$  for barrel EMC and forward endcap EMC respectively. For heavy targets the single crystal rate for the barrel EMC goes up to  $\approx 100 \text{ kHz}$  due to the

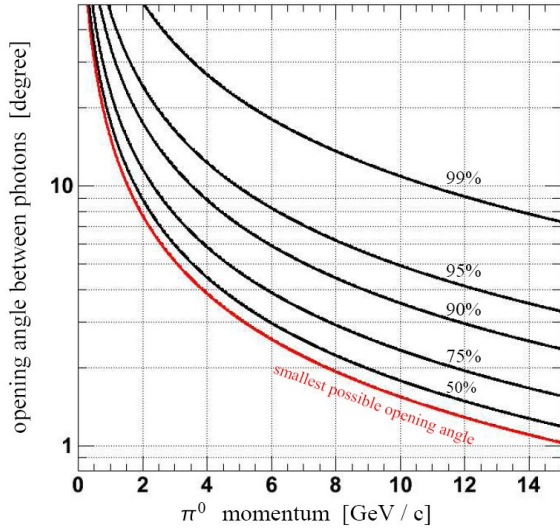


**Figure 3.5:** Minimum  $\pi^0$  opening angle vs. beam momentum.

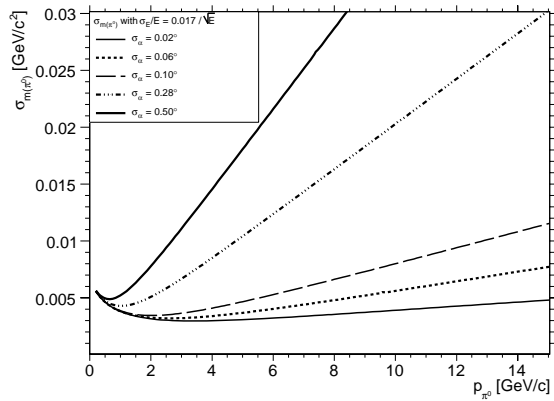


**Figure 3.6:**  $\pi^0$  mass resolution for various spatial resolution values vs. beam momentum.

reduced boost compared to  $p\bar{p}$  events.

### 3.2.2.2 Response and Shaping Time

The response time has to be short enough to allow event identification. Since the  $\bar{p}$  beam will have a time structure,  $\bar{P}$ ANDA has to be prepared to accept and instantaneous rate of up to 50 MHz on short timescales. This condition leads to a required time resolution for the relevant hit time  $t_0$  of 3 ns or less. The shaping time of the preamplification stage should be longer than the actual decay time of the scintillation mechanism to collect the whole signal. The shaping time should be maximised to improve the noise level. If the shaping time becomes too long pile-up occurs, since new hits are delivered on

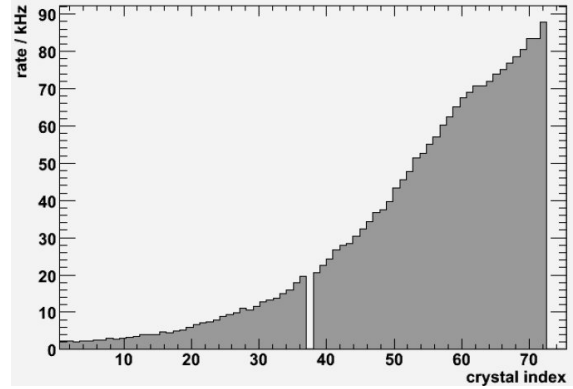


**Figure 3.7:** Hit rate in the barrel part from the DPM background generator at  $p_{\pi^0}=14$  GeV/c.

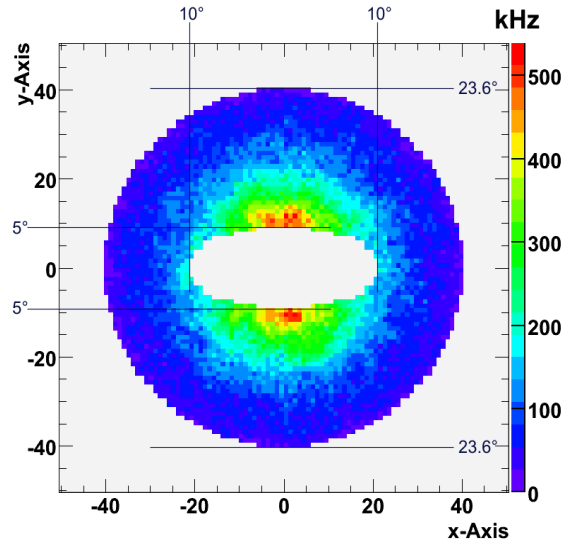


**Figure 3.8:** Hit rate in the forward part from the DPM background generator at  $p_{\pi^0}=14$  GeV/c.

top of a preceding hit. As mentioned previously, undetected photons are a severe cause of background. Therefore a maximum effective pile-up rate of less than 1% is required. In particular in the forward region this would lead to extremely short (and therefore unrealistic) shaping times. To reduce photon loss, the pile-up hits should be recovered. This can be achieved with a FADC system with appropriate sample frequency and proper hit detection (in hardware or software). In case of a FADC readout a pile-up rate up to 10% can be tolerated (including variations of the instantaneous rate) leading to shaping times of not more than  $\approx 100$  ns for the forward endcap EMC and  $\approx 400$  ns for barrel EMC and backward endcap EMC.

Using the hit rates from Sec. 3.2.2.1 and requiring less than 1% loss due to pile-up the shaping times would drop.

### 3.2.2.3 Radiation Hardness

Potential detector setups which fulfill the requirements already mentioned have been used to check for radiation doses. These simulations show that for the highest beam momenta the innermost crystals (setup as in Sec. 3.2.2.1) accumulate an energy dose of 25 mJ/h for  $p\bar{p}$  generic background (DPM background generator). The maximum dose does not increase with heavier targets. Due to the much reduced boost of the overall system, the hit rate in the innermost crystals is reduced dramatically (even with the same luminosity) and the dose in this case is distributed more evenly among crystal rings. For a crystal weight of 1 kg (in case of e.g. PWO or BGO) and a typical annual operation of not more than 5 kh the maximum annual dose would be 125 Gy (or 12.5 kRad/year). This strong constraint applies only to the forward crystals. For backward endcap EMC and barrel EMC the maximum energy doses (for  $p\bar{p}$  events) are  $30 \mu\text{J}/\text{h}$  (0.15 Gy annually) and 1.4 mJ/h (7 Gy annually), respectively. Due to the reduced boost, part of the barrel EMC and in particular the whole backward endcap EMC will have a much higher rate than with  $p\bar{p}$  events. To be on the safe side, all non-forward crystals should be radiation hard to an annual limit of 10 Gy.

## 3.2.3 Operational Aspects

### 3.2.3.1 Long- and Medium-term Stability

$\bar{\text{P}}\text{ANDA}$  will be operated in a factory mode, thus running for several months (up to 9 months) and will be suspended for the rest of the year for maintenance, repair and upgrade. This requires a long Mean-Time-between-Failure to the level of not more than 10 channels lost per year.

### 3.2.3.2 Maintenance of Sensors, Electronics and Environment

$\bar{\text{P}}\text{ANDA}$  is planned to operate for at least one decade. Therefore it is mandatory to allow access to all crystals, sensors and electronics for maintenance during down-time periods. It is envisaged to dismount the detector annually on the detector module level for service work. Therefore the overall mounting procedure has to be reversible and detector module oriented.

### 3.2.3.3 Calibration and Monitoring Prerequisites

The energy calibration has to be performed at a precision much better than the energy resolution, thus at the sub percent level. The  $\bar{\text{P}}\text{ANDA}$  DAQ relies on online trigger decisions performed on compute nodes. The use of the electromagnetic calorimeter for the trigger decisions requires the availability of calibration constants with sufficient precision in real time.

The monitoring system should detect any changes in the readout chain starting from the light transmission in the crystals to the digitizing modules.

## 3.3 Production and Assembly

### 3.3.1 Production Schemes

The fabrication of calorimeters has been exercised many times in the past. Many production and assembly procedures have been used in the past for other large scale projects. Whenever possible existing production schemes, equipment and personnel should be assimilated to reduce overall cost. Decent quality assurance processes are needed for all mass-produced parts.

### 3.3.2 Assembly Schemes

Modern large-scale detectors require a large number of channels and many mass-produced parts which have to be screened and stored for further assembly. Since not all parts can be stored and assembled at a single laboratory, complex logistics has to be arranged to ensure a smooth supply of parts throughout the production process.

## 3.4 Conclusion

The full list of requirements is compiled in Table 3.1.

In this technical design report of the EMC, we will demonstrate that a compact lead tungstate crystal calorimeter being operated at low temperatures and read out with LAAPDs and VPTs will fulfill the listed requirements on energy resolution, spatial resolution, energy threshold, timing and radiation hardness.

Test equipment of CMS, employed in the past for large-scale production, can be reused for  $\bar{\text{P}}\text{ANDA}$ .

	Required performance value		
Common properties			
energy resolution $\sigma_E/E$	$\leq 1\% \oplus \frac{\leq 2\%}{\sqrt{E/\text{GeV}}}$		
energy threshold (photons) $E_{thres}$	10 MeV (20 MeV tolerable)		
energy threshold (single crystal) $E_{xtl}$	3 MeV		
rms noise (energy equiv.) $\sigma_{E,noise}$	1 MeV		
angular coverage $\% 4\pi$	99 %		
mean-time-between-failures $t_{mtbf}$ (for individual channel)	2000 y		
Subdetector specific properties			
	backward ( $\geq 140^\circ$ )	barrel ( $\geq 22^\circ$ )	forward ( $\geq 5^\circ$ )
energy range from $E_{thres}$ to	0.7 GeV	7.3 GeV	14.6 GeV
angular equivalent of crystal size $\theta$		$4^\circ$	$1^\circ$
spatial resolution $\sigma_\theta$	$0.5^\circ$	$0.3^\circ$	$0.1^\circ$
maximum signal load $f_\gamma$ ( $E_\gamma > E_{xtl}$ )		60 kHz	500 kHz
( $\text{p}\bar{\text{p}}$ -events) maximum signal load $f_\gamma$ ( $E_\gamma > E_{xtl}$ )		100 kHz	500 kHz
(all events) shaping time $t_s$		400 ns	100 ns
radiation hardness	0.15 Gy	7 Gy	125 Gy
(maximum annual dose $\text{p}\bar{\text{p}}$ -events)			
radiation hardness		10 Gy	125 Gy
(maximum annual dose from all events)			

**Table 3.1:** Main requirements for the  $\bar{\text{P}}\text{ANDA}$  EMC. Rates and doses are based on a luminosity of  $L = 2 \cdot 10^{32} \text{ cm}^{-2} \text{ s}^{-1}$ .

Moreover, the expertise of technicians operating these devices can be advantageously exploited.

## 4 Scintillator Material

---

### 4.1 Inorganic Scintillators

The concept of  $\bar{\text{P}}\text{ANDA}$  places the target spectrometer EMC inside the super-conducting coil of the solenoid. Therefore, the basic requirement of any appropriate scintillator material has to be its compactness to minimize the radial thickness of the calorimeter layer [1, 2]. Of similar importance, high interaction rates, the ambitiously large dynamic range of photon energies, sufficient energy resolution and efficiency and finally a moderate radiation hardness rule out most of the well known scintillator materials. Finally, even a compact geometrical design requires due to a minimum granularity a large quantity of crystal elements, which rely on existing technology for mass production to guarantee the necessary homogeneity of the whole calorimeter. Presently and even in the near future, no alternative materials besides lead tungstate will become available.

Of the materials listed in the table below Bismuth Germanate ( $\text{Bi}_4\text{Ge}_3\text{O}_{12}$ , BGO) is a well known scintillator material since many decades [3]. It has been applied in several experiments, like L3 at CERN or GRAAL at Grenoble, providing well performing electromagnetic calorimeters [4, 5, 6]. However, presently it is only used in large quantities but small samples for medical applications such as Positron-Electron-Tomography (PET) scanners [7]. The properties of BGO, listed in Table 4.1, allow for the design of a very compact calorimeter. The light yield is comparable to cooled PWO-II crystals. The emission wavelength is well suited for an efficient readout with photo- or avalanche diodes. However, the moderate decay time imposes a strong limitation on the necessary high rate capability for the envisaged interaction rate of  $10^7/\text{s}$  of  $\bar{\text{P}}\text{ANDA}$ . In addition, it excludes in general any option for the generation of a fast timing information on the level of  $\leq 1\text{--}2$  ns or even below for higher energies. Concerning the radiation hardness, which has not been a major issue for the former applications, controversial results are reported in the literature. Some authors report recovery times in the order of days or online recovery by exposure to intense light from fluorescent lamps at short wavelengths [8, 9, 10, 11]. Since most of these studies are rather old, an update with new studies using full size scintillation crystals produced recently would become necessary.

$\text{CeF}_3$  has been invented already in 1989 by D. F.

Anderson [12] and identified as a fast scintillator with maximum emission wavelength between 310 and 340 nm. The luminescence process is dominated by radiative transitions of  $\text{Ce}^{3+}$  ions, which explains the fast decay time of  $\sim 30$  ns and the insensitivity to temperature changes. The luminescence yield is comparable or even higher than the fast component of  $\text{BaF}_2$ , corresponding to approximately 5% of  $\text{NaI(Tl)}$  as a reference. Since the crystal matrix is extremely radiation hard, it was considered for the CMS calorimeter during a long period of R&D, supported by the short radiation length and Molière radius, respectively. However, homogeneous crystal samples beyond  $10X_0$  length, grown by the Bridgeman method, have never been produced with adequate quality. Detailed studies of the response function [13] to low energy protons and high energy photons have documented excellent time and energy resolutions, which are limited only in case of the reconstruction of the electromagnetic shower energy by the inhomogeneity of the available crystals. Further improvement relies on a significant optimization of the manufacturing process. In case of  $\bar{\text{P}}\text{ANDA}$ , the implementation of  $\text{CeF}_3$  has not been considered. It would on one hand double the radial thickness of the calorimeter shell. On the other hand, the effective light yield would be degraded due to the mismatch of the emission wavelength in the near UV with the optimum quantum efficiency of LAAPDs.

In the last decade cerium doped silicate based heavy crystal scintillators have been developed for medical applications, which require high light output for low energy  $\gamma$ -ray detection and high density to allow for small crystal units. Mass production of small crystals of  $\text{Gd}_2\text{SiO}_5$  (GSO),  $\text{Lu}_2\text{SiO}_5$  (LSO) and  $\text{Lu}_{2(1-X)}\text{Y}_{2X}\text{SiO}_5$  (LYSO) has been established in the meantime. Because of the high stopping power and fast and bright luminescence, the latter material has also attracted interest in calorimetry. However, the need for large homogeneous samples and the presently high costs, partly justified by the high melting point, are retarding the R&D. LYSO, which has almost identical physical and scintillation properties as LSO and shows identical emission, excitation and optical transmittance spectra, has been recently produced in samples up to 20 cm length [14, 15, 16, 17]. The light output of small samples can reach values 8 times of BGO but with a decay time shorter by one order of magnitude,

Parameter		CeF <sub>3</sub>	LSO/LYSO:Ce	BGO	PWO	PWO-II
$\rho$	g/cm <sup>3</sup>	6.16	7.40	7.13		8.28
$X_0$	cm	1.77	1.14	1.12		0.89
$R_M$	cm	2.60	2.30	2.30		2.00
$\tau_{decay}$	ns	30	40	300		6.5
$\lambda_{max}$	nm	330	420	480		420
$n$ at $\lambda_{max}$		1.63	1.82	2.15		2.24/2.17
relative LY	% (LY NaI)	5	75	9	0.3 at RT 0.8 at -25°C	0.6 at RT 2.5 at -25°C
hygroscopic		no	no	no		no
dLY/dT	%/°C	0.1	0	-1.6	- 2.7 at RT	-3.0 at RT
dE/dx (MIP)	MeV/cm	6.2	9.6	9.0		10.2

**Table 4.1:** Relevant properties of CeF<sub>3</sub>, LSO/LYSO:Ce, BGO, PWO taken from the updated table of the Particle Data Group 2007. The specific parameters of PWO-II are deduced from the presented test measurements.

determined by the Ce-activation. Detailed studies even within the  $\bar{\text{P}}\text{ANDA}$ -collaboration have been performed and response functions have been obtained even for high-energy photons up to 500 MeV [16]. Aiming at applications for the next generation of homogeneous calorimeters, detailed studies of full size crystals with respect to homogeneity, scintillation processes and radiation hardness are part of a research program promoted by a group at Caltech [17].

#### 4.1.1 Specific Requirements for the target spectrometer EMC

As pointed out in the previous chapter in selected figures based on simulations assuming already to some extent parameters of PWO-II, the target spectrometer EMC requires very ambitious specifications to be adapted to the physics program. The main features are:

- high rate capability, which requires a fast scintillation kinetics, appropriate granularity to minimize pile-up as well as guarantee optimum reconstruction of the center of the electromagnetic shower;
- sufficient luminescence yield to achieve good energy resolution in particular at the lowest photon energies in the MeV range, which goes in parallel with a minimum energy threshold of the individual crystal;
- timing information, primarily to reduce background and to provide an efficient correlation with other detector components for particle identification;

- adapted geometrical dimensions to contain the major part of the electromagnetic shower and to minimize the impact of leakage fluctuations and direct ionization in the photo sensor;
- radiation hardness to limit the loss in optical transparency to a tolerable level.

Based on the its intrinsic parameters, PWO, as developed for CMS/ECAL, most of the requirements could already be met except the light output. Therefore, an extended R&D program was initiated to improve the luminescence combined with an operation at low temperatures such as T=-25°C. The different steps to achieve the quality of PWO-II, as described later, have shown that radiation hardness becomes a very sensitive parameter, when the operating temperature of the calorimeter is below T=0°C. Therefore, the estimated radiation environment is discussed here in more detail.

#### 4.1.2 Hit Rates and Absorbed Energy Dose in Single Crystals

The single crystal rates under the proposed running conditions have been simulated using the Dual Parton Model (DPM) as generator for primary events. The maximum beam momentum of 15 GeV/c has been used to evaluate the highest load for  $\bar{p}p \rightarrow X$  interactions. A full tracking of the primary generated events through the whole  $\bar{\text{P}}\text{ANDA}$  detector using GEANT3/4 was simulated. The results are scaled to the canonical interaction rate of 10<sup>7</sup> primary events/s. Fig. 4.1 and Fig. 4.2 show the integral rate for the forward end cap and the barrel part for an energy threshold E>3 MeV.

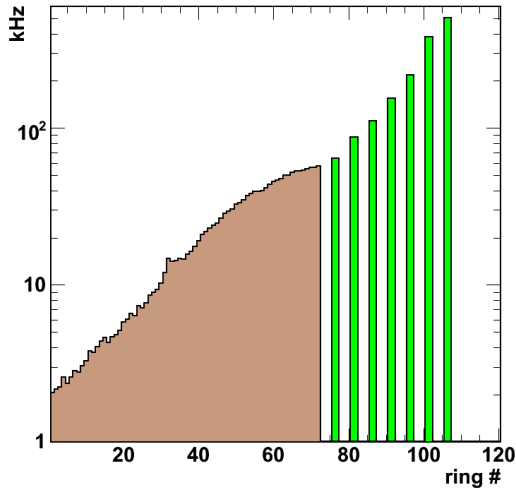


**Figure 4.1:** Integrated single crystal rate for the barrel section for an energy threshold of  $E > 3$  MeV using DPM at 15 GeV/c incident beam momentum.

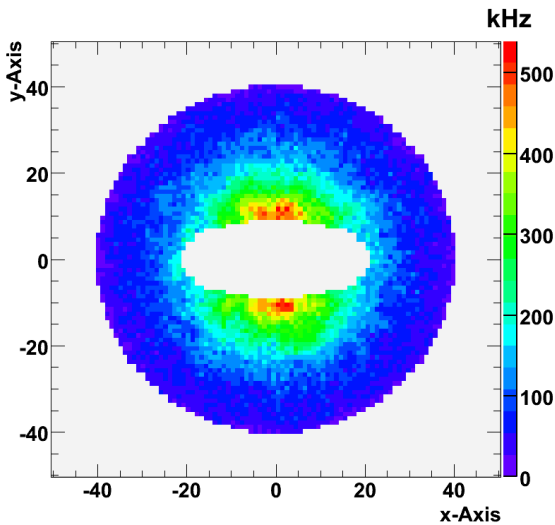


**Figure 4.2:** Integrated single crystal rate for the forward endcap for an energy threshold of  $E > 3$  MeV using DPM at 15 GeV/c incident beam momentum.

The energy spectrum of a single crystal depends strongly on the polar angle and is represented in Fig. 4.3 for four different polar angles ( $5^\circ$ ,  $25^\circ$ ,  $90^\circ$  and  $135^\circ$ ). The summation of the given energy distributions yields total absorbed energy rates of 27 mGy/h, 1.5 mGy/h, 0.16 mGy/h and 0.03 mGy/h, respectively, for each angle. The energy absorption is homogeneous in lateral direction of the crystals, but in radial depth the situation

changes. The different interaction mechanisms of the electromagnetic and hadronic probes with the scintillator material lead to a strong radial dependence of the energy absorption as shown in Fig 4.4 under similar conditions. The strong variation can bring the stated average numbers up to peak values, which can be higher by factors of 2-3 within the first few cm of the crystals. The centers of the electromagnetic shower of photons up to 10 GeV incident energy will be concentrated within the first third of the crystal length, which has to be considered for the optimization of a homogeneous collection of the scintillation light.

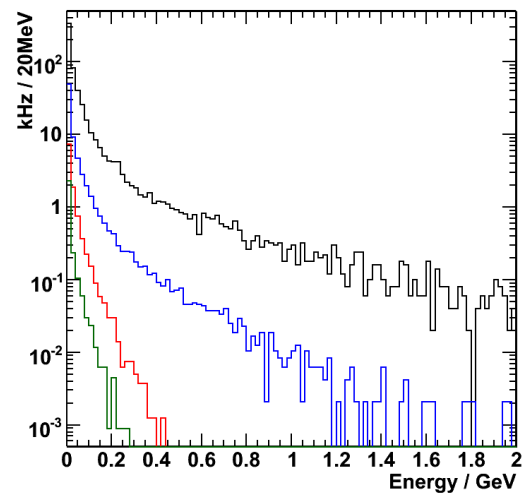


**Figure 4.3:** Single crystal energy differential rate spectrum for polar angles of  $5^\circ$  (black),  $25^\circ$  (blue),  $90^\circ$  (red) and  $135^\circ$  (green) using DPM at 15 GeV/c incident beam momentum.

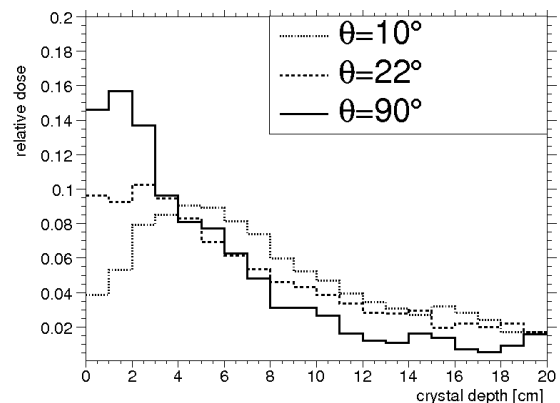


**Figure 4.4:** Relative energy dose normalized to 1 as function of the radial depth in a single crystal using DPM at 15 GeV/c incident beam momentum.

Summarizing, the individual scintillation crystals have to be capable to handle average hit rates above a threshold of 3 MeV of 100 kHz in the barrel EMC and increasing up to 500 kHz in the most forward parts of the forward endcap EMC. However, these values might be even exceeded due to fluctuations in the time structure of the beam. Considering the complete cocktail of impinging probes, absorbed dose rates up to 20-30 mGy/h have to be expected at most forward regions. The values in most parts of the barrel EMC are two orders of magnitude lower. Therefore, the absolute values are well below the environment expected for LHC experiments. Due to the significantly slower recovery processes at  $T=-25^\circ\text{C}$ , as outlined in chapter 3.4.1.1, radiation induced changes of the optical transmittance will reach a final level asymptotically on a time scale of a typical run period. However, these limits will only be reached at the most forward angles of the forward endcap EMC.

## 4.2 Lead Tungstate PWO

### 4.2.1 General Aspects

Lead tungstate,  $\text{PbWO}_4$  (PWO), crystals meet in general the requirements to represent an extremely fast, compact, and radiation hard scintillator material. However, a significant improvement of the light output was mandatory for the application in  $\bar{\text{P}}\text{ANDA}$ . Table 4.1 considers already the finally achieved quality described as PWO-II.

The specifications, which were developed and obtained for the application in experiments at LHC at CERN such as the **E**lectromagnetic **C**ALorimeter (ECAL) of CMS [18] and the **P**HOton **S**pectrometer (PHOS) of ALICE [19] served as a starting point for the further optimization of lead tungstate crystals [20]. Radiation hardness, fast scintillation kinetics, large-scale production and full size crystals of 23 cm length ( $28 X_0$ ) with a light output of 9–11 phe/MeV (measured with a bi-alkali photocathode at room temperature) became standard.

Looking backwards, in the R&D phase, performed in 1998–2002, the light output was improved by additional doping [21, 22, 23]. Co-doping with molybdenum (Mo) and lanthanum (La) at concentrations  $<100$  ppm delivered optimum results. However, an additional strong slow scintillation component ( $\tau_g = 1 - 4 \mu\text{s}$ ) appeared limiting applications at high count rates [24]. Two additional concepts were pursued:

1. increase of the structural perfection of the crystal, and
2. activation of the crystal with luminescent impurity centers. These have a large cross section to capture electrons from the conduction band, combined with a sufficiently short delay of radiative recombination.

Beside crystal activation with impurity centers, authors of Ref. [25] investigated the possibility to redistribute the electronic density of states near the bottom of the conduction band by the change of ligands contained in the crystal, which unfortunately introduced slow components in the scintillation kinetics. An obvious possibility to reduce the concentration of point structure defects is doping with yttrium (Y), lanthanum (La) or lutetium (Lu) ions, which suppress oxygen and cation vacancies in the crystal matrix. An activator concentration at a level of 100 ppm is needed. This concept has been followed up successfully by the CMS collaboration, and led to mass production technologies of radiation hard crystals at the Bogoroditsk Technical Chemical Plant [20]. A further increase of the scintillation yield by 30–50% can be achieved by a reduction of the La-concentration to  $\sim 40$  ppm or less, which can compensate vacancies only if point defects are further suppressed. That was realized by an improved control of the stoichiometric composition of the melt.

### 4.2.2 Basic Properties of $\text{PbWO}_4$ and the Scintillation Mechanism

The world's largest PWO crystal producer Bogoroditsk Technical Chemical Plant (BTCP) from Russia produces lead tungstate crystals with high yield by the Czochralski method, using standard "Crystal 3M" or "Lazurit" equipment. Crystals are grown from raw material with a purity level close to 6N specification in Pt crucibles. In order to grow high quality crystals an additional pre-crystallization is required. Ingots of 250 mm length and slightly elliptical cross-sections with a large axis between 36 and up to 45 mm in diameter became available. Crystals can be pulled with identical quality in the directions close to the a or c axis. Nevertheless, the production along the direction of the a axis appears to be the best for producing long samples. The process of pulling is carried out in an isolated chamber filled with nitrogen. Pulling rate and rotation speed can be varied over a wide

range adapted to the required ingot diameter. Several crystal ingots to produce modules for the forward endcap EMC are shown in Fig. 4.5.



**Figure 4.5:** Selected PWO-II ingots, which have been used to machine crystals in PANDA geometry.

Lead tungstate crystals occur in nature as tetragonal stolzite [26], scheelite type or monoclinic raspite [27]. The structure of the synthetic lead tungstate crystal is determined by X-ray diffraction as scheelite-type of tetragonal symmetry with a space group of  $I4_1/a$  and unit-cell parameters  $a = b = 5.456(2)$ ,  $c = 12.020(2)$  Å. The density of the synthetic crystal can vary by a few percent depending on the technology.

The electronic structures of the conducting and valence band for pure and defective lead tungstate crystals are described in detail in [28]. According to the electron band structure, luminescence appears in PWO crystals because of charge-transfer transitions in a regular  $(\text{WO}_4)^{2-}$  anionic molecular complex. Since the  $(\text{WO}_4)^{2-}$  complex has a  $T_d$  point symmetry of the crystalline field, the final configurations of the energy terms are found to be  $^3T_1$ ,  $^3T_2$  and  $^1T_1$ ,  $^1T_2$  with the  $^1A_1$  ground state. The spin and parity forbidden radiative transition  $^1T_1$ ,  $^1T_2 \rightarrow ^1A_1$  in the anionic complex is responsible for the intrinsic blue luminescence of the lead tungstate crystal. The luminescence has a large Stokes shift of 0.44 eV and therefore is characterized by a strong temperature quenching.

Crystalline material of lead tungstate is transparent in the visible spectral range and fully colorless. A typical transmission spectrum measured along the crystallographic axis  $a$  of a 200 mm long sample and the radio-luminescence spectrum measured at room temperature are compared in Fig. 4.6. There is an overlap of the distribution of luminescence with the cut-off of the transmission spectrum. Therefore, op-

timizing the light yield relies significantly on the crystal transmittance in the near UV region.

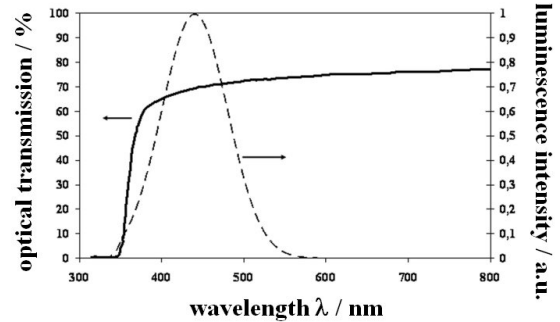


**Figure 4.6:** The optical transmission and radio-luminescence spectra at room temperature measured for a 200 mm long PWO crystal.

Due to strong temperature quenching of the luminescence in  $\text{PbWO}_4$ , the light yield shows a strong temperature dependence. As a consequence, the scintillation kinetics is fast at room temperature and is dominated by an exponential decay constant of  $\tau = 6.5$  ns. The temperature dependence of the scintillation light yield in the range  $+20^\circ\text{C}$  to  $-25^\circ\text{C}$  was found to be close to linear with a gradient of  $-2\%/^\circ\text{C}$ . The typical kinetics of the scintillation processes in PWO is shown in Fig. 4.7.

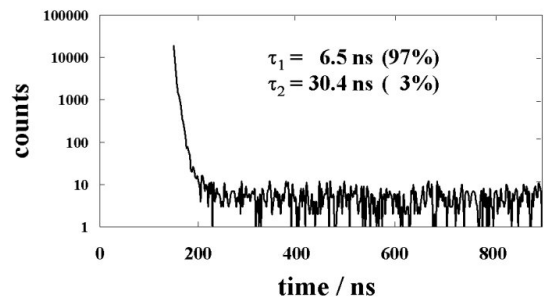


**Figure 4.7:** The scintillation kinetics of PWO measured at room temperature.

Both scintillation and optical properties of the currently produced lead tungstate crystals are rather uniform along the axis of crystal growth. The variation with respect to the wavelength of the opti-

cal transmission value of  $T=50\%$  does not exceed  $\Delta\lambda = 3$  nm for a 200 mm long crystal.

### 4.2.3 The Improved Properties of PWO-II

Up to date the CMS Collaboration has the largest comprehensive experience with the exploration and production of lead tungstate [29, 30]. Recently BTCF has completed the production of 77,000 scintillation crystals for the CMS/ECAL using the Czochralski method. A smaller percentage was delivered by the Shanghai Institute of Ceramics (SIC-CAS) using a modified Bridgeman method [31]. As an outcome of seven years of mass production the following quality parameters of the production technology were obtained [32], summarized in Table 4.2.

One can state that both crystal producers reached a high quality of the crystals. Moreover, the distributions of crystal parameters are significantly superior to the limits set by the CMS specifications. As a consequence, only a small fraction at the level of 1.5% was rejected by the certification of scintillation elements repeated by the customer at CERN.

Experimental applications for photon detection in the MeV range below 200 MeV are predominantly limited by the photon statistics [33, 34]. Obviously, further improvement of the crystal light yield became mandatory. Detailed studies of the different dopants in the crystal did not lead to a spectacular increase of the light yield [21], as illustrated in Fig. 4.8.

PWO is very sensitive to the conditions at the synthesis. During the crystal growth by the Czochralski method from stoichiometric raw material a dominant leakage of lead from the melt takes place leading to the creation of cation vacancies  $V_c$  on the lead site in the host. This holds also for crystals obtained by the modified Bridgeman method [31]. The systematic lead deficiency introduces a superstructure created by cation vacancies as identified by combined X-ray and neutron diffraction measurements [35]. In fact, cation vacancies  $V_c$  are compensated by oxygen vacancies  $V_O$  or Frenkel-type defects and their ordering is compensated by the distortion of the tungstate anionic polyhedra. During the development, point structure defects, such as electron capturing centers were identified by Thermo Stimulated Luminescence (TSL) and Electron Paramagnetic Resonance (EPR) measurements [36, 37, 38, 39]. As a result, the shallowest center occurs in all crystals as an intrinsic defect: an additional electron auto-localized at an anionic

$(\text{WO}_4)^{2-}$  complex via a Jahn-Teller distortion creating a  $(\text{WO}_4)^{3-}$  polaronic center [40, 41, 42]. This shallow trap is emptied near a temperature of 50 K with an activation energy of 0.05 eV. Part of the released electrons recombine radiatively or are caught by deeper traps. The second one is a  $\text{Pb}^{1+}\text{-V}_0$  center, which is stable in the crystal up to 175 K [43, 44]. It is not excluded that instead of Pb an other ion may create such a center near an anion vacancy. However, it counts that the electron is trapped by a hetero-valent cation in the vicinity of an oxygen vacancy. That can be proved by a relatively large deviation of the g-factor of all such magnetically non-equivalent species from  $g_e$ . This center is not clearly correlated with the detected TSL band, however it is photo-ionized by IR with the threshold 0.9 eV. The third one is a  $(\text{WO}_4)^{3-}$  electron center, which is created on a base of a regular tungstate anionic complex disturbed by a nearby rare earth (RE) trivalent impurity ion like La, Lu or Y [41]. It decays near 97 K and has an activation energy 0.2 eV. Careful partial annealing experiments showed that the rate of decrease of the EPR intensity of  $(\text{WO}_4)^{3-}\text{-La}$  coincides with the TSL emission in this temperature region [43]. In addition, the doping of the crystal with stable trivalent RE ions such as La, Lu, Gd and Y at concentrations of some tens of ppm redistributes electron trapping centers and reducing the number of deep ones [43, 45, 46]. Such ions localized at Pb sites introduce in the crystal an additional positive uncompensated charge and thus will compete with the creation of vacancies. In addition, the dopants introduced in the crystal above the stoichiometric ratio occupy empty lead sites in the lattice and suppress the superstructure fraction with its distorted tetrahedra in the crystal.

Another trap center with an activation energy of 0.13 eV appears in the crystal with RE doping. This  $\text{RE}\text{-}(\text{WO}_4)^{4-}$  center is not paramagnetic. This hypothesis is in agreement with the fact that RE-doped PWO crystals show higher TSL intensity in the vicinity of 100 K temperature. An electron release from the 0.13 eV traps causes simultaneous production of the lowest electron centers by re-trapping as well as by contributing to an increase of TSL intensity in that region via the creation of  $\text{RE}\text{-}(\text{WO}_4)^{3-}$ .

The deepest electron trap centers are double vacancy centers having an activation energy in the range of 0.4-0.5 eV and Frenkel-type defect with an activation energy 0.7 eV, which occurs in the crystal at the shift of the oxygen ion into the inter-site position. Double vacancies cause induced absorption in

number of samples	parameter	mean value	standard deviation
40607	length/mm	229.95	0.02
61267	LY/phe-MeV <sup>-1</sup>	10.2	1.2
61267	LY non-uniformity / %X <sub>0</sub>	-0.13	0.02
61267	opt. transm. at 420nm/%	69.5	2.2
61267	rad. ind. absorption at 420nm/m <sup>-1</sup>	1.04	0.4

**Table 4.2:** Distribution of the crystal properties of accepted PWO crystals for the CMS/ECAL project.

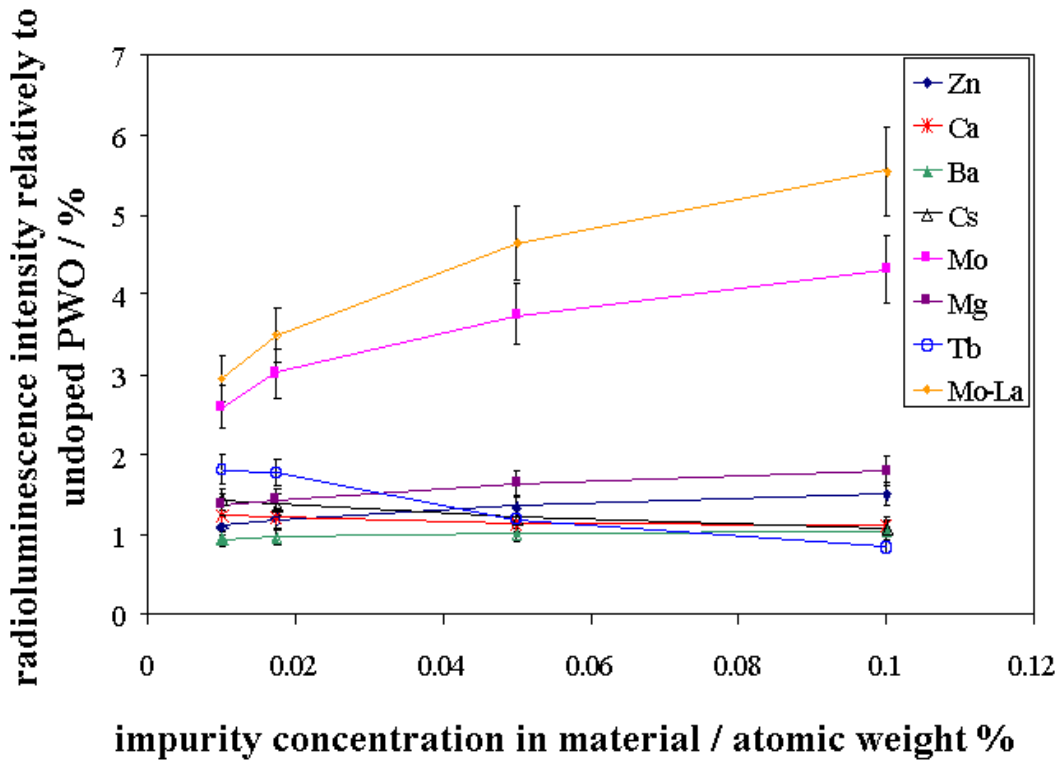


**Figure 4.8:** Integral dependence of the radioluminescence of lead tungstate crystals doped with different ions as a function of the activator concentration. The measurements have been performed at an absolute temperature of  $T=300$  K.

the near IR spectral region in the crystal. Frenkel-type defects cause an optical absorption band at a wavelength of 360 nm, which is converted under ionizing radiation in the absorption band with a maximum near 410 nm.

We attribute a molybdenum (Mo) based center to the characteristic luminescence centers in lead tungstate. It is related to a  $(\text{MoO}_4)^{2-}$ -anion complex impurity, which is a stable electron trap center. Although the raw material is purified before

crystal growth, especially of Mo, the molybdenum ion is chemically very close to the tungsten ion and it is rather hard to separate both at the production quality level of the raw material. The effective molybdenum impurity in PWO-II is typically at the level of  $<1$  ppm. The properties of the  $(\text{MoO}_4)^{3-}$ -center and its impact on the scintillation parameters of PWO are described in detail in [24].

Following the disposition of electronic centers near the bottom of the conducting band it appears to be

possible to describe the influence of each kind of defects on the crystal scintillation properties even at different temperatures. On one hand shallow polaronic and RE-distorted regular centers contribute to the scintillation via relatively fast electron exchange with the conducting zone. A reduction occurs due to loss of electrons into the deep traps. The increase of the concentration of  $(\text{WO}_4)^{3-}$ -RE centers in the crystal leads to a drop of the light yield. Therefore, an increase of the light yield is in conflict with optimization of radiation hardness by a higher concentration of activating ions such as La. To fulfill both, perfection of the crystal is the only way out.

Decreasing the operating temperature of the calorimeter down to  $T=-25^\circ\text{C}$  slows down the time constants of the spontaneous recovery of the electron centers by thermal activation. Table 4.3 shows the parameters of selected electron capturing centers in PWO crystals [38] obtained by the TSL method, where  $E_T$ ,  $S$ ,  $\gamma$  are the activation energy, the frequency factor and the order of the kinetics, respectively. The calculated spontaneous recovery constants for two temperatures are shown in addition. When the temperature is decreasing to  $T=-25^\circ\text{C}$  the deepest electron center becomes metastable and increases effectively the level of dynamic saturation of the radiation induced optical absorption in the crystal. This effect has to be considered and its consequences have to be investigated under the experimental conditions for PANDA.

Structural perfection of the crystal has been reached by an improved control of the stoichiometric composition of the melt. Since the full-size crystal samples have a length of 200 mm, crystal activation was pursued at different stages of the raw material preparation by Y and La ions with distribution coefficients of 0.95 and 1.47, respectively. EPR studies have confirmed that only single RE- $(\text{WO}_4)^{3-}$  (RE=La,Y) centers are formed, if the concentration of the dopants remains below 20 ppm for each ion species. These crystals contain finally at least two times less Frenkel type defects leading to an increase of light by 80% compared to CMS quality. The kinetics of the enhanced material remains fast and allows to integrate 97% of the light within a 100 ns wide time gate at room temperature.

### 4.3 Radiation Induced Absorption in PWO-II Crystals

The stability of the parameters of the scintillation material in a radiation environment is one of the most important properties required to build a precise electromagnetic calorimeter. As common for most of the scintillators, the scintillation mechanism in PWO itself is not damaged when grown under optimized conditions [29]. Irradiation affects only the optical transmission due to the creation of color centers with absorption bands in the visible spectral region. The induced absorption evolves with time, depending on the dose rate and the origin of the participating centers and their mechanism of annihilation and relaxation. The absorption is quantified by the absorption coefficient  $k$  given in  $\text{m}^{-1}$  assuming a pure exponential change of the transmission loss. Fig. 4.9 shows typical spectra of the induced absorption loss measured for PWO-II samples at room temperature after a total absorbed dose of 0.2 kGy using a  $^{60}\text{Co}$  source expressed by the difference of the coefficients before and after irradiation at given wavelengths.

The obtained values stay below the considered quality limit  $\Delta k=1\text{m}^{-1}$  in the relevant spectral range of the luminescence. Nevertheless, enhanced absorption is visible near the maximum of scintillation emission at 420 nm or at a broad structure near  $\lambda=550$  nm.

In contrast to previous applications, the calorimeter will be operated at  $T=-25^\circ\text{C}$ . Therefore, a detailed research program had to be started to investigate possibly new and unexpected effects due to irradiation at crystal temperatures below  $0^\circ\text{C}$ . Besides the facilities performing quality control during the phases of development and pre-production at the manufacturer locations BTCP or INP (Minsk, Belarus) two additional and complementary facilities at IHEP (Protvino, Russia) and JLU (Giessen, Germany) have been adapted for that purpose.

#### 4.3.1 The Irradiation Facility at IHEP, Protvino

An irradiation facility, dedicated to the investigation of the radiation damage of cooled and temperature stabilized scintillation crystals, was designed and installed at IHEP (Protvino, Russia). A  $^{137}\text{Cs}$  radioactive source, emitting  $\gamma$ -rays of 662 keV energy with an activity of  $5\cdot 10^{12}\text{Bq}$ , is used for the irradiation measurements. The dose rate can be con-

$E_T$ meV	S	$\gamma$	$\tau_{rec}$ at T=+25°C s	$\tau_{rec}$ at T=-25°C s
0.05	4.00E+03	1.1	1.80E-03	2.70E-03
0.135	1.0E+08	1.6	2.80E-06	8.36E-06
0.19	2.90E+08	1.35	6.40E-06	2.98E-05
0.23	6.7E+09	2.2	2.2E-06	1.42E-05
0.27	9.0E+10	2.2	7.3E-07	6.51E-06
0.40	2.0E+10	1.1	3.1E-04	7.93E-03
0.50	9.0E+11	1.4	5.0E-04	2.87E-02
0.49	2.0E+09	1,0	9.0E-02	4.77
0.58	1.1E+07	1.0	4.80E+02	5.28E+04
0.7	5.5E+7	1.0	1.00E+04	2.91E+06

**Table 4.3:** Selected parameters of the electron capturing centers in PWO crystals.

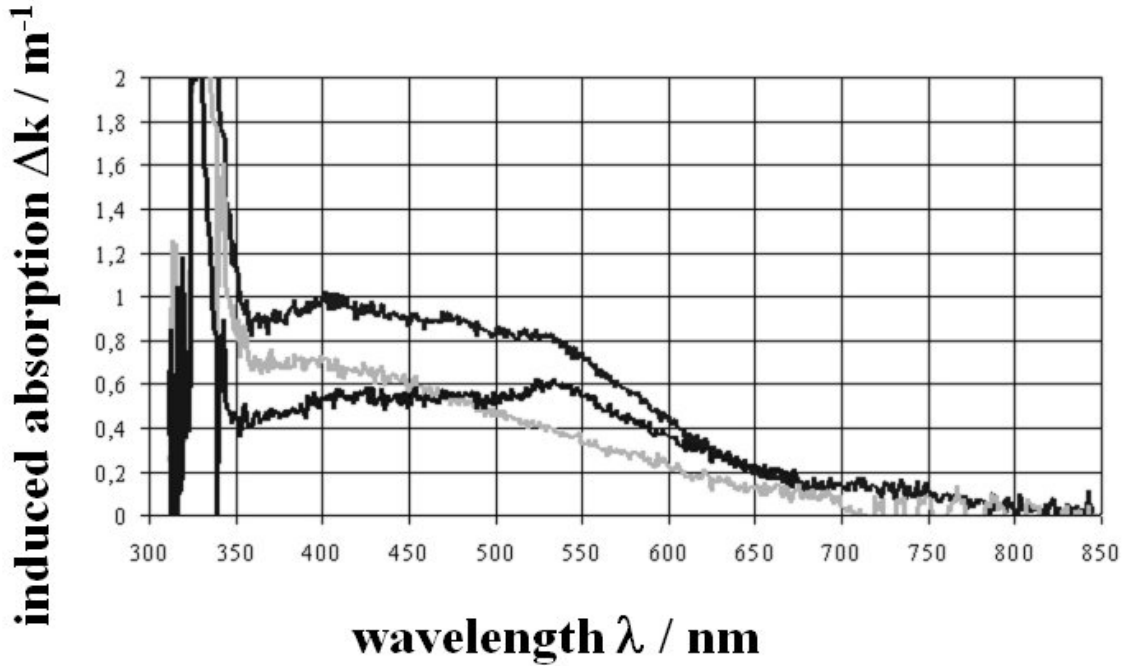


**Figure 4.9:** The measured change of the induced absorption coefficient of various PWO-II samples after irradiation with a dose of 0.2 kGy ( $^{60}\text{Co}$ ) over the relevant range of wavelength.

tinuously adjusted by changing the distance to the exposed crystals. The dose rate in air is measured close to the crystals with a commercial dosimeter (DKS-AT1123) with a typical accuracy of <20% [47]. Fig. 4.10 shows the schematic layout of the facility and Fig. 4.11 the major components of the

installed setup. All major components are remote controlled and the relevant parameters are recorded for the off-line analysis. The up to five full size crystals are mounted in an insulated container, which can be cooled and temperature stabilized by a cryostat (LAUDA RC6CP) with an absolute ac-

curacy of  $0.1^\circ\text{C}$  even during a test cycle of several days. The crystals are attached via air light-guides to photomultiplier tubes (PMT). A gas flow of dry nitrogen helps to equalize the temperature and to avoid condensation of moisture. Several thermosensors measure and control the temperature. Any change of the optical transmittance of the crystals due to irradiation as well as possible gain instabilities of the PMTs are controlled by a LED-based monitoring system distributed by optical quartz fibers. Two spectral regions near the wavelengths of 450 nm and 640 nm, respectively, are inspected using blue and red LEDs. The highly stabilized monitor system is similar to the one described in reference [48, 49].

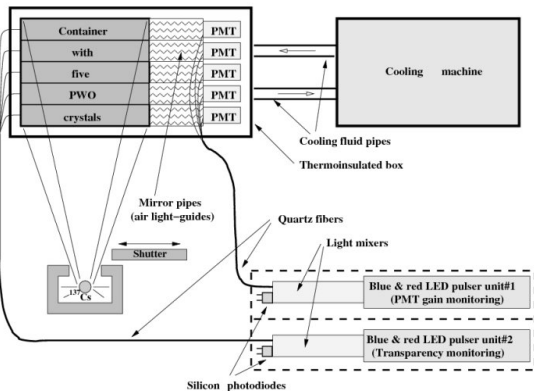


**Figure 4.10:** Schematic layout of the irradiation facility at IHEP, Protvino.

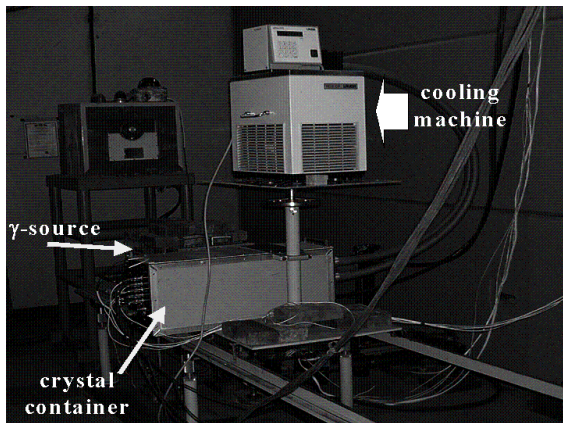


**Figure 4.11:** Photograph of the major components of the irradiation setup at IHEP, Protvino.

The DC current of the PMT is directly digitized via a  $10\text{ k}\Omega$  resistor. That signal, which is proportional to the product of light yield and light collection efficiency in the crystal, provides general information

on any change of the light output due to irradiation or temperature change. Complementary, the signal triggered by the LED pulses is monitoring any variation of the light transmittance of the crystal.

The facility will be used during final production to investigate selected crystal samples with respect to the radiation damage of cooled crystals, complementary to the standard procedures at the manufacturer location performed at room temperature. The measurements will confirm the linear relation between the radiation hardness at both temperature regions. Finally, tests will be performed for all crystal geometries in order to determine the correlation between the loss in transmission and the reduction of the integrated scintillation light collected after multiple reflections inside the crystal.

#### 4.3.2 The Irradiation Facility at the Justus-Liebig-University Giessen

The irradiation facility at Giessen at the so called Strahlencentrum is based on a set of five  $^{60}\text{Co}$  sources, which can be used in any combination. The maximum dose rate amounts to  $\sim 30\text{ Gy/h}$  measured at a distance of 1m. Complementary to the possibilities at Protvino an experimental setup including a double beam photospectrometer has been adapted to irradiate cooled crystals and measure immediately after irradiation or hours and days later any changes of the spectral distribution of the optical transmission. That arrangement allows to determine at various temperatures the induced absorption as a function of integral dose as well as the recovery as a function of time. Present experiments were performed with a typical dose rate of  $12\text{ Gy/h}$  at a distance of 1m (see Fig. 4.12).

For the future quality control, the crystal samples can be either exposed in a radiation protected laboratory room or placed into a sufficiently large container, which can be loaded outside and moved in front of the array of sources. The equipment includes a *Varian* photospectrometer to measure afterwards the radiation induced absorption via the longitudinal optical transmission. All measurements are meant to be performed at room temperature and will be the final acceptance test for a significant percentage of all the crystals as a cross check of the measurements performed at the manufacturer.

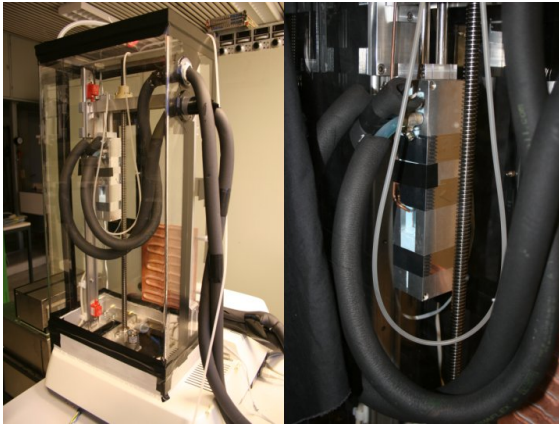


**Figure 4.12:** The experimental setup arranged on top of a photon spectrometer for irradiation studies at JLU, Giessen (left). The right part of the figure shows the movable crystal container with the open region for the measurement of the transmission.

### 4.3.3 The Irradiation Facilities at INP (Minsk) and BTCP

For the mass production for the CMS detector, an irradiation facility was installed at BTCP with technical assistance of INP (Minsk). A  $^{60}\text{Co}$  source of round geometry is placed in a well for radiation protection, see Fig. 4.13. Up to four crystals, placed in cylindrical light-tight containers, are irradiated laterally from all sides at a dose rate of 1200 Gy/h. In addition, an inner container equipped with optical windows allows to determine simultaneously the longitudinal induced absorption at three characteristic wavelengths in an optical spectrometer with four independent channels. The procedure of measurement is illustrated in Fig. 4.14.

The change of longitudinal transmission after irradiation is inspected at three wavelengths: 650 nm (RED), 570 nm (GREEN) and 420 nm (BLUE) [50]. According to these three colors the spectrometric setup is called RGB System. Three light emitting diodes emit alternately short (tens of nanoseconds), stable light pulses. The light emitted from each LED is mixed by four diffusion cavities and illuminates the samples in longitudinal direction as illustrated in Fig. 4.15. After traversing the crystal and the diffusion of the light on a receiving reflector, it impinges on PIN-photodiodes. The amplified signals are shaped and sent to a PC-based ADC card. Some fraction of the light from the LEDs is directed to a reference channel based on a thermo-stabilized PIN-diode to ensure the long-term stability at the level of  $10^{-4}$ . This concept of the automated con-



**Figure 4.13:** The irradiation facility operating at BTCP in Russia.

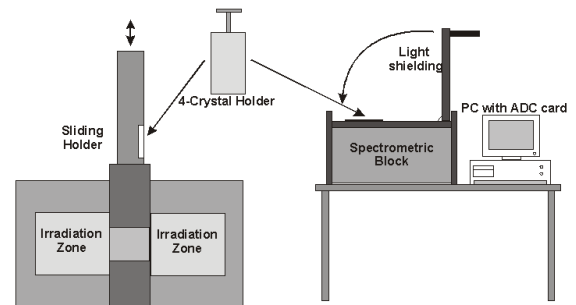


**Figure 4.14:** Schematic layout of the spectrometric setup at BTCP.

trol of the light pulse intensity is similar to one described in details in [51]. The measurement cycle of four PWO crystals includes 2.5 minutes of irradiation and optical transmission measurements before and after irradiation (taking about 2 minutes each). Due to short irradiation time and short time of the crystal transmission measurement after irradiation, unwanted fast crystal recovery components can also be measured along with induced optical absorption.

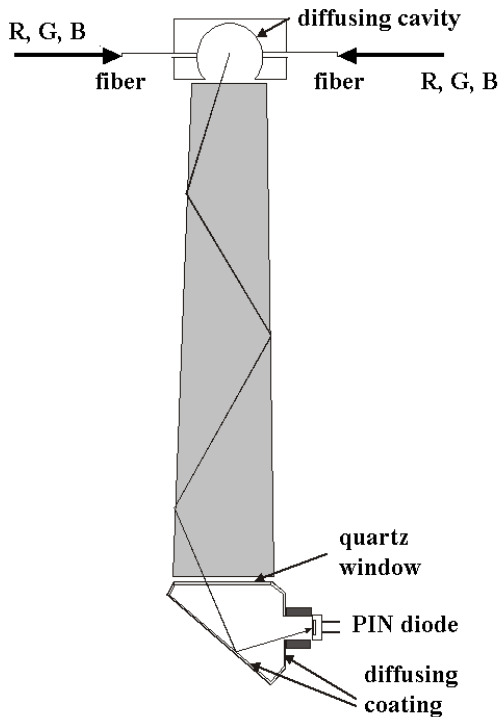


**Figure 4.15:** Schematic layout of a single spectrometric channel of the setup at BTCP.

Per working day at least 100 crystals can be characterized with respect to their radiation hardness. This equipment was adopted to measure PANDA barrel type crystals of 200 mm length. The radiation hardness of the crystals of the pre-production lot has been characterized already with the adapted equipment.

The irradiation facility at INP Minsk comprises a well shaped  $^{60}\text{Co}$  source with a constant dose rate of 2300 Gy/h. Variations of the crystal transmission are measured 60 min after irradiation by a Varian *Cary1E* photospectrometer in the wavelength range of 300-900 nm. The control of other scintillation parameters can also be carried out at INP.

BTCP and INP irradiation facilities are cross calibrated two to three times per year on the occasion of change of the crystal dimensions. It is agreed that a set of reference crystals including all types of PANDA scintillation elements will be produced before crystal mass production. It will be used for examination of the equipment before each measurement session and to verify the cross calibration of the irradiation facilities within the project.

#### 4.3.4 Irradiation Studies with Neutrons, Protons and High Energy $\gamma$ -rays

It is foreseen to perform selective irradiation studies with hadrons and electromagnetic probes. Within the collaboration there are several accessible facilities to perform such studies. The following options are available and have been already used for the characterization presented in the previous section.

- The irradiation facility at IHEP, Protvino provides a Pu- $\alpha$ -Be source with a fluence of  $3 \cdot 10^4$  neutrons/( $\text{cm}^2 \cdot \text{s}$ ). The emitted neutrons have a mean kinetic energy of  $E_n = 3.5$  MeV. However, there is an accompanying background of  $\gamma$ -rays with a mean energy of  $E_\gamma = 300$  keV corresponding to a dose of 7 mGy/h at the location of irradiation of samples.
- The cyclotron at the KVI at Groningen, (The Netherlands) provides a dedicated experimental area for irradiation studies with protons up to an energy of 150 MeV. The facility allows to irradiate locally as well as homogeneously over a typical surface of  $15 \times 15 \text{ cm}^2$  with an accurate control over the overall dose rate and integral dose.
- Besides the opportunity to measure response functions to high-energy photons over the range up to 3.5 GeV, both tagging facilities at the electron accelerators MAMI (Mainz, Germany) and ELSA (Bonn, Germany) allow to study the radiation damage in a controlled way. The absolute flux of the energy marked photons is known with high accuracy and can be used to test pure crystals as well as assembled detectors or arrays. High-energetic electrons can be simultaneously used with well known energies and rates directly behind the focal plane of the magnetic dipole

#### 4.4 The PWO-II Crystals for PANDA

The achievements in the understanding of the scintillation mechanism, the defect structures and the implications for the production technology have provided the quality of lead tungstate fully adequate for the PANDA application. PWO-II, when operated at  $T = -25^\circ\text{C}$  becomes a sufficiently bright scintillator, in particular when nearly 50% of the crystal endface are covered and readout with

LAAPDs of high quantum efficiency. The specific temperature keeps the decay time fast to cope with high count rates. However, the processes recovering the irradiation damage become extremely slow at low temperatures and cause an asymptotic reduction of the light yield due to the changing optical transparency. High quality crystals with a minimized concentration of defects limit the loss to a value below 30%. Therefore, for the operating scenario of the target spectrometer EMC a net increase of the light yield of a factor 3 compared to room temperature can be considered even for the most forward located modules in the forward endcap EMC. The next chapters are describing in detail the overall parameters of the scintillator material for PANDA.

#### 4.4.1 Light Yield and Decay Kinetics

As a result of the significant improvement of the technology of crystal production, full size crystals with 200 mm length deliver today a light yield of 17-20 phe/MeV at 18°C measured with a photomultiplier with bi-alkali photocathode (quantum efficiency  $\sim 20\%$ ). Documenting the breakthrough years ago, Fig. 4.16 shows for only 150 mm long PWO-II samples the light yield in comparison to CMS Endcap type crystals of 230 mm length. The light yield is shown as a function of the optical absorption at 360 nm wavelength, which is sensitive to the concentration of Frenkel-type defects in the crystal, in order to take in to account the different crystal dimensions.

Reducing the thermal quenching of the luminescence process by cooling the crystals leads to the expected increase of light yield. Obviously, the low concentration of deep traps in PWO-II does not distort the scintillation kinetics at least down to a temperature of  $T=-25^\circ\text{C}$ . Fig. 4.17 a) and b) show typical pulse height spectra, which were measured for a full size crystal ( $20\times 20\times 200\text{mm}^3$ ) at two operating temperatures of  $T=\pm 25^\circ\text{C}$  and two different integration gates of 75 ns and 4000 ns, respectively, using a photomultiplier as sensor (Hamamatsu R2059). The overall gain factor of the light yield at  $T=-25^\circ\text{C}$  compared to  $T=+25^\circ\text{C}$  amounts to more than 4 for both time gates.

Compared to the standard material, PWO-II crystals follow a different temperature dependence of the scintillation yield, as shown in Fig. 4.17 in the relevant temperature region between  $T=+25^\circ\text{C}$  and  $T=-25^\circ\text{C}$ , respectively. The average temperature gradient of the light yield amounts to  $\sim -3\%/^\circ\text{C}$ ,

which is 50% larger than for standard PWO. The obviously steeper increase of the light yield with lower temperature can be addressed to a lower concentration of capturing centers.

Fig. 4.19 shows for different temperatures the mean value of the scintillation yield per MeV deposited energy including standard deviations obtained for low energy  $\gamma$ -rays. The signals obtained with photomultiplier tubes equipped with bi-alkali photocathodes (Hamamatsu R2059) were integrated over a gate width between 75 ns up to 1  $\mu\text{s}$ , respectively. The figure confirms a mean gain factor up to 4 between the two extreme temperatures and a sufficiently fast decay time, which allows to collect 95% of the scintillation light within a time window of 300 – 400 ns.

Mass production requires sensitive criteria for the certification of crystals. As shown in Fig. 4.20, a strong correlation has been verified with a coefficient above 4 for the light yield observed at  $T=+25^\circ\text{C}$  and the corresponding value at  $T=-25^\circ\text{C}$ . Experimental data are shown in part a) and b) for ten PWO-II crystals after integrating the response within 100 ns and 1000 ns, respectively. Consequently, the linear correlation allows quality control to be performed in the more convenient environment at room temperature.

The overall light collection depends on the optical quality, the geometrical shape, surface treatment and reflector material. The distribution of the emission of the scintillation light and the variation of the light path cause a position dependence of the light yield collected at the photo sensor located at the rear end of the crystal. These effects cause a typical non-linearity, which can have an impact on the final energy resolution, explicitly the constant term. The effect has to be corrected in particular, when the maximum of energy deposition within the crystal is spread over a large region, which is not the case as illustrated in Fig. 4.4. Nevertheless, investigations have been started to optimize the additional surface treatment by partly de-polishing or selection of various reflector materials. Fig. 4.21 illustrates the change of light output for different geometries and reflector materials when a collimated source is moved relative to the sensor position along the crystal axis.

#### 4.4.2 Radiation Hardness of PWO-II

The radiation hardness and the effective loss of light yield as a functions of dose rate and accumulated

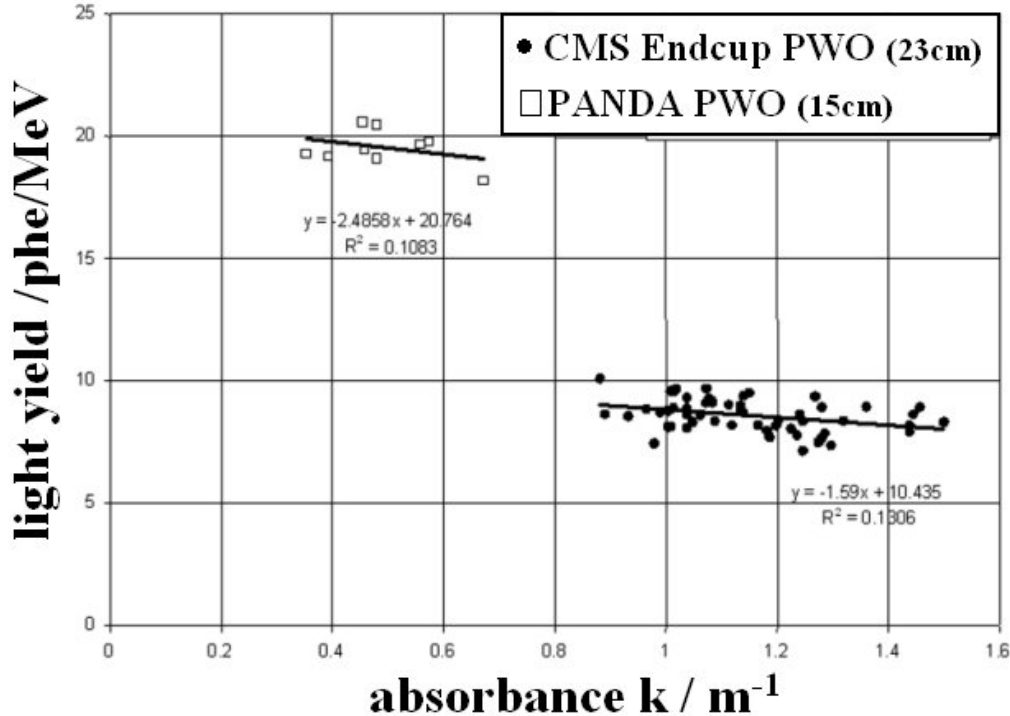


**Figure 4.16:** Light yield of full size polished scintillation crystals ( $28 \times 28 \times 230 \text{mm}^3$ ) used for CMS endcap construction (right distribution) and of PANDA prototypes of slightly smaller size ( $20 \times 20 \times 150 \text{mm}^3$ ) shown as a function of the absorbance to compensate for different geometries.

dose are well known from the studies for CMS but investigated at room temperature. The deterioration of the optical transmission in the experiment is caused by the interplay of damaging and recovering mechanisms. The latter are fast at room temperature and keep the loss of light yield moderate. First exploratory experiments at IHEP (Protvino) have shown a completely different scenario if the irradiated crystals are cooled down to  $T = -25^\circ\text{C}$  and are kept cool even after the irradiation has been stopped. Fig. 4.22 and Fig. 4.23 illustrate for two crystal samples the typical behavior. At a starting dose rate of  $20 \text{mGy/h}$  the scintillation response drops continuously and does not even reach saturation after 1000 hours. In a similar way, almost no recovery can be noticed after irradiation for the two samples kept at  $T = -25^\circ\text{C}$ .

Therefore, more specific studies became necessary in order to characterize the nature and properties of defects with slow decay times. The experimental installation at Giessen allows to measure in a wave-

length specific manner the deterioration of the optical transmission expressed as the change of the induced absorption coefficient for crystals, while they are kept cool after irradiation for a longer time. Investigations of full size crystals were performed at temperatures of  $T = -3.5^\circ\text{C}$ ,  $T = -10.0^\circ\text{C}$  and  $T = -22.5^\circ\text{C}$ . Fig. 4.24 shows the representative result obtained for the absolute loss in transmission at  $T = -3.5^\circ\text{C}$  right after irradiation as a function of photon energy. The contributions of two specific absorption bands are marked for further analysis. The shape of the spectrum is similar to the results at the two lower temperatures. Fig. 4.25 repeats the above data obtained at  $T = -3.5^\circ\text{C}$  but re-scaled as induced absorption as a function of wavelength. The previous measurement at room temperature (see Fig. 4.9) shows in a similar manner the induced absorption primarily in the same wavelength range between 400-600 nm and two broad absorption bands located at wavelengths of 528 nm and 420 nm, corresponding to photon energies of 2.35 eV

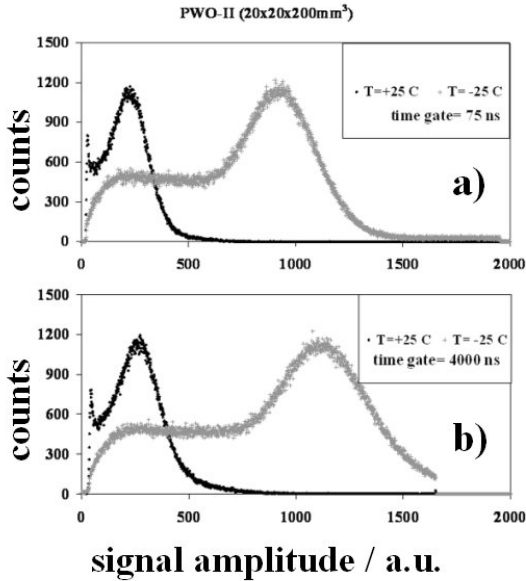


**Figure 4.17:** Pulse height spectra measured for a PWO-II crystal ( $20 \times 20 \times 200 \text{ mm}^3$ ) for  $\gamma$ -rays of a  $^{60}\text{Co}$ -source ( $E_\gamma \sim 1.2 \text{ MeV}$ ). The scintillation light has been converted with a photomultiplier tube (Hamamatsu R2059) at two temperatures and integrated over time windows of 75 ns (part a) or 4000 ns (part b), respectively.

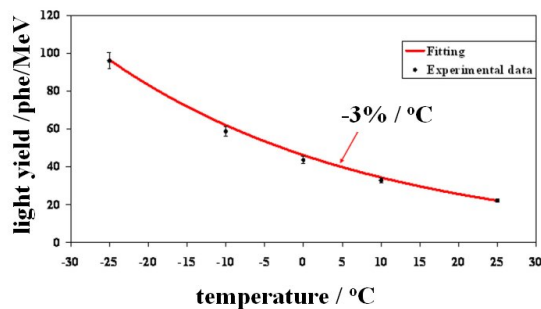


**Figure 4.18:** Temperature dependence of the yield of scintillation light of PWO-II in the temperature range between  $T=+25^\circ\text{C}$  and  $T=-25^\circ\text{C}$ , respectively.

and 2.95 eV, respectively.

Performing the irradiations of cooled crystals with significantly higher dose rates a saturation of the

damage can be observed at an integral dose of 30-60 Gy. This value does not depend on the temperature and might only reflect the individual concentration of defects in the crystal. In the final PANDA experiment such an integral dose will be accumulated only in the most forward part of the forward end-cap EMC at maximum beam intensity after 3000 hours of operation and might be never reached in the barrel region over a typical experimental cycle lasting 6 months.

The recovery of the optical transmission has been studied in a time range up to 5 days and at different temperatures. From the measurements similar to Fig. 4.24 but performed at different times after the end of irradiation an estimate of the lifetimes of the color centers can be deduced. Fig. 4.26 and Fig. 4.27 illustrate the kinetics of the two selected absorption regions. Besides a fast component the recovery times are in the order of hundreds of hours in both cases. At all investigated temperatures below  $0^\circ\text{C}$  the relaxation of the color centers remains slow and does not compensate even partially the damage in parallel.

Detailed studies of the impact of Mo impurity on the scintillation performance of the crystal allowed also to clarify its contribution to the radiation damage. It is well known that a contamination with  $\text{MoO}_4$ -complexes gives rise to green luminescence and extremely slow decay times in PWO crystals [24]. Therefore, the present generation of PWO-II crystals maintains the impurity on the level of several ppm. Our recent studies have identified the presence of  $(\text{MoO}_4)^{3-}$  centers exploiting the EPR technique. Spectral distributions of the induced absorption of various samples measured at room temperature gave first indications based on the broad absorption band peaked near 535 nm as already shown in Fig. 4.9. Systematic studies of paramagnetic resonance and thermoluminescence of  $\text{PbWO}_4/\text{PbMoO}_4$  mixed crystals [36] have investigated the properties of  $(\text{MoO}_4)^{3-}$  centers with respect to the molybdenum concentration. The temperature of maximum thermal decay depends strongly on the Mo concentration and reaches values near 250 K at concentrations below 1%. TL spectra of mixed crystals after 50 keV X-ray excitation show a pronounced glow peak slightly above 250 K for mixed crystals with low Mo concentration. Measurements of the concentration of  $(\text{MoO}_4)^{3-}$  and  $(\text{WO}_4)^{3-}$  paramagnetic centers in  $\text{CaWO}_4:\text{Pb}$  after X-ray irradiation and subsequent heating allow deducing the radiation induced optical absorption due to  $(\text{MoO}_4)^{3-}$  centers [37]. The spectral distribution indicates a broad

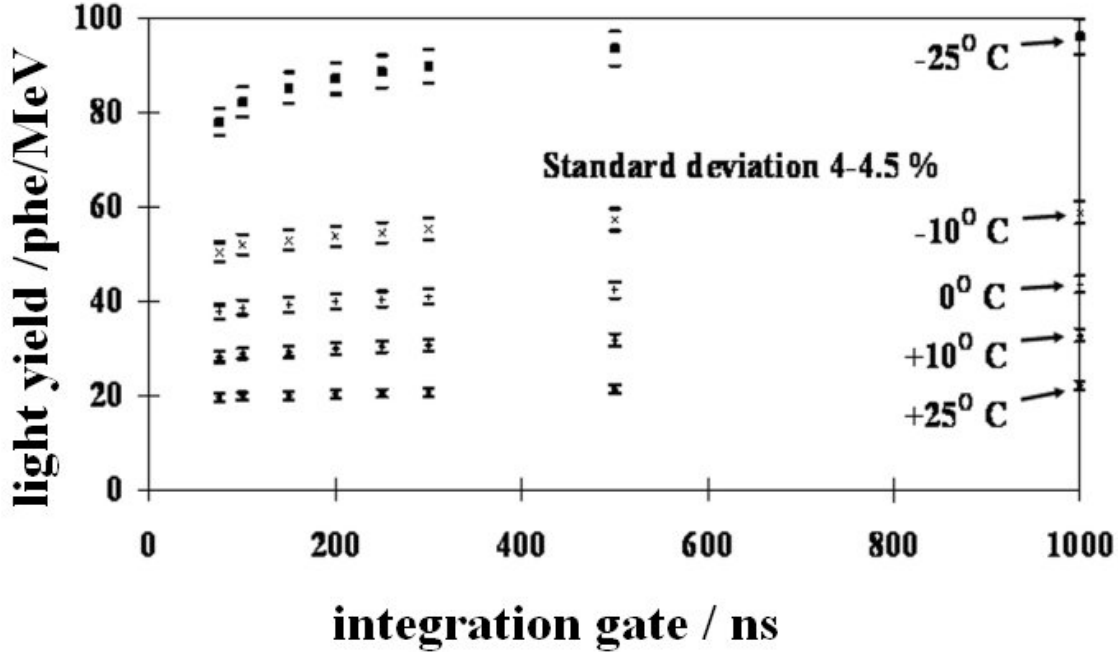


**Figure 4.19:** Dependence of the average light yield on the temperature and the integration gate for 10 PWO-II crystals ( $20 \times 20 \times 200 \text{ mm}^3$ ) produced at BTCF. The variations are given as error bars.

distribution peaked at a photon energy of 2.35 eV (FWHM=0.8 eV) corresponding to a wavelength of 528 nm. At  $T = -25^\circ\text{C}$ , which is below the activation temperature of  $(\text{MoO}_4)^{3-}$ , one observes as a consequence of the thermo-activation a slow decay time. Fig. 4.28 shows the EPR signal identifying the  $(\text{MoO}_4)^{3-}$  center in the PWO-II crystal, which was stored directly after the irradiation in liquid nitrogen. The drop of the signal intensity after a recovery of 96 hours was estimated to 25%. Similar measurements at different temperatures are in preparation.

Therefore, even a small concentration of Mo impurities can contribute to the reduced transmittance within that range of wavelengths. In order to ensure sufficient radiation hardness one has to put even a stronger limit on the Mo contamination in the crystal, even at a level below 1 ppm. This limit of Mo concentration has been so far specified for the crystal mass production.

#### 4.4.3 Radiation Hardness Required for $\bar{P}$ ANDA

The radiation damage reduces the output of the scintillation light and consequently the number of photoelectrons per unit of deposited energy. Therefore, the expectable light output has to be correlated with the quantified radiation resistivity. The latter is specified by the radiation induced absorption coefficient  $\Delta k$  at the wavelength of maximum scintillation emission at  $\lambda = 420 \text{ nm}$ , which can be easily measured and cross-checked, if it can be determined at the relevant facilities at a temperature of  $T = +20^\circ\text{C}$ . The correlation depends on the individual crystal shape, light collection and efficiency of the photo sensor and has not been experimentally determined for the target spectrometer EMC up to date. We intend to follow the approach used by CMS [52]. The information is obtained at small dose rates, which are similar to the experimental conditions of  $\bar{P}$ ANDA. The procedure determines the ratio of the changes of the scintillator and mon-

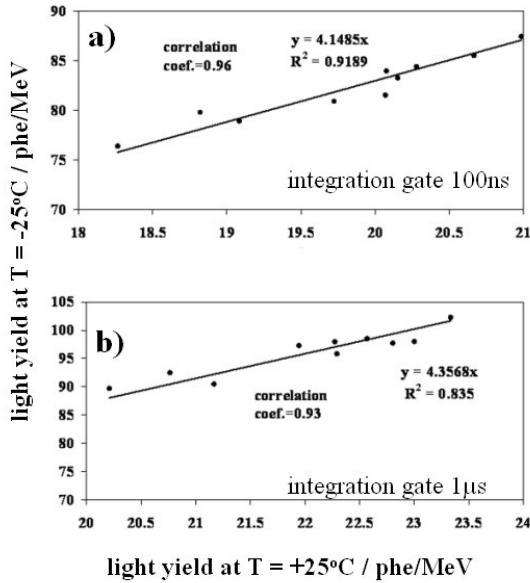


**Figure 4.20:** Correlation between the light yield induced by low energy  $\gamma$ -rays at temperatures of  $T=-25^\circ\text{C}$  and  $T=+25^\circ\text{C}$  for 10 PWO-II crystals ( $20 \times 20 \times 200 \text{mm}^3$ ). The photomultiplier response has been integrated over a time gate of 100 ns (part a) and 1000 ns (part b).

itoring response, respectively, and models the relationship by the expression  $S/S_0 = (R/R_0)^\alpha$ , where  $S/S_0$  and  $R/R_0$  are the relative variations of the response to the scintillation and monitoring signal, respectively. Since the geometrical shape of the crystals of CMS and PANDA are comparable, a typical value of 1.5 can be assumed for the parameter  $\alpha$ .

The measurement at the irradiation facility at IHEP (Protvino) estimates the change of optical transmission, deduced from the response to the transmitted light of two LEDs of different color, and the reduction of the scintillation response via the luminescence initiated by the absorbed  $\gamma$ -rays emitted from the  $^{137}\text{Cs}$  source. This measurement is not fully compatible with the response to electromagnetic probes hitting the crystal from the front face, but can give a first hint. Fig. 4.29 shows the dropping DC-current of the photomultiplier tube as a function of the irradiation time. The five investigated PWO-II samples were characterized before by the value of the induced absorption at  $\lambda=420 \text{nm}$  ( $\Delta k(420 \text{nm})$ ) determined at  $T=+20^\circ\text{C}$  at BTCP

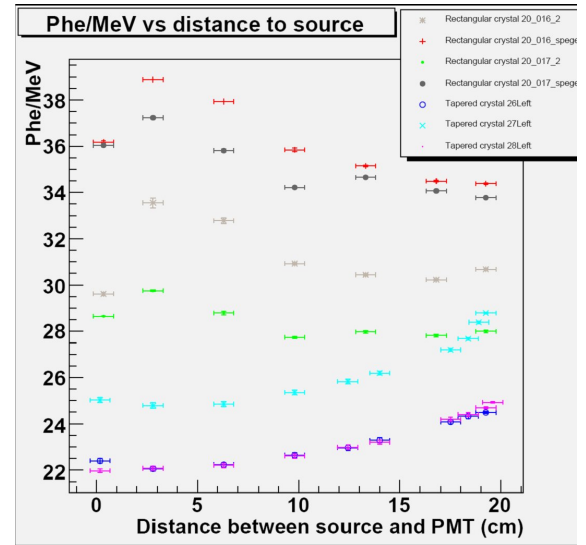


**Figure 4.21:** Variation of the light output measured for different crystal geometries and reflector materials when a collimated  $\gamma$ -source is moved relative to the sensor position along the crystal axis.

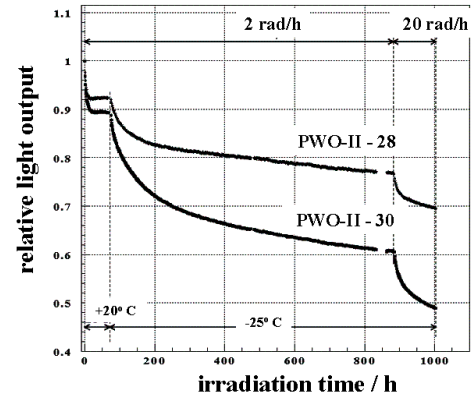


**Figure 4.22:** Relative change of the light yield of two PWO-II samples with irradiation time for two different dose rates and two temperatures. The curves are normalized to the initial light yield at  $T=+20^\circ\text{C}$ .

and afterwards annealed at  $T=200^\circ\text{C}$  for 2 hours. Table 4.4 summarizes the experimental data including the relative loss of scintillation response measured at  $T=-20^\circ\text{C}$ .

Both specification parameters are correlated in Fig. 4.30. In spite of the lack of sufficient statistics, a linear correlation can be proposed, which supports that the quality limits defined for control measurements at room temperature are sufficiently selective for the final operation at low temperatures. The data are consistent with the assumption of  $\alpha=1.5$

crystal ID	$\Delta k/m^{-1}$	$R/R_0$	estimated $S/S_0$
	T=+20°C	T=-20°C	T=-20°C
b4	0.402	0.905	0.86
b16	0.420	0.910	0.87
b17	0.289	0.915	0.88
b24	0.405	0.920	0.88
b30	0.753	0.890	0.84

**Table 4.4:** Comparison of the induced absorption  $\Delta k(420 \text{ nm})$  measured at BTCP, the value  $R/R_0$  at  $\lambda=450 \text{ nm}$  measured at IHEP (Protvino) and the estimated change of scintillation response.

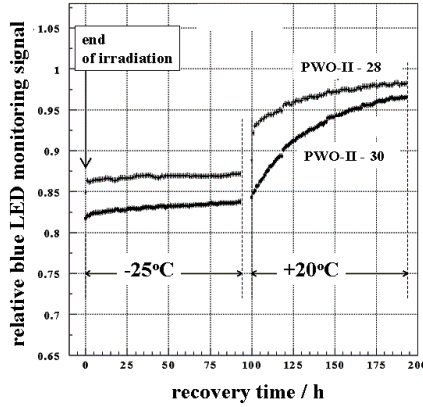


**Figure 4.23:** Relative change of the monitoring signal provided by the blue emitting LED illustrating the recovery of two PWO-II crystals after  $\gamma$ -irradiation at two different temperatures.

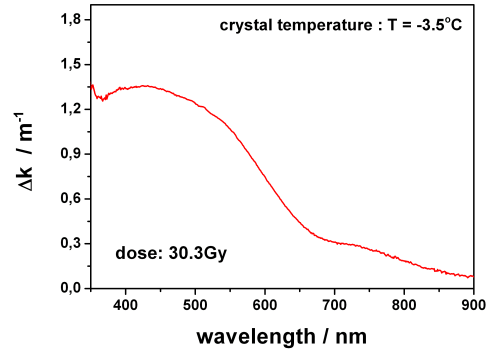


**Figure 4.25:** The induced absorption due to the irradiation of a PWO-II crystal with a dose of 30.3 Gy at a temperature of  $T=-3.5^\circ\text{C}$  given as a function of wavelength.

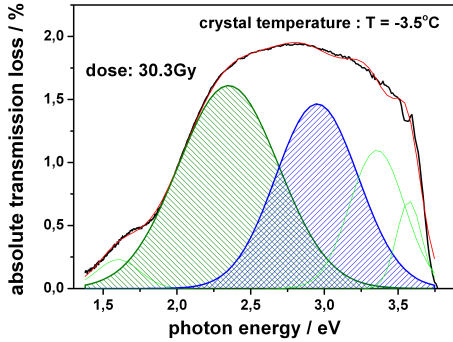


**Figure 4.24:** The absolute loss in transmission due to the irradiation of a PWO-II crystal with a dose of 30.3 Gy at a temperature of  $T=-3.5^\circ\text{C}$  shown as a function of photon energy. The contributions of two absorption bands at photon energies of 2.35 eV and 2.95 eV, respectively, are marked for detailed analysis.

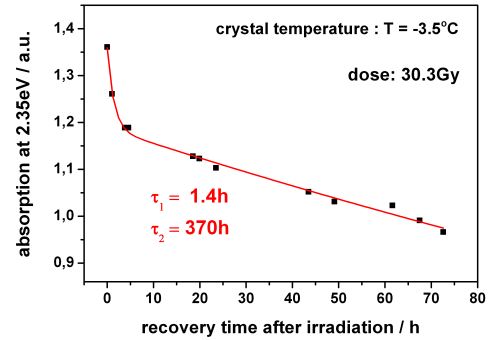


**Figure 4.26:** The decay kinetics of an absorption region near a photon energy of 2.35 eV ( $\lambda=528 \text{ nm}$ ) after the irradiation of a PWO-II crystal with a dose of 30.3 Gy at a temperature of  $T=-3.5^\circ\text{C}$ .

as discussed above. Therefore, due to the slow re-

laxation of color centers in cooled crystals one has to cope with a typical loss in scintillation response between 20 and 30 % as an asymptotic value after a deposited dose of 30-50 Gy for typical PWO-II

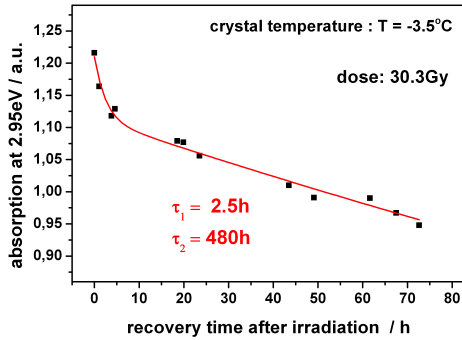


**Figure 4.27:** The decay kinetics of an absorption region near a photon energy of 2.95 eV ( $\lambda=420$  nm) after the irradiation of a PWO-II crystal with a dose of 30.3 Gy at a temperature of  $T=-3.5^\circ\text{C}$ .

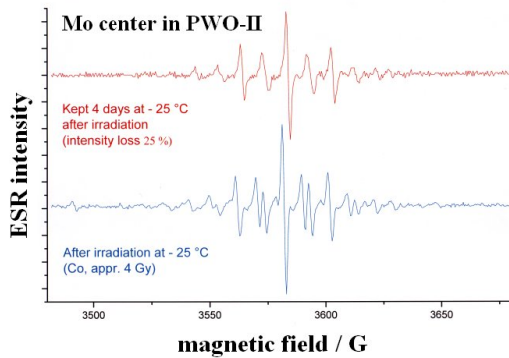


**Figure 4.28:** EPR signal of the  $(\text{MoO}_4)^{3-}$  center in a PWO-II crystal measured at  $T=-25^\circ\text{C}$  immediately after irradiation (upper part) and 96 hours later. Both probes were kept continuously at  $T=-25^\circ\text{C}$ .

crystals.

These results have been further confirmed by a direct measurement of the pulse height spectrum of the energy deposition of minimum ionizing cosmic muons measured with a cooled crystal detector assembly. Fig. 4.31 compares the spectra measured at  $T=+24^\circ\text{C}$  and  $T=-26^\circ\text{C}$ , before and after irradiation at the lower temperature with an integral dose of 53 Gy. In spite of a reduction of the light output by 31% the photon statistics remains a factor 3 above the value at room temperature. In spite of the significant asymptotic degradation of the response, the slow change can be very well monitored with high precision and stability.

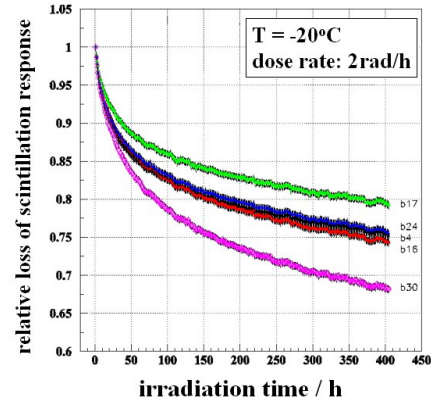


**Figure 4.29:** Change of the scintillation response due to a continuous irradiation with low-energy  $\gamma$ -rays ( $^{137}\text{Cs}$ ) for 5 samples of the pre-production run deduced from the DC-signal of the photomultiplier response. The measurement has been performed at IHEP, Protvino.

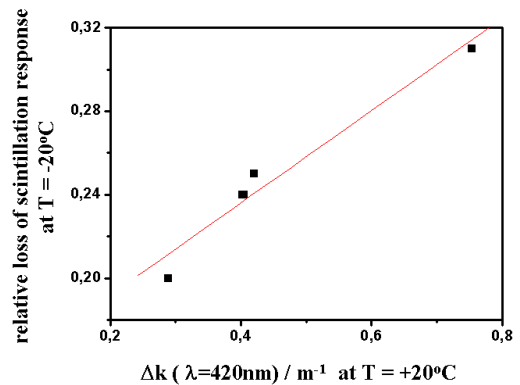


**Figure 4.30:** Correlation between the maximum change of the scintillation response, as shown in Fig. 4.29, and the induced absorption coefficient  $\Delta k$  at  $\lambda=420$  nm measured at BTCP at room temperature.

#### 4.4.4 Pre-Production Run of PWO-II Crystals

A subgroup of scintillator modules of the barrel EMC (40 crystals of each type: 8,9,10) has been produced by BTCP in December 2007/February 2008. Fig. 4.32 shows a few optically polished barrel type crystals produced at BTCP. The remaining crystals to complete one slice of the barrel EMC have been delivered in May 2008 and are presently inspected for a detailed quality control and to adjust and calibrate the ACCOS machine and test installations at CERN and JLU, respectively. The

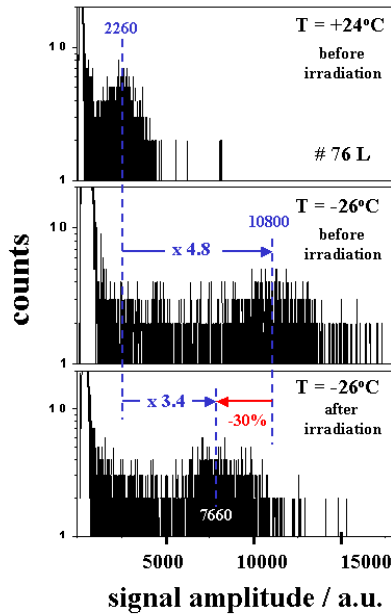


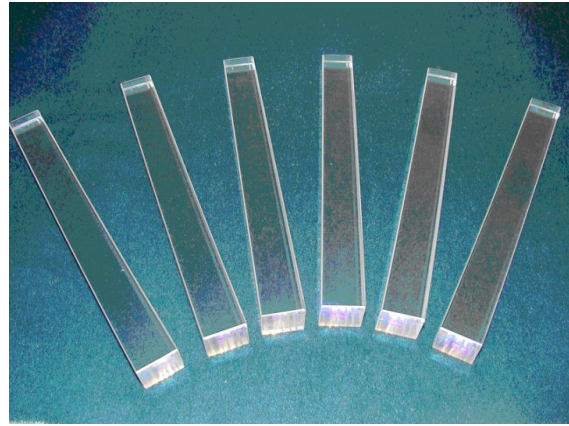
**Figure 4.31:** Change of the scintillation response expressed by the measured energy deposition of cosmic muons in an assembled PWO-II detector. The figure shows the measurement at  $T=+24^{\circ}\text{C}$  and  $T=-26^{\circ}\text{C}$ , respectively. The spectra at the lower temperature are obtained before and after irradiation with an integral dose of 53Gy. The measurement was carried out at Giessen.

pre-production run was aiming for:

1. check of the reproducibility of the production technology
2. confirmation of the correspondence of the crystal quality to the specification
3. production of several reference crystals to be used for adaptation of the certification tools to PANDA type crystals
4. estimation of the technological yields of the crystals at different modes of operation of the production.

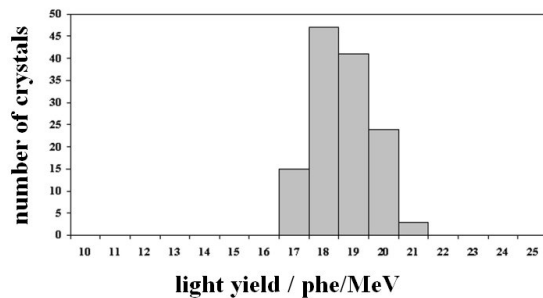
The performed tests of the first 120 units have confirmed, that all mechanical dimensions are within the specified tolerances. Some of the relevant quality parameters are summarized in the next three figures.

Fig. 4.33 shows the range of the achieved light yield measured with a standard photomultiplier with bi-



**Figure 4.32:** Machined and optically polished barrel type PWO-II crystals for the PANDA electromagnetic calorimeter.

alkali photocathode at room temperature. The next two figures document the variation of the induced absorption. Fig. 4.34 shows for 1 cm thick samples cut from the ingots of a pre-production lot the induced absorption as a function of wavelength. A  $^{60}\text{Co}$  source was used to deposit a total dose of 1 kGy at a rate of 2 kGy/h. Fig. 4.35 projects the distribution of the induced absorption value at the wavelength of 420 nm. These measurements were performed at the irradiation facility at BTCP.



**Figure 4.33:** Distribution of the light yield of barrel type PWO-II crystals of the pre-production lot measured at room temperature using a photomultiplier tube with bi-alkali photocathode.

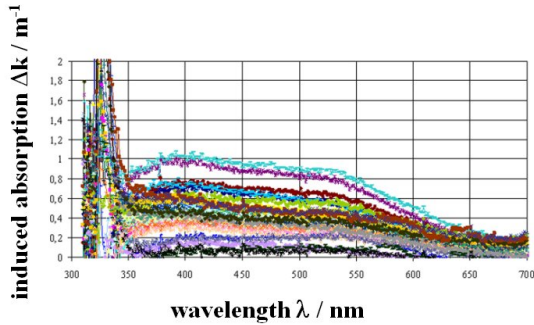


**Figure 4.34:** Radiation induced absorption spectra of 1cm thick PWO-II samples cut from the ingots of a pre-production lot measured at room temperature. A  $^{60}\text{Co}$  source has deposited a total dose of 1 kGy at a dose rate of 2 kGy/h.

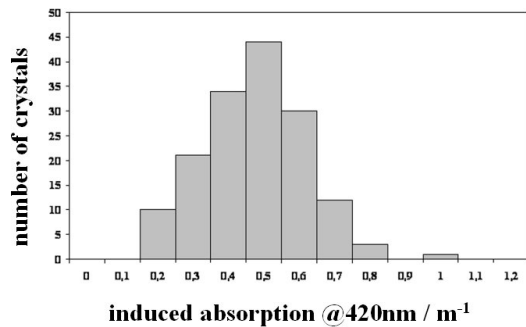


**Figure 4.35:** Distribution of the induced absorption measured at  $\lambda=420\text{nm}$  after an absorbed dose of 50 Gy at room temperature for PWO-II crystals of the pre-production run.

## 4.5 Quality Requirements and Control

The electromagnetic calorimeter of  $\overline{\text{PANDA}}$  requires the production of nearly 16,000 scintillating crystals. The envisaged high performance of the detector imposes strict requirements on the crystal parameters, such as sufficient and uniform light yield, short decay time free of slow components, very limited light yield loss under irradiation and finally precise geometrical dimensions. To ensure a high and efficient production rate, the certifying procedure for such a large scale project has been elaborated for both the producer and the customer site

taking advantage of the many years of experience for CMS/ECAL [53]. The equipment for automatic measurement of the optical and scintillation properties, the associated software tools as well as the methods and facilities for the radiation hardness tests are described in the upcoming sections.

The target spectrometer EMC requires the production of  $\text{PbWO}_4$  crystal elements of 200 mm length of one shape for both endcaps and 11 different shapes for the barrel. The latter ones are used in two symmetric versions. Each crystal has to pass two certifying procedures, one before delivery at the manufacturer site and a final one performed by the customer. Presently, the specification limits, which are listed below, are more stringent mainly due to the requested higher light yield and the operation at low temperature down to  $T=-25^\circ\text{C}$ .

### 1. General Properties

- Crystal dimensions have to conform to the drawings given in Fig. 7.3, Fig. 7.24, and Fig. 7.35.
- Crystals have to be oriented with their front face to the seed part of the ingot.
- The appearances of crystals with respect to color, visible spatial and surface defects have to conform to the coordinated reference crystal.
- The polished surfaces are polished with a roughness of  $R_a \leq 0.02\mu\text{m}$ , the lapped face has a roughness  $R_a = 0.40 \pm 0.05\mu\text{m}$ . This parameter may be subject of modification under mutual agreement with the producer.
- The surface finish of chamfers should be made at a roughness of not more than  $0.5\mu\text{m}$  (lapping).
- No cracks prolonging deeper than 0.5 mm into the crystal are allowed on the chamfers.

**2. Optical Properties:** These properties of all crystals should be measured with cross-checked equipment.

- (a) Longitudinal transmission (absolute values)
  - $\geq 35\%$  at  $\lambda=360\text{nm}$
  - $\geq 60\%$  at  $\lambda=420\text{nm}$
  - $\geq 70\%$  at  $\lambda=620\text{nm}$
- (b) The non-uniformity of the transversal transmission  $\delta\lambda$  at the transmission value of  $T=50\%$  has to be  $\delta\lambda \leq 3\text{ nm}$ , for 6

measurements every 4 cm; the first one is at 1.5 cm from the front face.

- (c) Light yield  $\geq 15$  phe/MeV at  $T=18^\circ\text{C}$  (for crystals with one lateral side de-polished).
- (d) Light yield  $\geq 16$  phe/MeV at  $T=18^\circ\text{C}$  (for crystals with all sides polished).
- (e) Decay time:  $\text{LY}(100 \text{ ns})/\text{LY}(1000 \text{ ns}) > 90\%$  at  $T=18^\circ\text{C}$ .

### 3. Radiation Hardness

- (a) Radiation hardness is evaluated by the measurement of the induced optical absorption in the crystal along its axis. The crystals shall be kept at all times at a temperature  $T=20 \pm 5^\circ\text{C}$  between the irradiation and the completion of the measurements. The value of the induced absorption calculated from the optical transmission of the crystal caused by the irradiation is limited to  $\Delta k \leq 1\text{m}^{-1}$  at  $\lambda=420 \text{ nm}$  due to lateral  $^{60}\text{Co}$  irradiation. The totally accumulated dose shall be 30 Gy at a rate of 50-500 Gy/h. The mean value of the  $\Delta k$  distribution defined for each lot and based on the measurements of not less than 50% of the lot shall be  $< \Delta k > \geq 0.75 \text{ m}^{-1}$ .

The conventional laboratory methods used for crystal measurements cannot provide the necessary throughput. Therefore, a high-productivity industrial system - Automatic Crystal Control System (ACCOS) has been constructed [54] and installed at both the crystal production facility and at CERN during implementation of the CMS project (see Fig. 4.36). There is an agreement with the CMS management on the use of this equipment and the directly related infrastructure. The equipment is highly automated in order to reduce the influence of the human factor and to provide an output of at least 30 crystals per day. The PWO crystal is mechanically fragile and can easily be damaged by contact with hard equipment parts. Therefore, unnecessary frequent handling of crystals should be strictly avoided. The adopted solution is to keep crystals lying on special supports during all measurements and to move the spectrometers along them. Consequently, special devices of a very compact layout were designed. The overall setup including the associated 3D-machine is installed in a temperature-controlled and light-tight room. A bar-code reader identifies each crystal from the bar-coded label glued on the small end-face at the production stage. Two identical ACCOS machines are

installed both at the production site and at CERN to provide non-stop operation even in case of malfunctioning.

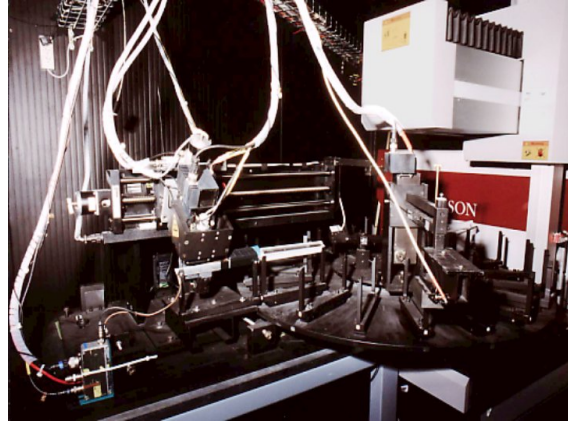


**Figure 4.36:** The ACCOS machine installed at the CMS regional center at CERN to perform the quality inspection of PWO-II crystals in a semi-automatic procedure.

### 4.5.1 Measurements of the Light Yield and the Light Yield Non-uniformity

A *start-stop* or delayed coincidence method is used both for the measurement of the scintillation decay time and light yield (LY). The proportionality between the count rate of the stop signals and the light yield of the scintillator for small quantities of light is used to determine the LY by integration of the decay time spectrum. It means that both parameters can be measured simultaneously. In this case, neither optical coupling between scintillator and PM nor scintillator wrapping are needed in contrast to the very widely used method of pulse-height spectrum measurement by using radioactive  $\gamma$ -sources (most commonly  $^{60}\text{Co}$ ) with consequent total absorption peak position determination. The *start-stop* method puts two constraints on the event rates, which limits the productivity. One is the limitation on the annihilation source activity. It should not exceed  $10^5 \text{ Bq}$ . At higher activity the probability of random coincidences of two  $\gamma$ -quanta from different decays becomes too high and leads to background. The second is the limitation on the probability of detecting scintillation photons in the stop channel per single excitation. A conventional TDC requires that the average number of detected photons to be not more than 0.1 per single excitation. Otherwise, the measured scintillation decay

curve will be distorted, especially in the slow component region. The use of a multi-hit TDC would avoid this problem. The dead time of the stop-channel detector can also cause distortion, in particular in the region of the fast component, when the fastest component in scintillation is less than or comparable to the stop channel dead time, which is the case for PWO. A single-hit TDC (or TDC with multi-stop rejection [55]) was implemented to overcome the distortion problem. The most comprehensive analysis of TDC with multi-stop rejection is made in [56]. The start-channel detector consists of a Hamamatsu UV-extended photomultiplier (R5900) coupled to a  $20 \times 20 \times 20 \text{ mm}^3$  BaF<sub>2</sub> scintillator. The <sup>22</sup>Na annihilation source with an activity of 200 kBq is mounted as close as possible to the scintillator and delivers about  $2 \cdot 10^4$  /s starts. The start photomultiplier with scintillator and source is mounted on a moving platform together with the transversal transmission photospectrometer for scanning along the crystal. The stop-channel is based on another Hamamatsu R5900 selected with a low count rate of dark pulses. The average number of stop signals (detected scintillation photons) amounts to  $\sim 0.3$  per single excitation for the most luminous PWO crystals. The overall count rate of good events (scintillation photons produced by scintillation decay in PWO and collected in the decay time spectrum) is typically 1 kHz, and a spectrum with acceptable statistics can be acquired within one minute.

#### 4.5.2 Inspection of the Optical Properties

The longitudinal transmission can be reconstructed using transmission data taken in transverse direction. However, it is impossible to obtain the required precision in case of PWO scintillation elements because of uncertainties in the Fresnel reflection level from crystal to crystal. These uncertainties are caused by the deviation of the crystal growth axis from the crystallographic axis by  $\pm 5^\circ$ . Therefore, both types of transmission measurements should be performed. Since PWO is a birefringent crystal and the shape of the scintillation elements varies, a wide-aperture photo detector is required. This prevents from the use of spectrometers, which are based on photodiode arrays with a light dispersing prism. On the other hand, the PWO transmission spectrum has no narrow absorption bands, so it is not necessary to measure the spectrum at many wavelengths. It can be measured only at several well-chosen wavelengths

with subsequent reconstruction of the total spectrum to speed up the measurements. For this purpose, a set of 11 interference filters was used. Two dedicated compact photospectrometers for optical transmission measurement have been designed and built. The optical part of each photospectrometer includes a 20 W halogen lamp, a four-lens collimator, three objective lenses, a rotating changer with interference filters, collecting mirrors, a  $20 \times 20 \text{ mm}^2$  UV-extended photodiode (Hamamatsu S6337) and readout electronics. The spectrometer dimensions are  $70 \times 80 \times 220 \text{ mm}^3$ . The compact design allows the fast movement of the spectrometer from the measurement zone to the calibration position (air measurement). During operation, the rotating wheel with interference filters crosses the light beam sequentially. Such a system provides a fast switching (0.5 s) of the wavelength. The time necessary to measure a transmission spectrum in the range from 330 nm to 700 nm takes less than 10 s for one spatial point.

#### 4.5.3 Measurement of the Geometrical Dimensions

All dimension measurements are carried out with the standard three-dimensional machine *TOPAZ 7* supplied by Johansson AB (Sweden), which provides three coordinates of several points on each crystal face with a precision of  $\pm 5 \mu\text{m}$  and subsequent calculation of the crystal dimensions and the planarity of all faces.

#### 4.5.4 Analysis and Documentation

Software is provided for a user interface, acquisition, data processing, results storage and presentation. It also supports communication with the C.R.I.S.T.A.L. database software [57] and the 3D-machine. Software components are implemented in LabView<sup>TM</sup> graphical programming system and Microsoft<sup>TM</sup> Visual C++ and runs on an IBM-compatible PC under Microsoft<sup>TM</sup> Windows operating system. A special algorithm was developed for the processing of the scintillation kinetics data [58]. Instead of a non-linear iterative fitting procedure usually used for multi-exponential functions and giving sometimes unstable results due to inherent convergence problems, a new approach is based on non-iterative 3-step integrating/subtraction procedure working without user intervention.

### 4.5.5 Control Measurements of Production Stability

To provide the stability of the technology and minimize the number of rejections the following set of control measurements should be carried out in addition to the certification measurements along the total manufacturing process.

- **Quality check** of the raw material provided by pilot crystal growth and measurements (1 per 100 crystals) - the only acceptable rate in terms of time and expenses;
- **Technology discipline check:**  
analysis of average crystals parameters per lot;  
analysis of average crystals parameters during some period for each growing machine;  
analysis of rejected crystals
- **Radiation hardness characterization on the sampling basis:**  
measurement of radiation induced absorption in top parts of crystals (5-10 top parts per 100 crystals);  
measurement of radiation induced absorption in full-size crystals devoted to the specific oven in case a previous check gives marginal results

Pilot crystals along with top parts of regular crystals will be analyzed in detail at the INP (Minsk) using the same methods and laboratory equipment as were exploited during the development phase of PWO crystals. All crystals rejected by the certification measurements have to be investigated by independent laboratory methods with full confirmation of the results. Even accepted crystals, which have passed the certification procedure, will be checked by laboratory methods on the sampling basis. All required measurements during PWO mass-production can be summarized in a 3-level scheme to make decisions. On the first level, the manufacturer and INP provide pilot crystal growth and tests to prove the specific raw material batch to be acceptable for crystal production. On the second level, the produced crystals pass through the certification procedure on the ACCOS system and radiation hardness checks at the manufacturer plant. The data analysis is performed at INP including the decision on the delivery of the crystals to the customer. On the third level, the customer carries out the visual inspection, the certification on the ACCOS machine and radiation hardness tests. If all requirements are fulfilled the crystals will be accepted for the assembly into the calorimeter. The first two steps of the final acceptance will be performed at

the CERN facilities. Final radiation tests will be done at the facility at Giessen. Depending on the overall productivity and stability of the manufacturing process some tests at the customer facilities might be done either on all crystals or on selected samples.

### 4.5.6 Manufacturer for the Final Production

All presently installed or operating calorimeters, such as ECAL (CMS), PHOS (ALICE) and HYCAL of the PrimEx experiment at JLAB [59] are composed of PWO crystals manufactured by ShanghaiInstituteofCeramics (SICCAS, China) or the two Russian producers BogoroditskTechnicalChemicalPlant or NorthCrystals. The latter one, the major producer for PHOS, has moved out of the scintillator business. As outlined in the previous chapters, the specification limits for the calorimeter crystals have to be identical to the quality of PWO-II, which was developed in close collaboration with BTCP and the CMS/ECAL group. Up to now a first pre-production run performed at BTCP was completed in May 2008 comprising more than 710 crystals of all 23 different shapes with an overall length of 200 mm. The first lot allows to complete one out of the 16 slices of the barrel EMC and a first subarray of the forward endcap EMC. Some of the achieved quality parameters were shown in the previous chapter.

There exists a long collaboration with the Shanghai Institute of Ceramics and many state-of-the-art test crystals of various sizes were investigated. Finally, a full matrix comprising 25 modules of 200 mm length with identical cross section of  $20 \times 20 \text{ mm}^2$  were delivered in 2005 for comparison.

These crystals are grown along the  $c$ -axis by a modified Bridgeman method [61] and consequently differ in the longitudinal and transverse optical transmittance. Fig. 4.37 shows a comparison of measured transverse and longitudinal transmission. The measurements performed for a sample from both manufacturers are compared to theoretical limits assuming no internal absorption [62, 60]. The chosen crystal from BTCP corresponds to CMS quality. The three different calculations are using the refractive index of ordinary light, which propagates along the  $c$ -axis and has a polarization perpendicular to the  $c$ -axis. Extraordinary light propagates perpendicular to the  $c$ -axis and has a polarization along the  $c$ -axis. Finally, unpolarized light is assumed to propagate perpendicular to the  $c$ -axis. Because of the birefringence, the theoretical limit of the extraordi-

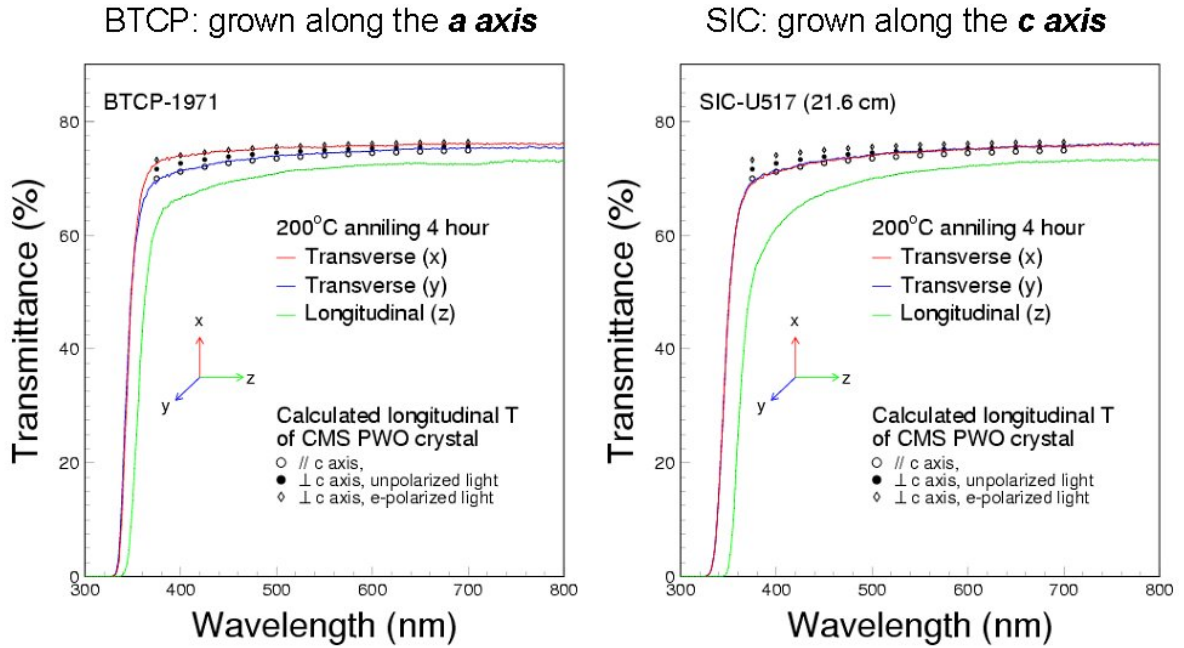


**Figure 4.37:** Comparison of the optical transmission of two crystal samples from the manufacturers BTCP and SICCAS. The experimental data are compared to theoretical calculations described in the text. The figures are taken from Ref. [60].

ary light is about 3% higher than that of the ordinary light. Since the crystals produced in China are grown along the  $c$ -axis, the experimental longitudinal transmission should be compared to the theoretical limit for propagation along the  $c$ -axis independent of polarization. Consistent with the theoretical calculations, the samples from BTCP show a better longitudinal transmission. However, the measurement of the absolute yield of the detected scintillation light is slightly superior for the Chinese products, which are doped exclusively with yttrium ions. Compared to CMS standards, these crystals show approximately 30–40% more light.

Small crystal samples ( $16 \times 16 \times 30 \text{ mm}^3$ ), which were readout with photomultiplier tubes, confirm the good photon statistics expressed by the excellent energy resolution of  $\sigma_E/E=14.5\%$  obtained for 662 keV  $\gamma$ -rays at a temperature of  $T=-26^\circ\text{C}$ . The 25 full size crystals at room temperature deliver a mean light yield of  $\sim 18.0 \text{ phe/MeV}$  and are comparable to PWO-II. Both values are determined with photomultiplier tubes. Fig. 4.38 summarizes for one of the brightest samples the change of light yield at reduced temperatures. The values are obtained with a calibrated photomultiplier tube (Hamamatsu R2059, quantum efficiency  $\text{QE}(420 \text{ nm})=20.5\%$ ) by integrating the response over time gates ranging between 75 ns and  $1 \mu\text{s}$ , respectively. The figure

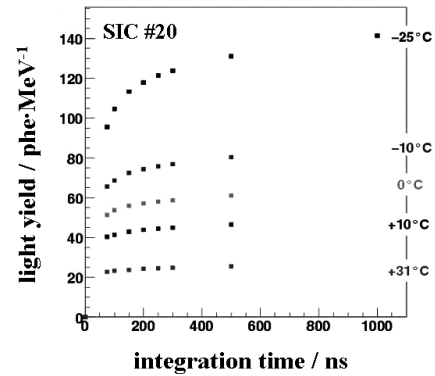


**Figure 4.38:** Absolute light yield of a 200 mm long rectangular crystal manufactured by SICCAS. The scintillation light has been measured with a photomultiplier tube with bialkali photo cathode. The response is shown at different temperatures as a function of integration gates varying between 75 ns and  $1 \mu\text{s}$ , respectively.

shows a high and nearly constant light yield at  $T=+31^\circ\text{C}$ . There is a strong increase of the emitted light when the temperature is decreased down to  $T=-25^\circ\text{C}$ . However, in strong contrast to crystals of similar size from BTCP, there is a significant and rising contribution of slow scintillation components.

Therefore, in order to collect  $\geq 90\%$  of the light output, integration times between  $0.5$  and  $\gg 1.0 \mu\text{s}$  become mandatory leading to a severe impact on the count rate capabilities of a calorimeter [63].

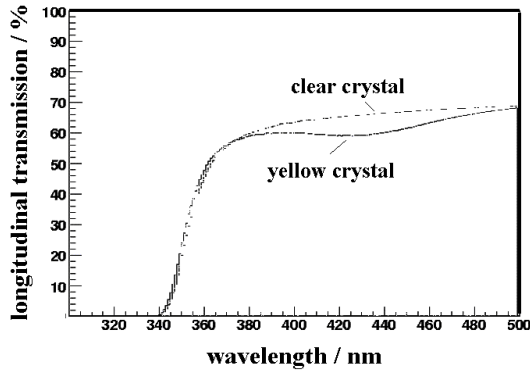


**Figure 4.39:** Longitudinal optical transmission of two 200 mm long crystals manufactured by SICCAS. The slightly colored sample shows a strong absorption band peaking at  $\lambda \sim 420$  nm.

In addition, detailed investigations have observed significant inhomogeneities of the crystals. In particular, about half of the delivered samples show a yellowish color, which leads in the optical transmission spectrum to a strong absorption region peaked at  $\lambda \sim 420$  nm as shown in Fig. 4.39. A complementary study of the transversal optical transmission, determined at several positions along the crystal axis, documents an insufficient homogeneity of several crystals. Fig. 4.40 shows strong deviations of the transmission values appearing typically at both ends of the crystal when measured at the critical wavelength of  $\lambda \sim 420$  nm.

As a consequence, the manufacturer SICCAS has started further developments in order to adapt the scintillation kinetics at lower temperatures to the PANDA needs. Some of the samples with a volume of a few  $\text{cm}^3$  show faster decay kinetics but there has been up to date not yet the delivery of full size scintillation crystals for a realistic comparison.

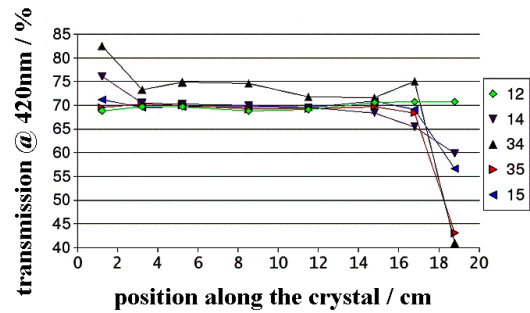


**Figure 4.40:** Inhomogeneity in the transversal optical transmission of several 200 mm long crystals manufactured by SICCAS and measured at the wavelength  $\lambda \sim 420$  nm. The cross section of the rectangular crystals is  $20 \times 20 \text{ mm}^2$ . Most of the samples indicate deviations even at both end sections of the crystal.

## References

- [1] R. Novotny, Nucl. Instrum. Meth. **A537**, 1 (2005).
- [2] R. Novotny, High-resolution electromagnetic calorimetry in medium and high energy physics based on inorganic scintillators, in *Proceedings SCINT 2005*, edited by A. Gektin and B. Grinyov, page 310, ISBN 9666-02-3884-3, 2005.
- [3] E. Lorenz, Nucl. Instrum. Meth. **A225**, 500 (1984).
- [4] R. Sumner, Nucl. Instrum. Meth. **A265**, 252 (1988).
- [5] J. A. Bakken et al., Nucl. Instrum. Meth. **A343**, 456 (1994).
- [6] O. Adriani et al., Nucl. Instrum. Meth. **A302**, 53 (1991).
- [7] W. W. Moses et al., Nucl. Instrum. Meth. **A353**, 189 (1994).
- [8] G. J. Bobbink, A. Engler, R. W. Kraemer, J. Nash, and R. B. Sutton, Nucl. Instrum. Meth. **A227**, 470 (1984).
- [9] C. Laviron and P. Lecoq, Nucl. Instrum. Meth. **A227**, 45 (1984).
- [10] S. K. Sahu et al., Nucl. Instrum. Meth. **A388**, 144 (1997).

- [11] K. C. Peng et al., Nucl. Instrum. Meth. **A427**, 524 (1999).
- [12] D. F. Anderson, IEEE Trans. on Nucl. Sci. **36**, 137 (1989).
- [13] R. Novotny, Nucl. Instrum. Meth. **A486**, 131 (2002).
- [14] J. Chen et al., Trans. on Nucl. Sci. **52**, 3133 (2005).
- [15] R. W. Novotny et al., IEEE NSS 2006, Conference Record , 1118.
- [16] M. Thiel et al., Trans. on Nucl. Sci. **55**, 101 (2008).
- [17] J. Chen et al., Trans. on Nucl. Sci. **54**, 1319 (2007).
- [18] CERN-LHCC-97-33.
- [19] CERN-LHCC-95-71.
- [20] A. A. Annenkov, M. V. Korzhik, and P. Lecoq, Nucl. Instrum. Meth. **A490**, 30 (2002).
- [21] A. Annenkov et al., Nucl. Instrum. Meth. **A450**, 71 (2000).
- [22] M. Kobayashi et al., volume A537, page 312, 2005.
- [23] M. Korzhik, Talk at FEMC03, FZ Jülich, Germany, March 10-11, 1003.
- [24] M. Böhm et al., phys. stat. sol. A. **167**, 243 (1998).
- [25] X.Liu, G.Hu, X.Feng, Y.Huang, and Y.Zhang, Phys. Stat. Sol. (a) **190**, R1 (2002).
- [26] P. Richter, G. Kruger, and C. Pistorius, Acta Crystall **B32**, 928 (1976).
- [27] T. Fujita, I. Kawada, and K. Kato, Acta Crystall **B33**, 162 (1977).
- [28] R. Williams, Y. Zhang, Y. Abraham, and N. Holzwarth, 1999.
- [29] P. Lecoq et al., Nucl. Instrum. Meth. **A365**, 291 (1995).
- [30] R. Y. Zhu et al., Nucl. Instrum. Meth. **A376**, 319 (1996).
- [31] B. Han, X. Feng, G. Hu, Y. Zhang, and Z. Yin, J. Appl. Phys. **86**, 3571 (1999).
- [32] E. Auffray, IEEE Trans. on Nucl. Sci. **55**, 57 (2008).
- [33] R. N. K. Mengel et al., IEEE Trans. on Nucl. Sci. **45**, 681 (1998).
- [34] R. Novotny et al., IEEE Trans. on Nucl. Sci. **47**, 1499 (2000).
- [35] J. Moreau, R. Gladyshevski, P. Galez, J. Peigneux, and M. Korzhik, J. of Alloys and Compound **284**, 104 (1999).
- [36] A. Hofstaetter et al., phys. stat. sol. B. **89**, 375 (1978).
- [37] M. Böhm et al., Journal de Physique C **6**, 508 (1980).
- [38] M. Böhm et al., Proceedings of SCINT99, Moscow, Russia, Aug. 16-29, 1999 , 619 (2000).
- [39] S. Baccaro et al., Proc. Intern. Workshop on Tungstate Crystals, Rome, Italy, Oct 12-14 (1998).
- [40] M. Böhm et al., Proc. Intern. Workshop on Tungstate Crystals, Rome, Italy, Oct 12-14 , 139 (1998).
- [41] M. Böhm et al., Rad. Effects and Defects in Solids **150**, 413 (1999).
- [42] V. Laguta, J. Rosa, M. Zaritski, M. Nikl, and Y. Usuki, J. Phys. Condensed Matter” **10**”, 7293” (1998”).
- [43] A. Hofstaetter et al., Proceedings of SCINT99, Moscow, Russia, Aug. 16-29, 1999 , 128 (2000).
- [44] A. Hofstaetter et al., Radiation Measurements **33**, 533 (2001).
- [45] M. Nikl et al., Applied Phys. Lett. **71**, 3755 (1997).
- [46] S. Baccaro et al., Phys. Stat. Sol. (a) **160**, R5 (1997).
- [47] <http://www.atomtex.com>.
- [48] V. A. Batarin et al., Nucl. Instrum. Meth. **A550**, 543 (2005).
- [49] P. A. Semenov et al., Nucl. Instrum. Meth. **A582**, 575 (2007).
- [50] G. Drobychev et al., IEEE Trans. on Nucl. Sci. **48**, 1177 (2001).

- [51] A. Fedorov et al., Nucl. Instrum. Meth. **A413**, 352 (1998).
- [52] P. Adzic et al., Eur. Phys. J. **C44**, 1 (2006).
- [53] E. Auffray et al., CMS Note (1998/038).
- [54] O. Missevitch et al., Nucl. Instrum. Meth. **A456**, 325 (2001).
- [55] W. W. Moses, Nucl. Instrum. Meth. **A336**, 253 (1993).
- [56] A. F. Cherniavskii et al., Atomizdat (in Russian) , 352 (1974).
- [57] J.-M. L. Goff et al., CMS Note (1996/003).
- [58] O. V. Missevitch et al., Instruments and Experimental Techniques **45**, 34 (2002).
- [59] A. Gasparian, Proceedings of 11th Int. Conf. on Calorimetry in Particle Physics, Perugia, Italy, 2004 , 109 (2005).
- [60] R. Y. Zhu, private communication.
- [61] X. Qu et al., Nucl. Instrum. Meth. **A480**, 470 (2002).
- [62] R. Mao et al., IEEE Trans. on Nucl. Sci. **51**, 1777 (2004).
- [63] F. Hjelm et al., Proceedings of SCINT05, Alushta, Ukraine, 2005 , 381 (2006).

## 5 Photo Detectors

The detection of scintillation light of lead tungstate under the given conditions for the PANDA EMC requires excellent photo detectors.

The magnetic field of about 2 T precludes the use of conventional photomultipliers. On the other hand the signal generated by ionization in a PIN photodiode by a traversing charged particle is too large for our applications. To solve these problems a photosensor insensitive to magnetic fields and with a small response to ionizing radiation has to be used.

Since lead tungstate ( $PbWO_4$ ) has a relatively low light yield, the photosensor is required to have internal gain in addition. Due to the increase of the crystal light yield accomplished by cooling the scintillator down to a temperature of  $T = -25^\circ\text{C}$ , the used photo detectors have to be radiation hard in this temperature regime, which implies detailed studies concerning possibly occurring radiation damages.

For the barrel EMC an Avalanche Photodiode (APD) which has an internal signal amplification in the silicon structure is chosen as photo detector. The low-energy photon threshold in the order of 10 MeV requires to maximise the coverage of the readout surface of the crystals, leading to the development of Large Area APDs (LAAPD) with an active area of  $10 \times 10 \text{ mm}^2$ , which have been tested for the given requirements. During the development of the readout system for the EMC the typical size of the crystal readout surface of  $27 \times 27 \text{ mm}^2$  was leading to the development of an LAAPD with a rectangular shape to cover a maximum of this space with two neighboring photo detectors.

The photon detection in the forward endcap EMC has to deal with rates up to 500 kHz and magnetic fields up to 1.2 T. Therefore we have chosen vacuum phototriodes (VPT) with a diameter of 22 mm as photon detectors. The main reasons for this choice are rate capability, radiation hardness, absence of nuclear counter effect and absence of temperature dependence. Standard photomultipliers are excluded due to the magnetic field environment. In contrast to the barrel region, the magnetic field is oriented in the axial direction of the VPTs and thus makes it feasible to use VPTs for the endcap. Vacuum phototriodes are essentially a photomultiplier tube with only one dynode and weak field dependence.

### 5.1 Avalanche Photodiodes (APD)

#### 5.1.1 Introduction

The requirements to detect the scintillation light of lead tungstate in the barrel part of the EMC can be satisfied by silicon avalanche photodiodes (APDs). Avalanche photodiodes are reverse biased diodes with an internal electric field used for avalanche multiplication of charge carriers. The CMS collaboration has developed APDs in collaboration with Hamamatsu Photonics optimized to detect the scintillation light from lead tungstate crystals. Those APDs have several advantages: compactness with an overall thickness of  $\approx 200 \mu\text{m}$  (Fig. 5.1), high quantum efficiency of 70–80% at the wavelength of maximum emission intensity of lead tungstate, insensitivity to magnetic fields and low cost in mass production. A disadvantage of this photosensor is its relatively small active area of  $5 \times 5 \text{ mm}^2$  compared to the area of the crystal end faces. Therefore we started the R&D of large area APDs (LAAPDs) with an active area of  $(10 \times 10) \text{ mm}^2$  in collaboration with Hamamatsu Photonics. Our R&D of LAAPDs is based on the same internal structure that has already been tested by the CMS collaboration (see Fig. 5.1): Light enters the APD via the  $p^{++}$  layer and is absorbed in the following  $p^+$  layer, where electron-hole pairs are generated. The electrons drift in the electric field towards the p-n junction where they are amplified by impact ioniza-

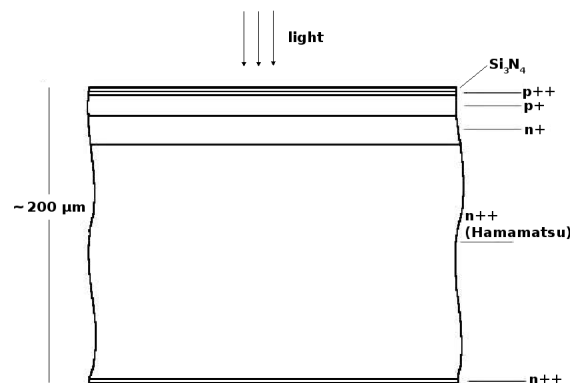


**Figure 5.1:** Schematic view of an APD with reverse structure [1].

tion, yielding avalanche gain, and drift through the n-material to the  $n^{++}$  electrode where the charge collection takes place. In front of the  $p^{++}$  layer a passivation layer made of silicon nitride  $\text{Si}_3\text{N}_4$  is used which reduces the decrease of quantum efficiency caused by reflection losses from the surface of the Si wafer.

Due to the large capacitance of the  $(10 \times 10) \text{ mm}^2$  LAAPDs (see Table 5.1) an additional prototype of same dimensions but lower capacitance has also been tested. As shown in the Technical Progress Report [2] the first prototype of the  $(10 \times 10) \text{ mm}^2$  APDs showed a nonsatisfying radiation hardness concerning proton irradiation. Therefore the APD internal structure was modified by adding a groove to reduce the occurring surface current and in the present status of R&D work mainly two different APD types are under investigation. Those are LAAPDs with an active area of  $(10 \times 10) \text{ mm}^2$  with different capacitance values developed in cooperation with Hamamatsu Photonics: a so called 'normal C' type LAAPD ( $C = 270 \text{ pF}$ ) and a 'low C' type LAAPD with a capacitance of  $C = 180 \text{ pF}$ . The foreseen rear side dimensions of the lead tungstate crystals (typ.  $(21.4 \times 21.4) \text{ mm}^2$ ) make it impossible to use two LAAPDs with quadratic active area of our dimensions (package size:  $(14.5 \times 13.7) \text{ mm}^2$ ). Therefore LAAPDs with rectangular package/active area have to be used to cover the main part of the crystal readout area. Those diodes with rectangular shape are presently under development and first prototypes will be available mid of 2008. A preliminary drawing of the LAAPD dimensions of the rectangular LAAPD type is shown in Fig. 5.2. This avalanche photodiode will have an active area of  $(7 \times 14) \text{ mm}^2$ . Two of these rectangular LAAPDs will be used to detect the scintillation light of one crystal in the barrel part of the electromagnetic calorimeter.

## 5.1.2 Characteristics

To ensure a stable operation of an avalanche photodiode several device properties have to be measured during screening or rather recorded during operation. The main parameter to be reported is the temperature of the APD during operation, because the dark current as well as the internal gain are strongly depending on temperature. Therefore the temperature has to be held stable down to an uncertainty of  $\Delta T = \pm 0.1^\circ\text{C}$ . Another essential parameter is the value of the applied bias voltage, which has to be kept constant down to  $\Delta U_R = \pm 0.1 \text{ V}$  to ensure a proper determination of the internal gain as well as a proper measurement of the device dark

current depending on bias voltage. Special attention will be devoted to the main APD parameters in the following paragraphs.

### 5.1.2.1 Dark Current and Gain

Due to interactions of charge carriers with phonons the gain of an APD decreases with increasing temperature. On the other hand the free mean path and the band gap of semiconductor devices are temperature dependent. In our case these two parameters can be neglected because of the envisaged operation temperature of  $T = -25^\circ\text{C}$ . The degree of sensitivity to temperature changes can be determined by the proximity of the applied bias/reverse voltage ( $U_R$ ) to the value of breakdown voltage ( $U_{Br}$ ) and by the device characteristics as a result of internal structure:

A decrease of capacitance of the APD results in an increasing sensitivity to temperature changes. The temperature dependence of gain has a value of  $-2.2\%/^\circ\text{C}$  at an internal gain of  $M = 50$  in case of a CMS-APD [3].

The dark current  $I_d$  of an APD can be divided into the bulk current  $I_b$  and the surface current  $I_s$ . While the surface current is independent from the applied gain  $M$  the value of the bulk current increases with increasing gain. The contributions of those two can be calculated separately by using the following relation if the gain  $M$  and the overall dark current  $I_d$  have been determined:

$$I_d = I_b \cdot M + I_s. \quad (5.1)$$

The internal gain  $M$  of the APDs at a fixed temperature is measured by using the following method: The dark current ( $I_d$ ) and the current under continuous illumination ( $I_{ill}$ ) at a fixed wavelength of  $\lambda = 420 \text{ nm}$ , according to the maximum emission wavelength of  $\text{PbWO}_4$ , is recorded for several bias voltages up to breakdown. From the ratio of photo currents ( $I_{ill} - I_d$ ) of high bias voltages and the voltage value where no amplification occurs (equivalent  $M = 1$ ) the gain  $M$  is calculated by:

$$M = \frac{I_{ill}(U_R) - I_d(U_R)}{I_{ill}(M=1) - I_d(M=1)}. \quad (5.2)$$

The results of these measurements done at room temperature are shown for a 'normal C' type APD in Fig. 5.3 and for a 'low C' type version in Fig. 5.4.

For the evaluation of the maximum gain of the device up to which a stable operation of the diode can be ensured, the dark current dependence of gain has to be regarded in parallel. For the investigated 'normal C' LAAPD gains up to a value of  $M = 3300$

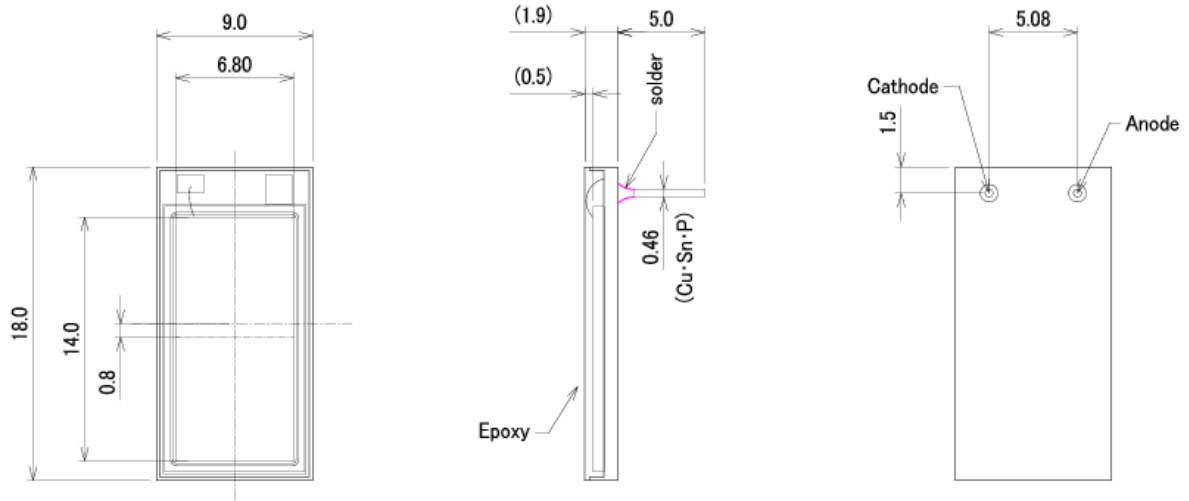


**Figure 5.2:** Technical drawing of the developed rectangular APD type.

could be reached before the breakdown voltage of the diode was reached. A closer look on the dark current reduces this value down to  $M = 500$ , because at higher gains the linearity of the dark current given by Eq. 5.1 is no longer guaranteed (see Fig. 5.3). Similar behaviour can be observed in case of the 'low C' version, where the maximum gain decreases from  $M = 460$  to a value of  $M = 160$  due to the observed dark current nonlinearity. The discrepancy in the maximum usable gain of the two APD types may originate from their different dark current behaviour depending on the internal APD gain and is caused by their different internal structure. This circumstance could be clarified by considering the ratio  $I_d/M$  depending on gain which is shown in Fig. 5.5. As it can be seen the two APD types behave completely different for gain values larger than  $M = 20$ : In case of the 'normal C' LAAPD the ratio is decreasing with increasing gain in contrast to the  $I_d/M$  behaviour of the 'low C' version diode where the ratio is slightly increasing. The values of the gain variation depending on bias voltage changes  $1/M \cdot dM/dV$  were also determined. At gain  $M = 50$  a value of  $1/M \cdot dM/dV = 3.4\%/V$  has been evaluated for the 'normal C' version and a similar value for the 'low C' version of  $1/M \cdot dM/dV = 3.2\%/V$ . These values are in good agreement with the value given for CMS-APDs in [3].

### 5.1.2.2 Excess Noise Factor

The APD internal charge carrier multiplication via avalanche is a statistical process. A characteriza-

tion of these statistical fluctuations of the APD gain  $\sigma_M$  is given by the excess noise factor  $F$  and has its origin in inhomogeneities in the avalanche region and in hole multiplication. The value of the excess noise factor is determined by the internal structure of the APD and is related to the amplification of electrons and holes at a given value of the internal gain  $M$ :

$$F \approx k \times M + \left(2 - \frac{1}{M}\right) \times (1 - k), \quad (5.3)$$

with  $k$  defined as the ratio of the ionization coefficients for electrons to holes. Its value is determined by the shape of the electric field near the p-n junction. Its r.m.s. broadening of a signal from  $N_{pe}$  photoelectrons is given by  $\sqrt{F/N_{pe}}$ . If  $N_\gamma$  photons per MeV are emitted by the crystal the number of photoelectrons created inside the conversion layer of the diode with quantum efficiency QE can be calculated by  $N_{pe} = N_\gamma \cdot QE$  (assuming full coverage of the crystal rear side by the APD). Therefore a shower of energy  $E(\text{MeV})$  creates  $EN_{pe}$  photoelectrons.

The processes mentioned above result in an additional contribution to the energy resolution of [4]

$$\begin{aligned} \frac{\sigma_E}{E} &= \frac{1}{\sqrt{EN_{pe}}} \cdot \frac{\sqrt{M^2 + \sigma_M^2}}{M} \\ &= \frac{1}{\sqrt{E}} \cdot \sqrt{\frac{F}{N_{pe}}}. \end{aligned} \quad (5.4)$$

From Eq. 5.4 it can be clearly seen that the excess noise factor should be as small as possible to maintain an excellent energy resolution. The value

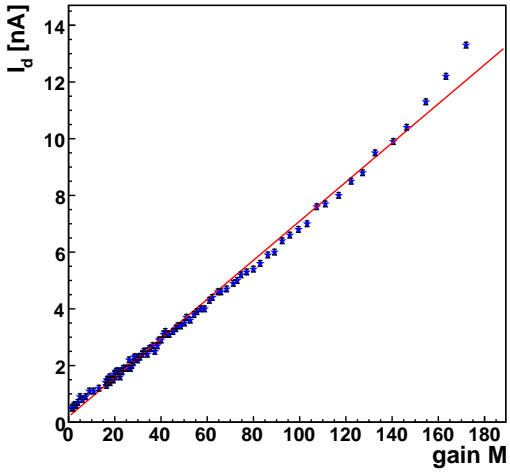
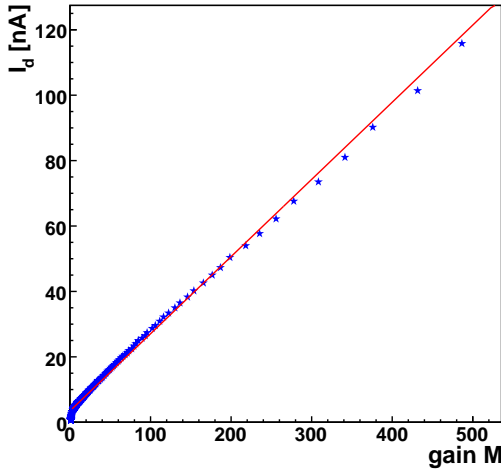
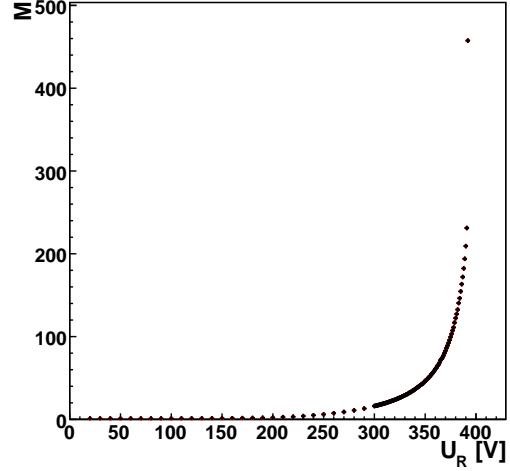
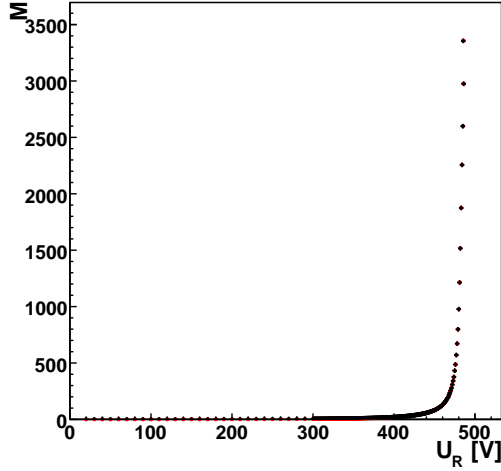


**Figure 5.3:** Determined gain  $M$  of the 'normal C' version LAAPD (above) and the corresponding dark current dependence of  $M$  in the range of linear dark current behaviour (below).

**Figure 5.4:** Determined gain  $M$  of the 'low C' version LAAPD (above) and the corresponding dark current dependence of  $M$  in the range of linear dark current behaviour (below).

of the excess noise factor at an internal gain of  $M = 50$  of the CMS-APDs is  $F = 2.0$  (Fig. 5.6), at gain  $M = 100$  the excess noise factor is increasing to  $F = 2.33$ . The excess noise factor of the first LAAPD 'normal C' prototype was measured at the APD laboratory of the CMS collaboration at CERN in April 2004. The result of this measurement is shown in Fig. 5.7. At an internal gain of  $M = 50$  the excess noise factor of these LAAPDs has a value of  $F = 1.38$ , at gain  $M = 100$  its value is  $F = 1.57$ .

### 5.1.2.3 Nuclear Counter Effect (NCE)

The Nuclear Counter Effect (NCE) describes an extra amount of charge produced inside a photodiode

by a charged particle directly hitting it, in addition to the charge produced by the scintillation light of the used crystal [6]. Therefore the NCE can cause a decrease of resolution in the energy measurement of an electromagnetic shower due to the leakage (secondary produced electron/hole pairs) of charged particles from the crystal.

Charged particles crossing a silicon layer of given thickness create a number of electron/hole pairs calculated by:

$$\frac{dn}{dx} = \frac{dE}{dx} \cdot \rho \cdot \frac{1}{E_{e/h}} \approx 100 \text{ e/h pairs} / \mu\text{m}. \quad (5.5)$$

In an APD only the photoelectrons created in front of the avalanche region, inside the conversion

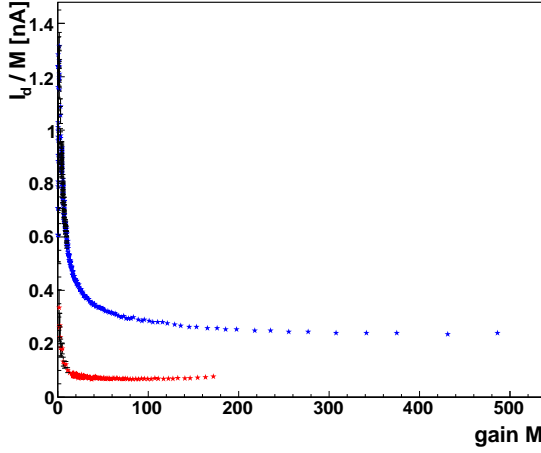


**Figure 5.5:**  $I_d/M$  depending on  $M$  of the 'normal C' version (blue) and the corresponding contribution for the 'low C' type APD (red).

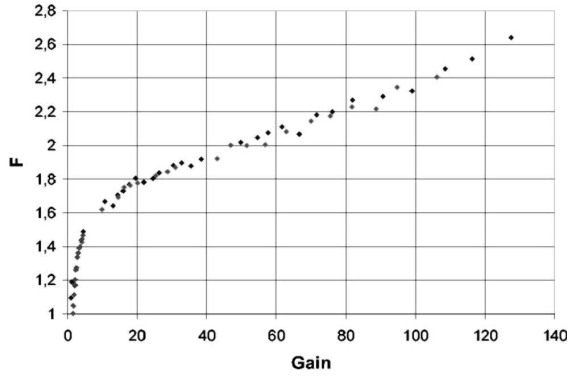


**Figure 5.6:** Measured excess noise factor  $F$  as a function of the internal gain of a CMS APD [5].

layer, always experience full amplification. Are the electrons created inside the avalanche region their reachable amplification depends on their place of creation (see details Sec. 5.1.3). To give a quantitative measurement of this effect, an effective thickness  $d_{eff}$  of the APD can be defined. Its value can be determined by exposing the APD directly to a  $^{90}\text{Sr}$  source, emitting beta electrons up to an energy of 2 MeV. The charge  $Q$  collected in the APD, operating at gain  $M$ , will be compared to the value measured with a PIN diode of well-known thickness  $d_{PIN}$  which results in the following relation [4]:

$$d_{eff} = \frac{d_{PIN}}{Q(PIN)} \cdot \frac{Q(APD)}{M}. \quad (5.6)$$

The calculation of the NCE includes the determination of the number of photoelectrons  $N_{pe}$  detected by the crystal-APD system. Its value depends on

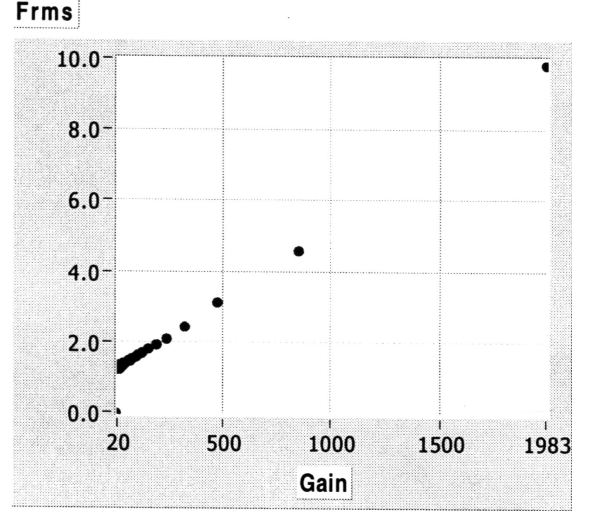


**Figure 5.7:** Measured excess noise factor  $F$  as a function of the internal gain of the first prototype of the LAAPD S8664-1010SPL with 'normal C' manufactured by Hamamatsu.

the light yield (LY) of the crystal, the APD quantum efficiency QE and the fraction of the crystal rear area covered by the APD ( $f$ ). The assumption of a 22 % coverage using a  $(10 \times 10) \text{ mm}^2$  large APD mounted on a  $(2.14 \times 2.14) \text{ cm}^2$  crystal endface ( $f = 0.22$ ) results in:

$$\begin{aligned} N_{pe} &= LY \cdot QE \cdot f \approx 500 \times 0.7 \times 0.22 \\ &= 77.0 \frac{pe}{\text{MeV}} \end{aligned} \quad (5.7)$$

at an operation temperature of  $T = -25^\circ\text{C}$ . Based on these values one MIP creates a signal inside the APD (operating at  $T = -25^\circ\text{C}$ ) equivalent to the light signal released in the crystal by a photon of energy:

$$E_{MIP} = \frac{dn}{dx} \times \frac{d_{eff}}{N_{pe}} \approx 1.3 \text{ MeV} \times d_{eff}(\mu\text{m}). \quad (5.8)$$

From Eq. 5.8 it can clearly be seen, that the effective thickness of the diode should be as small as possible to minimize the influence of the Nuclear Counter Effect (assuming  $d_{eff} = 5.6 \mu\text{m}$  (CMS)  $E_{MIP}$  would have a value of 7.28 MeV). On the other hand a reduction of  $d_{eff}$  increases the capacitance of the APD. Therefore a compromise has to be found and in fact as shown in Fig. 5.8 one of the tested APD types appears to fulfill these requirements. While the exposure with electrons seems to have no measurable effect on the 'normal C' version LAAPD (Fig. 5.8 b), the 'low C' version shows a clear signal created by the electrons directly hitting the APD (Fig. 5.8 c). The determination of

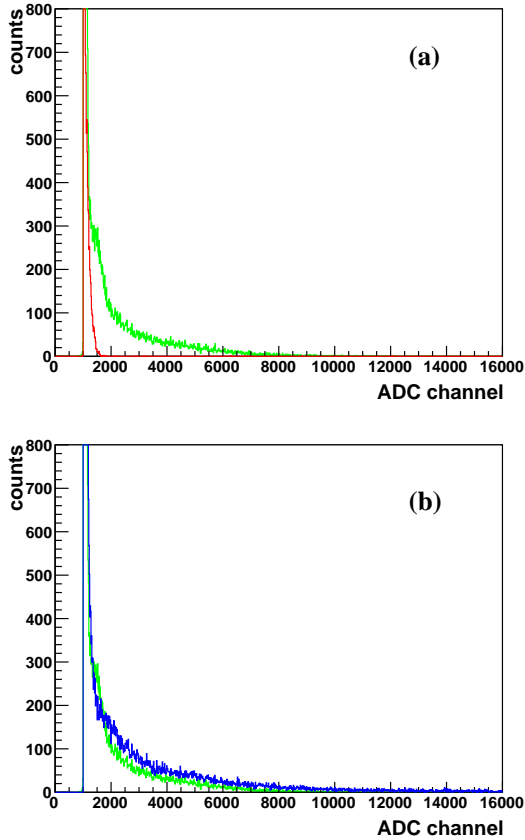


**Figure 5.8:** Measured Nuclear Counter Effect of a PIN diode of  $300\ \mu\text{m}$  thickness (green), of the 'normal C' version LAAPD (red) and of the 'low C' version LAAPD (blue). In part a) the comparison between PIN diode and 'normal C' version APD is shown and b) shows the corresponding comparison between PIN and the 'low C' version LAAPD.

the effective thickness of the used LAAPDs is hindered compared to the measurement done by CMS because of the much larger device capacitance. This value gives a major impact on the diodes noise behaviour and has to be known to conceive the layout of a low noise preamplifier which will be a major part of the APD readout chain. For PANDA the measurement of  $d_{eff}$  requires the minimization of any possible noise source and is currently under development.

#### 5.1.2.4 Electrical and Optical Properties of the Tested APD Types

The optical and electrical properties of the tested two LAAPDs mentioned above are summarized in Table 5.1 and compared to the APDs to be used in the electromagnetic calorimeter ECAL of the

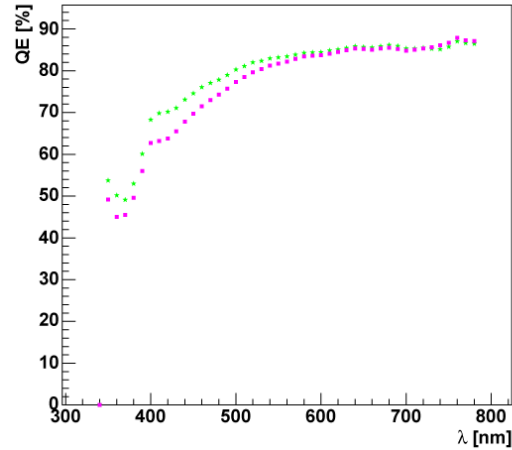


**Figure 5.9:** QE of a PIN diode (squares/pink) compared to the QE measured for a LAAPD (stars/green).

CMS experiment. Most of the measured parameters of the LAAPDs are in good agreement with the properties of the APDs developed by the CMS group in collaboration with Hamamatsu Photonics. The measured quantum efficiency of the PANDA-LAAPDs is shown in Fig. 5.9 compared to values measured with a PIN diode. Due to the four times larger active area of the LAAPD prototypes their capacitance is much larger than those of the tested  $(5 \times 5)\ \text{mm}^2$  APD type of CMS.

### 5.1.3 Radiation Damage due to Different Kinds of Radiation

To analyze the influence of radiation on a semiconductor device the knowledge of the internal device structure has to be assumed. Therefore several measurements to gain inside on the internal APD structure are inevitable. The possibility of calculating the effective thickness  $d_{eff}$  of the tested devices was already mentioned in Sec. 5.1.2.3. Another important parameter of the diode which was not discussed in detail so far and has also influence on the NCE is the conversion layer thickness  $d_{conv}$ . In Sec. 5.1.2.3 it was already mentioned that the longitudinal position  $x$  where the electron hole creation inside the diode takes place has influence on the reachable amplification of the photoelectrons passing the device structure: For light absorbed before reaching the avalanche region the gain is constant. The absorption of light inside the avalanche region leads to a decrease of the internal gain and therefore to additional gain fluctuations. Assuming

Property	Condition	CMS APD	S8664-1010SPL 'normal C'	S8664-1010SPL 'low C'
Active area [mm <sup>2</sup> ]		5 × 5	10 × 10	10 × 10
Quantum efficiency $QE$ [%]	$M = 1, \lambda = 420 \text{ nm}$	70	70	70
Breakdown voltage $U_{br}$ [V]	$I_d = 100 \mu A$	400	400	500-600
Dark current $I_d$ [nA]	$M = 50$	5	10-40	20-50
Capacitance $C$ [pF]	$M = 50$	80	270	180
Excess noise factor F	$M = 50$	2.0	1.38	not measured
Excess noise factor F	$M = 100$	2.33	1.57	not measured

**Table 5.1:** Electrical and optical properties of the tested APD types.

a constant electric field in the avalanche region of width  $W$ , the gain  $M$  could be calculated by using the relation

$$M = e^{\alpha_i \cdot (W-x)} \quad (5.9)$$

in which  $\alpha_i$  defines the ionization coefficient. Additionally the light absorption inside the avalanche region follows the exponential law

$$N(x) = N_0 \cdot e^{-(\alpha(\lambda, T) \cdot x)}. \quad (5.10)$$

The absorption coefficient  $\alpha(\lambda, T)$  respectively  $\alpha(E_\gamma, T)$  of silicon is shown in Fig. 5.10 depending on the incident photon energy. The conversion layer thickness of the APD could be determined by applying the definition of the optical mean depth of penetration [8]:

$$d_{conv} = \frac{1}{\alpha(\lambda, T)}. \quad (5.11)$$

By normalizing the measured gain values depending on wavelength, as shown in the lower plot of Fig. 5.11 for the 'normal C' type APD (Fig. 5.12

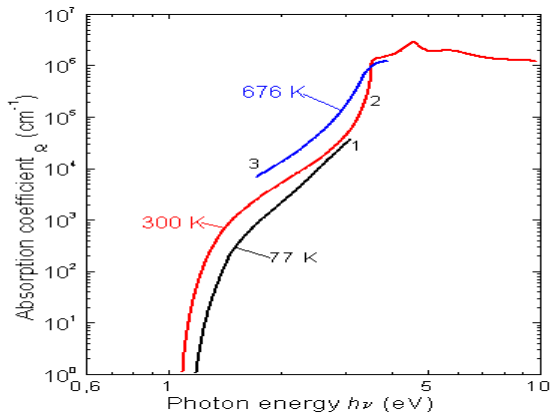


**Figure 5.10:** Absorption coefficient  $\alpha(\lambda, T)$  of Si depending on the photon energy for different temperatures [7].

APD version	wavelength $\lambda_{cut}$ [nm]	$\alpha(\lambda)$ [1/cm]	$d_{conv}$ [μm]
'low C' type	500	$1.1 \cdot 10^4$	0.9
'normal C' type	540	$7.05 \cdot 10^3$	1.4

**Table 5.2:** Determined conversion layer thicknesses  $d_{conv}$  of the tested APD types.

for the 'low C' type respectively), it is possible to define a 'cut-off' wavelength  $\lambda_{cut}$  above which light is absorbed inside the avalanche region [9]. The evaluated conversion layer thicknesses of the two different APD types and their corresponding 'cut-off' wavelengths are assorted in Table 5.2 using the  $\alpha(\lambda)$ -values given for a temperature of 300 K. It is quite obvious that any kind of irradiation of the APD has an impact on the  $M(\lambda)$  behaviour of the device. Therefore measurements as e.g. shown in Fig. 5.11 will lead to a more consolidated understanding of the caused radiation damages and their locations inside the APD structure.

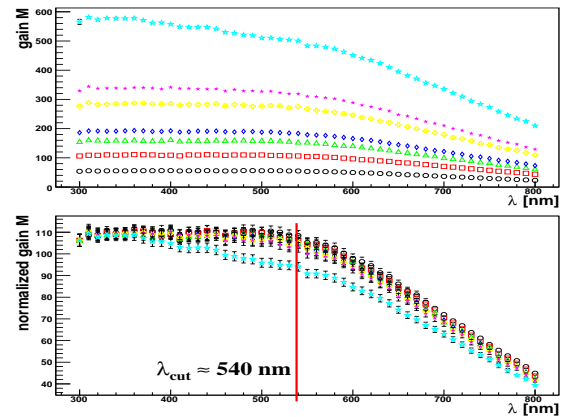


**Figure 5.11:**  $M(\lambda)$  for the 'normal C' version APD for different  $U_R$  values (above). Determination of  $\lambda_{cut}$  by normalizing the data (below).

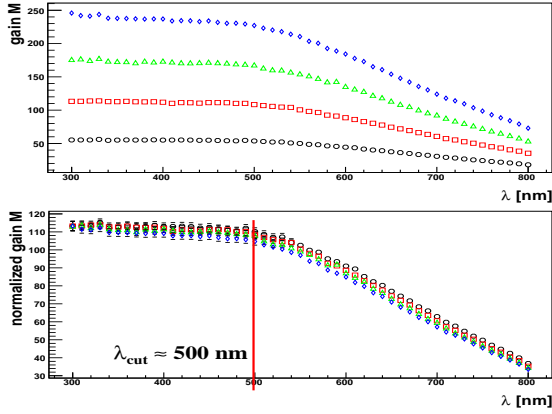


**Figure 5.12:**  $M(\lambda)$  for the 'low C' version APD for different bias voltages (above). Determination of  $\lambda_{cut}$  by normalizing the data (below).

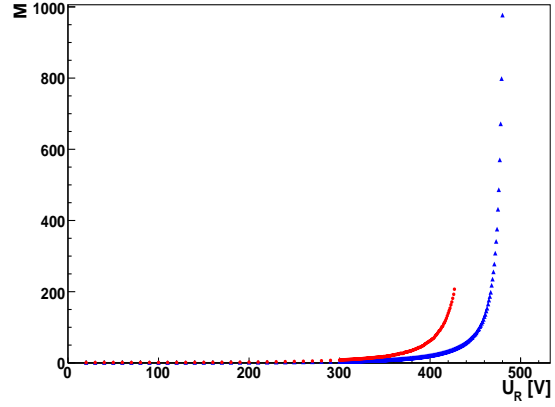


**Figure 5.13:** Determined gain values  $M$  of the 'normal C' type APD before (blue) and after (red) exposure with  $1.1 \cdot 10^{13} p$  of  $E_p = 90$  MeV.

The results of different irradiation experiments will be reported in the following section. All irradiations have been done at  $T = -25^\circ\text{C}$  to account for the real operation conditions of the PANDA electromagnetic calorimeter.

### 5.1.3.1 Proton Irradiation

Irradiation of an APD with protons causes two different kinds of radiation damage:

- ionization effects at the surface reflected in the surface current  $I_s$ , and
- atom displacements inside the silicon bulk increasing the bulk current  $I_b$ .

The proton irradiation of the diodes has been done at the KVI Groningen (the Netherlands) using a 90 MeV proton beam providing a homogenous beam profile. The diodes were irradiated until an integrated fluence of  $1.1 \cdot 10^{13} p$  was reached which is comparable with the dose expected for 10 years of PANDA operation. Using the NIEL theory this proton fluence corresponds to an equivalent neutron fluence of  $1.42 \cdot 10^{13} n$  of an energy of 1 MeV [10].

The first step in evaluating the influence of irradiation on the APD characteristics is the remeasurement of the internal gain of the diode. The typical change of  $M(U_R)$  due to proton irradiation is shown for instance in Fig. 5.13 for the 'normal C' version. It can be clearly seen that the gain of this diode type has dramatically decreased. Taking into account the assumed linearity of the dark current depending on  $M$  (see Fig. 5.14), the usable maximum

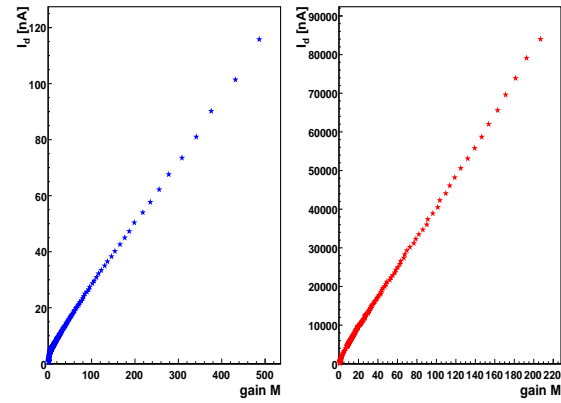


**Figure 5.14:** Comparison of the measured dark current values of the 'normal C' type APD before (left/blue) and after (right/red) proton irradiation.

gain decrease of the 'normal C' type APD after proton exposure is in the order of 60%. The decrease in case of the 'low C' version diode (see x-axes of Fig. 5.15) has a similar value about 50-60%. The influence of proton irradiation on the internal APD structure and the associated characteristic changes could be concretized by having a closer look on the dark current behaviour. For the two tested APD versions the dark current was measured in dependence of the internal gain before and after proton exposure. The results are shown in Fig. 5.14 and Fig. 5.15. As already mentioned above this kind of measurement makes it possible to evaluate the different rates of the surface current and the bulk current to the overall dark current. The values of the single dark current contributions shown in Table 5.3 were evaluated by fitting Eq. 5.1 to the dat-

APD version	$I_{b1}$ [nA]	$I_{b2}$ [nA]	$I_{s1}$ [nA]	$I_{s2}$ [nA]	$I_{b2}/I_{b1}$	$I_{s2}/I_{s1}$
'low C' type	0.07	268	0.2	$\approx 1554$	$\approx 3829$	$\approx 7770$
'normal C' type	0.24	389	3.47	$\approx 1770$	$\approx 1621$	$\approx 510$

**Table 5.3:** Influence of proton irradiation on the APD dark current. The values  $I_{s1}$  and  $I_{b1}$  have been measured before irradiation,  $I_{s2}$  and  $I_{b2}$  afterwards.

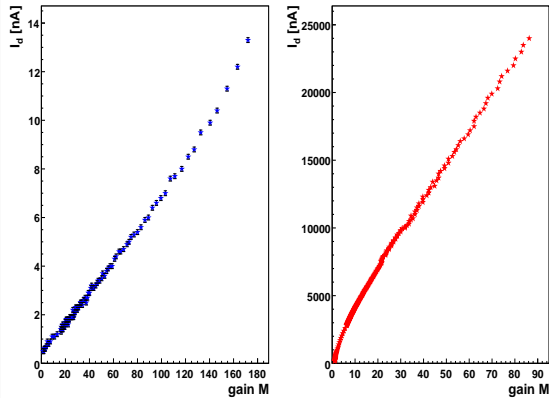


**Figure 5.15:** Comparison of the measured dark current values of the 'low C' type APD before (left/blue) and after (right/red) proton irradiation.

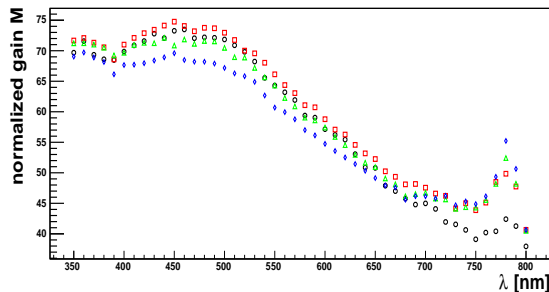


**Figure 5.16:**  $M(\lambda)$  of 'normal C' type after proton exposure with  $1.1 \cdot 10^{13} p$  at KVI Groningen.

apoints in Fig. 5.14 and Fig. 5.15 respectively. The enormous increase of the 'low C' bulk current compared to the increase factor  $I_{b2}/I_{b1}$  measured for the 'normal C' type APD has its origin in the increased layer thickness of this diode type used for the required reduction of the device capacitance. To get an impression where these observed proton induced damages are mainly located the measurement of the gain dependence on wavelength has to be reconsidered after proton exposure for the two different kinds of tested avalanche photodiodes. The results of this measurement are shown in Fig. 5.16 and Fig. 5.17. Obviously in case of

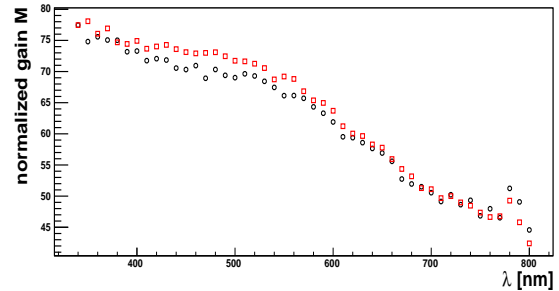


**Figure 5.17:**  $M(\lambda)$  of 'low C' type after proton exposure with  $1.1 \cdot 10^{13} p$  at KVI Groningen.

the 'normal C' type APD the proton induced damages are mainly located inside the conversion layer and at the end of the avalanche region. To clarify the corresponding situation in case of the 'low C' version APD more APDs of that type have to be irradiated. Nevertheless Fig. 5.17 provides an indication of the locations of the damages similar to those found in case of the normal capacitance APDs.

### 5.1.3.2 Photon Irradiation

The  $\gamma$ -irradiation of the diodes took place at the Strahlencentrum Giessen, Germany. The APDs were irradiated using  $^{60}Co$  sources of different dose rates to reach the envisaged integrated dose of  $10^{12} \gamma s$  per APD. To determine the influence of  $\gamma$  exposure on the APD characteristics basically the same procedure was used as described in the former paragraph in case of proton exposure. The irradiation has been accomplished for the 'normal C' version only, due to the fact that only 5 pieces of the 'low C' type APDs were available at the specific date of measurement. Similar to the proton irradiation done at KVI the photon exposure of the diodes has been done at  $T = -25^\circ C$ . The remeasurements of the APD characteristics have been done after a storage of the diodes at room temperature in the order of one month. Similar to the results presented for the proton irradiation measurement the gain values after  $\gamma$  exposure are compared to those measured using an unirradiated diode of the same internal structure

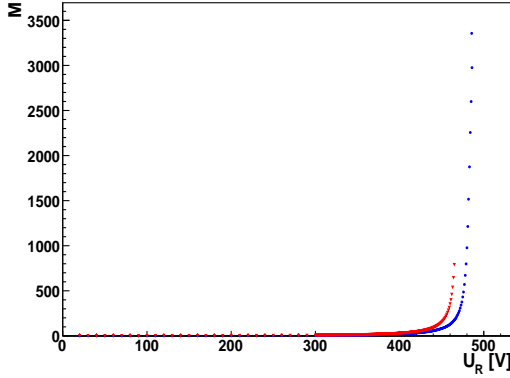


**Figure 5.18:** Determined gain values  $M$  of the 'normal C' type APD before (blue) and after (red) exposure with a  $^{60}\text{Co}$  source.

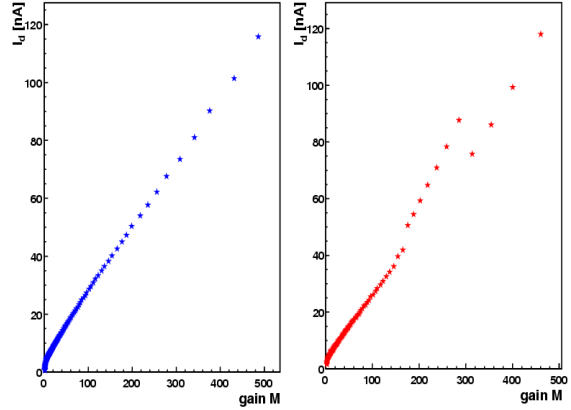
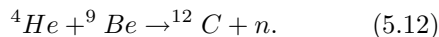


**Figure 5.19:** Dark current dependence on gain of the 'normal C' type APD before (blue/left) and after (red/right) exposure with  $10^{12} \gamma\text{s}$ .

(Fig. 5.18). Taking into account the determination of the maximum usable gain of the 'normal C' type APD no obvious gain decrease could be observed (see x-axes of Fig. 5.19), which is in contrast to the dramatical gain decrease of the diode in terms of proton exposure. Comparing the measured dark current after  $\gamma$  irradiation and one month of storage with the values determined for an unirradiated diode (Fig. 5.19) a nearly complete annealing of the dark current could be observed (see y-axes values). Looking at the gain range between 180 and 300 the dark current behaviour is dramatically changing so that the required linearity of the dark current depending on the internal gain seems to be no longer ensured. Detailed studies have to be done in the near future to determine the influence of surface defects caused by photon irradiation in this gain region. On closer examination of Fig. 5.20 no indication for any kind of bulk damage induced by the accomplished photon exposure could be observed. This result suggests some kind of surface damage to be cause of the atypical behaviour of the dark current shown in Fig. 5.19.

### 5.1.3.3 Neutron Irradiation

The neutron irradiation of the quadratic shaped APDs which has been done until now was executed at the APDlab Frankfurt using a  $^{241}\text{Am} - \alpha - \text{Be}$  source. This source generates approximately  $0.65 \cdot 10^{-4}$  neutrons per emitted  $\alpha$  particle of the alpha decay of americium via the reaction



Taking into account the activity of the employed source (1.1GBq) a neutron rate of  $7.15 \cdot 10^4 n/s$

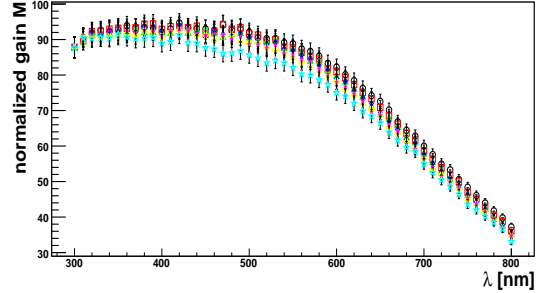


**Figure 5.20:**  $M(\lambda)$  of 'normal C' type after photon exposure with an integrated dose of  $10^{12} \gamma\text{s}$  at Strahlenzentrum Giessen.

could be reached.

In contrast to the exposure procedures described in the former paragraphs the irradiation results described in this section are based on measurements done at  $T = 20^\circ\text{C}$ . The measuring equipment providing a safe handling of the neutron source and which has to be completely filled with boron silicate due to radiation protection reasons is shown in Fig. 5.21. As already discussed in cases of proton and photon exposure of the diodes the gain of the two tested APD types has decreased after irradiation. The curve progression of the measured gain dependence on the applied bias voltage is shown exemplarily for the 'normal C' type in Fig. 5.22 in comparison to the behaviour observed before exposure. The dark current dependence on the determined gain values is shown for both APD types in Fig. 5.23 and in Fig. 5.24 respectively. In case of the 'normal C' type the dark current shows nearly no increase and its linearity depending on  $M$  is still ensured. The converse situation could be ob-

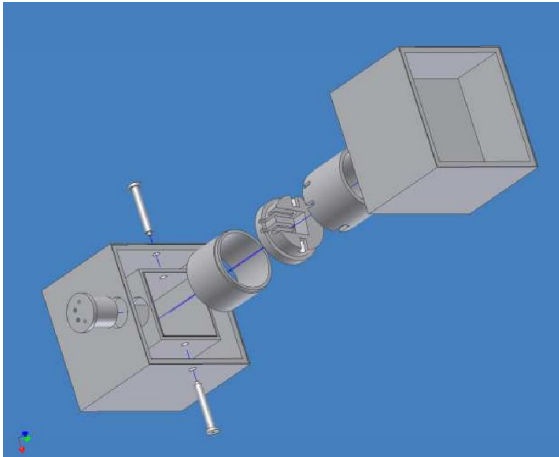


**Figure 5.21:** Schematic of the apparatus used for neutron irradiation of the avalanche diodes including APD housing and holder for the used neutron source.

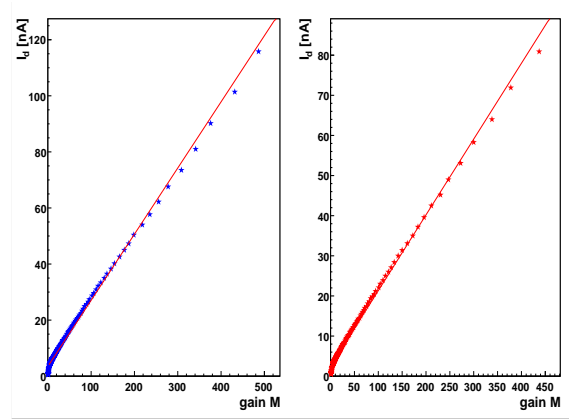


**Figure 5.23:** Dark current dependence on gain of the 'normal C' type APD before (blue/left) and after (red/right) exposure using a  $^{241}\text{AmBe}$  source (linear fits are added).

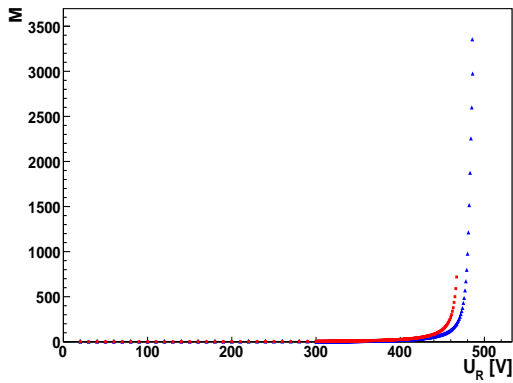


**Figure 5.22:** Determined gain values  $M$  of the 'normal C' type APD before (blue) and after (red) exposure using a  $^{241}\text{AmBe}$  source.

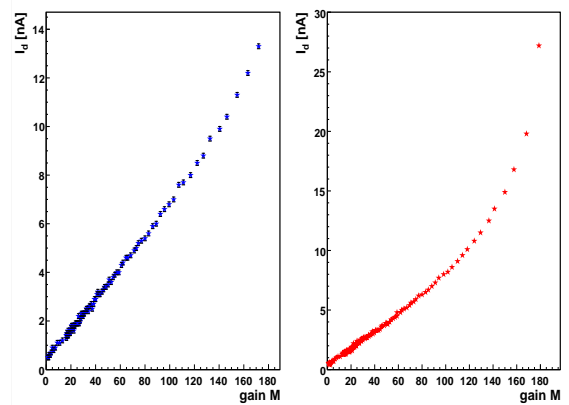


**Figure 5.24:** Dark current dependence on gain of the 'low C' type APD before (blue/left) and after (red/right) exposure using a  $^{241}\text{AmBe}$  source.

served in case of the 'low C' type APD where the maximum useable gain has dramatically decreased to a value 50% below the determined one for the unirradiated device. Having a closer look on the wavelength dependence of the gain measured after neutron exposure lead to the situations shown in Fig. 5.25 and Fig. 5.26. For both APD types, 'normal C' and 'low C', no indication of the existence of any kind of bulk damages could be found using the  $^{241}\text{Am} - \alpha - \text{Be}$  source described above.

To complete the radiation hardness studies of the APDs an irradiation of the devices using a neutron generator located at the FZ Rossendorf providing neutrons with an energy of 14 MeV is foreseen. This beamtime will take place during first half of 2008 and will clarify open questions concerning the de-

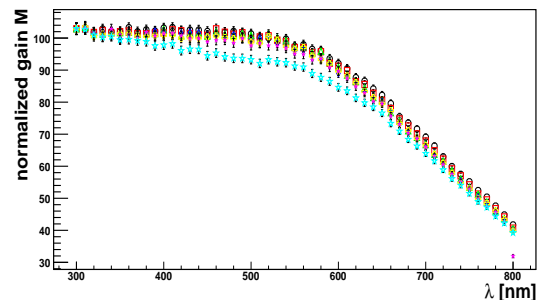


**Figure 5.25:**  $M(\lambda)$  of 'normal C' type after neutron exposure using a  $^{241}\text{AmBe}$  source.

vice radiation hardness due to neutron exposure.

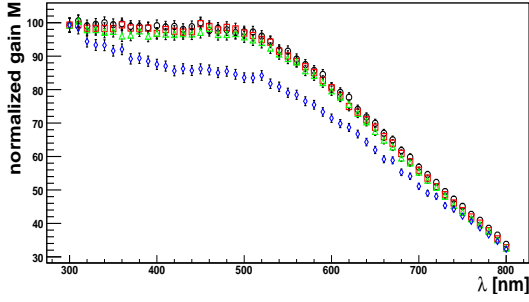


**Figure 5.26:**  $M(\lambda)$  of 'low C' type after neutron exposure using a  $^{241}\text{AmBe}$  source.

### 5.1.4 APD Screening Procedure

To ensure an optimum operation of the calorimeter all components have to be tested before their mounting as a part of the EMC. In case of the readout devices of the EMC barrel several stations of the APD testing have to be passed before the APDs will be definitively glued on the rear side of the scintillator crystals. The screening procedure for the LAAPDs described in this section contains the timeline from delivery of the diodes until their mounting to the crystals.

Due to the stability of one APD production run provided by Hamamatsu Photonics some properties of the APDs will only be measured for control samples and are not foreseen as a part of the APD mass screening:

- the quantum efficiency QE,
- the Excess Noise Factor at an internal gain of  $M = 50$  and  $M = 100$  at room temperature and at  $T = -25^\circ\text{C}$ ,
- the capacitance of the APD depending on bias voltage/gain and
- the gain uniformity of the APD active area surface.

To ensure a stable operation of the large amount of LAAPDs the stability of several parameters during operation have to be guaranteed in addition. Therefore a complex screening procedure for the diodes used for the EMC crystal readout has to be conceived. The measurements of the APD parameters have to be done for each single diode at room temperature (to be comparable to the parameter values given by Hamamatsu) and at the envisaged operation temperature of  $T = -25^\circ\text{C}$ . For each APD the gain-bias voltage characteristic has to be measured as well as the dark current dependence of  $U_R$ .

From these measurements several APD parameters, which will be stored in a database, will be extracted:

- Bias voltage values for the corresponding envisaged operation gain (in case of CMS:  $M = 50$ ) and other gain values,
- Dark current  $I_d$  for different fixed gain values (e.g.  $M = 50$  and  $M = 100$ ) and
- the gain variation with varying bias voltage  $U_R$ :  $1/M \cdot dM/dV$  [%/V] for different gain values.

To accommodate the influence of radiation on all these parameters an irradiation of all APDs using a high dose  $^{60}\text{Co}$  source will be part of the screening process. After irradiation all APDs have to be annealed (under bias voltage) using an oven operating at a temperature of  $T = 80^\circ\text{C}$  until the monitored dark current of the APDs will reach an equilibrium. After this procedure all APD parameters listed above have to be measured again and have to be compared to the values determined before irradiation.

Due to the application of one preamplifier board (including two channels) per crystal one additional step, as part of the screening procedure, has to be done: Based on the results of the remeasured APD characteristics two of them have to be assorted in terms of similar dark current and bias voltage values at a given gain value for the readout of one lead tungstate crystal of the EMC barrel part.

### 5.1.5 Mounting Procedure

After all APDs have passed the screening procedure explained above they have to be mounted on the rear side of the lead tungstate crystals. The mounting technique has to fulfill three main requirements:

1. The thermal contact between the APD and the crystal has to be as good as possible to guarantee an overall temperature stability of the crystal-APD system down to  $\Delta T = \pm 0.1^\circ\text{C}$  at  $T = -25^\circ\text{C}$ .
2. The optical coupling between crystal and APD has to be done as proper as possible to avoid any kind of light/signal loss in this region. Additional emphasize should lie on the optical temperature dependent properties of the used coupling material especially in view of the envisaged operation temperature of the calorimeter.

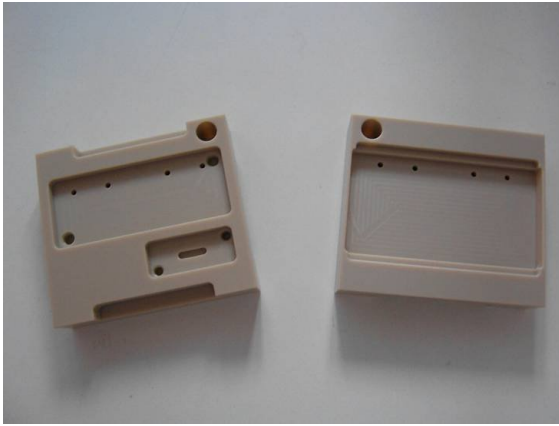


**Figure 5.27:** PEEK capsule designed to carry two  $(10 \times 10)$  mm<sup>2</sup> LAAPDs.

3. The readout diodes have to be as good as possible electrically insulated to avoid the appearance of additional noise sources (increase of dark current, etc. . . .).

Most of these specifications could be fulfilled by using a special kind of plastic (PEEK) produced by injection-moulding as carrier for the APDs. During the ongoing R&D work a so called 'capsule' built out of PEEK was designed and manufactured for the housing of 2 APDs of quadratic shape. A picture of one of the first prototypes is shown in Fig. 5.27. In addition to its function as APD housing a hole for one fibre of the envisaged light pulser system (see Sec. 8.2) used for radiation damage monitoring during the PANDA operation was implemented. On the rear side of the capsule space for the ASIC preamplifier and for a possibly needed temperature sensor is allocated (see right side of Fig. 5.27). To avoid scintillation light losses due to a low reflectivity of the capsule material the admixture of titanium oxide of different granularity to the moulding process is under investigation. The assembled capsule (including light fibre, preamplifier, thermistor and cables) offers a proper adjustment of the APDs on each crystal of the EMC barrel part and will be coupled to the scintillator using a special kind of optical glue between the APD entrance window and the rear side of the crystal.

## 5.2 Vacuum Phototriodes (VPT)

### 5.2.1 Introduction

For the photon detection in the forward endcap EMC we have chosen vacuum photo triodes (VPT). A schematic view of a VPT is shown in Fig. 5.28. Typical high voltage settings are: cathode at  $-1000$  V, the anode on ground and the dynode at  $-200$  V. Photoelectrons emitted from the photocathode are accelerated towards the anode consisting of a fine metal mesh. The electrons passing the anode strike the solid metal dynode, located behind the anode. The secondary electrons ejected from the dynode are accelerated back towards the anode and are collected there. The VPTs have a high rate capability and can be produced radiation hard, thus they are matching the requirements of the forward endcap EMC.

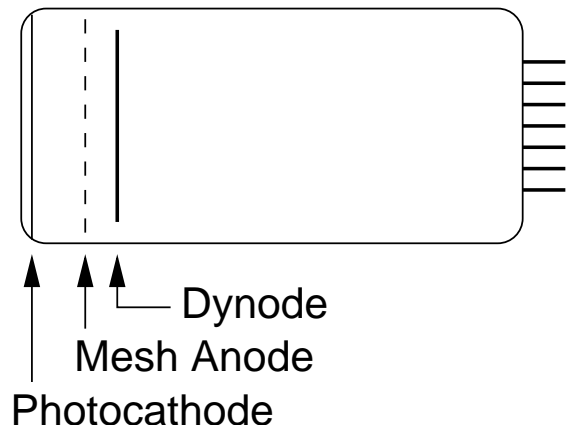


**Figure 5.28:** Schematic diagram of a 22 mm diameter VPT. Typical distances between the photocathode and the mesh anode are 4.5 mm. The distance between mesh anode and dynode is 4.5 mm. The total length is around 46 mm and is needed for connections in and outside the tube and for production purposes.

Vacuum phototriodes were previously in operation at the electromagnetic calorimeter endcap of the OPAL [11], DELPHI [12] and CMD-2 [13] experiments. Recently radiation hard vacuum phototriodes were developed for the CMS endcap electromagnetic calorimeter for operation in a magnetic field of up to 4 T.

### 5.2.2 Available Types

Vacuum phototriodes produced by three different companies are investigated for PANDA. Samples of

the R2148 from Hamamatsu<sup>1</sup> provide a typical gain of 10 and were tested in the lab. The Research Institute Electron<sup>2</sup> produced 15000 radiation hard VPTs for the CMS endcap. Presently Photonis<sup>3</sup> is developing phototriodes with high quantum efficiency photocathodes and high gain ( $>40$  at 1000 V). The latter VPTs may produce only about a factor of two less charge per deposited energy in PWO as  $1\text{ cm}^2$  sized APDs. Currently we assume only the availability of VPTs with a standard quantum efficiency and gain of about 10 as already available from RIE and Hamamatsu.

### 5.2.3 Characteristics and Requirements

For the forward endcap EMC 4000 phototriodes are needed. To match the size of crystals a maximum diameter of 22 mm and to stay within the space assigned to the detector an overall length of 46 mm is available. The specifications are listed in Table 5.4. Parameters of the RIE FEU-189 VPT are listed in Table 5.5. It matches most of the specifications, though further development is needed.

In Fig. 5.29 and Fig. 5.30 the gain is shown as a function of anode voltage for Hamamatsu R2148 and CMS FEU-188 VPT, respectively. Compared to APDs they exhibit only a small dependence of the gain on the high voltage. Typical values are less than 0.1% per volt. New developments in the material design of the dynodes allow the production of VPTs with gain above 40. Prototypes from Photonis are currently investigated. The high gain is favourable since it reduces the noise contribution for low energy calorimeter signals.

The spectral response of the photocathodes should cover a region from 350 nm to 650 nm. Typical quantum efficiencies of bi-alkali photocathodes are above 15%, much less than the quantum efficiencies of APDs, which are above 65%. In Fig. 5.31 the quantum efficiency of VPTs are compared to the PWO emission spectrum. An increase of the quantum efficiency would be desirable to improve the signal over noise ratio. Recently photocathodes with quantum efficiencies above 30% were produced by Photonis and Hamamatsu [15, 16]. These would be favourable. However, in the current design and simulations we assume only the availability of standard photocathodes.

The endcap is located close to the door of the solenoid magnet. At the position of the photodetectors the magnetic field varies between 0.5 T and 1.2 T and has a direction between 0 and 17 degrees

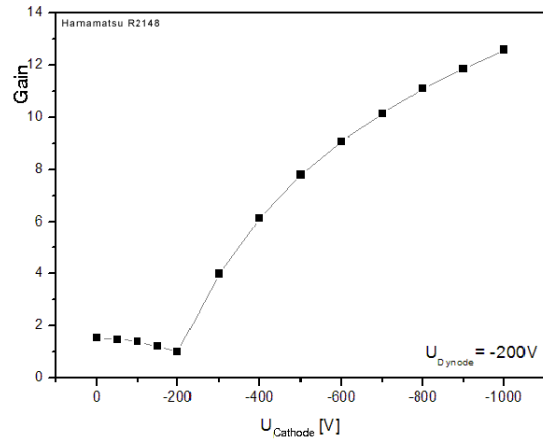


**Figure 5.29:** Variation of VPT gain as a function of cathode voltage at a dynode voltage of -200 V for R2148 VPT.

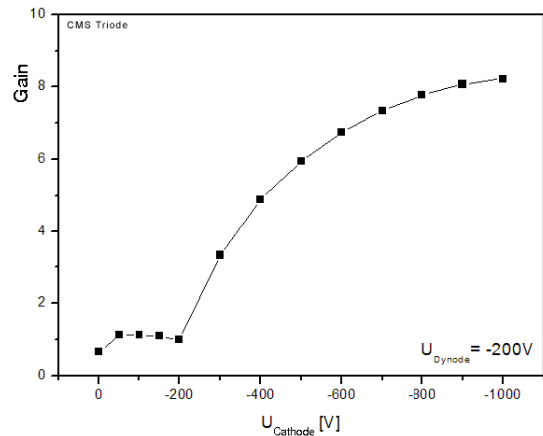


**Figure 5.30:** Variation of VPT gain as a function of cathode voltage at a dynode voltage of -200 V for CMS VPT.

with respect to the axial direction of the VPTs. The gain variation under a magnetic field depends on the mesh size of the anode. In Fig. 5.32 the variation of the anode response is shown as a function of angle to the axial field for the VPTs produced for the CMS experiment.

The dependence of the VPT quantum efficiency and gain on the temperature has been measured to be small and can be completely neglected compared

1. Hamamatsu Photonics, Electron Tube Division Export Sales Dept. 314-5, Shimokanzo, Iwata City, Shizuoka Pref., 438-0193, Japan

2. National Research Institute Electron (RIE), Ave M. Toreza 68, 194223 St. Petersburg, Russia

3. PHOTONIS France SAS, Avenue Roger Roncier, 19100 Brive La Gaillarde, France

Parameter	Value
External diameter	max. 22 mm
Overall length	about 46 mm
Dynode number	1 or 2
Gain	10 to 30 or more
Region of max. spectral response	420 nm (PbWO <sub>4</sub> )
Magnetic field	max 1.2 T in 0-17 degrees in axial direction of VPT
Photocathode useful diameter	16-20 mm
Quantum efficiency at 430 nm	20% or higher
Radiation hardness	10 Gy per annum
Operational temperature range	-30°C to 35°C
Rate capability	above 500 kHz

**Table 5.4:** Specifications for the PANDA VPTs.

Parameter	Value
External diameter	21 mm
Photocathode useful diameter	15 mm
Overall length	41 mm
Operating bias voltage: $V_u, V_d (V_c = 0V)$	1000 V, 800 V
Dark current	1 - 10 nA
$(dM/dV)/M$	< 0.1%/V
$(dM/dT)/M$	< 0.1%/C
Quantum efficiency at 430 nm	> 15%
Range of spectral response	300 - 620 nm
Effective gain ( $B=0$ T)	12
Effective gain ( $B=4$ T, $\Theta = 0^\circ$ )	6
Effective gain ( $B=4$ T) $\Theta = 20^\circ$ )	8
Anode pulse rise time	1.5 ns
Excess noise factor $F$ at $B = 0$	2.0 - 2.5
Excess noise factor $F$ at $B = 1 - 4$ T, $\Theta = 20^\circ$	2.2 - 2.6

**Table 5.5:** Parameters of the RIE FEU-189 VPT [14].

to the temperature dependence of the light yield of PWO. VPTs can be operated like photomultipliers in temperature ranges down to  $-30^\circ\text{C}$ .

Unlike PIN diodes, where energetic charged particles may produce electron-hole pairs in the silicon (nuclear counter effect), photomultipliers and VPTs are not susceptible to charged particles, due to the thinness of the entrance window and photocathode.

The capacitance of the VPT is small compared to the cables connecting to the preamplifiers, such that low noise values can be reached. Typical values are about 22 pF or less. Therefore the cables to the preamplifiers must be kept as short as possible. In the design it is foreseen to place the preamplifiers within less than 10 cm to the VPTs (see Chap. 6). Also the dark current of 1 nA is very small compared

to the maximum accepted 50 nA of the LAAPD.

## 5.2.4 Testing

### 5.2.4.1 Radiation Hardness

Radiation may change the response of the anode and the excess noise factor. Damages resulting in severe modifications of the response would deteriorate the energy resolution. Extensive studies of the radiation hardness were performed by the CMS experiment for the FEU-188 VPTs [18]. It was shown that under gamma irradiation the VPT anode response is fully determined by the loss of the VPT faceplate transmittance (Fig. 5.33). The CMS VPTs use the UV glass type US-49A. The VPTs

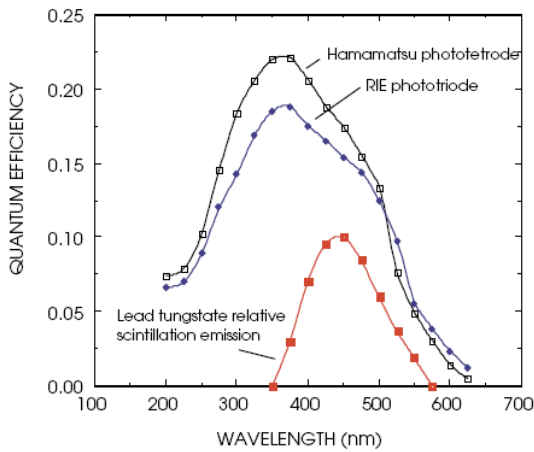


**Figure 5.31:** Quantum efficiencies of a caesium antimony photocathode in a Hamamatsu R5189 tetrode and a RIE triode compared with the emission spectrum of PWO [1].

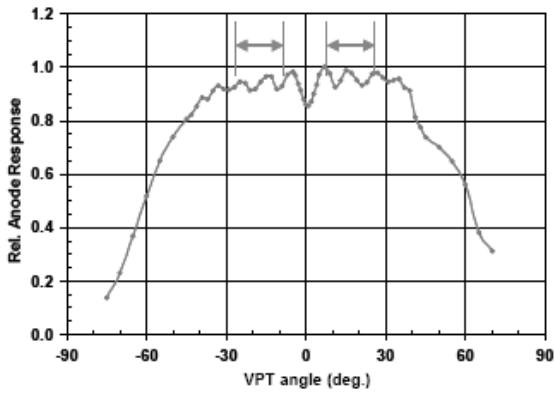


**Figure 5.32:** Variation of anode response for constant pulsed LED illumination as a function of the VPT angle to the axial field of 1.8 T for the CMS type VPT [17].

were irradiated in Russia with 20 kGy at a dose rate of 0.24 kGy/h. The decrease of the VPT anode signal did not exceed 4% at 20 kGy (Fig. 5.34) [18]. At PANDA we do not expect gamma dose rates above 0.2 kGy.

Radiation hardness tests with reactor neutrons have a high level of gamma background and activate the VPT material by a thermal neutron flux. Therefore they are difficult to evaluate. To circumvent this problem the FEU-188 VPTs were irradiated at a neutron generator providing  $E_n = 14$  MeV. The anode response of VPTs with cerium-doped glass was found independent of the neutron fluence up to  $2.4 \cdot 10^{15}$  n/cm<sup>2</sup> within the experimental error of  $\pm 5\%$  (Fig. 5.35).

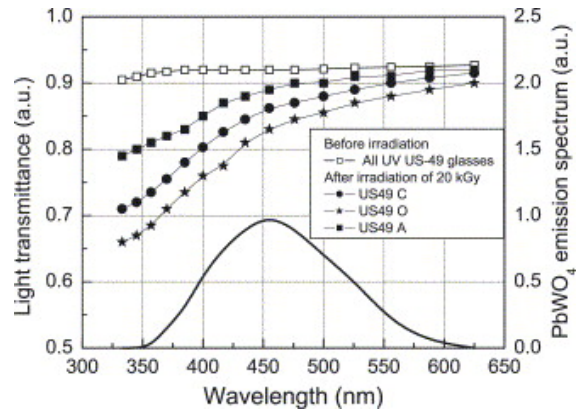


**Figure 5.33:** Light transmittance spectra of different UV glasses produced in Russia before and after 20 kGy <sup>60</sup>Co gamma irradiation and the emission spectrum of PWO. Dose rate is 0.24 kGy/h [18].

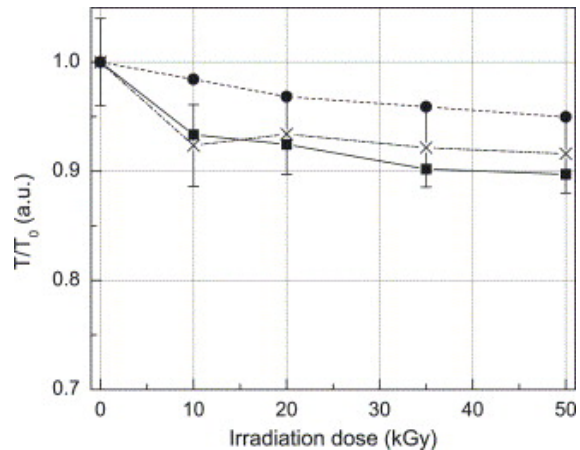


**Figure 5.34:** Relative US-49C (squares) and US-49A (circles) faceplate light transmission in the range of the PWO emission spectrum and relative anode response of the VPT as a function of the gamma dose at  $B = 0$  T (crosses) [18].

#### 5.2.4.2 Rate Studies

The particle rate in the forward endcap EMC can be as high as 500 kHz. Signals of the VPT are as short as the PWO scintillation pulses. To check the rate capabilities of the VPTs a LED pulser producing 445 nm pulses not shorter than the PWO scintillation pulses was built. The VPTs of the different producers will be tested with the light pulser at varying rates up to 1 MHz.

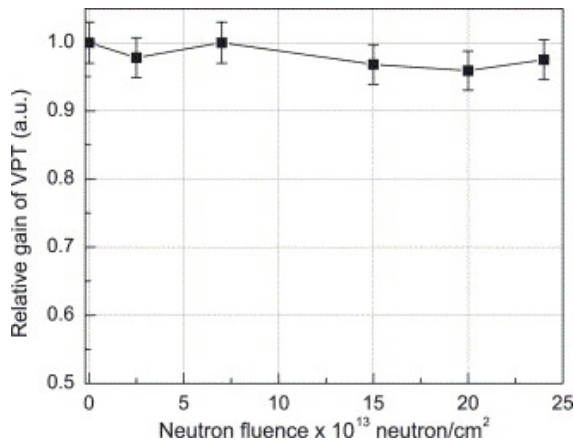


**Figure 5.35:** Relative anode response of VPT FEU-188 with faceplates from cerium-doped glass C1-96 versus the neutron fluence ( $E_n = 14$  MeV) [18].

### 5.2.5 Screening Procedure

After delivery of the VPTs they will undergo a screening procedure to check relevant parameters. The results of the test of each of the 4000 VPTs will be stored in a database. Basic dimensions of the VPTs and the connectors will be checked first after the arrival. Following a burn-in procedure the anode leakage current and the gain times the quantum efficiency will be tested with an LED pulser system at wavelengths of 455 nm and 470 nm. The stability of the gain will be checked by varying the frequency of the LED pulser system between 500 kHz and 0 kHz and back to 500 kHz. Finally the variation of gain between 0 T and 1 T axial magnetic field and the excess noise factor will be measured.

## References

- [1] CMS: The electromagnetic calorimeter. Technical design report, Technical report, 1997, CERN-LHCC-97-33.
- [2] Panda Technical Progress Report, Technical report, 2005.
- [3] D. Renker, Status of the avalanche photodiodes for the CMS Electromagnetic Calorimeter, Annecy, 2000, Prepared for 9th International Conference on Calorimetry in Particle Physics (Calor 2000).
- [4] CMS Conference Report: Progress on Avalanche Photodiodes as photon detectors for  $PbWO_4$  crystals in the CMS experiment, Technical report, 1997.
- [5] B. Patel et al., (1999), Prepared for 5th Workshop on Electronics for the LHC Experiments (LEB 99), Snowmass.
- [6] K. Ueno et al., arXiv:physics/9704013v1 (1997).
- [7] S. M. Sze, Physics of Semiconductor Devices, 1981.
- [8] M. Kneifel and D. Rabe, Halbleiterbauelemente, 1993.
- [9] T. Kirn et al., Nucl. Instrum. Meth. **A387**, 202 (1997).
- [10] M. Moll, Radiation Damage in Silicon Detectors, 1999, DESY-THESIS-1999-040.
- [11] M. Akrawy et al., Nucl. Instrum. Meth. **A290**, 76 (1990).
- [12] M. Bonesini et al., Nucl. Instrum. Meth. **A387**, 60 (1997).
- [13] P. M. Bes'chastnov et al., Nucl. Instrum. Meth. **A342**, 477 (1994).
- [14] N. A. Bajanov et al., Fine-Mesh Photodetectors for CMS Endacap Electromagnetic calorimeter, Technical report, CMS NOTE 1998/080, 1998.
- [15] R. Mirzoyan, M. Laatiaoui, and M. Teshima, Nucl. Instrum. Meth. **A567**, 230 (2006).
- [16] J.-C. Lefort, UBA/SBA PMTs - Hamamatsu's "Bialkali Climbing Party" has now reached 43% QE, Technical report, Hamamatsu News 2008, Vol. 1, 2008.

- [17] K. W. Bell et al., Nucl. Instrum. Meth. **A504**, 255 (2003).
- [18] Y. I. Gusev et al., Nucl. Instrum. Meth. **A535**, 511 (2004).

## 6 Electronics

---

The  $\overline{\text{PANDA}}$  Electromagnetic Calorimeter (EMC) will consist of  $\text{PbWO}_4$  (PWO-II) crystals arranged in the cylindrical barrel EMC with 11360 crystals, the forward endcap EMC with 3600 crystals and the backward endcap EMC with 592 crystals. The purpose of this detector is an almost full coverage, as far as the acceptance of the forward spectrometer allows, of the final state phase space for photons and electrons. Since one of the physics goals is e.g. precision spectroscopy of the charmonium spectrum, the low-energy photon threshold should be around 10 MeV, which requires the threshold for individual crystals to be about 3 MeV and correspondingly low noise levels of 1 MeV. Neutral decays of charmed mesons require the detection of a maximum photon energy deposition of 12 GeV per crystal at the given maximum beam energy of the HESR. These requirements dictate a dynamic range of 12000 for the readout electronics.

The placement of the calorimeter inside the 2 T solenoidal magnetic field requires photo sensors which provide a stable gain in strong magnetic fields. Therefore a Large Area Avalanche PhotoDiode (LAAPD) has been developed for the  $\overline{\text{PANDA}}$  EMC and will be employed in the barrel EMC part where typical event rates of 10 kHz and maximum 100 kHz are expected (see Sec. 4.1.2). Because of higher rates (up to 500 kHz) vacuum photo triodes (VPTs) have been chosen for the forward endcap EMC. The photo sensors are directly attached to the end faces of the individual crystals and the preamplifier has to be placed as close as possible inside the calorimeter volume for optimum performance and minimum space requirements. The readout of small and compact subarrays of crystals requires very small preamplifier geometries. In order to gain maximum light output from the PWO-II crystals, the calorimeter volume will be cooled to  $-25^\circ\text{C}$ . Efficient cooling thus requires low power consumption electronics to be employed in combination with extremely low-noise performance.

To minimize the input capacitance and pickup noise, the analogue front-end electronics is placed near the APD and kept at the same temperature as envisaged for the PWO-II crystals, namely at  $-25^\circ\text{C}$ . The low-temperature environment improves the noise performance of the analogue circuits and, at the same time, constrains the power consumption of the analogue front-end electronics. The  $\overline{\text{PANDA}}$  collaboration has developed two comple-

mentary low-noise and low-power (LNP) charge-sensitive preamplifier-shaper (LNP-P) circuits.

First, a LNP design was developed based on discrete components, utilizing a low-noise J-FET transistor. The circuit achieves a very good noise performance using signal shaping with a peaking time of 650 ns. Second, a state-of-the-art CMOS ASIC was developed, which achieves a similar noise performance with a shorter peaking time of 250 ns. The advantage of the CMOS ASIC is the very low power consumption. Both designs are complementary since the preamplifiers, based on discrete components, will be used for the readout of the forward endcap EMC for which we expect a maximum rate per crystal of 500 kHz. Such an approach minimizes the overall power consumption and keeps the probability for pileup events at a moderate level well below 1 %.

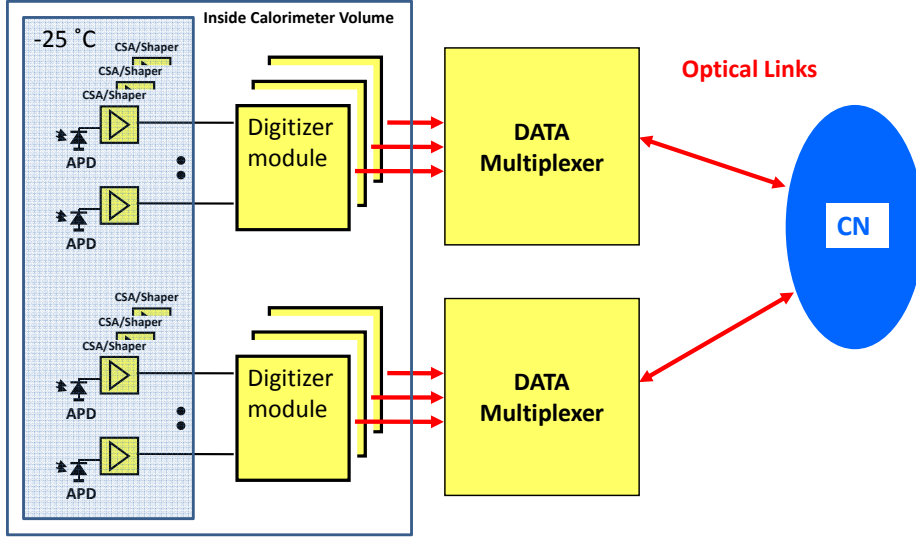
The subsequent digitization stage will be placed as close as possible to the calorimeter volume but outside the low-temperature area. This allows signal transfer from the front-end over short distances by flat cables with low thermal budget. Optical links will be employed to transfer digitized data via a multiplexing stage to the compute node outside the experimental setup.

In the following paragraphs the requirements and performance of the various stages of the readout chain will be discussed: the general readout scheme, the preamplifiers, the digitizer modules, the multiplexer stage and, finally, the detector control system supervising the performance of the whole detection chain.

### 6.1 General EMC Readout Scheme

The readout of the electromagnetic calorimeter is based on the fast, continuous digitization of the amplified signal-shape response of LAAPD and VPT photo sensors to the light output of PWO-II crystals. The readout chain will consist of extremely low-noise front-end electronics, digitizer modules and data multiplexer (see Fig. 6.1).

The digitizer modules are located at a distance of 20–30 cm and 90–100 cm for the barrel EMC and the forward endcap EMC, respectively, away from the analogue circuits and outside the cold volume.



1

**Figure 6.1:** The readout chain of the Electromagnetic Calorimeter.

The digitizers consist of high-frequency, low-power pipelined ADC chips, which continuously sample the amplified and shaped signals. The sampling is followed by the digital logic, which processes time-discrete digital values, detects hits and forwards hit-related information to the multiplexer module via optical fibers. At this step the detection of clusters of energy deposition can be efficiently implemented. A cluster seed requires an energy deposition of typically at least 10 MeV with a number of neighboring crystals surpassing the single-crystal threshold of typically 3 MeV. The multiplexer modules will be located in the DAQ hut and they perform advanced signal processing to extract amplitude and signal-time information.

The front-end electronics of the barrel EMC is located inside the solenoid magnet where any access for maintenance or repair is limited to shutdown periods of the HESR, expected to occur once a year. This condition requires to implement a redundancy in the system architecture. One of the most important decisions, that has been taken by the collaboration, is to equip every EMC crystal with two APDs. Apart from redundancy, the system with

two independent readout channels offers a significantly (max.  $\sqrt{2}$ ) improved signal to noise ratio and a lower effective threshold level.

## 6.2 Preamplifier and Shaper for barrel EMC APD-readout

A low-noise and low-power charge preamplifier ASIC (APFEL) was designed and developed for the readout of the LAAPD for the  $\bar{P}$ PANDA EMC. Two LAAPDs with an active area of  $7 \times 14 \text{ mm}^2$  each are attached to the end face of the lead tungstate scintillating crystals (PWO-II) which have a typical geometry of  $(200 \times 27 \times 27) \text{ mm}^3$ . Contrary to a photomultiplier, the LAAPDs can also be operated in a strong magnetic field. In the barrel EMC the LAAPDs act as photo detectors converting the scintillating light to an electrical charge signal. The preamplifier linearly converts the charge signal from the LAAPD to a voltage pulse which is transmitted to the subsequent electronics.

## 6.2.1 Requirements and Specifications

### 6.2.1.1 Power Consumption

Since the complete barrel EMC, together with the APDs and the preamplifiers, will be cooled to low temperatures ( $-25^{\circ}\text{C}$ ) to increase the light-yield of the PWO-II crystals, the power dissipation of the preamplifier has to be minimized. Low power dissipation leads to a smaller cooling unit and thinner cooling tubes; it also helps to achieve a uniform temperature distribution over the length of the crystals.

### 6.2.1.2 Noise

To reach the required low detection threshold of about 1 MeV, the noise performance of the preamplifier is crucial. The newly developed rectangular LAAPD from Hamamatsu (Type S8664-1010) has an active area of  $14 \times 7 \text{ mm}^2$  resulting in a quite high detector capacitance which requires a low-noise charge preamplifier. The total output noise is a combination of the preamplifier noise and the noise generated by the dark current flowing through the APD. By cooling the APD to  $-25^{\circ}\text{C}$  the dark current is reduced by a factor of about ten, with respect to room temperature. Using a low-leakage LAAPD at low temperature, the charge preamplifier is the dominating noise source due to the relatively high detector capacitance of around 270 pF. The noise floor of the APFEL ASIC at  $-20^{\circ}\text{C}$ , loaded with an input capacitance of 270 pF, has a typical equivalent noise charge (ENC) of 4150  $e^-$  (rms) (see Sec. 6.2.2.2).

Investigations of PWO-II light production (see Fig. 4.19) yield on average 90 photoelectrons per MeV, measured at  $-25^{\circ}\text{C}$  with a photomultiplier tube of 18% quantum efficiency and an integration gate width of 300 ns. This value results in 500 photons/MeV at the end face of the cooled ( $-25^{\circ}\text{C}$ ) PWO-II crystal. With the average back face cross section of barrel crystals of  $745 \text{ mm}^2$  (see Fig. 7.3) we obtain 66 photons/MeV on the active area of  $7 \times 14 \text{ mm}^2$  of a single rectangular LAAPD. The quantum-efficiency of the LAAPD is around 70% for the scintillating light of the PWO-II crystals and the voltage biased LAAPD will be operated at an internal gain  $M = 100$ . Applying these numbers, a primary photon with the energy of 1 MeV induces an input charge of 0.74 fC ( $4620 e^-$ ) to the preamplifier. Thus, an ENC of 4150  $e^-$  (rms) corresponds to an energy noise level of about 0.9 MeV (rms).

### 6.2.1.3 Event Rate

To cope with the expected event rates in the barrel EMC of maximum 100 kHz per crystal, a feedback time constant has to be chosen which is a trade-off between noise performance and pile-up problematic. The preamplifier is designed for an event rate up to 350 kHz.

### 6.2.1.4 Bias Voltage

At the maximum event rate of 100 kHz with the maximum expected photon energy deposition per crystal of 12 GeV (8.9 pC from the LAAPD) a mean current of 890 nA is flowing through the LAAPD. Under these extreme conditions, the voltage drop over the low-pass filter for the APD bias voltage gets relevant, since the internal gain ( $M = 100$ ) of the LAAPD varies by about 3%/V. This means, that the measured energy will be dependent on the event rate. To minimize this effect one can design the low-pass filter with low series resistance resulting in a degraded noise performance of the preamplifier and the need for larger filter capacitors. Eventually, the various regions of the barrel EMC with different event rates could be equipped with adapted low-pass filters to obtain an optimum noise performance combined with low rate/energy dependence. Another solution is that the APD bias-voltage supply sources a voltage which is corrected on the output current (the more current the more voltage). This means, that the output resistance of the bias-voltage supply is negative and therefore compensates the series resistance of the low-pass filter. The advantage is a better noise performance of the preamplifier due to the highly resistive APD bias-voltage filter. This solution would demand a more complex bias-voltage supply system with a sophisticated overvoltage and overload control. Each LAAPD has its own measured bias voltage where it reaches the nominal internal gain of  $M = 100$ . To reduce the number of APD bias-voltage channels, it is foreseen to group LAAPDs with similar bias-voltages. Since this grouping will be very local, in regions where similar event rates are expected, the solution with the negative resistance bias-supply could still be feasible.

### 6.2.1.5 FADC Readout

Readout with a flash ADC (FADC) does not need a dedicated timing amplifier. Only a good anti aliasing low-pass filter/amplifier has to be implemented in front of the FADC. The low-pass filter/amplifier can be safely installed at distances below 70 cm from

the preamplifier directly at the FADC in the room-temperature environment. The cut-off frequency of that filter is given by the sampling frequency of the FADC divided by 2.5; this prevents aliasing effects due to the sampling. To determine the energy with a high signal to noise ratio, the digitized values are processed by a digital shaping filter followed by a digital peak determination. It could be possible to choose different digital energy shaping filters for the different regions of the barrel EMC: A short peaking-time for the small angles in forward direction and the region orthogonal to the target position, where high event rates are expected. For other regions of the detector, where lower event rates are estimated, the peaking-time could be larger and therefore result in a better energy resolution. Even a rate-dependent automatic adaptation of the digital energy shaping filter could be imagined. The timing information is extracted by processing the digitized values similarly to the traditional signal chain with a fast digital timing filter followed by a digitally implemented CFD. Measurements have shown, that a timing resolution well below 1 ns can be reached with that regime. One has to point out, that the processing for the energy- and timing information extraction must be performed in real time. This can be implemented by using programmable digital signal processors (DSPs) or completely in hardware by using field programmable gate arrays (FPGAs). The needed signal throughput at the high sampling frequency (80 MHz) combined with the complex algorithm will result in a remarkable power dissipation.

## 6.2.2 Integrated Circuit Development

The high compactness of the electromagnetic calorimeter in connection with the required temperature homogeneity at low operation temperature puts high demands on space and power consumption. It appears almost mandatory to integrate the preamplifier and shaper on a single chip to fulfill these demands. For this reason an Application Specific Integrated Circuit (ASIC "APFEL") for the readout of Large Area APDs as foreseen at the PANDA EMC was developed.

### 6.2.2.1 Circuit Description

For the front-end amplifier design a single ended folded cascode architecture was chosen as it is frequently described in literature [1, 2, 3] and shown

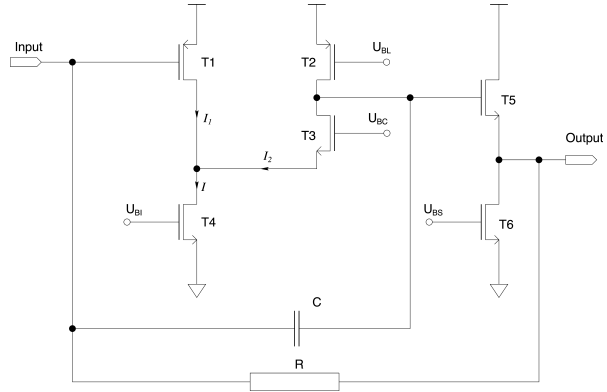


**Figure 6.2:** Schematic diagram of the folded cascode front end.

in Fig. 6.2. This architecture combines a high open loop gain with a large output swing.

A signal at the input transistor T1 effects a current change of  $I_1$ . As the current  $I = I_1 + I_2$  is kept constant by the current sink T4 also  $I_2$  changes by the same value. This variation creates a voltage drop at the output node of T2. The cascode transistor T3 separates the input transistor from the output node. To get the best gain and stability the ratio of the currents  $I_1$  and  $I_2$  in Fig. 6.2 should be in the order of  $I_1/I_2 = 9$ .

The signal charge is integrated on a capacitance C which has to be discharged by a resistor R to prevent the preamplifier from saturation. The integration capacitance is not across the feedback resistor as usual but between the input and the dominant pole node realizing a Miller compensation. This results in a reduction of wideband output noise [1] and minimizes the sensitivity to variations in detector capacitance [4].

For the preamplifier design the noise consideration played the leading part. The parts in equivalent input noise of transistors T2 and T4 scale with their transconductances  $g_{m2}/g_{m1}$  and  $g_{m4}/g_{m1}$ , respectively, so they can be minimized by a dedicated choice of parameters [5]. The main noise contributor is the input transistor T1. From noise theory one can see, that the drain source current  $I_{DS}$  and the transistor width  $W$  are the free parameters to control the transistor noise which decreases with increasing  $I_{DS}$  and  $W$ . Since at  $W \approx 10^4 \mu\text{m}$  the noise reaches a minimum,  $W = 12.8 \text{ mm}$  was chosen. A tradeoff between noise performance and the power consumption led to a current of  $I_{DS} = 2 \text{ mA}$ . Another tradeoff is the choice of the feedback resistor to balance low parallel noise (large R) and the

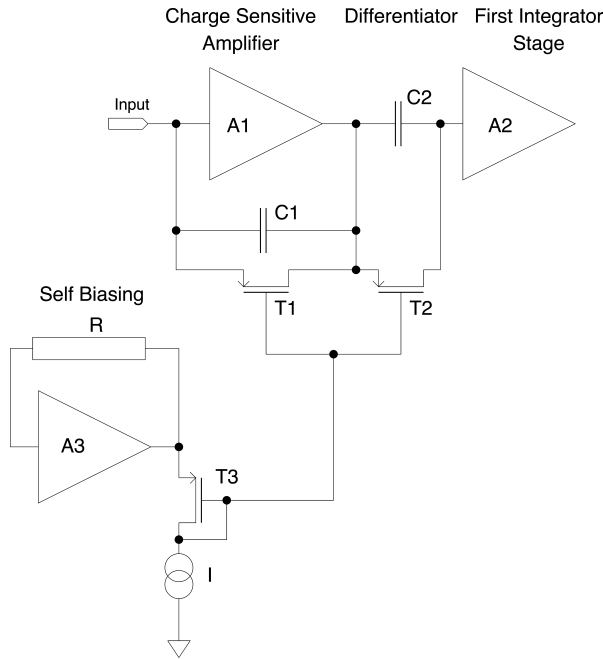


**Figure 6.3:** Principle diagram of the self biasing feedback network.

hit rate the preamplifier has to cope with (small  $R$ ). The capacitance  $C$  is given by the maximum of the input charge the preamplifier has to deal with.

To realize the mandatory high resistivity for the feedback resistor  $R1$ , a transistor operating in the subthreshold region is used. Concerning the temperature and process independence, a self biasing technology as described by O'Connor et al. in [3] is realized. As shown in Fig. 6.3 a MOS transistor  $T3$  in diode connection is used together with a current sink to generate the gate source voltage  $V_{GS}$  of the feedback transistor  $T1$ . The source potential of this MOS diode is fixed by a downscaled version  $A3$  of the preamplifier circuit  $A1$ .

The pole which is introduced by the output resistance  $r_{oT1}$  of  $T1$  and the capacitance  $C1$  is compensated by transistor  $T2$  in parallel connection to the differentiation capacitance  $C2$ . This way a zero is introduced into the transfer function. By choosing the time constants  $\tau_2 = \tau_1$  with  $\tau_1 = C1 \cdot r_{oT1}$  and  $\tau_2 = C2 \cdot r_{oT2}$  any undershoot in the pulse shape is eliminated.

The gate of  $T2$  is connected to the same potential as the gate of  $T1$ . To ensure that the drain and source potentials of  $T1$ ,  $T2$  and  $T3$  are equal, the amplifiers  $A2$  and  $A3$  are downscaled versions of the input amplifier  $A1$ .

The amplifier  $A2$  is used as the first stage of a 3rd order integrator. With a capacitive feedback

a 1st order low pass filter with a time constant of  $\tau = 90$  ns is realized. At this point the signal is split into two paths. To add two more poles to the transfer function, a 2nd order integrator stage based on a fully differential operational amplifier follows on each path.

On one of these paths an amplification factor of 16 is realised so this signal path is optimised to measure at the low energy part of the dynamic range with a minimized influence of pick up noise on the connection between preamplifier and ADC. The other path has no additional amplification so it covers the whole upper part of the dynamic range.

After the shaper build up by the differentiator stage and the integrators, detector pulses have a semi Gaussian pulse shape with a peaking time of 250 ns. The shapers are followed by output drivers with a driving capability of 10 pF parallel to 20 k $\Omega$ . For shaper operation two reference voltages are needed. To guarantee the full dynamic range over a temperature range from  $-30^\circ\text{C}$  to  $+30^\circ\text{C}$  these reference voltages have to be adjusted. An adjustable voltage reference based on two 10 bit digital to analogue converters is implemented on the ASIC to provide this functionality.

A charge injection unit for each channel is implemented on the chip which gives the possibility to inject a defined amount of charge into the preamplifier input for readout electronics monitoring. The amount of charge can be programmed in four steps. For programming of the adjustable voltage references as well as for programming and triggering of the charge injection a serial interface to a two-wire serial bus is implemented on the integrated circuit. Data transfer has to follow a specific bus protocol which was defined for this circuit. Each transfer consists of 20 bits. After a start signature the first eight bits are used as an address to select a readout chip. The next two bits are used to select one of four internal data registers into which the following 10 data bits are written.

To avoid introduction of additional noise by substrate coupling from a running digital logic, there is no continuous clock signal for the digital logic. Receiving data and latching into the internal registers is triggered by the external serial clock signal. After data transmission the clock line stays on high level and the on-chip digital logic is inactive. So it neither produces any additional noise nor it consumes power.

An overall block diagram of the integrated preamplifier circuit is shown in Fig. 6.4 on the left side. The choice of technology was driven by the fact that

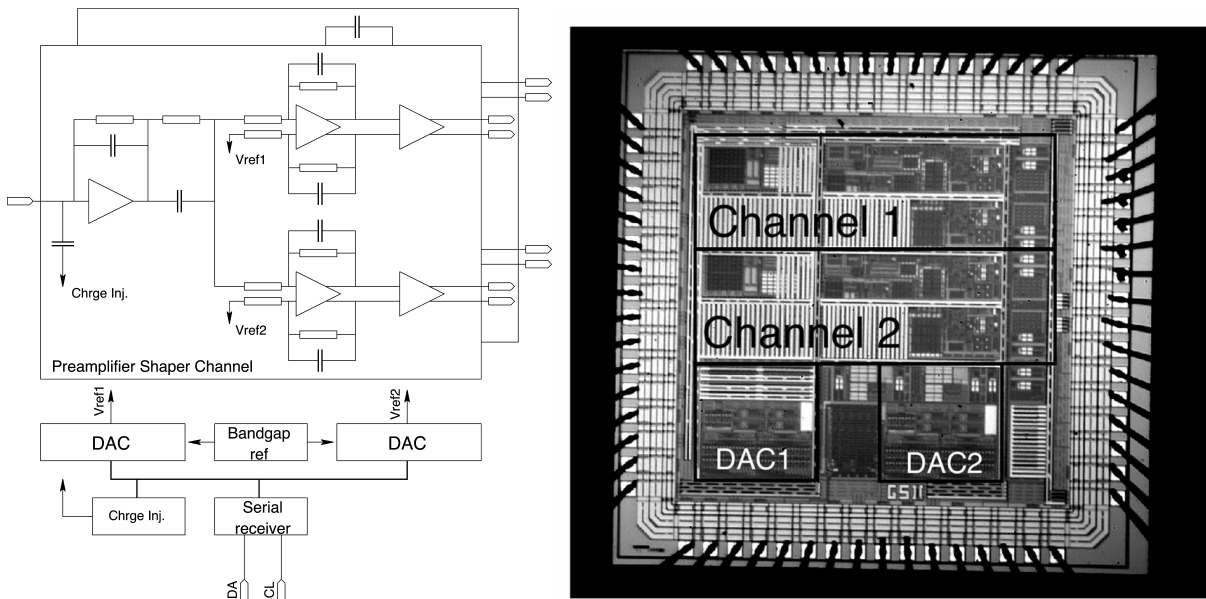


**Figure 6.4:** Left side: Overall block diagram of the preamplifier and shaper ASIC. Right side: Photograph of the prototype preamplifier ASIC.

larger feature size technologies have the advantage of higher core voltages, which affects directly the dynamic range. On the other hand, the noise performance benefits from a smaller feature size only on a minor level. Therefore, for the preamplifier design a 350 nm technology from AMS<sup>1</sup> was chosen, which provides a sufficient high core voltage and which is widely used e.g. in automotive industry. Thus, we may expect that this technology is available with a long term perspective. The prototype shown on the right side of Fig. 6.4 was produced in 2007. Since summer 2007 several measurements have been done to specify the ASIC prototype.

### 6.2.2.2 Prototype Performance

For specifying the preamplifier prototype over a temperature range from  $-20^{\circ}\text{C}$  to  $+20^{\circ}\text{C}$  the ASIC was mounted on a printed circuit board (see Fig. 6.5) which can be cooled by a Peltier element. To avoid condensation of air humidity the setup is placed in an evacuated chamber. For measurements a voltage step generated by an AWG 510 on a well defined capacitor is used as charge injection. A second well defined capacitor connected parallel to the amplifier input simulates the detector capacitance. The output signals are monitored with a digital oscilloscope type DPO 7254. Serial programming is done with a data timing generator DTG 5078. For the temperatures  $-20^{\circ}\text{C}$ ,  $-10^{\circ}\text{C}$ ,  $+10^{\circ}\text{C}$  and  $+20^{\circ}\text{C}$  dynamic range, gain and output

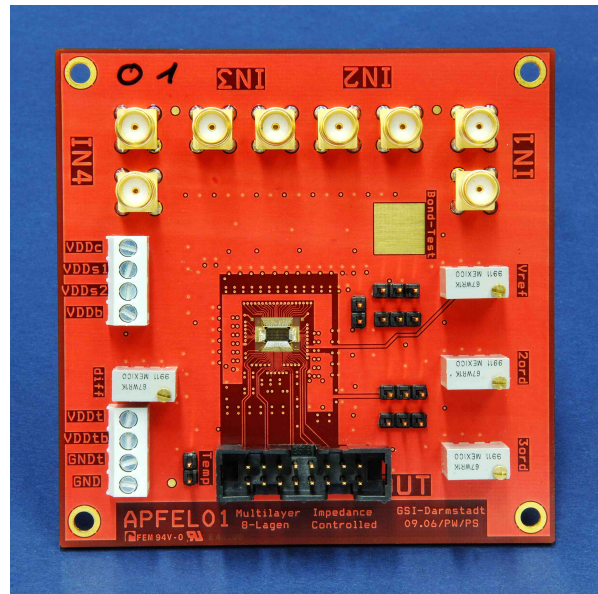


**Figure 6.5:** Test PCB with glued and bonded preamplifier ASIC.

noise voltage were measured so that the equivalent input noise charge could be calculated. The results for four different detector capacitances are plotted in Fig. 6.6. As expected, the noise increases linearly with the detector capacitance. Also the temperature dependence is clearly visible.

A linear fit indicates that the slope  $S_{ENC} = (5.73 \pm$

1. Austria Mikrosysteme AG

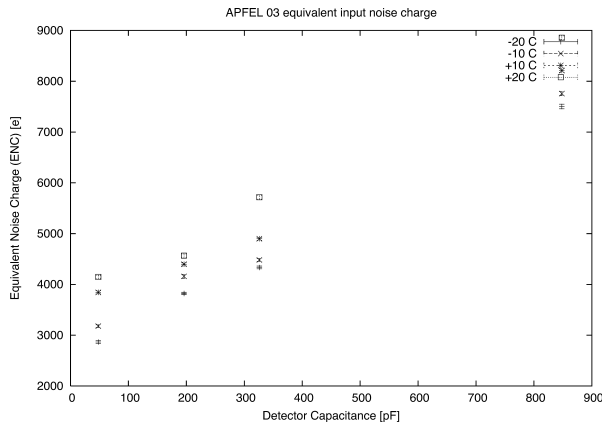


**Figure 6.6:** Measured noise values of the preamplifier prototype.

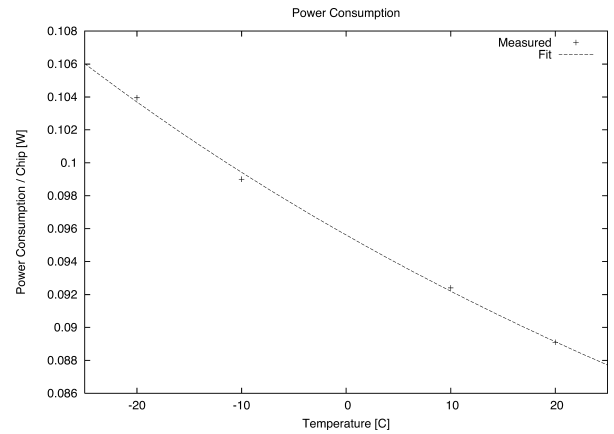


**Figure 6.8:** Power consumption for one chip with two channels in dependence of temperature.

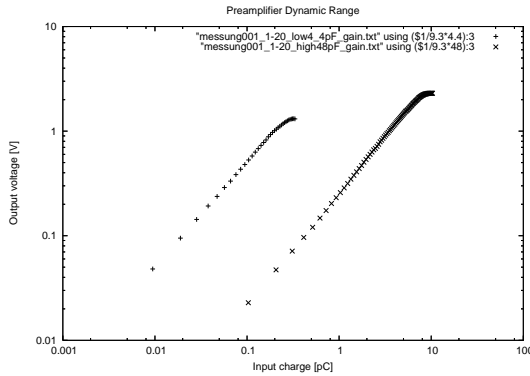


**Figure 6.7:** Amplification characteristics of the preamplifier at  $-20^{\circ}\text{C}$ .

$0.5) e^{-}/\text{pF}$  of the equivalent noise charge is almost independent of temperature. The constant term increases linearly with temperature with a temperature coefficient of  $S_T = 26.15 e^{-}/^{\circ}\text{C}$ .

For an operating temperature of  $-20^{\circ}\text{C}$  the measured noise of the preamplifier prototype is

$$ENC = [2610 \pm 103 + (5.69 \pm 0.3) \cdot C_{Det}] e^{-}$$

so with a detector capacitance of  $C_{Det} = 270 \text{ pF}$  a noise of  $ENC = (4146 \pm 131) e^{-}$  (rms) can be expected. This value corresponds (see Sec. 6.2.1.2) to an energy of  $0.9 \pm 0.02 \text{ MeV}$ .

Fig. 6.7 shows the measured characteristics of the integrated preamplifier for the high and the low amplification path. The measurement covers a range from  $10 \text{ fC}$  to  $10 \text{ pC}$  input charge. Both paths show an excellent linear behavior with an overlapping range up to  $200 \text{ fC}$ . The  $-1 \text{ dB}$  compression point of the low amplification path can be determined at

$7.84 \text{ pC}$ . Together with the measured noise of  $0.66 \text{ fC}$  this leads to a covered dynamic range of 11900.

In Fig. 6.8 the dependence of power consumption on the temperature is shown. For a temperature of  $T = +20^{\circ}\text{C}$  the power consumption for one channel amounts to  $10 \text{ mW}$  for the charge sensitive amplifier, to  $15 \text{ mW}$  for the shaper stages and to  $17 \text{ mW}$  for the buffers. In addition there are about  $3 \text{ mW}$  for the bias circuit and the digital part. So the overall power consumption for one chip with two channels is  $90 \text{ mW}$  at  $+20^{\circ}\text{C}$ . At the temperature of  $-20^{\circ}\text{C}$  the power consumption slightly increases to  $104 \text{ mW}$  for one chip with two channels. Neither simulations nor measurements revealed any significant dependence of the power consumption on the event rate for an event rate up to  $350 \text{ kHz}$ .

A compilation of the measured results is given in Table 6.1.

Parameter	
ENC ( $-20^{\circ}\text{C}$ , $270 \text{ pF}$ )	$4146 \pm 131 e^{-}$
Max. input charge	$7.84 \text{ pC}$
Dynamic Range	11900
Max. Event rate	$350 \text{ kHz}$
Peaking Time	$250 \text{ ns}$
Power Consumption (2 channel, $-20^{\circ}\text{C}$ )	$104 \text{ mW}$

**Table 6.1:** Measured preamplifier parameters.

## 6.3 Preamplifier and Shaper for forward endcap EMC VPT-readout

### 6.3.1 Requirements and Specifications

A discrete charge preamplifier, the Low Noise / Low Power Charge Preamplifier (LNP-P) has been developed in first instance for the LAAPD readout of the barrel EMC and was implemented in the barrel EMC prototype detector. It has an excellent noise performance in combination with low power consumption. This preamplifier has been further developed and adapted for the readout of Vacuum Photo Triodes (VPTs). VPTs will be used as photo detectors in the forward endcap EMC. The VPT is attached to the end face ( $26 \times 26 \text{ mm}^2$ ) of the lead tungstate scintillating crystals (PWO-II) which have a length of 200 mm. Due to the higher event rates and large photon energies in the forward endcap EMC with respect to the barrel EMC, the APDs would suffer from radiation damage (increased noise) and from the nuclear counter effect. Therefore, APDs are not suitable at that position of the EMC. The VPT is a single-stage photomultiplier with only one dynode which can also be operated in a strong magnetic field without losing significantly in gain. The VPT translates the scintillating light of the PWO-II crystals into an electrical charge which is linearly converted by the LNP-P to a positive voltage pulse; this output pulse is then transmitted via a  $50 \Omega$  line to the subsequent electronics. The low capacitance of the VPT favors the development of a faster low-noise preamplifier with discrete components which is suitable for the high-rate environment. For the following design considerations, we adopt the parameters of the VPT type RIE-FEU-188 used in the CMS ECAL. A new VPT with a significantly higher quantum efficiency ( $> 30\%$ ) combined with a larger internal gain ( $> 40$ ) is under development and will be produced by the company Photonis. By using this new VPT, the energy noise level will be reduced remarkably.

#### 6.3.1.1 Power Consumption

Since the complete forward endcap EMC, including VPTs and preamplifiers, will be cooled to low temperatures ( $-25^\circ\text{C}$ ) to increase the light-yield of the PWO-II crystals, the power dissipation of the preamplifier has to be minimized. Low power dissipation leads to a smaller cooling unit and thin-

ner cooling tubes; it also helps to achieve a uniform temperature distribution over the length of the crystals. The LNP-P has a quiescent power consumption of 45 mW. The power dissipation is dependent on the event rate and the photon energy; Fig. 6.9 shows the measured power dissipation on the LNP-P versus count-rate in the worst case of maximum output amplitude. Since the high rates are predominantly occurring at lower energies, a reasonable maximum power consumption of 90 mW can be presumed.

#### 6.3.1.2 Noise

To reach the required low detection threshold of only several MeV, the noise performance of the preamplifier is crucial. The VPT has an outside diameter of 22 mm and a minimum photocathode diameter of 16 mm (see Table 5.4), resulting in an active area of ca.  $200 \text{ mm}^2$ . This area is the same as the combined active area of two rectangular  $7 \times 14 \text{ mm}^2$  LAAPD. The VPT anode capacitance is around 22 pF which is more than 10 times lower than the capacitance of the LAAPD; this results in a much lower noise from the LNP-P. Thus, the shielded cable between the VPT and the LNP-P has a significant impact on the total detector capacitance; it must be kept as short as possible. The dark current of the VPT (1 nA) is significantly lower than the one from the LAAPD (50 nA), both measured at room temperature. The quantum efficiency of the standard available VPT type RIE-FEU-188 is about 20%, compared to 70% of the LAAPD. Further, the internal gain of the VPT is around ten, which is five times lower than that of the LAAPD. The noise floor of the LNP-P at  $-25^\circ\text{C}$  loaded with an input capacitance of 22 pF, has a typical equivalent noise charge (ENC) of  $235 e^-$  (rms). This is measured with an ORTEC450 shaping filter/amplifier with a peaking-time of 650 ns. Because the VPT has almost no dark current, the noise is not increased due to the leakage current of that photo detector.

As already discussed in Sec. 6.2.1.2, measurements of PWO light production yield 500 photons/MeV at the end face ( $26 \times 26 \text{ mm}^2$  for the forward endcap EMC) of the cooled ( $-25^\circ\text{C}$ ) PWO-II crystal. This results in 150 photons/MeV on the active area of the VPT. By applying the quantum efficiency and the internal gain of the VPT, a primary photon with the energy of 1 MeV induces an input charge of 48 aC ( $300 e^-$ ) to the preamplifier. So an ENC of  $235 e^-$  (rms) corresponds to an energy noise level of 0.78 MeV (rms). This is about the same level

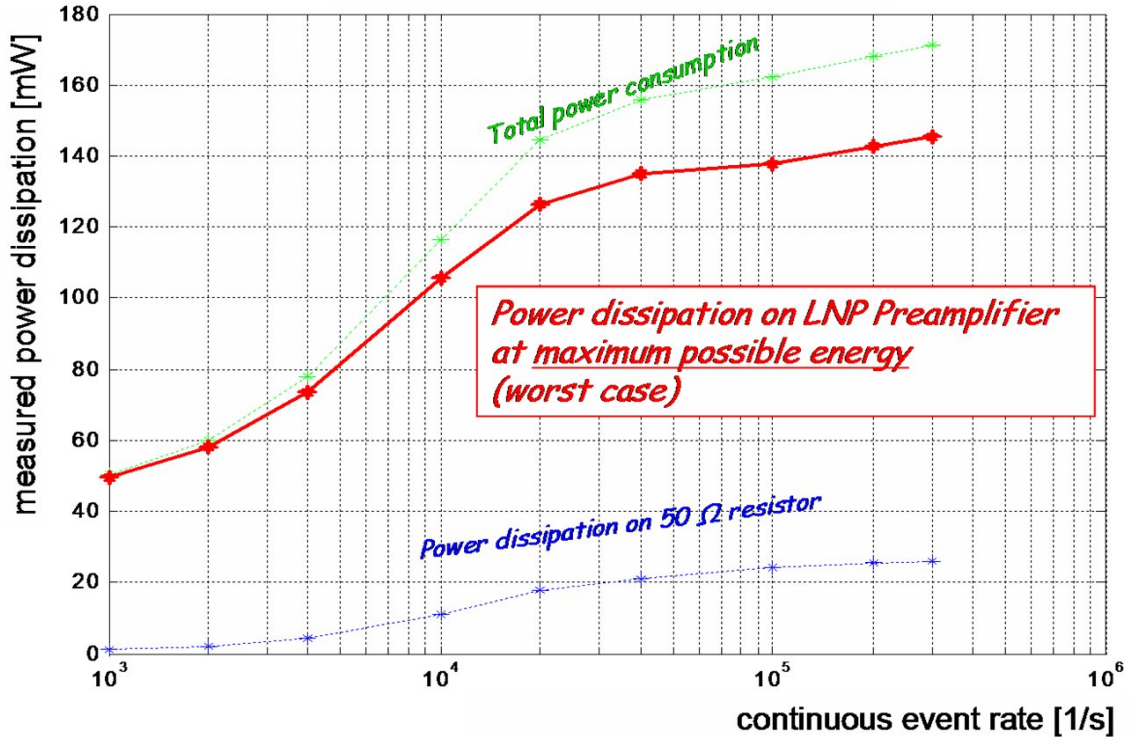


Figure 6.9: Power dissipation as function of continuous event rate for the LNP preamplifier for the VPT readout.

as achieved under the same conditions in the barrel EMC with the LAAPD readout (0.9 MeV (rms)). Therefore, the signal to noise is in the same order when using a VPT or an LAAPD for the readout of a PWO-II crystal. The noise level is increased as the shaping time is decreased. Shorter shaping times are mandatory to cope with the expected high event rates in the forward endcap EMC. By decreasing the peaking-time from 650 ns (reference values) to 200 ns, the noise level is raised by around 25%. So, the noise floor with the more realistic shaping using a peaking-time of 200 ns corresponds to about 1 MeV (rms) for the presently available VPT. As already mentioned in Sec. 6.3.1, a new VPT with a significantly higher quantum efficiency (ca. 30%) combined with a larger internal gain (ca. 40) is under development and will be produced by Photonis. By applying these values for quantum efficiency and the internal gain of the VPT, a primary photon with the energy of 1 MeV induces an input charge of 290 aC (1800 e<sup>-</sup>) to the preamplifier. In this case the ENC of 235 e<sup>-</sup>(rms) corresponds to a significantly reduced energy noise level of 160 keV (rms) for a peaking-time of 200 ns.

### 6.3.1.3 Event Rate

The expected event rate in the forward endcap EMC is maximum 500 kHz per crystal. The LNP-P has a feedback time constant of 25 μs. This feedback time constant is a trade-off between noise performance and pile-up problematic. Reducing the feedback time constant by a factor of two will increase the noise by about 10%. For a single pulse (or very low rates) the LNP-P accepts an input charge of up to 4 pC; for a continuous event rate of 500 kHz an input charge of up to 8 pC is allowed. This discrepancy is due to the following reason: A single output pulse starts from zero output voltage and is limited by the positive supply voltage (+6 V) of the LNP-P. At high continuous event rates the output pulses will swing between the negative (-6 V) and the positive (+6 V) supply voltage; therefore the maximum input charge is doubled. If a 500 kHz event rate is applied abruptly (burst) to the LNP-P it takes around one second until a continuous input charge of up to 8 pC is allowed. During that transition period, a maximum input charge of 0.3 pC can be handled. With this charge restriction, the output voltage of the preamplifier stays always in the linear

range and is never limited by the power supply voltages. Nevertheless, the electronics after the preamplifier has to perform a good base-line correction, because at higher rates it is likely that one pulse sits on the trailing edge of the previous one. If a charge of 48 aC/MeV (290 aC/MeV) is assumed from the VPT (see Sec. 6.3.1.2) the maximum expected photon energy deposition of 12 GeV per crystal results in an input charge of 0.58 pC (3.5 pC). Under the expected operational conditions with high rates predominantly occurring at low energy, the LNP-P will not be restricted by pile-up even with the relatively long feedback time constant of 25  $\mu$ s.

### 6.3.1.4 Bias Voltage

Because the anode of the VPT will be referenced to ground by the LNP-P, the photocathode (PC) and the dynode (DY) must be biased with negative high voltages (HV). To have the input of the preamplifier referenced to ground has the advantage that any noise on the HV supply is not directly coupled into the charge sensitive input. The typical bias voltages for the VPT type RIE-FEU-188 are: Photocathode:  $V_{PC} = -1000$  V; Dynode:  $V_{DY} = -250$  V. Even if these bias voltages do not directly couple to the charge input of the preamplifier, they have to be cleaned from external noise by an efficient low pass (LP) filter before they are wired to the VPT. Also, if all the VPT are biased with the same two high voltages, each VPT must have its own LP filter to prevent crosstalk. These LP filters for the two negative bias voltages ( $V_{PC}$ ,  $V_{DY}$ ) are not integrated on the preamplifier printed circuit board (PCB). A separate LP filter board has to be used; to minimize the noise level it is important that the ground of this LP filter board is tightly connected to the ground of the LNP-P. During the prototyping phase it is reasonable that both bias voltages of the VPT can be adjusted independently. In the final realization a passive voltage divider can eventually be used to generate the two bias voltages. At the maximum event rate of 500 kHz with the maximum expected photon energy deposition per crystal of 12 GeV (0.58 pC from the VPT) a mean current of 290 nA is flowing through the VPT. This current is mainly drawn from the dynode bias supply. Since the internal gain of the VPT varies only by about 0.1%/V, the voltage drop over the LP filter for the VPT dynode bias is not critical.

### 6.3.1.5 Dynamic Range

As explained in the Sec. 6.3.1.3, the LNP-P is designed for a single pulse charge input of maximum 4 pC. With an input charge of 48 aC/MeV (290 aC/MeV) coming from the VPT (see Sec. 6.3.1.2) this corresponds to a maximum photon energy of 83 GeV (14 GeV). Therefore the dynamic range of the LNP-P is restricted by the noise floor only. Thus, the specification of a dynamic range is strongly dependent on the applied shaping filter. In principle, the energy range of the LNP-P spans from the noise floor of 1 MeV (rms) (presently available VPT, peaking-time of 200 ns, see Sec. 6.3.1.2) up to the maximum input charge corresponding to an energy of 83 GeV; this corresponds to a theoretical dynamic range of 83000. In practice, the typical energy range will start at 2 MeV ( $2 \cdot \sigma_{noise}$ ) and end at 12 GeV which corresponds to an effective dynamic range of 6000.

### 6.3.1.6 FADC Readout

For the readout with a flash ADC (FADC) the same arguments apply as discussed in Sec. 6.2.1.5. The distance from the preamplifier in the cold volume to the digitizing electronics in the warm environment is maximally 110 cm which can be bridged with flat cables and differential signal lines. Therefore also in this case the anti-aliasing low-pass filter/amplifier will be placed right in front of the FADC.

## 6.3.2 Circuit Description

The LNP-P (Version SP 883a01) for the VPT is a further development of the charge preamplifier described in [6]. Some modifications on the circuit are made and a couple of components are changed to SMD types. The circuit diagram of the LNP-P is shown in Fig. 6.10. The AC-coupled input stage consists of a low-noise J-FET of the type BF862 from the company NXP Semiconductors (former Philips). This industrial standard J-FET is often used in preamplifiers of car radio receivers. It is specified with a typical input voltage noise density of 0.8 nV/ $\sqrt{\text{Hz}}$  at 100 kHz and at room temperature. The J-FET input capacitance is 10 pF and the forward transductance is typically 30 mS at a drain-source current (IDS) of 5 mA. Along with the 470  $\Omega$  AC-dominant drain resistor this transductance results in a typical AC-voltage gain of 14 for the J-FET input stage. The gate of the J-FET is protected against over-voltages by two low-leakage silicon diodes of the type BAS45AL. The input stage is

followed by a broadband (300 MHz), fast (2000 V/s) and low power (1 mA) current feedback operational amplifier of the type AD8011AR from the company Analog Devices. With its typical input voltage noise density of only  $2 \text{ nV}/\sqrt{\text{Hz}}$  at 10 kHz, this amplifier suits well for such a low noise design. The proper frequency compensation is performed by the capacitor C13 (100 pF), in combination with R2 (10  $\Omega$ ); this leads to high-frequency feedback to the inverting input of the operational amplifier. Overshoot and ringing can be efficiently suppressed and this compensation also prevents from oscillations when no VPT is connected.

The output of the operational amplifier is DC-coupled via the feedback network (1 pF || 25 M $\Omega$ ) to gate of the J-FET. In parallel the output is AC-coupled via a 1  $\mu\text{F}$  capacitor and a 47  $\Omega$  series resistor to the output of the LNP-P. Therefore, the output voltage is divided by a factor of two if it is terminated with 50  $\Omega$ .

With a symmetrical supply voltage of  $\pm 6 \text{ V}$  the output voltage can swing symmetrically between the positive and negative supply when high continuous event rates at high energies occur. The LNP-P draws a typical quiescent current of 6.3 mA from the +6 V supply and 1.2 mA from the -6 V supply; this leads to a total power consumption of only 45 mW.

To set the 5 mA operating point of drain-source current through the J-FET, a gate voltage in a range of -0.2 V to -0.6 V (typically -0.3 V, depending on the DC characteristics of the individual J-FET) has to be applied. This negative DC voltage is fed from the output of the operational amplifier via the 25 M $\Omega$  resistor to the gate of the J-FET. The operating point ( $I_{DS} = 5 \text{ mA}$ ) is fixed by the well filtered DC voltage applied to the inverting input of the operational amplifier. This set-point voltage is obtained by subtracting 2.5 V from the positive supply voltage (+6 V) by using a 2.5 V reference diode. So, the same voltage drop of 2.5 V must also be present over the total drain resistor of 503  $\Omega$  (470  $\Omega$  + 33  $\Omega$ ); this results in a stabilized DC drain current of 5 mA.

As shown in Fig. 6.10 the anode of the VPT is referenced to ground by a 20 M $\Omega$  resistor and the gate input of the J-FET is decoupled by a 4.7 nF high voltage capacitor.

As already discussed in the Sec. 6.3.1.4, the voltage drop over the LP filter for the VPT bias voltage has to be proven. At high rates in combination with high energies, a maximum current of 240 nA is flowing through the VPT, mainly drawn from the dynode bias voltage supply. The planned series re-

sistance of the LP filter is 40 M $\Omega$ , resulting in a maximum voltage drop of about 10 V. By using the typical gain sensitivity of 0.1%/V of the VPT, this voltage drop corresponds to a maximum energy/rate error of 1%. By reducing the series resistance of the LP filter, this energy/rate error can be kept at an acceptable level.

### 6.3.3 Performance Parameters

A summary of the LNP-P (Version SP 883a01) performance and specifications is given below:

- J-FET (BF862, NXP Semiconductors) in combination with a low power, high-speed current-feedback operational amplifier (AD8011AR, Analog Devices)
- Supply +6 V at 6.3 mA, -6 V at 1.2 mA leading to 45 mW quiescent power consumption
- Rise-time 13 ns at  $C_d = 22 \text{ pF}$
- Feedback time-constant 25  $\mu\text{s}$
- Gain: 0.5 V/pC at 50  $\Omega$  termination
- Maximum single pulse input charge: 4 pC
- Maximum 500 kHz burst input charge: 0.3 pC
- Maximum continuous 500 kHz input charge: 8 pC
- Single channel LNP-P version: PCB size 48  $\times$  18 mm<sup>2</sup>
- Typical noise performance at -25  $^\circ\text{C}$  and  $C_d = 22 \text{ pF}$  (see also Fig. 6.11)
  - ENC = 235 e<sup>-</sup> (rms) (shaping with a peaking-time of 650 ns)
  - ENC = 300 e<sup>-</sup> (rms) (shaping with a peaking-time of 200 ns)

The single-ended output of the LNP-P is designed to drive a 50  $\Omega$  transmission line. The charge sensitivity is 0.5 V/pC and so the maximum input pulse with a peak voltage of 2 V at 50  $\Omega$ . As an incident photon energy of 100 MeV corresponds to a pulse peak of only 2.4 mV, the subsequent electronics has also to be designed with low-noise performance. If the following electronics is located at distances of several 10 cm from the preamplifier, it may be necessary to add an additional amplifier onto the LNP-P printed circuit board. Advantageously an amplifier with a differential output driver should be integrated because differential signals are less sensitive

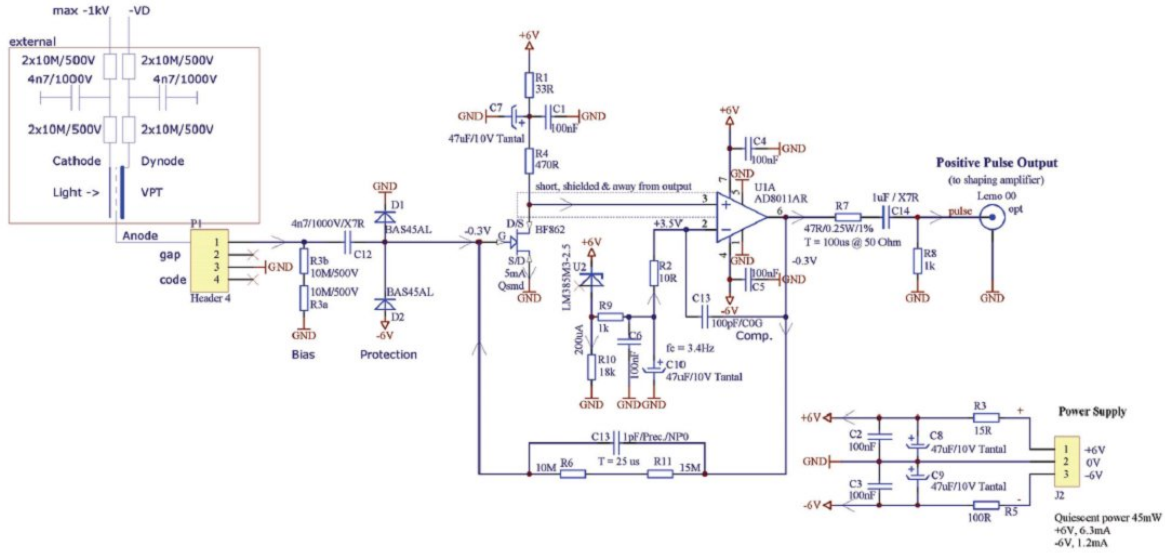


**Figure 6.10:** Circuit diagram of the LNP-P prototype for the VPT readout. The flexibility of the discrete design allows easy modifications in the future development process. The HV filter indicated in the top left is not integrated on the preamplifier PCB. This is the revision 1 of the LNP-P and it has the identification number SP 883a01.

to noise-pickup caused by an improper ground system. The differential driver AD8137YR from the company Analog Devices seems to be applicable for an extra gain of 5, while capable to drive a  $120\ \Omega$  terminated differential line. It has a typical voltage noise density of only  $9\ \text{nV}/\sqrt{\text{Hz}}$  at  $10\ \text{kHz}$ . By using such an additional amplifier/driver, the quiescent power consumption of the preamplifier would increase to around  $85\ \text{mW}$  and a larger rise time of about  $20\ \text{ns}$  is expected at a detector capacitance of  $22\ \text{pF}$ . Also more space on the printed circuit board of the LNP-P would be needed for such an additional amplifier.

The LNP-P (Version SP 883a01) can handle detector capacitances in a range from  $0\ \text{pF}$  to  $250\ \text{pF}$ . To reach an optimal rise time, the frequency compensation of the amplifier can be tuned by a capacitor. For different ranges of detector capacitances the frequency compensation must be matched. The actual frequency compensation is suitable for detector capacitances in a range of  $0\ \text{pF}$  to  $100\ \text{pF}$ . It results in a short rise-time of only  $13\ \text{ns}$  at a detector capacitance of  $22\ \text{pF}$ ; this allows precise timing measurements. The anode of the VPT is connected to the LNP-P via a short and shielded cable.

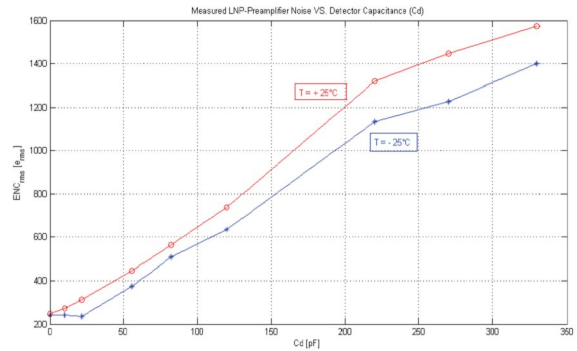


**Figure 6.11:** The measured noise performance of the LNP-P versus the detector capacitance ( $C_d$ ) at room temperature and at  $-25^\circ\text{C}$ . Measurements are performed by using an ORTEC450 Research Amplifier with  $T_{int} = 250\ \text{ns}$  and  $T_{diff} = 2\ \mu\text{s}$  which corresponds to a peaking-time of  $650\ \text{ns}$ . One can notice the strong decrease of the noise if the detector capacitance drops from  $270\ \text{pF}$  for a LAAPD, ( $1250\ e^-$  (rms)) to  $22\ \text{pF}$  for the VPT ( $235\ e^-$  (rms)). At high event rates, a more adequate shaping filter with a peaking-time of  $200\ \text{ns}$  must be used; in that case the noise for a detector capacitance of  $22\ \text{pF}$  is increased by 25%, which results in an ENC of around  $300\ e^-$  (rms).

### 6.3.4 SPICE Simulations

A precise SPICE model of the LNP-P including the shaping filter (peaking-time  $650\ \text{ns}$ ) has been de-

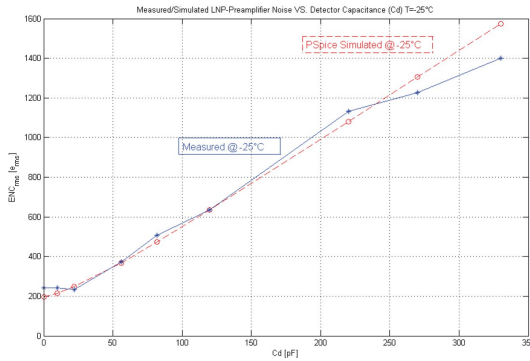


**Figure 6.12:** PSPICE simulation of ENC versus the detector capacitance (dashed red) together with the measured ENC (blue line), both at  $-25^{\circ}\text{C}$ . The simulation and the measurement are in very good agreement over the entire capacitance range.

veloped. The LNP-P circuit is based on the SPICE models of the BF862 (March 2007, NXP Semiconductors) and the model of the AD8011 (Rev. A 1997, Analog Devices). The shaping filter is modeled noiseless by using the Laplace block from the analog behavioral modeling (ABM) library. All simulations are made with PSPICE version 16.0 from the company Orcad/Cadence. An example of the good agreement between simulation and measurement is given in Fig. 6.12.

## 6.4 APD Timing Performance with FADC Readout

The EMC readout electronics is being designed to provide the best possible energy resolution and highest dynamic range. However, a time resolution in the order of at least 1 ns is desirable to reject background hits or random noise. To investigate the timing performance of the APD readout a series of test measurements was performed. The experimental setup consisted of two Hamamatsu APD S8664-1010 mounted on opposite sides of a 150 mm long PWO-II crystal. The crystal was mounted in an alcohol-cooled aluminium case placed in a dry-nitrogen flooded dark box. Light pulses of 3 ns rise time and variable intensity were supplied by a LED pulser using quartz fibers, coupled perpendicularly to either crystal end face. The APD signals after the LNP preamplifier were shaped using a newly developed two-channel two-stage shaper unit and were digitized by 10 bit 80 MHz sampling ADC. The full pulse shape was digitized in typically 60 time samples with 7 time samples in the leading edge of

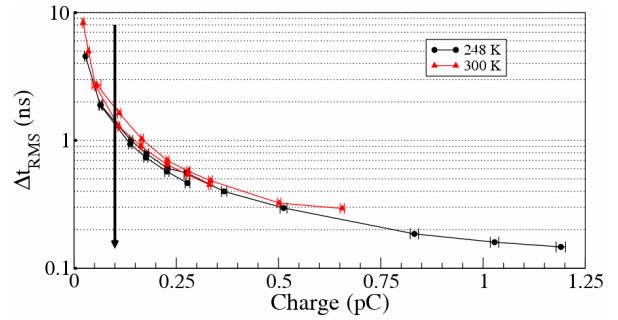


**Figure 6.13:** Time resolution as function of the corresponding pulse energy.

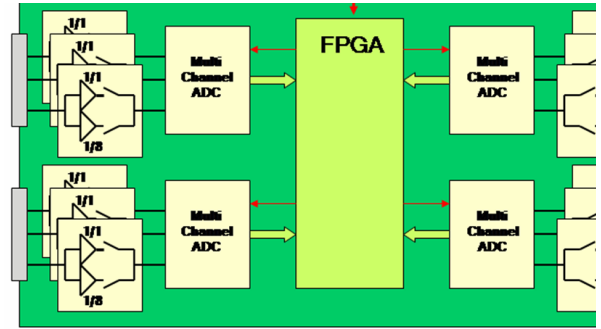


**Figure 6.14:** The functional diagram of the digitizer module.

the pulse. Time information for each pulser event was determined using the method of constant fraction timing. Fig. 6.13 shows the time resolution as function of the collected charge. The measurements were performed at room temperature and at  $-25^{\circ}\text{C}$ . An arrow indicates the position of the cosmic-ray peak with an energy deposit of roughly 22 MeV, which was used to establish the charge-energy calibration. At the lower energies the time resolution is limited by APD- and preamplifier-noise. These measurements show that it is possible to achieve a time resolution better than 1 ns at energy deposits above 60 MeV and 150 ps at energies above 500 MeV using the proposed sampling ADC readout scheme of the APD signals.

## 6.5 Digitizer Module

A functional diagram of the digitizer module is shown in Fig. 6.14. The module employs commercial multi-channel 12 bit ADC chips. One module houses up to 120 ADC channels, FPGAs and two fiber optic links.

There will be two versions of the digitizer module with Low and High digitization frequency for the

ASIC and for the LNP preamplifier, respectively. In both cases the digitization frequency is a factor of three higher than the frequency of the highest harmonic. The digitization frequency range will be arranged between 40 MHz for Low and 80 MHz for High frequencies. These values will be implemented for test experiments with the Proto60 prototype of the barrel EMC equipped with a prototype version of the ADC module and the LNP preamplifier.

The ADC chips have a resolution of 12 bit so that with two overlapping amplification ranges (see Fig. 6.7) digitized in two ADC channels the full dynamic range of 12000 can be covered. A special range selection circuit, suitable for operation in conjunction with the LNP preamplifier, is introduced in front of the ADC chip. The circuit multiplexes direct or attenuated signals depending on the signal amplitude. The range selection circuit consists of a comparator, an attenuator and an analogue switch. The switch is synchronized with the ADC clock. Since the switching time is less than one clock period, one sample can be distorted during switching. The two endcaps, equipped with VPT and LNP preamplifier, thus require in total 4192 ADC channels. The APFEL preamplifier ASIC provides two outputs with different gain and does not require the range selection circuit. For the independent readout of two LAAPD per crystal we thus require  $4 \times 11360$  ADC channels for the barrel part.

The FPGAs perform the following tasks:

- time adjustment and distribution of the global clock signal;
- noise calibration;
- common mode noise suppression;
- pedestal subtraction;
- autonomous hit detection;
- conversion of ADC data and linearization of the full data range;
- transporting the hit information together with the time stamp to the data multiplexer;
- slow control.

The architecture of the digitizer module preserves the redundancy policy, introduced by equipping every crystal with two APDs. The digitizer consists of two blocks of 60 channels each. The blocks have interconnections at the level of FPGAs but may function independently. The EMC channels are mapped in a way that the first APD of the crystal is connected to block one and the second APD to block

two. In case of failure of any component at most 60 channels out of 120 will not provide data. However, during normal operation the data of two APDs of the crystal are merged inside one of the FPGAs by using high-speed links between FPGAs.

An important parameter for the construction of the detector system is the power consumption and the channel density of the readout system. If one would start the development of the digitizer module today, using presently available commercial components, the power consumption of the digitizer would be below 400 mW per channel and the channel density would be about  $3 \text{ cm}^2/\text{channel}$ .

A prototype ADC module, shown in Fig. 6.15 [7], has a size of  $70 \times 130 \text{ mm}^2$  and contains 32 channels of 12 bit 65 MSPS ADCs. The total power consumption of the module is 15 W. The parameters of this prototype module are used as a reference for the design of the final readout system. The module is part of the setup for experiments with the Proto60 prototype of the barrel EMC.

## 6.6 Data Multiplexer

The data multiplexer provides the interfaces between the user program and the front ends, and between the front-end and the DAQ system. The foreseen data multiplexer module will comply to the new Advanced Telecommunication Architecture standard. The following Physical Interfaces will be included:

- 1 bidirectional 1 Gbit/s optical link to/from the Time Distribution System;
- 10 bidirectional 1 Gbit/s optical links to/from the front-end electronics (the digitizer modules);
- 2 bidirectional 2 Gbit/s copper links to/from the backplane to the neighboring multiplexers for
- 2 bidirectional 2 Gbit/s links to the DAQ system;
- 1 Ethernet link to a general purpose network for configuration and slow control.

The data multiplexer performs advanced data processing by extracting the signal amplitude and time, combining single hits into clusters, and sorting the clusters in a time-ordered sequence. A data flow through the module of up to 200 MBytes/s seems feasible.

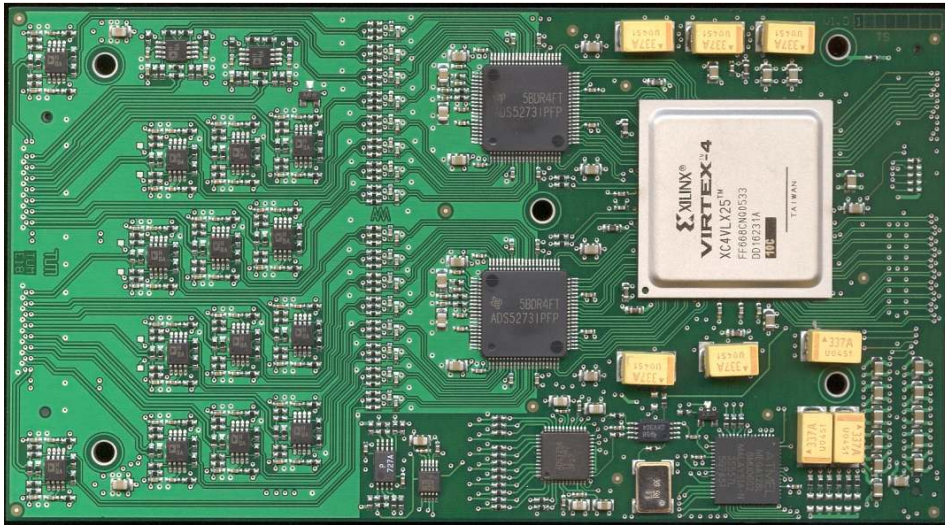


**Figure 6.15:** The layout of the prototype ADC module.

For transmission to the data acquisition system a maximum data rate of 4 GByte/s is estimated. This estimate is based on an event rate of  $2 \cdot 10^7$  antiproton annihilations per second, a multiplicity of 5 detected clusters with a typical cluster size of 10 crystals, 8 Bytes per hit crystal using two independent readout channels per crystal (as foreseen in the barrel). Further is assumed, that a clusterization process is applied before sending data to the data acquisition system. If clusterization would not be included, the data rate would increase by a factor 2 to 3. For 4 GByte/s a number of 40 optical links is required, assuming an optical link capacity of 100 MByte/s, and an equivalent number of data multiplexers.

heterogeneous types of conductors it is planned to implement flexible flat multilayer cables (FPC) instead of conventional bulky flexible solutions with coax cables. The signal,  $\pm 6$  V power supply and the bias voltage (HV) is designed in one 4-Layer cable per channel. These flexible cables are usually custom made in different lengths (for PANDA EMC about 350 mm for the barrel EMC and 1000 mm for the forward endcap EMC) and not available as a standard product. Long cables are increasing the noise, especially between APD/VPT and the preamplifier, but also between the preamplifier and the Shaper/ADC. Therefore, good shielding is essential. The temperature sensors (0.2 mm thermocouples) and the light guides for calibration are not discussed here.

## 6.7 Signal Routing and Cabling

### 6.7.1 Requirements

The detector system cooled to  $-25^\circ\text{C}$  requires a minimum amount of heat conducting copper into the system. However, to provide shielded, controlled impedance of  $50 \Omega$  signal lines and high voltage insulation, we can not use standard solutions. In Proto60 we designed a rigid multilayer-back-PCB (Fig. 6.16). The drawback was the reduction of flexibility in mechanical design. Possible solutions are, apart from round cables, flat ribbon cable, Flat Foil Cable (FFC), Flat Laminated Cable (FLC), exFC and Flexible Printed Circuit (FPC). Because of the

### 6.7.2 Cable Performance and Specifications for Proto60 Assembly

The distance between the preamplifier and the APD acts as a thermal decoupling to the APD and the crystals but must not be too long because of noise induced into the cable. A four fold device reduces the amount of cables from the warm to the cooled zone and saves space. Serviceability is provided through the use of a removable multilayer backplane-PCB (Fig. 6.16, which is a cheap and technically suitable solution to distribute supply voltages to the preamplifiers with a minimum amount of copper and to break out to ambient with maximum signal integrity through impedance con-

trolled signal lines. Further connections are then made through Lemo00-connectors and RG174 coax cables. At the moment, the disadvantage of this solution is the limitations imposed on the mechanical construction in the rigid PCB version.

From APD to the preamplifier a 70 mm long shielded twisted pair cable (Krophon Liff2Y-DY  $2 \times 0.073 \text{ mm}^2$ ) with an outer diameter of 2.2 mm and specified operating voltage of 500 VDC. The flexibility of the cable is sufficient to mount the parts using 2.54 mm connectors.

### 6.7.3 Cable Performance and Specifications for barrel EMC and forward endcap EMC

#### 6.7.3.1 Barrel

The cabling between preamplifier and ADC for each channel is planned to be provided by a 350 mm  $\times$  ca. 15 mm Flex-PCB flat cable (see scheme in Fig. 6.17). The bias voltage is maximum 500 VDC for the barrel EMC.

#### 6.7.3.2 Forward Endcap

A new version of the single-channel LNP preamplifier (SP883a01) was designed for use in the forward endcap EMC with improved stability also for the small capacitance of the VPT's. This preamplifier will be implemented in a "Proto16" VPT-subunit. The cabling between preamplifier and ADC for each channel is planned to be provided by 1000 mm  $\times$  ca. 15 mm Flex-PCB flat cable. The preamplifier works also with a 50  $\Omega$  line over 1000 mm to the ADC or one of the eight patch panels from where RG178 (diameter 1.8 mm) or other coax cables can be connected. The maximum bias voltage is 1000 VDC and two high voltages might be supplied to the forward endcap EMC VPTs.

From the HV-Filter to the VPT and from the VPT to the preamplifier the distance must be as short as possible. The signal must be shielded and hold the 1000 VDC bias voltage.

The distance between the preamplifier and the Patchpanel/Shaper/ADC is about 1 m. The VPT gives about 10 times lower pulse height (with VPT gain of 10) than the APD at the moment. A new VPT with gain up to 40 is under development.

### 6.7.4 Circuit Description

The AC coupled signal is transmitted over a 50  $\Omega$  line. A suitable conductor width for an impedance controlled microstrip design is for example 0.2 mm on an isolation layer of 0.1 mm to ground, but depends on the material specifications. Crosstalk is minimized by separate shielding of every channel.

### 6.7.5 Manufacturing, Operation, and Safety

The materials are polyimide (e.g. Kapton), copper, tin-lead and are not flammable. Connectors have only local relevance but care has to be taken also (UL94-V0 approval). Polyimide (e.g. Kapton) is widely used in accelerator environments. Solder-type Sn60Pb40 is used to avoid "tin pest" of lead-free solder points at long time temperature exposure of  $< 13^\circ\text{C}$  ( $\beta$ -Sn to  $\alpha$ -Sn transformation).

#### 6.7.5.1 Manufacturing and Connectors

Economic automatic processing of connectors without soldering can be provided with the use of crimping contacts (e.g. with Schleuniger HFC) or/and press-fit connectors.

### 6.7.6 Alternatives

There are alternatives to custom made cables with separated signal line, power supply and HV-cables. This is probably cheaper but needs also more space and has a significantly higher thermal impact, which also leads to higher costs. An additional differential amplifier stage on the preamplifier can reduce the sensitivity of the signal lines but causes higher power consumption in the cooled stage. The solution with the ADC directly mounted behind the preamplifier is not recommended because of higher cooling power required at that point. A resistive voltage divider near the VPT consumes roughly 1 mW ( $1000 \text{ V} \times 1 \mu\text{A}$ ) but can save a separate bias voltage line.

## 6.8 Detector Control System

### 6.8.1 Goals

The aim of a Detector Control System (DCS) is to ensure the correct and stable operation of an experiment, so that the data taken by the detector are of

Layer	Application
1. 35 $\mu$ m Cu	GND
2. 18 $\mu$ m Cu	Signal layer, Impedance controlled 50 $\Omega$ , max. ca. +/-5 $\Omega$
3. 18 $\mu$ m Cu	GND
4. 18 $\mu$ m Cu	LV Power Supply (+/-6V)
5. 18 $\mu$ m Cu	Max. 500VDC Power Supply
6. 35 $\mu$ m Cu	GND

Figure 6.16: The layout of the Layer Stack Back-PCB "SP903" used in the barrel EMC prototype Proto60

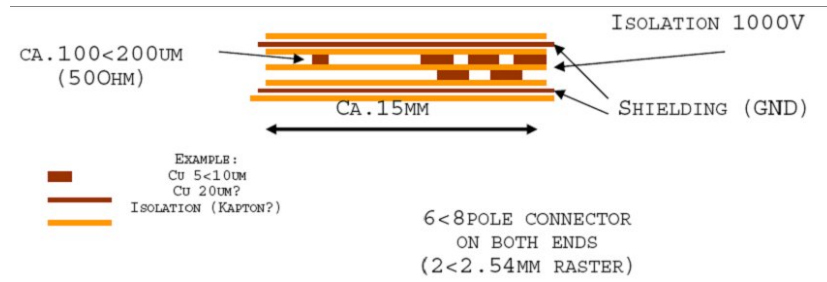


Figure 6.17: Scheme of the layer stack of flat cables.

high quality. The scope of the DCS is therefore very wide and includes all subsystems and other individual elements involved in the control and monitoring of the detector. The EMC and its subcomponents will therefore be embedded in the more general DCS structure of the complete PANDA detector. Here we will focus primarily on DCS aspects relevant for design and operation of the electromagnetic calorimeter.

The DCS extends from the active elements of the complete setup of the experiment, the electronics at the detector and in the control room, to the communications with the accelerator. The DCS also plays a major role in the protection of the experiment from any adverse occurrences. Many of the functions provided by the DCS are needed at all times, and as a result some parts of the DCS must function continuously, on a 24-hour basis, during the entire year. The primary function of the DCS will be the overall control of the detector status and its environment. In addition, the DCS has to communicate with external entities, in particular with the run control and monitoring system, which is in charge of the overall control and monitoring of the data-taking process and of the accelerator. System wide we require the DCS to be:

- partitionable in order to allow independent control of individual subdetectors or parts of them;
- automated to speed up the execution of commonly requested actions and also to avoid human errors in highly repetitive actions;
- easily operated such that a few non-experts are able to control the routine operations of the experiment;
- scalable, such that new subdetectors or sub-detector components can be integrated;
- generic: it must provide generic interfaces to other systems, e.g. the accelerator or the run control and monitoring system;
- easily maintainable;
- homogeneous, which will greatly facilitate its integration, maintenance and possible upgrades, and displays a uniform 'look and feel' throughout all of its parts.

The DCS has to fulfill the following functions (see Fig. 6.18):

- reliable, with respect to safe power, as well as redundant and reliable hardware in numerous places;
- modular and hierarchical;
- process control
- detector control
- detector monitoring

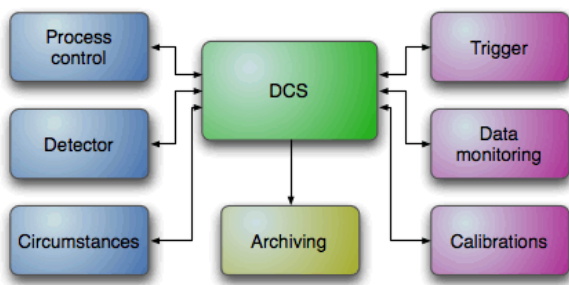


**Figure 6.18:** The various functions of the Detector Control System.

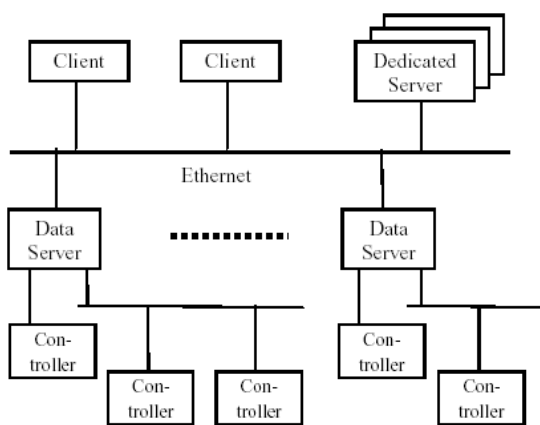


**Figure 6.19:** The DCS network structure.

- ambient circumstances control
- trigger control
- data monitoring
- calibrations
- archiving

## 6.8.2 Process Control

The Electromagnetic Calorimeter (EMC) is one part of a complex detector system and it is called a subdetector. The subsystem must be compatible with the requirements imposed on the Detector Control System as stated above. One important requirement is the process control, realized by the Supervisory Control and Data Acquisition (SCADA) software. The process control supervises the following items:

- system status

- data flow
- run start/stop status
- critical conditions

The definite knowledge of the system status is the heart of each control system. It enables a high level of abstraction and a simplified representation of detector control systems. A finite set of well-defined states is introduced, in which each of its subsystems can be, and rules are defined, that govern transitions between these states. The system status of each subsystem depends on the current state of the underlying hardware. At the same time, the system status enables a logical grouping of DCS subsystems into a hierarchical tree-like structure, where "parent" states are uniquely determined by states of its children and system-specific logic. Each parent in such system status tree can issue an action command to its children. Action commands at the lowest level imply appropriate commands issued to the controlled hardware. The PANDA EMC control software will be implemented in this way. The software granularity is driven by the EMC subsystem structure. The High Voltage (HV), Low Voltage (LV), cooling, temperature, humidity and safety systems are controlled by independent applications. On top of these applications there is the EMC supervisory application that implements an hierarchical structuring of the whole EMC control software. In addition the EMC DCS applications include numerous other functionalities, such as e.g. full parametrization and visualization of each subsystem, loading from and storing to the PANDA configuration database the start-up and operational parameters for EMC DCS subsystems. Among the characteristics of the SCADA system we can distinguish two of them as most important: its capability to collect data from any kind of installation and its ability to control these facilities by sending (limited) control instructions. The standard SCADA functionality can be summarized as follows:

- data acquisition
- data logging and archiving
- alarm and alert handling
- access control mechanism
- human-machine interface, including many standard features such as alarm display.

Two basic layers can be distinguished in a SCADA system: the 'client layer', which caters for the man-machine interaction, and the 'data-server layer',

which handles most of the process data control activities (see Fig. 6.19). The data servers communicate with devices in the field through process controllers. The latter, e.g. programmable logic controllers (PLCs), are connected to the data servers either directly or by networks or fieldbuses. Data servers are connected to each other and to client stations via an Ethernet local area network (LAN). There should be also a detector database fully integrated into the SCADA framework. This database should be accessible from the SCADA so that the SCADA features (e.g. alarming or logging) can be fully exploited. This database can incorporate:

- firmware
- readout settings (thresholds etc.)
- hardware settings (e.g. HV, LV)
- alignment values
- calibration constants.

### 6.8.3 Detector Control and Monitoring

The EMC Detector Control System should provide the monitoring of the detector conditions of the on-detector electronics as well as of all EMC subsystems (HV, LV, cooling system, gas system, status of laser monitoring system). All these monitored data should be recorded and archived as part of the common PANDA 'conditions database'. The DCS also has to provide early warnings about abnormal conditions, issue alarms, execute control actions and trigger hardwired interlocks to protect the detector and its electronics from severe damage. Regarding control functions, the DCS will switch on/off and ramp up/down the HV and LV, as well as set up their operational parameters. Overall PANDA will have a hierarchical DCS tree. This tree is a software layer built on top of the experiment controls. Every detector integrates its controls in this tree-like structure. The PANDA DCS supervisor, which is connected to the PANDA run control, will sit on top of the tree. In this way the EMC DCS will be directly controlled by the PANDA supervisor. However, when EMC runs separately (i.e. commissioning) its DCS is under control of an EMC run control. The EMC DCS also has connections to the PANDA detector safety system. All of the DCS functionalities must be constantly available during the EMC (PANDA) run time and some functionality practically non-stop (24h/365d) during the whole PANDA detector life time. Parts of the DCS functionalities

are going to be implemented through software applications running on dedicated DCS computers, as is the case with the HV, LV, cooling and laser monitoring systems. These applications communicate to hardware or to embedded computers using standard network or field-bus protocols. The other part of the functionalities will be implemented via dedicated DCS applications whose readout systems are completely independent of the EMC DAQ. These are the EMC monitoring system for temperature and humidity, and the monitoring system for the air temperature of the EMC electronics environment, the water leakage sensors, the proper functioning of the EMC cooling and LV cooling systems, and the control system to automatically perform predefined safety actions and generate interlocks in case of any alarm situation. The EMC DCS must have an interface to the data acquisition system (DAQ). A communication mechanism between DAQ and the DCS is needed for several purposes. During normal physics data taking, the DCS will act as a slave to the run control and monitoring system and will therefore have to receive commands and send back status information. Partitions will also have to be synchronized between the DAQ and the DCS: the run control and monitoring system will instruct the DCS to set up specific partitions, which will be put under the control of the run control and monitoring system. Furthermore, alarms will be sent from one system to the others.

## 6.9 Production and Assembly

### 6.9.1 ASIC preamplifier

Since the beginning of the integrated preamplifier development in 2005 two prototypes have been designed. These prototypes have been produced on Multi Project Wafer (MPW) runs of the EURO-PRACTICE IC prototyping program. At least one more prototype iteration is expected to be needed before a final ASIC design is reached for production.

Typically the designer gets some 20 chips by each MPW prototyping run which is sufficient for testing and device characterisation but may be not sufficient for a detector test setup with a medium scale detector array like the Proto60. For such cases the EURO-PRACTICE program offers the possibility to process additional wafers on a MPW run. Each additional wafer yields about 50 pieces. If the decision will be made to adapt the existing integrated preamplifier for the VPT readout of both endcaps of the EMC as well, additional prototypes have to be designed, produced and tested for this versions.

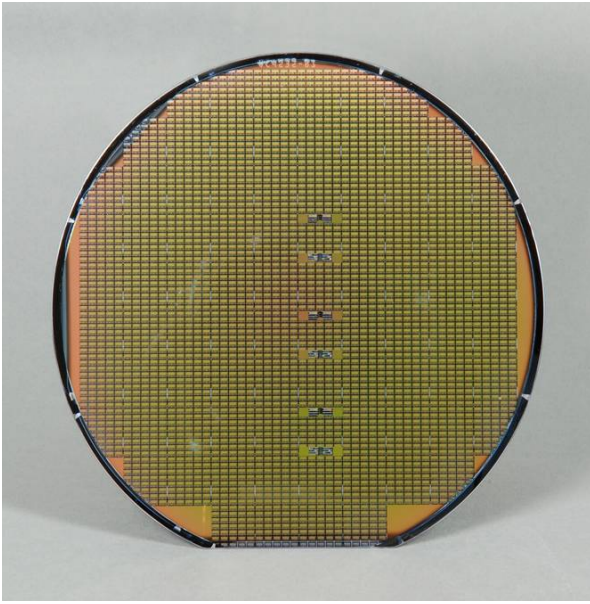


**Figure 6.20:** Microchip wafer.

Also these prototypes can be produced very cost effective by MPW runs.

For instrumentation of the electromagnetic calorimeter about 23000 pieces of the preamplifier are needed for the barrel EMC part (2 ASICs for one crystal with 2 LAAPD) and about 5000 pieces for both endcaps (1 ASIC for one crystal with VPT readout). These amounts of ASICs can no longer be produced cost effectively with MPW runs, so one has to start a chip production campaign. Such a campaign starts with the production of a set of photomasks for the lithography steps during chip production. With this mask set an engineering run is started to optimize the production parameter for this design. During this engineering run 6 wafers are produced but only 2 wafers are guaranteed to be within the specifications.

With a die size of  $10 \text{ mm}^2$  and a wafer diameter of 8 inches one will get about 3000 pieces on each wafer, see Fig. 6.20, so two wafers do not suffice to get enough preamplifier ASICs for the whole detector. That means, after testing the dies produced on the engineering run, one has to order the production of 1 wafer lot in addition which, in case of a production run at Austria Mikrosysteme, is 25 wafers.

After wafer production an intensive test phase has to follow. For wafer tests so called needle cards are used to connect the circuits on the wafer temporary. These needle cards are special printed circuit boards with very fine needles which are placed to fit the bonding pads of the integrated circuit. On a wafer prober this needle card is lowered on the wafer so a

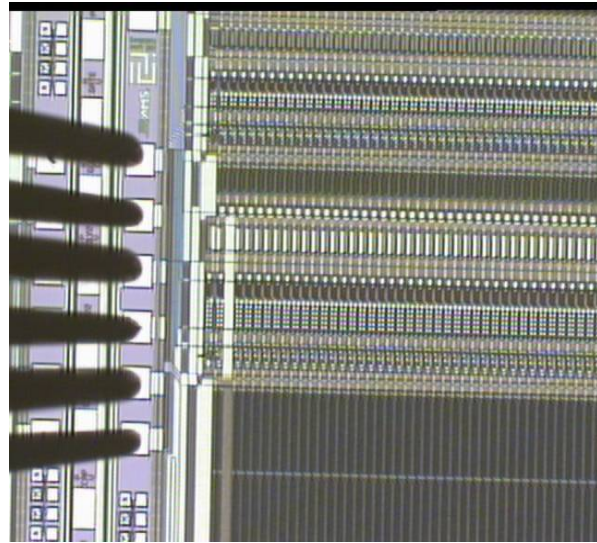


**Figure 6.21:** An integrated circuit connected by needles during a wafer test.

single circuit on the wafer can be tested electrically. After the test is finished the needle card is left off and the wafer has to be moved by one chip to start the next test. In Fig. 6.21 one can see 6 needles connecting an integrated circuit.

For mass tests this procedure has to be done with a semiautomatic prober which can do the lowering, lifting and wafer stepping in an automatic manner. Nevertheless, wafer changing and frequently cleaning of the needles has to be done manually. As all of these tests have to be done 3000 times for each wafer and 81000 times in total, test-algorithms have to be very efficient and fast. After testing, the chip assembly has to be started by an external assembly company. Assembly for Chip On Board (COB) technology consists of several steps:

- Sawing wafers into single dies
- Picking up good dies controlled by a wafermap which was compiled from wafer test results
- Placing and gluing dies on a PCB
- Wire bonding the dies
- Globtop the dies for mechanical protection
- Placing additional components
- Soldering discrete components

The preamplifier printed circuit board modules produced this way have to be tested once again before they are ready to be mounted on the detector.

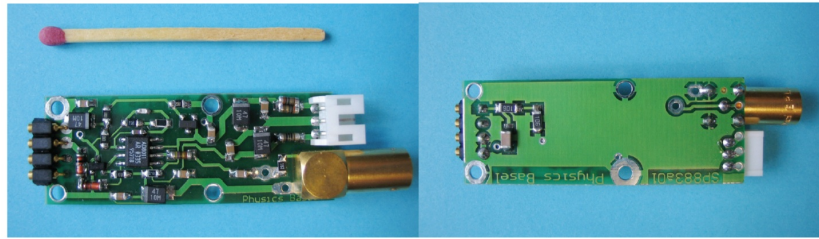


**Figure 6.22:** The top- and the bottom side of the single-channel LNP-P prototype for the VPT readout. It has a PCB size of  $48 \times 18 \text{ mm}^2$  and four holes (connected to ground) with a diameter of 2.3 mm are foreseen for mounting. The connector for the VPT is on the left side and the supply voltage ( $\pm 6 \text{ V}$ ) is connected via the white socket on the right. For the testing phase a Lemo-00 connector is equipped at the signal output. On the bottom side the two  $10 \text{ M}\Omega$  HV resistors and the HV gate decoupling capacitor are located.

### 6.9.2 Discrete preamplifier

The LNP-P is a simple, robust and low-cost combination of a standard J-FET with a fast integrated operational amplifier. The single-channel version of the LNP-P prototype for the VPT readout is implemented on a small-size double layer printed circuit board (PCB) with the mechanical dimensions of  $48 \times 18 \text{ mm}^2$  (see Fig. 6.22).

All components, except the connectors, are surface-mount devices (SMD). Therefore the LNP-P is well suited for automated mass production. Due to the discrete design of the LNP-P for the VPT readout, adaptations and modifications can be smoothly made in the future. For example, the power consumption can be easily reduced by changing only the value of two resistors. Of course, lowering the power consumption would also increase the noise level of the preamplifier.

### References

- [1] D. M. Binkley et al., *IEEE Trans. Nucl. Sci.* **39** No. 4, 747 (1992).
- [2] T. Suharli, J. vd Spiegel, and H. H. Williams, *IEEE Journal of Solid-State Circuits* **30** No. 2, 110 (1995).
- [3] G. Gramegna, P. O'Connor, P. Rehak, and S. Hart, *Nucl. Instrum. Meth.* **A390**, 241 (1997).
- [4] R. G. Meyer and R. A. Blauschild, *IEEE Journal of Solid-State Circuits* **21** No. 4, 530 (1986).
- [5] K. R. Laker and W. M. C. Sansen, *Design of Analog integrated circuits and systems*, McGraw Hill, 1994.
- [6] Panda Technical Progress Report, section 8.5.2, page 204ff, 2005.
- [7] I. Konorov, A. Mann, and S. Paul, A Versatile Sampling ADC System for On-detector Applications and the Advanced TCA Crate Standard, 15th IEEE-NPSS Real-Time Conference, 2007.



## 7 Mechanics and Integration

The electromagnetic calorimeter of  $\overline{\text{PANDA}}$  comprises two main parts: the central target calorimeter covers in cylindrical geometry almost completely the target area. A second planar arrangement located further downstream behind the dipole magnet serves the most forward range up to an azimuthal angle of  $5^\circ$  with respect to the beam axis. The target calorimeter is illustrated in Fig. 7.1 and comprises three major parts as summarized in Table 7.1.

The present design concept is based on a homogeneous electromagnetic calorimeter composed of fast and compact scintillator crystals as active absorber material to be operated within the solenoidal magnetic field of maximum  $2T$  field strength. Large area avalanche photodiodes (LAAPD) are considered as photosensors in the barrel part. To achieve the envisaged large dynamic range in energy reaching from  $10\text{ GeV}$  down to  $10\text{ MeV}$ , the proposed scintillator  $\text{PbWO}_4$  (PWO) has to be operated at low temperatures down to  $-25^\circ\text{C}$  to guarantee sufficient luminescence yield. The limited size of the photosensor and, consequently, the restricted coverage of the crystal endface can be compensated by a significantly higher quantum efficiency of the sensor compared to a standard bialkali photocathode and an improved scintillator performance.

The operation conditions impose additional, but still feasible, requirements on the mechanical construction, the insulation and the temperature sta-

bility in order to control the strong temperature dependence of the luminescence yield and keep the LAAPD gain at a tolerable level.

This report presents the principles of the calorimeter design focusing on:

- the definition of crystal geometry
- the mechanical housing and support structure
- the thermal aspects with respect to cooling ( $-25^\circ\text{C}$ ) and its fine regulation ( $\pm 0.1^\circ\text{C}$ )
- the integration with respect to the other detector components and the overall geometry as shown in Fig. 7.2.

The calculations are based on PWO as detector material. The proposed crystal depth is chosen in order to obtain 22 radiation length ( $X_0$ ). The overall granularity of the calorimeter is related to the Molière radius, which describes the radial shower profile. The granularity has to guarantee the reconstruction of the electromagnetic showers with an adequate energy and position resolution and to limit the occupancy even for the highest event multiplicities.

The presented concept is based on experience within the collaboration and on similar calorimeter concepts for BaBar [1], CMS [2], ALICE [3] or CLAS-DVCS [4].

This design relies on the construction of prototypes primarily to study the technology of extremely light crystal containers as well as the cooling and temperature control. The prototype results are also presented in this report.

Parts	Barrel	Forward downstream	Backward upstream
Crystals	11360	3600	592
Axial depth	2.5 m	-	-
Distance from target	-	2.05 m	0.55 m
Inner radius	0.57 m	0.18 m	0.1 m
Outer radius	0.94 m	0.92 m	0.3 m
Inner angle	$22^\circ$	$5^\circ$ vert. $10^\circ$ horiz.	$169.7^\circ$
Outer angle	$140^\circ$	$23.6^\circ$	$151.4^\circ$
Solid angle ( $\%4\pi$ )	84.7	3.2	5.5

**Table 7.1:** Geometrical parameters of the EMC referring to the front face of the crystal arrangement of 200 mm long crystals.

### 7.1 The Barrel Calorimeter

The barrel calorimeter including the mechanical structure covers the polar angular region between  $22^\circ$  and  $140^\circ$  with an inner radius of  $570\text{ mm}$  and an outer radius of  $950\text{ mm}$ .

#### 7.1.1 The crystal geometry and housing

The basic crystal shape is a tapered parallelepiped, shown in Fig. 7.3, and is kept fixed for all calorime-

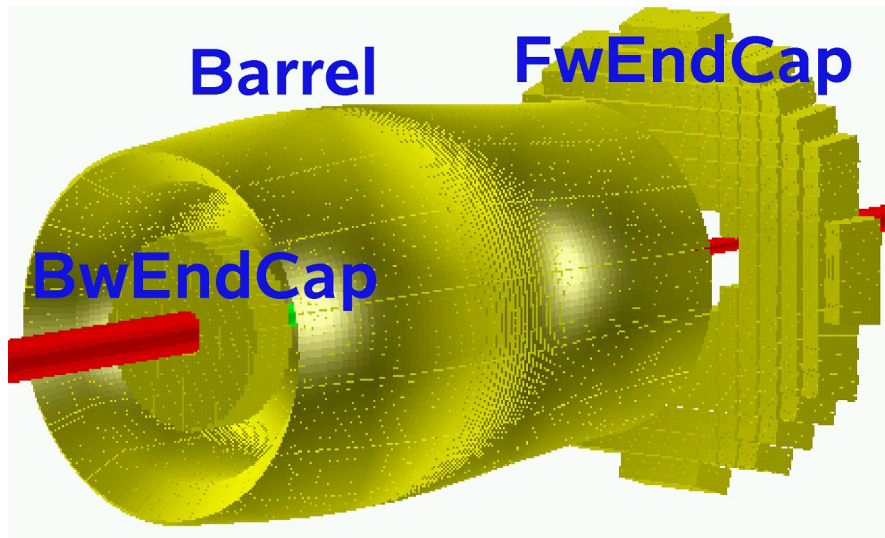


**Figure 7.1:** The components of the  $\bar{\text{P}}\text{ANDA}$  electromagnetic calorimeter and their acronyms as used in the PandaRoot simulation framework: barrel EMC (Barrel), forward endcap EMC (FwEndCap) and backward endcap EMC (BwEndCap), with the beam going from left to right.

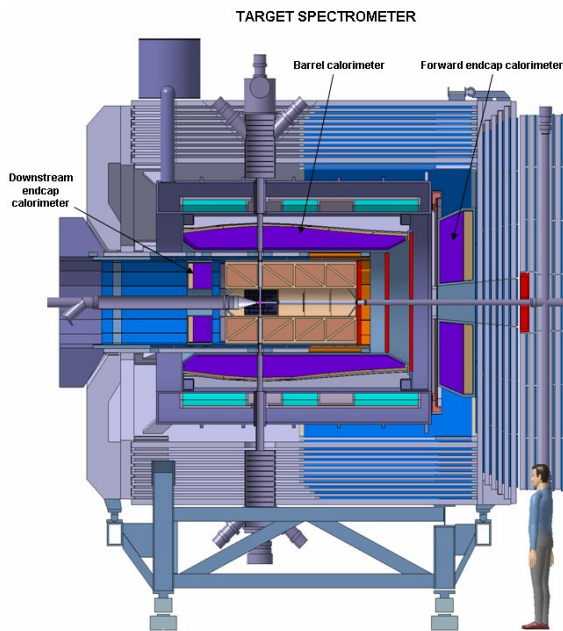


**Figure 7.2:** Overall view of the integration of the electromagnetic calorimeter into  $\bar{\text{P}}\text{ANDA}$ .

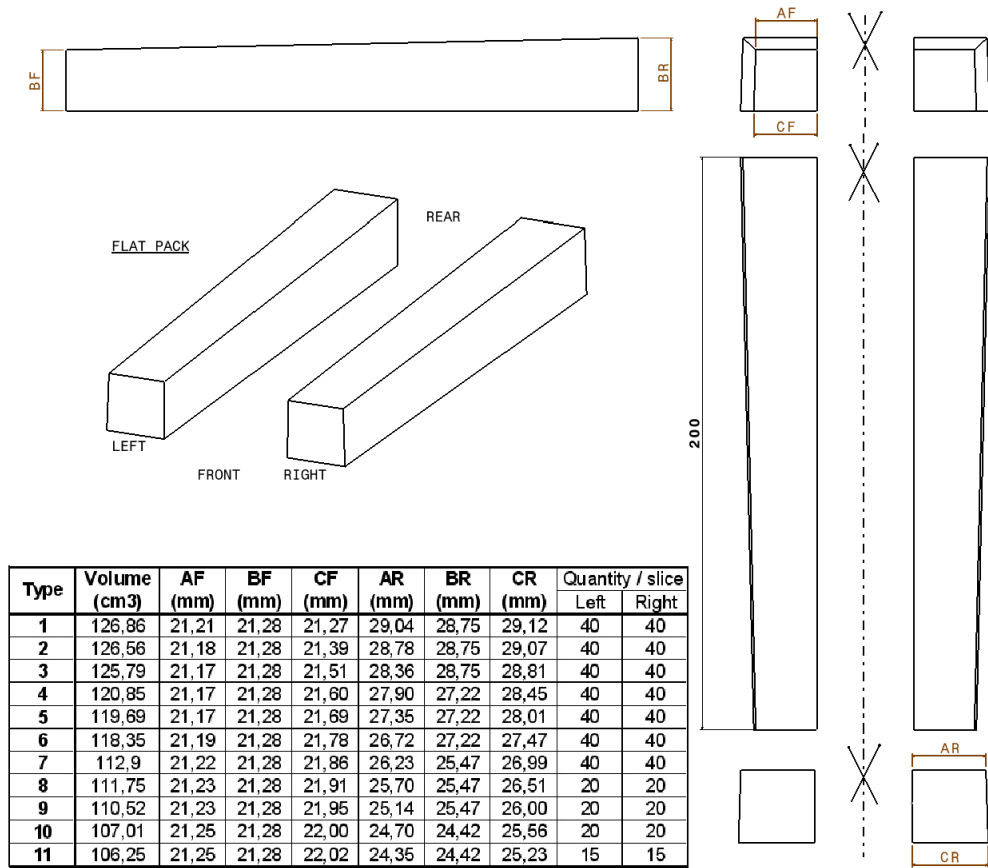
ter elements. It is based on the “flat-pack” configuration used in the CMS calorimeter. Right angle corners are introduced in order to simplify the CAD design and the mechanical manufacturing process to reduce machining costs. The average mass of one crystal is 0.98 kg (from 0.88 to 1.05 kg). All given dimensions are nominal and the tolerances

of the crystals are  $0/-100 \mu\text{m}$  (the achievable tolerance is based on the present delivery for CMS from the Bogoroditsk plant as well as for the DVCS calorimeter at JLAB). The dimensions of the individual crystals are related to the global shape and to the discretization of the calorimeter, defined circumferentially and longitudinally in Sec. 7.1.1.1 and Sec. 7.1.1.2, respectively.

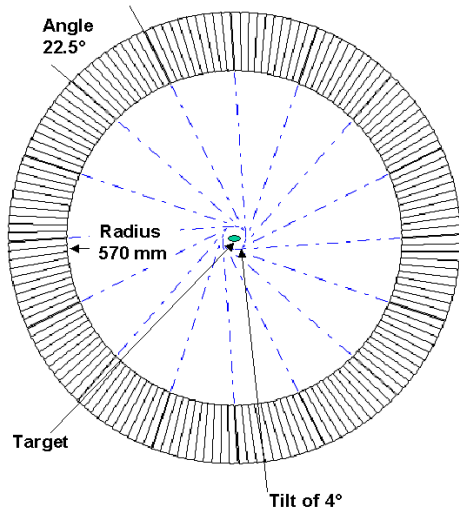
#### 7.1.1.1 Crystal Arrangements along the Circumference

Fig. 7.4 shows the crystal arrangement on the ring based on the gap dimensions defined in Sec. 7.1.1.5. Choosing the front size of an individual crystal close to 20 mm (21.28 mm exactly) at a radius of 570 mm, which corresponds to the Molière radius, the ring is divided into 160 crystals. The crystals are grouped into packs of  $4 \times 10$  (one alveole pack) leading to 16 sectors of  $22.5^\circ$  coverage, which are termed slices.

The presented geometry foresees that the crystals are not pointing towards the target position. A tilt of  $4^\circ$  is added on the focal axis of the slice to reduce the dead zone effect. This means, that tracks originating at the target never pass through gaps between crystals, but always cross a significant part of a crystal.



**Figure 7.3:** The shape of the scintillator crystal and the definition of geometrical parameters. The average crystal corresponds to squares of 21.3 mm for the front face and 27.3 mm for the back face and its mass is 0.98 kg.



**Figure 7.4:** The segmentation of the calorimeter along the circumference of the barrel part. The 160 crystals are grouped into 16 subunits named slices.

### 7.1.1.2 Longitudinal Crystal Positioning

Along the length of the barrel (parallel to the beam axis) the crystal positions and individual geometries are shown in Fig. 7.5. The mirror symmetry with respect to the vertical axis reduces the number of different crystal shapes in the arrangement from 18 to 11. The lateral sizes of the rear (read-out) faces vary between 24.35 mm and 29.04 mm and the average area is equivalent to a square of 27.3 mm ( $\pm 15\%$  area variation between the 11 types of crystals). For the front face, the lateral sizes vary between 21.18 mm and 22.02 mm and the average area is equivalent to a square with lateral size of 21.3 mm. In total 71 crystals are aligned at the radius of 570 mm. A tilt angle of  $4^\circ$  is introduced to reduce the dead zone effect and this angle corresponds to a shift of the focus by  $\approx 37$  mm downstream. In one slice of 710 crystals, 3 or 5 alveole packs are grouped together into 6 modules: 4 modules of 120 crystals each, 1 module with 70 and 1 with 160 crystals. The entire barrel contains 11360 crystals for a total length of 2466 mm and a volume

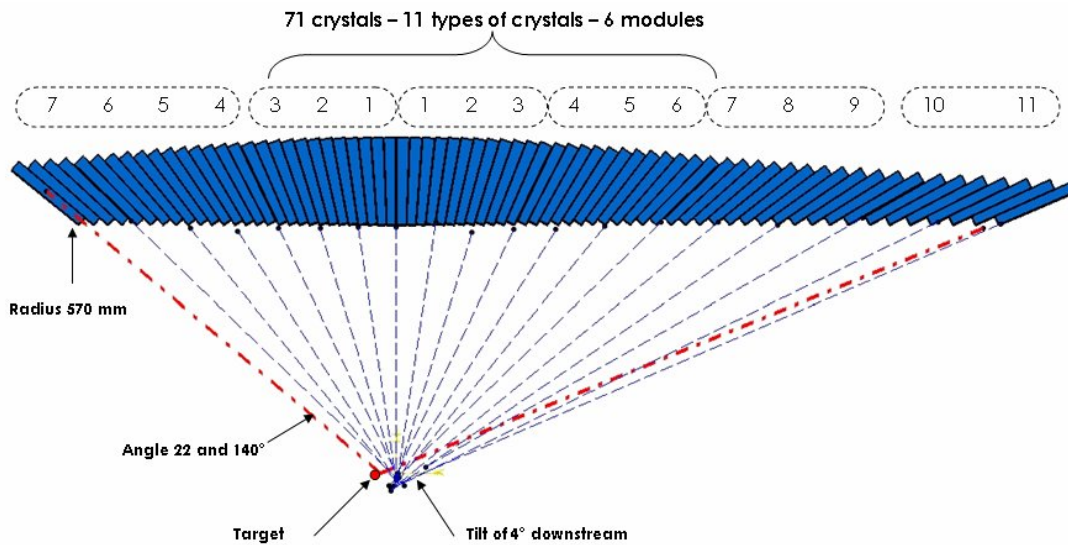


**Figure 7.5:** Geometrical arrangement of the crystals of the barrel in a cut along the beam axis. The definition of subgroups by pack of 4 and by module is indicated. The use of the mirror symmetry decreases from 18 to 11 different types of shapes according to the definition in Fig. 7.3.

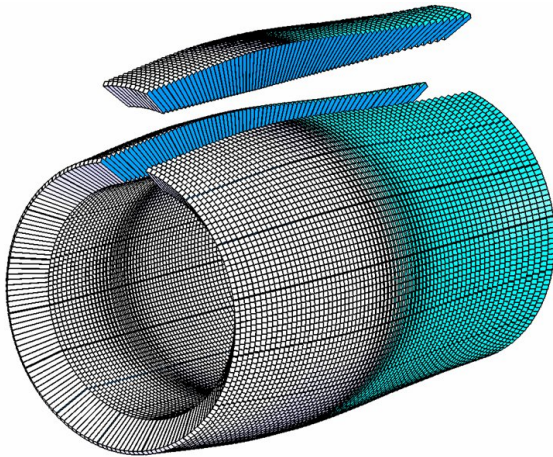


**Figure 7.6:** View of the total barrel volume composed of 11360 crystals and, separated, a single slice of 710 crystals covering 1/16 of the barrel volume.

of  $1.3\text{m}^3$ . Fig. 7.6 highlights one slice out of the total barrel volume.

### 7.1.1.3 Crystal Light Collection

The crystals are wrapped with a reflective material in order to optimize light collection as well as to reduce optical cross talk. Considered material is Radiant Mirror Film ESR from 3M, commonly called "VM2000" in the past, accounting for a thickness of  $63.5\ \mu\text{m}$ . This wrapping material, a non-

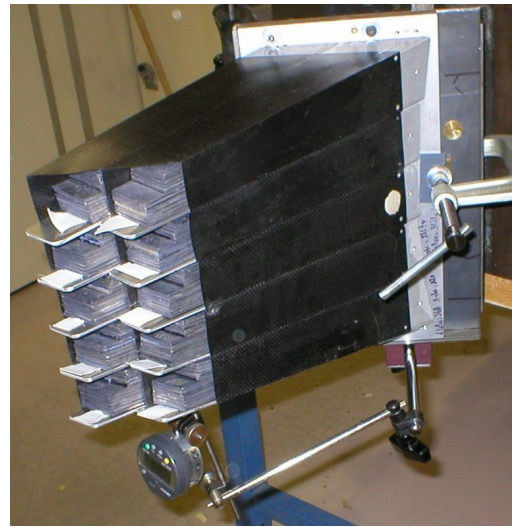


**Figure 7.7:** Deformation test of carbon alveoles in vertical position. Here the measure is around  $10\ \mu\text{m}$  compared to the  $80\ \mu\text{m}$  in the horizontal position.

metallic multilayer polymer, was employed for the crystals of the DVCS calorimeter at JLAB) and the GLAST calorimeter. In order to foresee a small air gap between the reflector and the crystal face, the foil must be shaped in a mold heated at  $80^\circ\text{C}$  to sharpen the corners. In order to compensate for the longitudinal dependence of the light collection, the structure of the crystal surface (optically polished, roughed, lapped) can be modified or an inhomoge-

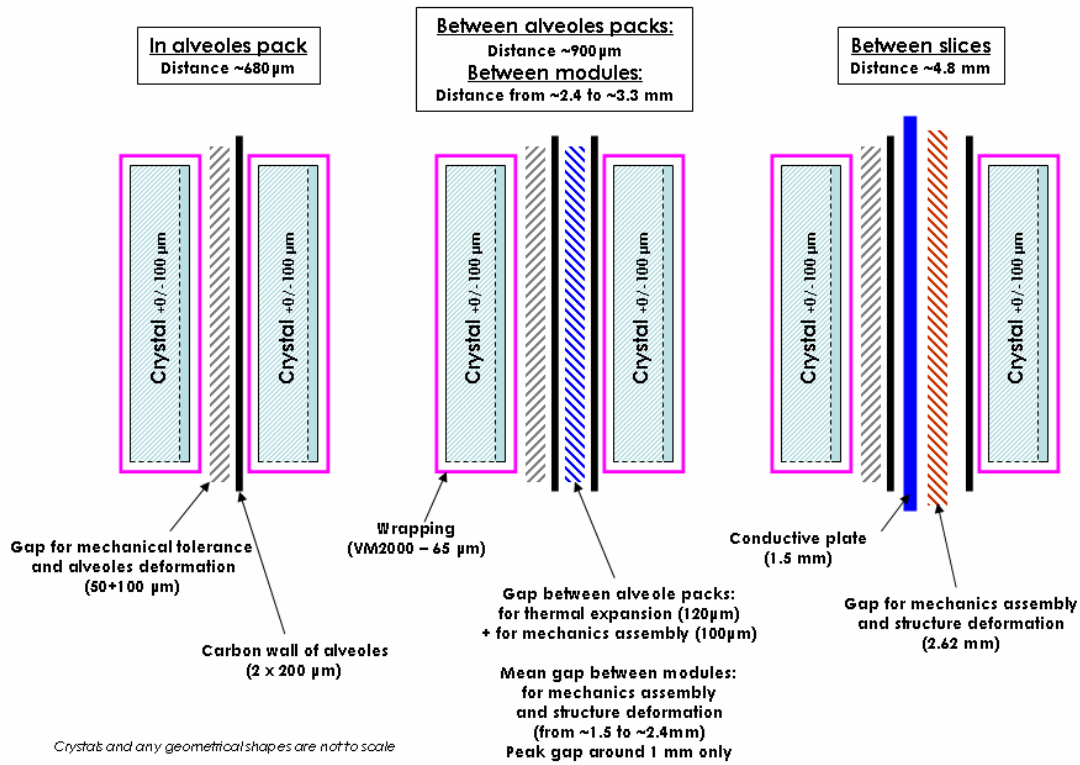


Figure 7.8: Summary of the expected dead space between calorimeter elements.

neous reflector can be selected. This is still under study.

#### 7.1.1.4 Carbon Fiber Alveoles

In the present design, 4 crystals will be contained in one carbon fiber alveole in order to avoid any load transfer to the fragile PWO while the crystals are held in place by their rear end. The expected wall thickness of the alveoles is  $200\ \mu\text{m}$  and they are grouped to compose an alveole pack of 40 crystals. Each alveole is epoxy-glued to an aluminum insert which is the interface with the support elements. Temperature cycling tests of the gluing between  $-40^\circ\text{C}$  and  $30^\circ\text{C}$  are performed to check the reliability of this support stressed by the differential thermal expansions. In front of the alveoles, a carbon plate is added to avoid the movement of crystals. Epoxy pre-impregnated carbon plain weave fabric is precisely moulded in complex tools to fabricate the alveoles. Each type of crystal corresponds to one mold composed, for technical reasons, of 2 alveoles to overlap the 2 wrapping joints. Real size alveole prototypes have been produced to check the feasibility, to optimize the final thickness and to perform mechanical tests. Fig. 7.7 shows one of the

deformation tests, here in the vertical position. The results  $80\ \mu\text{m}$  horizontally and  $10\ \mu\text{m}$  vertically are tolerable and are in agreement with the analytical calculation.

#### 7.1.1.5 Distances between Crystals

The distance between two crystals is calculated from the thickness of materials, structure deformation and mechanical tolerances. Fig. 7.8 presents drawings of the different gaps which are explained in detail below. A conservative concept has been chosen, which can be considered as an upper limit of the expected dead space.

The basic distance between crystals inside a pack is defined to  $0.68\ \text{mm}$  and represents the sum of:

- $400\ \mu\text{m}$ , the double thickness of the carbon alveoles;
- $130\ \mu\text{m}$ , the double thickness of the wrapping material;
- $100\ \mu\text{m}$ , the free distance left for the alveole deformation;
- $50\ \mu\text{m}$ , the approximate manufacturing tolerance.

This calculation is based on the nominal dimension of the crystal. There might appear an additional distance of  $< 0.2\text{mm}$  between two adjacent crystals due to polishing tolerances. Gaps between the identical shapes of 4 crystals in one alveole pack might introduce an additional lateral spacing up to  $350\ \mu\text{m}$ .

Between alveole packs, the thermal expansion of the mounting plate amounts to about  $120\ \mu\text{m}$  and the mounting tolerance is assumed  $100\ \mu\text{m}$ . Together with the basic distance between crystals of  $0.68\text{mm}$  this adds up to a total value of  $0.9\text{mm}$ .

Between modules, a distance varying between  $2.4$  and  $3.3\text{mm}$  has to be considered to take into account the mounting feasibility and tolerances in the mechanical assembly, and in the structure deformations.

Between adjacent slices, a first gap up to  $2.62\text{mm}$  due to mechanical mounting tolerances caused by the deformation of the whole structure and a second gap of  $1.5\text{mm}$  have to be assumed. The distance between crystals in this area amounts to  $< 4.8\text{mm}$ .

## 7.1.2 Mechanics around Crystals - Slice Definition

Fig. 7.9 presents the design principle of one slice coping with all constraints: thermal, mechanical and electrical integration.

### 7.1.2.1 Insert and Module Definition

The inserts, glued to the carbon alveoles, make the precise connection to the back module plates and also hold the preamplifiers and the optical fibers which are shown in Fig. 7.10. The shape of these inserts are all different and complex to fabricate due to the tapered slopes of crystals and due to the faceted shape of the barrel calorimeter. Corresponding to the 6 modules defined in the Sec. 7.1.1.2, the back module plates have a thickness of  $14\text{mm}$  machined with a good flatness in order to stay a reference plane even under the weight of the crystals. Each plate is linked to a support beam through 6 support feet designed for low thermal transfer and low deformation. In addition, these feet have motional freedom in particular directions in order to allow translations due to the thermal expansion. The back module plates are cooled down by the upper thermal screen. Further thermal details are given in Sec. 7.1.4. Fig. 7.11 shows an exploded view of one module with all individual components.

### 7.1.2.2 Support Beam Definition

The 710 crystals of one slice are supported by a stainless steel support beam whose shape is a rectangular tube of  $2.7\text{m}$  length. The bending of this beam is calculated to be between  $0.1$  and  $0.4\text{mm}$  for the horizontal and the vertical position of the slice, respectively, as shown in Fig. 7.12. These values show its rigid behavior but the position of the modules will have to be corrected in order to align all the crystals. The magnetic field of the solenoid requires to verify that the applied stainless steel material is indeed of sufficient non-magnetic quality. The magnetic quality may have been altered by the machining or the welding process of this part and a magnet-relieving anneal is foreseen in an oven. The internal part of this tube is used for storing all the services as electronics boards and power supply cables. The details about the integration of services are provided in Sec. 7.1.3. These services are located at room temperature and access must be possible simply by opening the top external cover when the barrel is in maintenance position. The support beam is fixed on 2 support rings at its both extremities, where a possibility to adjust the alignment of the slices is foreseen. These rings (shown in Fig. 7.13), rest on support points added to the inner vessel of the coil cryostat.

### 7.1.2.3 Adapted Design for the Target

The target system is passing through the calorimeter barrel on the vertical axis. It is foreseen to place two slices, an upper and a lower one, specially designed with a central hole. Some crystals are removed, the mechanics and the thermal shields are modified and a hollow cylinder of insulation is added. In any case, the target tube will not be in contact with the cold area and will be let free to move.

## 7.1.3 Electronics Integration

### 7.1.3.1 Photosensor, Preamplifier, Flat Flexible Cables

Due to the magnetic field, Large Area Avalanche Photo Diodes (LAAPD) are employed. Two LAAPD of  $7 \times 14\text{mm}^2$  each are used and glued on the back face of the crystal. Each LAAPD is connected to a charge preamplifier with a  $40\text{mm}$  long twisted wire. The length is discussed in the Sec. 7.1.4.5 as it plays a role in the heat transfer to the LAAPD. The preamplifier has a power

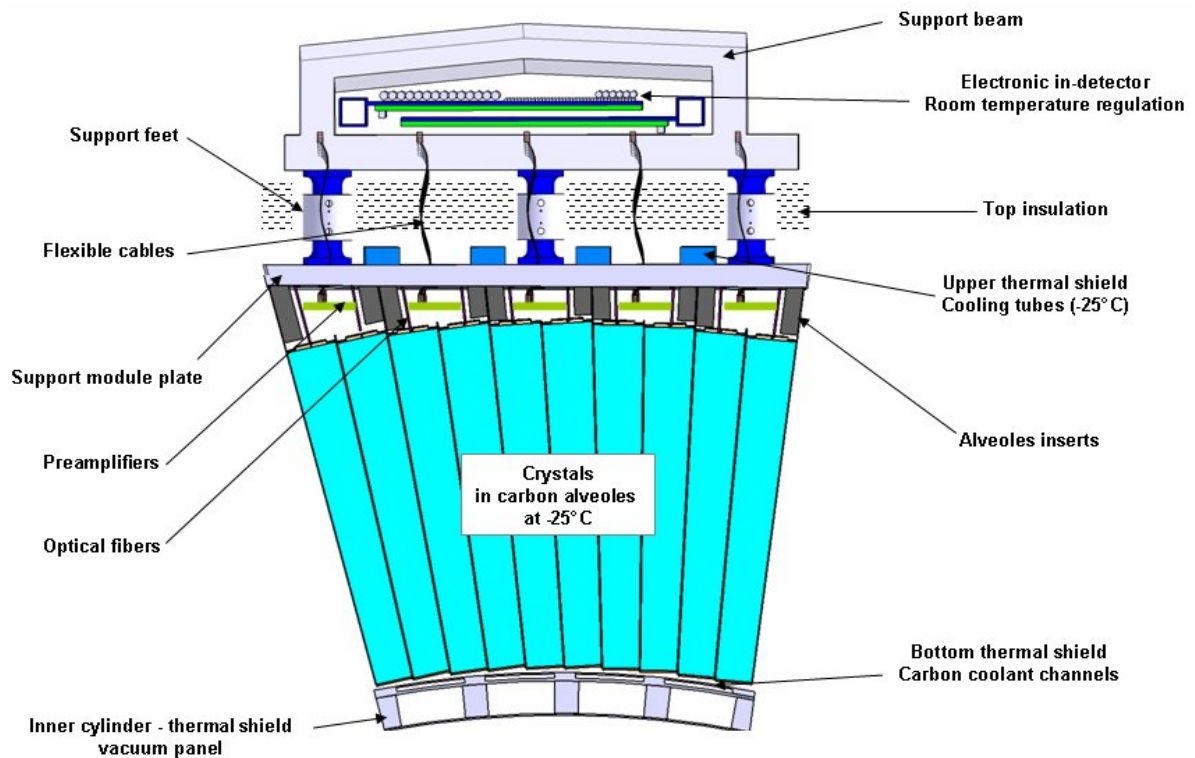


Figure 7.9: Schematic view of the concept and of the major components of a slice.

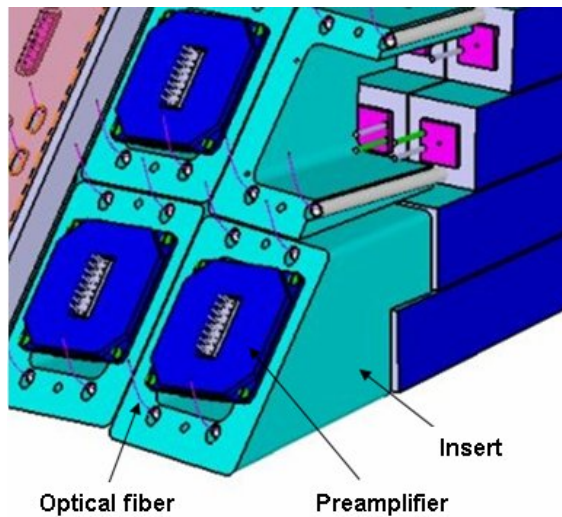


Figure 7.10: CAD integration of the insert with the preamplifier and optical fiber at the back of crystals. First design uses single square LAAPD but 2 rectangular LAAPDs fit as well.

consumption of 52 mW/channel and is fixed on the inserts. It is connected to the read-out electronics through a 350 mm long flat flexible cable which drives: the 8 signals, 1 high and 2 low voltages,

stacked between 2 shielding layers. The sections are resumed in Fig. 7.14. The lack of space requires high density connectors. The length of the flat flexible cables is calculated in order to be able to group them and thus reduce the number of holes in the bottom face of the support beam. Besides, a increased length and a smaller cross section decrease the conductive heat transfer.

### 7.1.3.2 Read-out Electronics

Sec. 7.1.2.2 indicated that the read-out electronics is integrated into the support beam. This electronics comprises the digitizing ADC boards. In addition to this equipment, the support beam also contains services as the high and low voltage power supply, the ADC read-out optical fibers, the ADC power supply and the water cooling tubes for the room temperature regulation (discussed in Sec. 7.1.4.9). Fig. 7.14 illustrates this arrangement and resumes the sections of the services. The size of the boards is  $300 \times 150 \times 10 \text{ mm}^3$ . Using high-density connectors and a stacking in pairs, 2 boards can fit even in the small central region of the beam and could perform the readout of up to 240 channels, equivalent to a module equipped with 2 LAAPD per crystal.

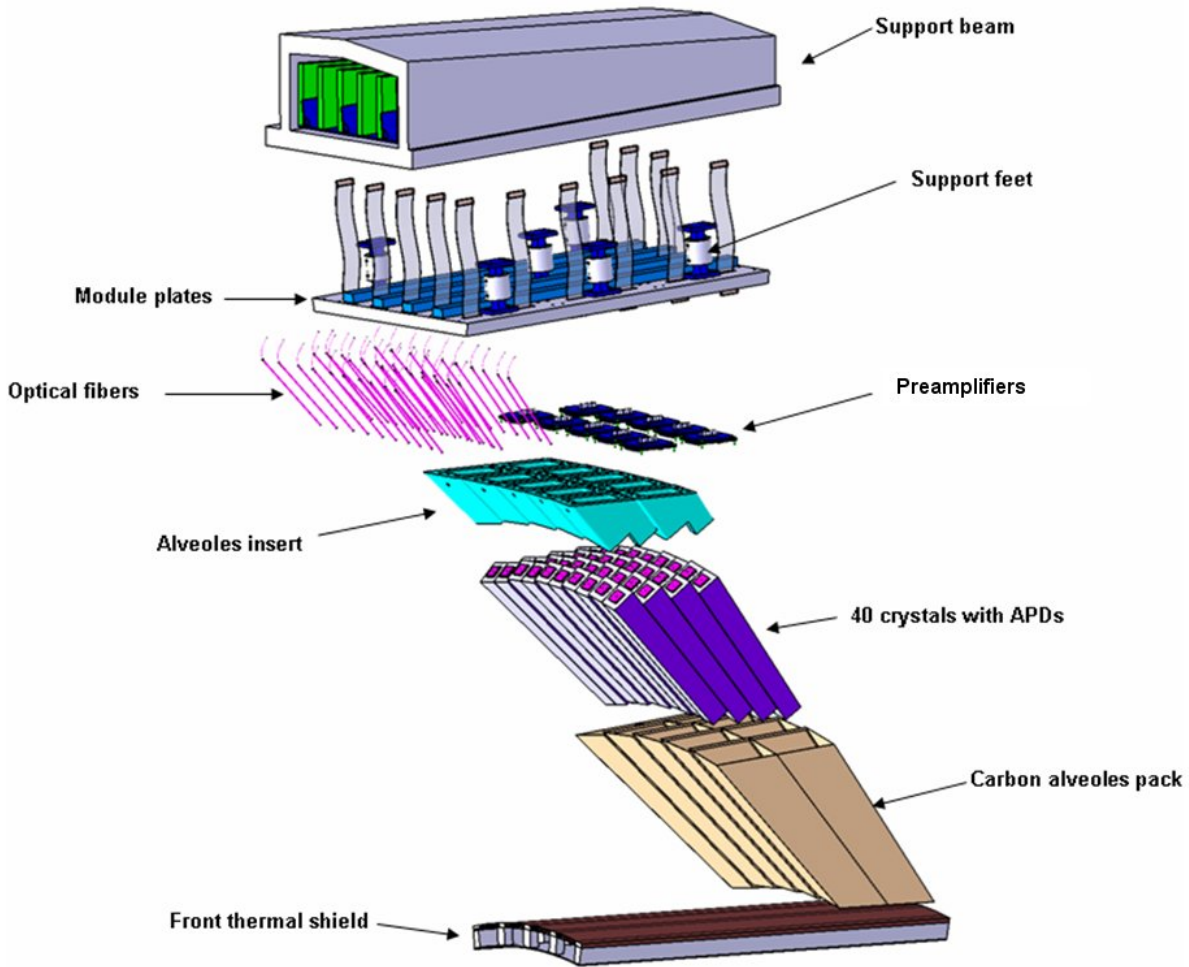


**Figure 7.11:** Exploded view of one slice showing all the individual components.

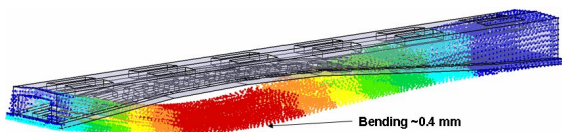


**Figure 7.12:** Deformation of 0.4 mm of the support beam in the upper position (horizontal beam).

### 7.1.3.3 Laser Calibration System

The LAAPD is enclosed in a light tight plastic box into which an optical fiber for light injection is inserted in one corner. This LED- or LASER-light is injected from the rear side of the crystals due to the limited space in front of the calorimeter. The light pulser system is primarily intended for stability control of the complete readout chain including the LAAPD. A first prototype is under construction based on a LED light source with optical fiber

distribution (see Sec. 8.2.1). The routing of the optical fibers is taken care of in the early stage of the design in order to respect the minimum bending radius and to integrate special guiding tubes inside the mechanical construction. The fiber installation must be finished before the upper thermal insulation is closed. The use of a non-rigid insulator, as vermiculite granulate mentioned in the Sec. 7.1.4.3, is a reasonable solution due to the high number of fibers in random positions.

## 7.1.4 Thermal Cooling

### 7.1.4.1 Requirements and Method

The crystals are to be cooled down to a nominal operating temperature of  $-25^{\circ}\text{C}$ . The temperature gradients of the LAAPD gain and of the crystal light yield of  $-2.2\%/^{\circ}\text{C}$  and  $-1.9\%/^{\circ}\text{C}$ , respectively, require a stable temperature with peak to peak vari-

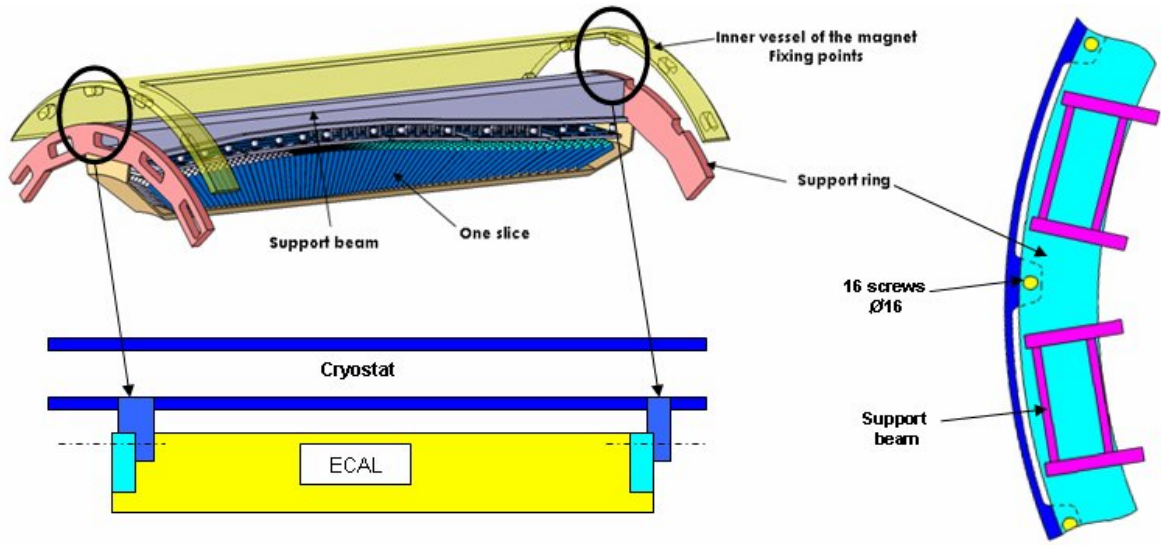


Figure 7.13: Barrel supported on the magnet.

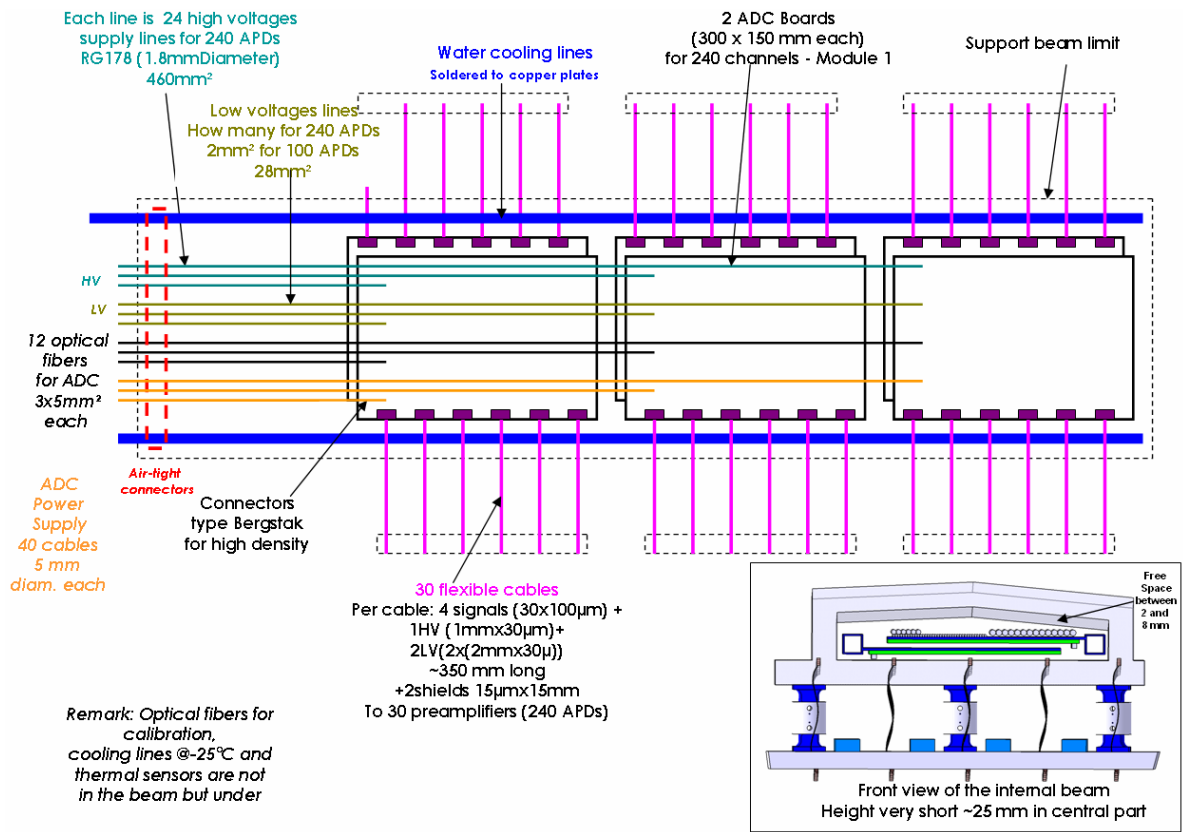


Figure 7.14: Integration of the services in the support beam.

ation over time of at most  $\pm 0.1^\circ\text{C}$  in order to keep the initial calibration. The read-out electronics is stabilized at room temperature and this regulation

is described in the Sec. 7.1.4.9.

Parameter	PWO	
$\rho$	8.28	g/cm <sup>3</sup>
Specific heat	262	J/kg.°C
Conductivity	3.22	W/m.°C

**Table 7.2:** The relevant properties of PbWO<sub>4</sub> (PWO).

#### 7.1.4.2 Thermal Properties of the PbWO<sub>4</sub>

Based on information from the CMS/ECAL Collaboration, the thermal properties of PWO are listed in Table 7.2 and are used in the thermal analysis discussed below.

#### 7.1.4.3 Thermal Shields

The crystals are surrounded by thermal shields basically made of panels, cooled by serpentines filled with a coolant, and of foam to insulate from the ambient air. As shown in Fig. 7.9, two thermal shields are introduced:

- Above the crystals, the module plate is cooled via a thin copper plate and serpentine tubes brazed on it. These tubes have a square cross section of  $10 \times 20 \text{ mm}^2$  to limit the height and keep enough insulating foam. This upper area, containing lots of services like flexible read-out cables and optical fibers, is filled with 50 mm of vermiculite granulate. The module plate and the insert are made of aluminum because of its good thermal conductivity and thus keep a good thermal transfer for the preamplifier and for the area up to the rear end of the crystal.
- For the front side of the crystals, a special thin thermal screen was developed, in order to reduce the distance to the DIRC for achieving a better resolution. Carbon fiber material is used for its low radiation length, in order to improve the transparency for particles, and for its negligible thermal expansion coefficient. This shield has a thickness of only 25 mm distributed in 4 mm of carbon coolant channels and in 21 mm of a vacuum super-insulating panel, respectively. Super-insulation is used in the cryogenic technology and is in our case 2.5 times more efficient in terms of thermal conductivity versus total thickness. The vacuum (0.03 Torr), however, is absolutely necessary and is contained between two skins linked with Rohacell blocks, a structural and vacuum tight foam. The warm side is aluminum, in order to homogenize the temperature and avoid

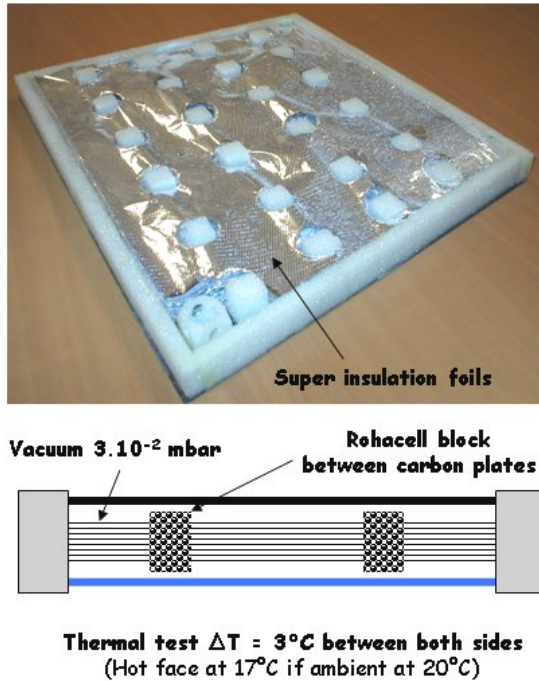


**Figure 7.15:** Front thermal screen.

local cold points in front of each Rohacell block, while the cold side is a skin of carbon material. Its low thermal expansion reduces the differential constraints between the two faces of the sandwich, which thus keeps a good flatness in any case. Fig. 7.15 shows the first sandwich structure constructed for the thermal and mechanical tests. Installed on prototype, it shows on its external face a satisfactory temperature variation of 3°C below room temperature.

The temperature on the sides of the slice is assumed to be constant at  $-25^\circ\text{C}$ , because of the adiabatic boundary condition with the neighboring slice at the same temperature. For reasons of protection, a 1.5 mm thick aluminum plate is inserted between two slices, which additionally improves the thermal cooling homogeneity. In fact, the insulation between slices is achieved at the level of the thermal shields.

The heat transfer through the thermal shields is the first external heat source of the cooling system. The definition of their thickness minimizes the heat transfer and the limit is to have their external faces at approximately room temperature (above the dew point). This criterium ensures that the internal temperature stability is nearly independent of the ambient air temperature variation. A ratio of 25 has been found from measurements performed with

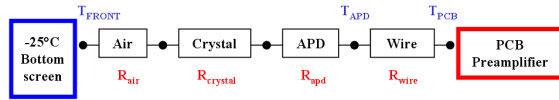


**Figure 7.16:** Equivalent chain for the analytical computation of the LAAPD temperature.

crystals in the prototype detector Proto60, which means that for an ambient temperature change of 1°C the internal temperature could vary by as much as 0.04°C without chiller regulation.

#### 7.1.4.4 Thermal Bridges

The second external heat source is introduced by the heat transfer through the mechanical supports and the metallic conductors of cables for the readout. In this conductive process, the section and the number of these thermal bridges have to be minimized. Design studies and simulations have been performed on the support feet in order to reduce the thermal transfer. Flexible long cables are preferred.

#### 7.1.4.5 Internal Heating of LAAPD and Crystal

The preamplifiers introduce an internal heat source in the calorimeter. Their total power consumption is 50 mW/channel, and due to the thermal impedance of their components (200°C/W maximum), the hottest point is +4°C higher. This heat produced is partially transferred by direct contact to the metallic support through its fixing screws or through the conductive silicone interface (Bergquist gap pad) put on top of the printed circuit board of the preamplifiers. But the heat propagates overall to the LAAPD connector, and therefore to the LAAPD itself through the twisted pair wire. The LAAPD temperature is calculated and settles at an equilibrium under the influence of the bottom thermal screen in front of the crystals. The analytical formula is given in Eq. 7.1 and is deduced from the crystal/LAAPD/preamplifier model illustrated in Fig. 7.16.

$$T_{apd} = T_{pcb} + R_{wire}^{th} * \frac{(T_{front} - T_{pcb})}{R_{air}^{th} + R_{crystal}^{th} + R_{apd}^{th} + R_{wire}^{th}} \quad (7.1)$$

From this equation, the calculated length of the twisted pair wire must be at least 150 mm in order

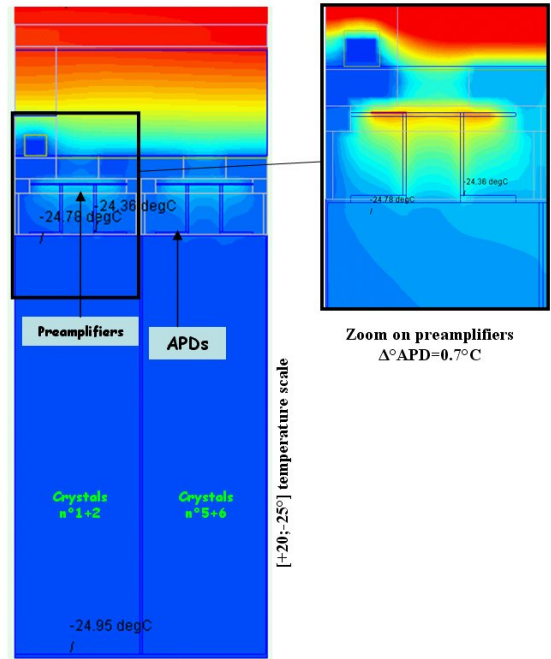


**Figure 7.17:** Thermal simulation with a preamplifier of 50 mW linked to the LAAPD with a 40 mm wire.

to have less than 0.1°C of temperature variation on the LAAPD. This length, however, is not compatible with the available space on top of the crystals and with the good electronics functioning where the preamplifiers have to be placed as close as possible. In the present design, the length is fixed to 40 mm, and the LAAPD temperature rises up to 0.7°C. Unfortunately, the temperature inside the barrel will not be uniform and the LAAPD stability will be dependent of the preamplifier power consumption which has to be stable in the order of 10%. The low thermal conductivity of PWO (see Table 7.2) attenuates any crystal temperature changes on a short timescale ( $\approx 10$  sec). The crystals are affected linearly, however, by their longitudinal temperature non-uniformity which, in fact as for the LAAPD, is corrected during the pre-calibration. Fig. 7.17 shows a simulation of the design model.

#### 7.1.4.6 Definition of the Cooling System

Three types of heat sources have been defined previously and are resumed in Fig. 7.18. The total power consumption for 16 slices is  $\approx 2600$  W. The external cooling circuit is subject to heat transfer, too, estimated to be  $\approx 700$  W. Finally, the cooling machine must have a minimum effective cooling capacity of 3300 W.

The coolant is SYLTHERM XLT from Dow Corn-

ing. This liquid is a high performance silicone polymer designed for use at low temperature. Compared with water/alcohol or with hydrofluoroether (used in ALICE/PHOS) fluids, it offers the best ratio based on the heat transfer versus pumpability due to its high specific heat and low viscosity. It has essentially no odor, and is not corrosive for long term use.

The design of the cooling circuit is taking in account the pump capacities, flow rate and pressure in order to optimize the flow and thus minimize the temperature variation along the longitudinal axis of the crystal. Inside a slice, the nominal flow is around 15 liters/min which gives a non-uniformity of  $1.1^{\circ}\text{C}$  between the inlet and the outlet. Two cooling machines, one for each half-barrel, will supply the barrel circuit, basically split into 4 parallel sectors.

The stability of the coolant temperature at the entrance of the barrel must be much better than the required stability in the barrel. A starting point for the specifications in the machine design is  $\pm 0.05^{\circ}\text{C}$  and a time reactivity of the order of tens of seconds. This value depends mainly of the quality of the cooling machine. Further studies will be performed and industrial solutions are foreseen to get the optimal reliability versus price ratio. The low thermal conductivity of the 20 tons of PWO material creates a very long time constant for the barrel. The expected time to reach the final temperature is several tens of hours.

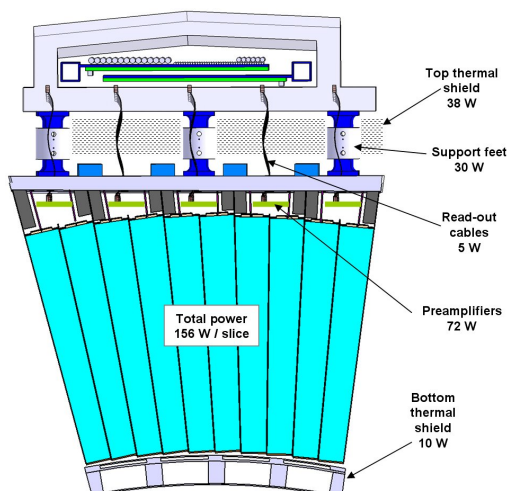


Figure 7.18: Cooling power summary.

#### 7.1.4.7 Read-out of the Temperatures

A slice is equipped with up to 50 thermal sensors placed in representative positions: along the length of the crystals, in the center or in the extremities of the slice, near the LAAPD, close to the thermal shields and in contact with inlet and outlet cooling tubes. Sensors are also placed externally, in the support beam to check the water regulation. In fact, the temperature measurement controls the stability of the calibration but also can return information about possible problems in the cooling system. All the thermal sensors will be cross-calibrated at the nominal temperature. Two types of thermal sensors are used: a) type T thermocouples working at low temperatures which give correct results for relative measurements and are thin enough to be inserted into carbon fiber alveoles, or b) a few Pt100 sensors installed in parallel to give a better absolute value. The data acquisition is performed reliably and cheap with a commercial system at a frequency of one readout per several minutes.

#### 7.1.4.8 Air-tightness Studies and Risk Analysis for Low-temperature Running

The condition for a feasible operation at low temperature is to avoid any ice generation as well inside as outside of the calorimeter. If this would not be achieved, the ice could introduce water at reheating of the detector or could break the crystals by ice pressure between the crystals. The method is to remove the humidity of the air by circulating a dry gas like nitrogen inside an air-tight envelop surrounding all the calorimeter. The continuity of this sealing is kept at the boundaries with a feed-through like those used for electrical or supply connectors. This envelop is mainly made with plastic covers wrapped with a special industrial thick adhesive developed for long term domestic gas sealing. For the outside part, the method is to avoid any temperature lower than the dew point (around  $12^{\circ}\text{C}$ ) on the structure like on the external cooling tubes or on the mechanical supports for instance. Thermal studies are done on every critical part and massive parts at room temperature are used in order to equilibrate the low temperature transferred by conduction. From a risk analysis the following 2 difficulties arise:

- Danger for the calorimeter in case of ice and moisture: if the dry gas is not completely well circulating or if humidity remains after any switch off of the dry gas circulation. Humidity

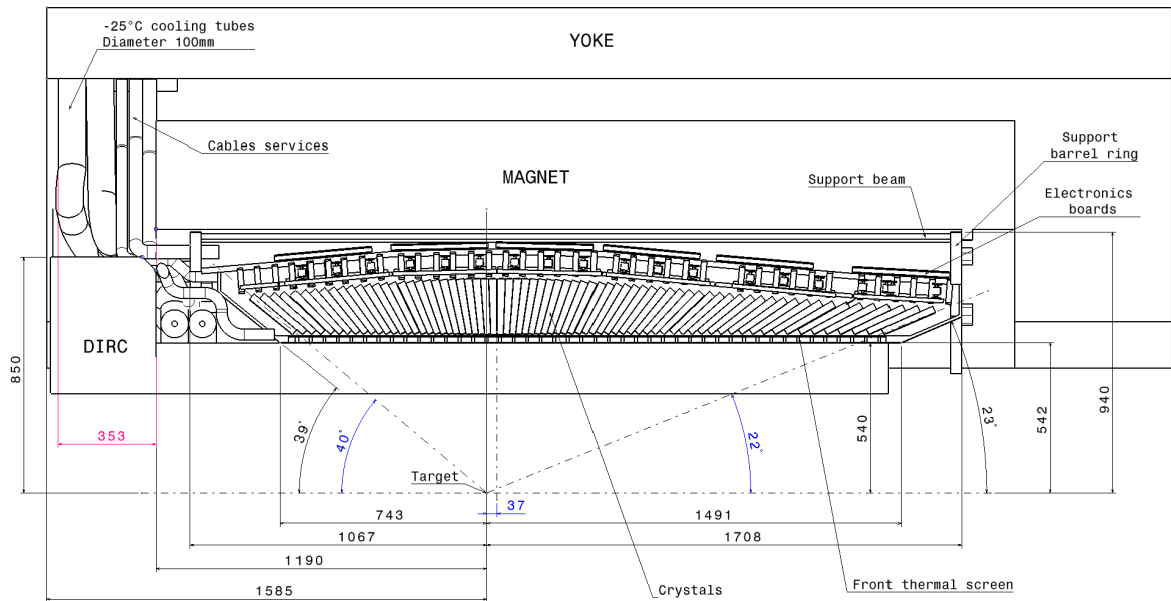


Figure 7.19: Dimensions and volume of one slice.

sensors can provide some information on the quality of the atmosphere. A break of the air-tightness envelop can lead to ice, too, and even alter the quality of the thermal shields.

- Danger for the other detectors if the thermal shields break. The cold can reach the outside sides and put moisture and water in the target spectrometer.

The Proto60 crystals have shown the feasibility of this air-tightness envelop. Thermal studies and risk analysis will continue and be performed with the next prototype of 480 crystals to improve the reliability and define the emergency procedures. Fig. 7.20 introduces the CAD design of this set-up which will be available in summer 2008. It integrates all the components of a slice in their final shape (e.g. support feet, front thermal shield). It is equipped with stainless steel dummy crystals for cost reasons but should exhibit the same thermal behavior.

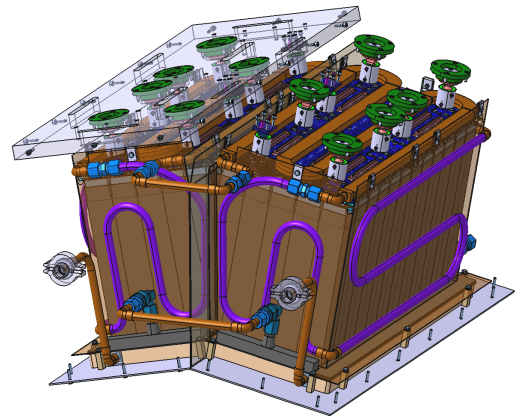


Figure 7.20: Next thermal prototype 480.

a total flow of 65 liters/min. This level of requirements can be found in standard industrial systems.

#### 7.1.4.9 Room Temperature Stabilization for the Electronics

The electronics is dissipating 560 W/slice and is mounted on copper plates brazed to cooling tubes (see Fig. 7.14). Water flows inside the tubes to regulate the support beam at approximately room temperature ( $\pm 2^\circ\text{C}$ ). The machine must have a minimum effective cooling capacity of 9 000 W, and

#### 7.1.5 Integration in the $\bar{\text{P}}\text{ANDA}$ Target Spectrometer

Fig. 7.19 defines the complete volume of the barrel. The overall dimensions are required for the integration of the neighboring detectors. The total mass is  $\approx 20$  tons composed of 11 tons of crystals and 7 tons of support structure. The services are going out

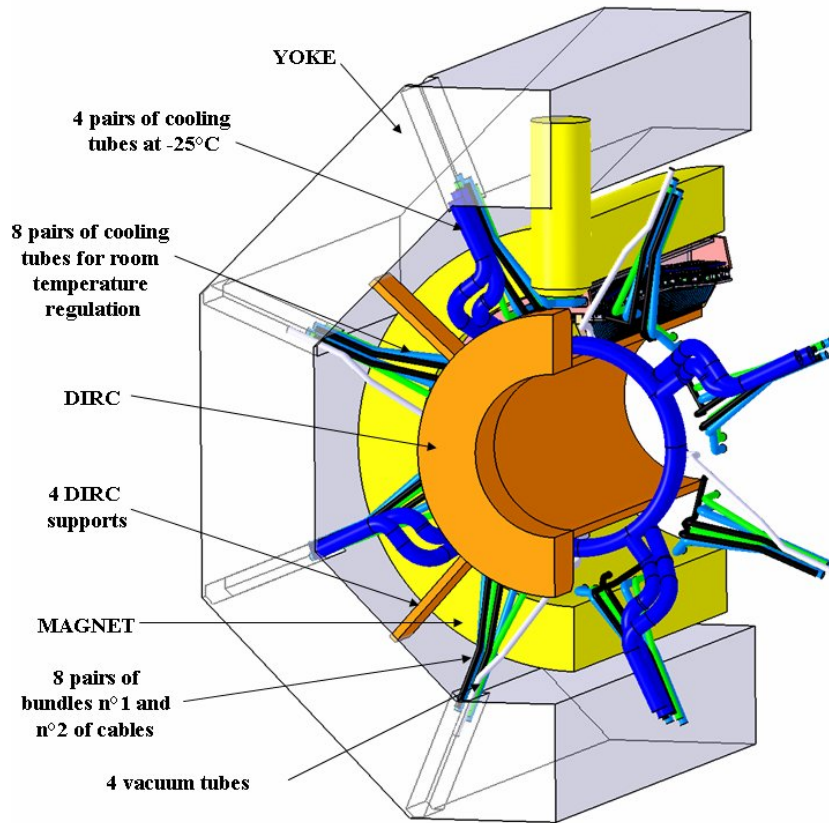


Figure 7.21: Services going outside the barrel into the corners of the octagonal yoke.

Service	Detail	$\varnothing$ (mm)	Qty.
Bundle 1	High/Low volt. ADC supply optical fibers	50	16
Bundle 2	Gas, humidity/ temperatur sensors calibr. opt. fibers	40	16
Tube 1	Water 20°C	50	16
Tube 2	Coolant -25°C	105	8
Vacuum		50	4

Table 7.3: List of services in the backward area.

of the slices in the backward area and afterwards through the corners of the octagonal shape of the yoke as shown in Fig. 7.21. A list of services and respective details is given in Table 7.3.

### 7.1.6 Construction of the Slices and Assembly of the Barrel

This report presents the design of a slice. A preliminary mounting sequence is proposed here:

1. Gluing of LAAPD onto crystals (after control and reference measurements).
2. Wrapping of crystals.
3. Insertion into alveoles. Installation of thermal sensors between crystals. Gluing of the insert after having controlled the good functioning of the LAAPD with twisted pair wire.
4. Assembly of the alveole pack on the module plate. Installation of the guiding tube for the optical fiber. Fixing the preamplifier. Control of the alignment.
5. Mounting of the modules plates on the main-frame tool (as in CMS). Adding top and bottom cooling circuit. Adding calibration optical fibers. Checking of the keep in volume and alignment. Mounting the support feet and spreading the insulation.

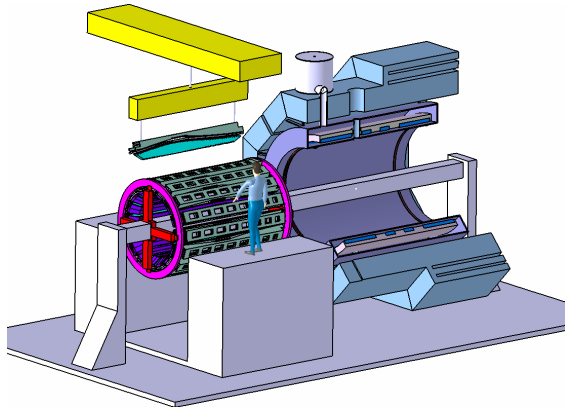


**Figure 7.22:** Barrel final mounting.

6. Put the support beam. Connecting flexible cables to the boards and adding all electronics. First-level air sealing.
7. Transfer the slice to its support for storage and shipment and for the support with insulation sides to cool it down. This prepares the test with cosmic muons.
8. Mount the rings on the rolling mounting tool. Then mount the slices one by one.

To perform all these tasks, special tools need to be designed and manufactured. The construction of the first prototype of a slice is foreseen and will validate this sequence.

The construction of a single slice and the assembly of the complete barrel require a large amount of manpower, installation space and time for testing. The production time is of the order of 3 or 4 years and will need a good coordination between the different laboratories.

#### 7.1.6.1 Final Assembly of the Barrel

Each slice is installed one by one on the two support rings and a special rolling system (as in CMS) can be used. Fig. 7.22 presents a sketch of the mounting sequence of the barrel. Once the barrel is complete, tested and air-tight insulated, it can slide to its final position on a stable central beam going through the PANDA detector.

## 7.2 Forward Endcap

### 7.2.1 Requirements

The envisaged physics program of PANDA requires measurements of photons and charged particles with good position and timing resolution over a wide dynamic range from a few MeV up to several GeV energy. The electromagnetic calorimeter of PANDA comprises the barrel EMC, the forward endcap EMC, and the backward endcap EMC, see Fig. 7.1.

The forward endcap EMC is designed as a wall structure with off-pointing projective geometry, i.e. the crystals are oriented to a point on the beam axis which is located at a certain distance (in this case 890 mm) away from the target. This arrangement guarantees that particles originating from the target will never pass exactly along the boundaries between two neighbouring crystals where they could remain undetected. Since at the same time quadrant symmetry is required, this condition can not be maintained for the boundaries between the four quadrants of the forward endcap EMC which will be oriented along the lines  $(x,y=0)$  and  $(x=0, y)$ .

In order to catch electromagnetic showers completely at the boundary between the Barrel and the forward endcap EMC, the acceptance of the forward endcap EMC must foresee one full crystal overlap with the Barrel. The acceptance is limited at the most forward angles by the space required for the forward magnetic spectrometer. This defines the outer opening angle to be  $< 23.6^\circ$  and the inner opening angle to be  $> 5^\circ$  in vertical and  $> 10^\circ$  in horizontal direction.

Simulations performed at 15 GeV (see Sec. 4.1.2) indicate that the particle rates per calorimeter cell with a detection threshold of 3 MeV reach 500 kHz at the smallest angles and still amount to 100 kHz at the largest angles. Because of these high rates and the increased risk of radiation damage the large-area avalanche photodiodes (LAAPD), foreseen for the Barrel, will be replaced by vacuum phototriode (VPT) photosensors in the forward endcap EMC. From two production sites VPT's are available with an outer diameter of 22 mm. This size can be accommodated on a crystal with a rear cross section of  $26 \times 26 \text{ mm}^2$ , while still maintaining the condition for optimum position resolution, namely an average crystal width of about one Molière radius (20 mm for PWO). The forward endcap EMC will contain PWO crystals (PWO-II) of 200 mm length, which is equivalent to 22 radiation length and sufficient for 95% containment of the maximum expected photon

energy of 15 GeV.

### 7.2.2 Crystal shape

In the forward endcap EMC the crystals are closely packed in "off-pointing" geometry, i.e. oriented towards a point on the beam axis 950 mm farther than the target and 3000 mm away from the front face of the crystal plane. The off-pointing geometry is illustrated in Fig. 7.23. The ratio of target distance to off-pointing distance has been chosen such that the angle of incidence of particles on the crystal front face is minimally  $1.6^\circ$  with respect to normal incidence. This arrangement guarantees that particles originating from the target will never pass more than 15% of the crystal length in the gap between two neighbouring crystals. Including photo sensors, front-end electronics, cooling and insulation, the overall depth of the forward endcap EMC will amount to 430 mm. The off-pointing geometry and the VPT diameter determine that each crystal has a front-face of  $24.4 \times 24.4 \text{ mm}^2$ , see Fig. 7.24. In order to save costs for cutting and polishing crystals, each crystal will be shaped with two tapered and two right-angled sides. A cluster of 4 crystals, touching at the right-angled sides, thus forms a mini-unit of trapezoidal cross section, mounted in a single carbon-fiber alveole with 0.18 mm wall thickness. The crystals should be manufactured with tolerance of  $+0/-0.1 \text{ mm}$  in all transversal and longitudinal dimensions. An angular precision of  $< 0.01^\circ$  will be requested while a planarity within 0.02 mm should be maintained for all faces with chamfers between 0.5 and 0.7 mm. All surfaces will be polished with roughness  $R_a < 0.2 \text{ mm}$ .

### 7.2.3 Subunit Structure

Since PWO crystals are very fragile, they must not be exposed to bending- or shear forces. Therefore crystals are mounted in frames made from composite material (carbon fiber alveoles) which are designed to absorb tolerances in crystal dimensions and accommodate the thickness of the light-reflecting foils ( $100 \mu\text{m}$ ). Four mini-units of crystals will be combined to form a 16-crystal subunit of ca. 19 kg that can be attached individually to the 30 mm thick aluminum mounting plate. Fig. 7.25 shows the alveole wall thickness and the space foreseen between crystals. The front face of the alveole will be covered with 1 mm thick composite C-fiber/epoxy material. The company FiberWorx B.V. (Netherlands) has designed, engineered and prototyped a C-fiber alveole for 16 crystals.

Loaded with the weight of the crystals the alveole material is requested to stretch less than 1.5%. The proposed and prototyped design results in a maximum stretch of 0.04%, which results in a comfortable safety factor of 30. Fig. 7.26 shows three C-fiber alveoles produced according to the above given specifications.

The alveoles carrying 16 crystals will be mounted individually to the aluminum backplane without touching the neighboring alveole. For this purpose aluminum inserts will be glued into the rear part of the alveole downstream of the crystal, thus allowing a good thermal contact, providing a rigid support for the VPT photosensor, and creating a mounting structure for the backplane. Fig. 7.27 shows the explosion view of a subunit housing 16 crystals, VPT and inserts. In Fig. 7.28 is demonstrated how the subunits will be attached to the mounting plate using angled interface-pieces which allow a precise arrangement. In total 3520 crystals will be mounted in this way in  $4 \times 4$  subunits, and 80 crystals in smaller  $2 \times 2$  subunits in order to approach as much as possible a homogeneous coverage between minimum and maximum acceptance angle of the forward endcap EMC. Optionally, for even larger coverage at the expense of more specific alveole development, an additional number of ca. 40 subunits housing only 1 or 2 crystals is being considered.

Preliminary thermal calculations indicate a temperature gradient in the crystal of ca.  $4^\circ\text{C}$  if only the mounting plate will be cooled. Presently a prototype setup for 16 crystals is being constructed in order to test the mechanical accuracy, the thermal properties and photon response in photon-beam experiments.

#### 7.2.3.1 Mounting Structure and Implementation in the Solenoid

One quadrant of the forward endcap EMC houses 900 crystals in subunits of mostly 16 and occasionally 4 crystals. The arrangement as seen from the target is shown in Fig. 7.29. The backplane is constructed from 30 mm thick aluminum with elliptic holes at the center of every alveole in order to feed the cables from the front-end electronics to the downstream part of the mounting plate and from there to the circumference of the forward endcap EMC structure.

The total weight of the forward endcap EMC will amount to ca. 5100 kg. For the design of the mounting plate the stiffness is the most important criterion. The loads acting on the mounting plate are

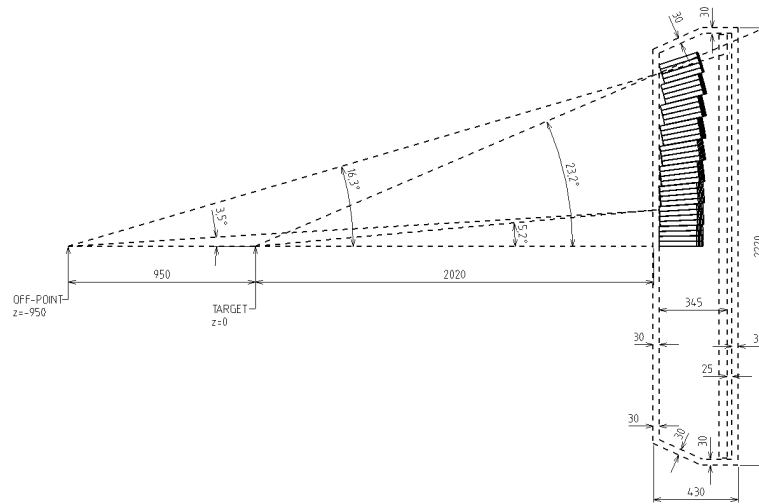


**Figure 7.23:** The position of the forward endcap EMC with respect to the target.

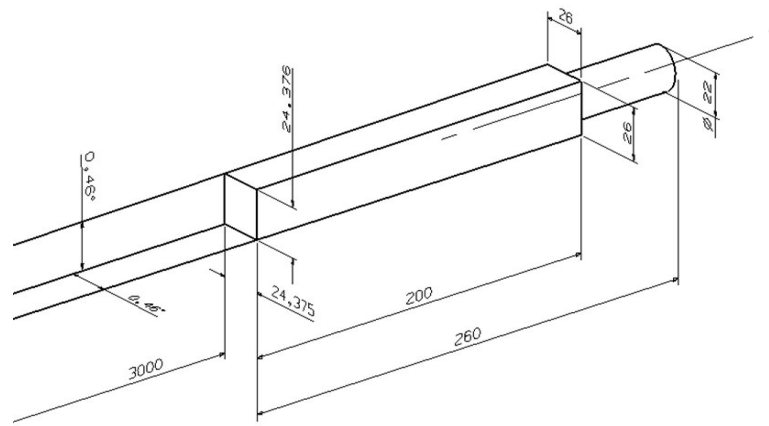


**Figure 7.24:** The geometry of a single forward endcap EMC crystal.

the gravity and the moment caused by the center of gravity of the crystals attached in front of the plate. In its final vertical position the maximal Von Mises stress is ca. 20 MPa which results in a maximum deflection of 0.23 mm.

The endcap mounting plate will shrink by 0.16 mm per row or column of subunits at the operation temperature of  $-25^{\circ}\text{C}$ . With 18 rows and columns of subunits, there are 17 gaps in between in horizontal and vertical direction. Per gap a space has to be reserved of approximately 0.16 mm in order to absorb shrinking or expansion. In addition we have to take into account that the magnetic field of the solenoid will cause deflections of the mounting structure. It is foreseen that the forward endcap EMC will be

completely constructed outside the  $\bar{\text{PANDA}}$  area, inserted into the downstream part of the solenoid magnet yoke, and held in place by 8 holding arms inside an octagonal frame structure. This structure must be able to absorb a shrinking or expansion of maximally 3 mm.

### 7.2.3.2 Insulation and Cooling

For the thermal insulation of the crystal area at  $-25^{\circ}\text{C}$  from room temperature, a space of 30 mm is reserved for a layer thermal-insulation foam. Detailed thermal calculations are needed and have been started in order to determine the required cooling power and shielding material. Preliminary

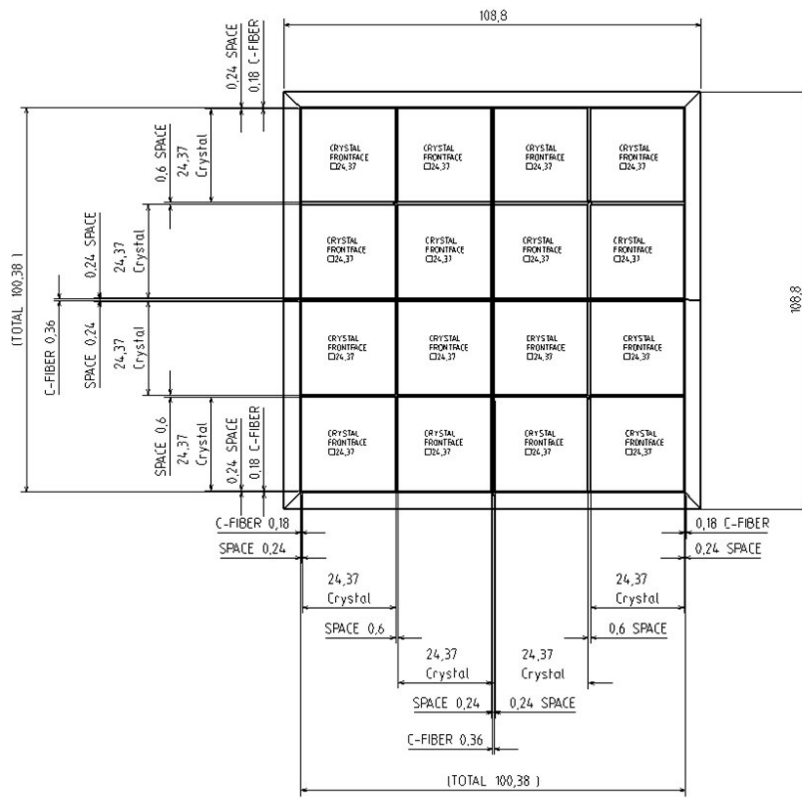


Figure 7.25: The geometry of a C-fiber alveole for 16 crystals.

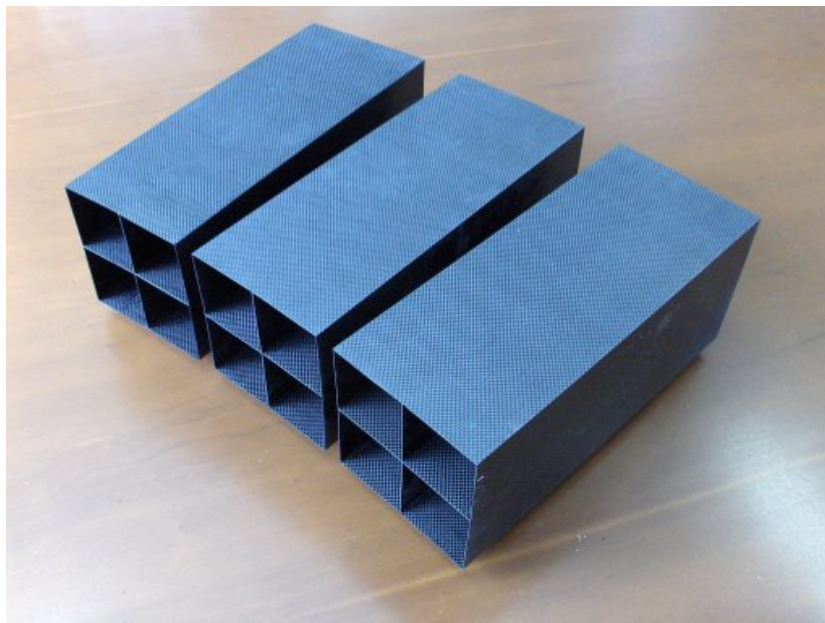
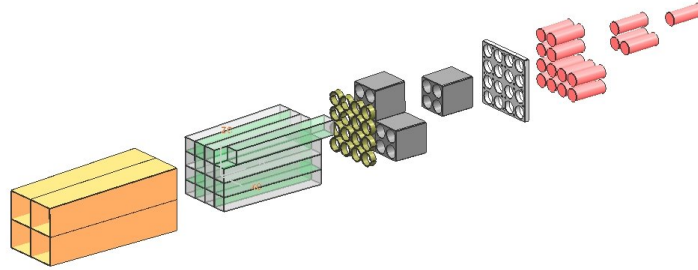


Figure 7.26: Photograph of three produced C-fiber alveoles for 16 crystals each.

calculations and experience with the Barrel proto-  
type indicate, that the crystals also need cooling

from the front side in order to avoid a temperature  
gradient in the crystal. However, maintaining a sta-



**Figure 7.27:** The explosion view of a 16-crystal subunit.

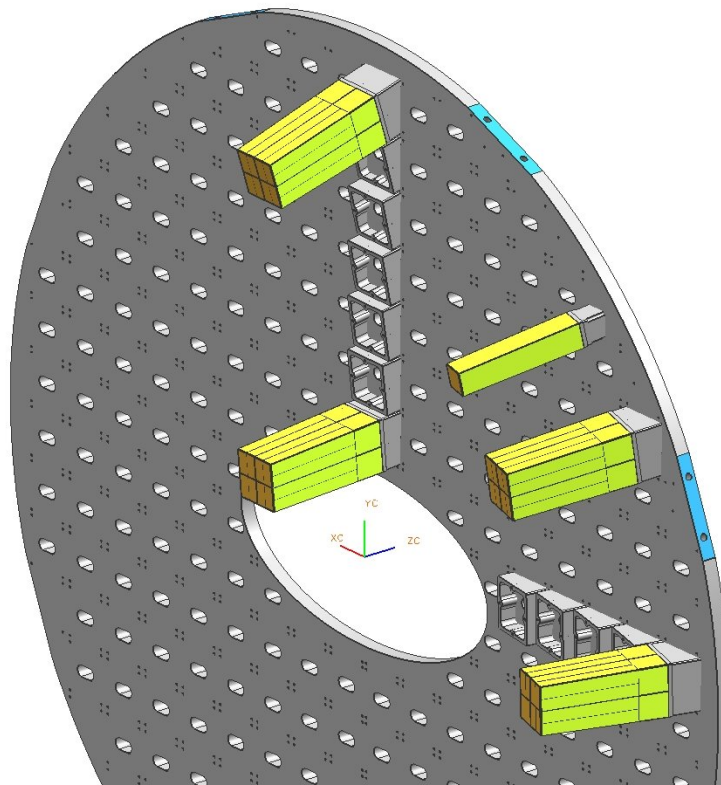


**Figure 7.28:** The attachment of the C-fiber alveoles in front of the mounting plate using angled interface pieces.

tionary temperature gradient will be investigated, since the corresponding gradient in light production could compensate inhomogeneities due to light collection in a tapered crystal. This method would avoid an expensive and time consuming "depolishing" treatment of the crystal surface. Cooling at

the front side of the crystal wall could be achieved by cooling a thin (ca. 2 mm) carbon plate in front of the crystals. A flow of cooled dry  $N_2$  gas inside the insulated volume would support an homogeneous cooling of the crystal volume. To prevent ice forming around the crystals, dry  $N_2$  gas will be

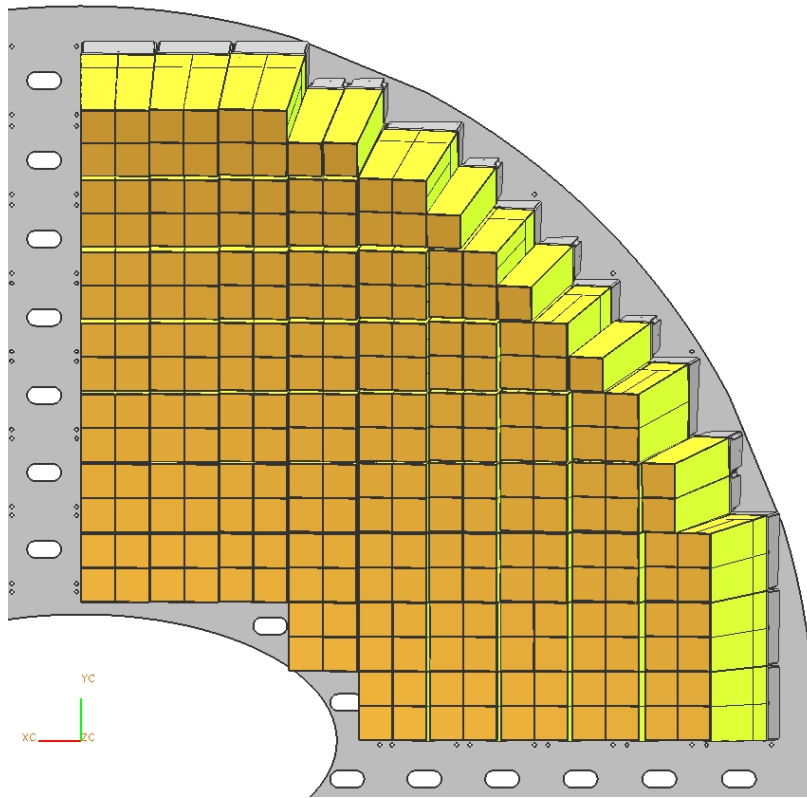


**Figure 7.29:** One quadrant of the  $\bar{P}$ PANDA forward endcap calorimeter.

supplied to the individual alveoles by gas pipes inserted through the cable-feedthrough holes in the mounting plate. Fig. 7.30 shows part of the thermal insulation cover and the holding structures to facilitate the mounting inside the solenoid.

It is foreseen to embed four separate cooling circuits into grooves in the downstream part of the mounting plate. The total cooling circuit will consist of a meander of 10 mm diameter cooling pipes with a length of 56 m.

### 7.2.3.3 Sensors and Front-End Electronics

The crystals of the forward endcap EMC will be equipped with VPT's as photosensors for which a gain of 30 to 50 is expected. Development of a highly sensitive VPT with super-photocathode and quantum efficiency above 40% is in progress. A Low Noise / Low Power (LNP) Charge Pre-amplifier has been developed on basis of the equivalent LNP preamplifier for LAAPD readout. The output pulse is transmitted via a 50  $\Omega$  line to the subsequent digitizer module electronics at the circumference of the forward endcap EMC. The LNP-Preamp has a qui-

escent power consumption of 45 mW and is suited for operation in the cooled volume. It is foreseen to attach the preamplifier directly to the VPT on the upstream side of the mounting plate.

### 7.2.3.4 Cabling and Supplies for Monitoring

For signal transmission from the VPT preamplifier to the digitizer electronics a multi-pin flexible laminate cable of .15 mm thickness is foreseen. Q.P.I. BV Netherlands is able to produce a double-sided, copper-clad all-polyimide composite (Pyr luxAP). This is a polyimide film bonded to copper foil. Fig. 7.31 gives the relation between impedance and conductor width and allows to make a suitable choice for 50  $\Omega$  signal transmission.

### 7.2.3.5 Arrangement of Readout Electronics

The digitizing electronics will use sampling ADC's for signal-shape analysis and timing determination and will be located near the detector in the warm

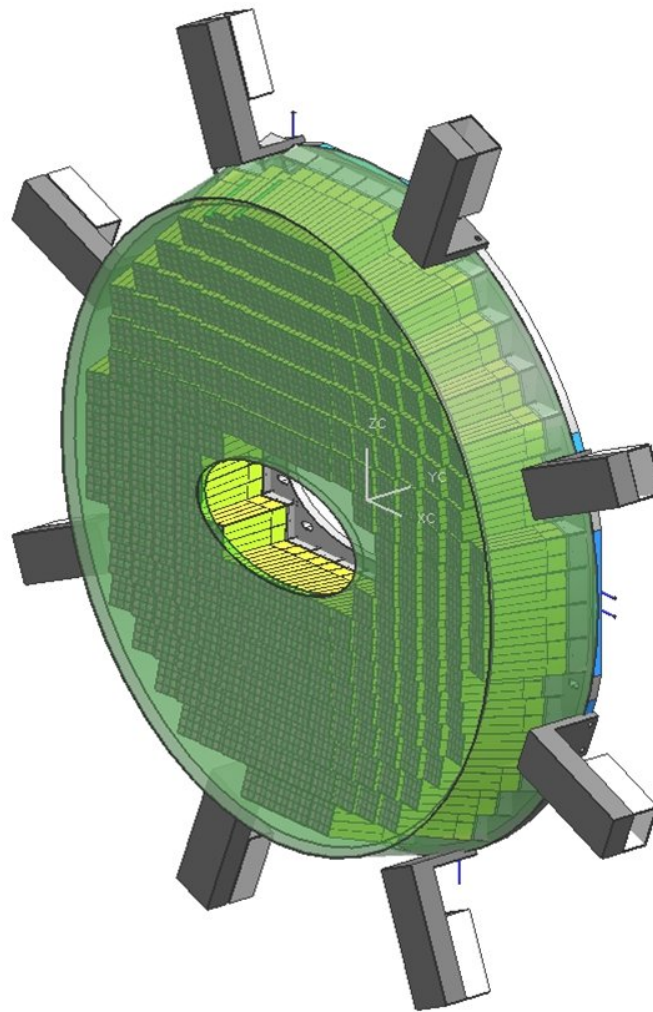


**Figure 7.30:** The complete endcap with thermal insulation cover and holding structures.

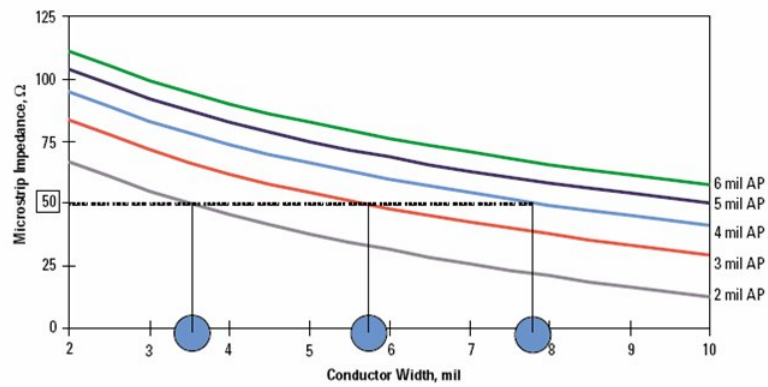


**Figure 7.31:** Impedance of laminate cable as function of conductor width.

volume inside the solenoid magnet. From there signals can be transmitted via optical link to multi-

plexer units and compute nodes outside the PANDA experimental area. With commercial components

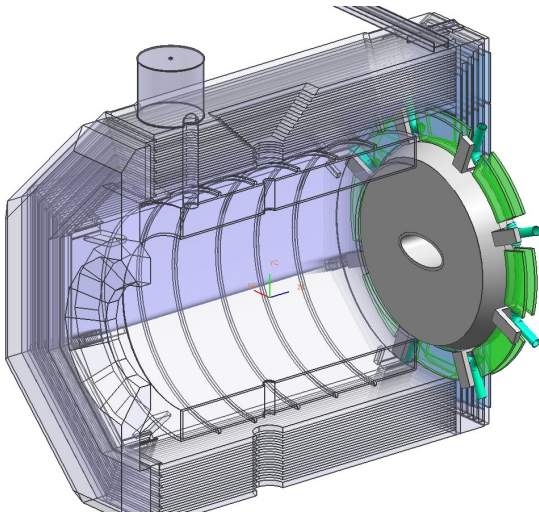


**Figure 7.32:** Arrangement of Digitizer modules at the circumference of the forward endcap EMC.

an ADC channel density of about  $300 \text{ mm}^2/\text{channel}$  can be reached. This means that per octant of the forward endcap EMC an area of  $3200 \text{ cm}^2$  must be available. Between the circumference of the forward endcap EMC mounting plate (radius =  $1050 \text{ mm}$ ) and the inner boundary of the solenoid (radius =  $1450 \text{ mm}$ ) a surface area of maximally  $2000 \text{ cm}^2$  is available. Thus with a sandwich of two ADC boards there is sufficient space available for accommodating the digitizing electronics. Fig. 7.32 shows the position of the endcap inside the solenoid structure and the space available at the forward endcap EMC circumference for arranging the electronics boards in a sandwich layer. In addition, the 8-fold mounting structure is indicated and the routing of cables and cooling pipes.

### 7.3 Backward Endcap of the Calorimeter

The backward endcap EMC is required in order to complete the hermetic coverage of the target spectrometer EMC for electromagnetic energy, with exception of the beam entrance and the acceptance of the forward spectrometer. As shown in Fig. 4.3, at polar angles above  $135^\circ$  the differential rates per crystal are about  $1 \text{ kHz}$  per  $20 \text{ MeV}$  at energies of  $50 \text{ MeV}$  and the maximum energy deposition is about  $200 \text{ MeV}$ . Since both endcaps require an almost planar arrangement of crystals, the basic design concept of the forward endcap EMC has been chosen also for the backward endcap EMC. This

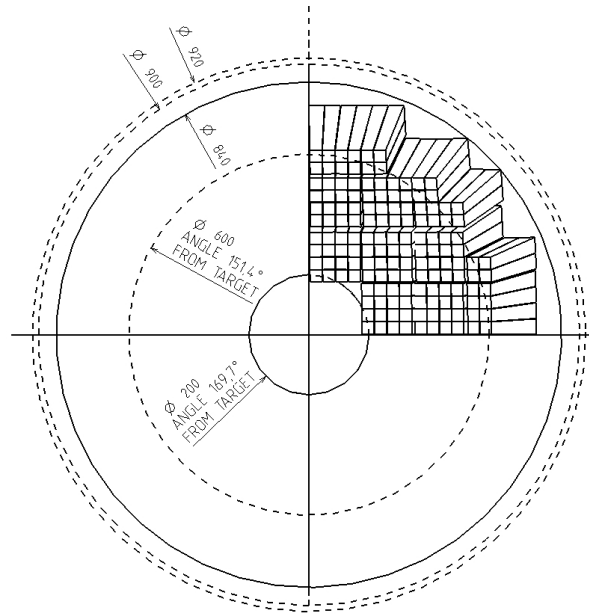


**Figure 7.33:** Acceptance of the backward endcap EMC.

approach simplifies the mechanical construction of crystals and submodules and creates synergy in the application of photosensors and readout electronics. In addition, the readout with VPT is superior in timing performance at the low energies expected in the backward region which allows efficient reduction of background. Since design and development work on other detectors in the surrounding of the backward endcap EMC is still in progress, the mechanical constraints are not yet defined well enough, so that the integration in PANDA could not yet be specified in detail. In Fig. 7.33 the angular acceptance is presented which is allowed by the radial space available inside the target spectrometer EMC and the distance of  $550 \text{ mm}$  of the crystal front face to the target (see Fig. 7.2). The maximum opening diameter is  $920 \text{ mm}$ . Allowing  $20 \text{ mm}$  for tolerances and mounting space and  $60 \text{ mm}$  for thermal insulation, we arrive at  $840 \text{ mm}$  maximum diameter of the mounting plate to which the readout end of the crystals is attached. The inner hole of  $200 \text{ mm}$  diameter of the backward endcap EMC is determined by the beam pipe and a safe distance to prevent disturbance from beam halo. This defines the maximum polar angle of  $169.7^\circ$ . The tilting of the crystals due to the off-pointing projective geometry, oriented towards a point  $200 \text{ mm}$  farther than the target, determines the minimum polar angle of  $151.4^\circ$ . The off-pointing geometry is illustrated in Fig. 7.34. The same ratio of target distance to off-

pointing distance has been chosen as for the forward endcap EMC. Including photo sensors, front-end electronics and insulation, the overall depth of the backward endcap EMC will amount to 430 mm.

The geometry of a single crystal is shown in Fig. 7.35. Given the cross section of  $26 \times 26 \text{ mm}^2$  of the readout face to accommodate the VPT, the front face of each individual crystal will result under the given geometrical conditions in  $20.5 \times 20.5 \text{ mm}^2$ . The overall dimensions are close to the average dimensions of the barrel crystals. The arrangement of individual crystals in one quadrant of the backward endcap EMC is shown in Fig. 7.36. As for the forward endcap EMC, the size of the carbon fiber alveoles, the tolerances and the configuration in subunits of  $4 \times 4$  or  $2 \times 2$  crystals has been chosen. The optimum coverage of the available geometrical acceptance is achieved with 7 subunits of 16 crystals and 9 subunits of 4 crystals. This results in 148 crystals per quadrant and 592 crystals for the whole backward endcap EMC. The provisions for nitrogen gas flow and cooling will be arranged as in the forward endcap EMC. Due to space restrictions, the Digitizer modules can not be attached to the mounting plate, but will be positioned further upstream between the upstream barrel part and the solenoid yoke.

## References

- [1] B. Aubert. et al., Nucl. Instrum. Meth. **A479**, 1 (2002).
- [2] CERN-LHCC-97-33.
- [3] CERN-LHCC-99-4.
- [4] P. Rosier, R&D Detection - IPN Orsay, France, internal report RDD 2004-02, 2004.

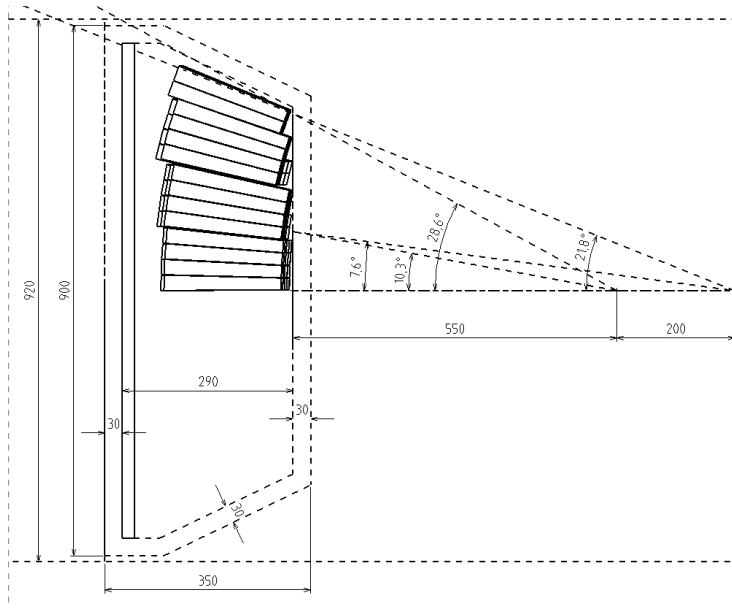


**Figure 7.34:** The position of the backward endcap EMC with respect to the target.

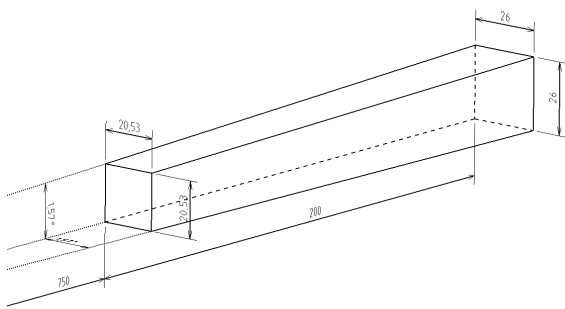


**Figure 7.35:** The dimensions of a single crystal of the backward endcap EMC.

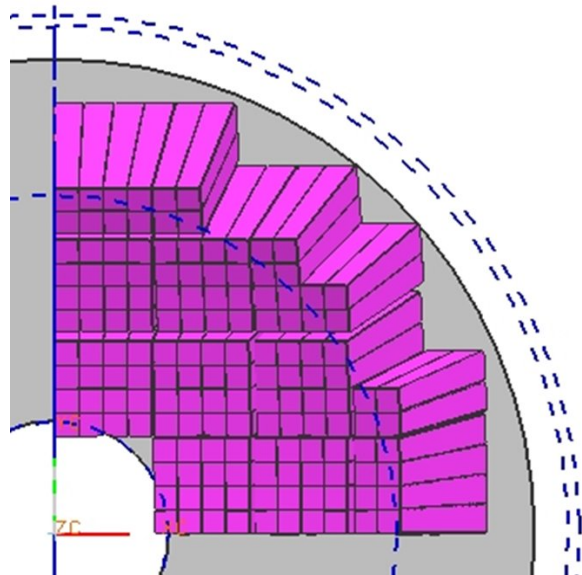


**Figure 7.36:** The geometry of one quadrant of the backward endcap EMC.

## 8 Calibration and Monitoring

---

To achieve the required energy and spatial resolution of the electromagnetic calorimeter it is essential to precisely calibrate the individual crystal channels. Time dependent variations of the calibration factors are expected due to several effects: change in light transmission, change in the coupling between the crystal and the photodetectors and variations in the photodetectors itself and the following electronics. Both the scintillation of the crystals and the amplification of the APDs depend on the temperature. Therefore stable cooling at the level of  $0.1^\circ\text{C}$  is required. Long term variations in the temperature need to be tracked by the calibration. Given an energy resolution between 1% and 2% at energies above 1 GeV, the precision of the calibration needs to be at the sub-percent level.

For the calibration several methods performed in stages are planned:

- Precalibration at test beams and with cosmic muons at the level of 10%
- In situ calibration with physics events (neutral mesons and electrons)
- Continuous monitoring with a light-pulsar system

They are discussed in the following subsections.

### 8.1 Calibration

#### 8.1.1 Calibration with Physics Events

Based on the present experience with the temperature sensitivity of the complete detector elements including the crystal and the photosensor, a final in-beam calibration of the whole calorimeter does not appear appropriate. All calibrations have to be performed using the complete setup operating at the final temperature.

Therefore energy calibration of each crystal channel will be performed in situ with physics events. Low multiplicity events with  $\pi^0$  and  $\eta$  decaying into two photons will be selected. The constraint on the invariant mass  $m_{\text{meson}}^2 = E_{\gamma_1} E_{\gamma_2} (1 - \cos\theta_{12})$  gives corrections to the reconstructed photon energy in the crystal channels of the well separated clusters

$\gamma_1$  and  $\gamma_2$ . After a few iterations all calibration constants are available with a sufficient precision. The precalibration of the crystals with cosmic muons will provide the initial seed to start the procedure for the first time. The method was applied successfully at the Crystal Barrel experiment. There 1.2 million  $\bar{p}p$  events with up to 8 photons in the final state (mainly  $\bar{p}p \rightarrow 3\pi^0$ ) were used to calibrate 1380 crystals [1, 2].

For a full calibration of the  $\bar{\text{P}}\text{ANDA}$  electromagnetic calorimeter a total number of about  $5 \cdot 10^7$  events are required. It is essential to select low occupancy channels to avoid the overlap of clusters in the electromagnetic calorimeter. The channels  $\bar{p}p \rightarrow \pi^0\pi^0\pi^0$  and  $\bar{p}p \rightarrow \pi^0\pi^0\eta$  have a cross section of about  $30 \mu\text{b}$ , thus producing 4200 events per second at a luminosity of  $10^{32} \text{ cm}^{-2}\text{s}^{-1}$  ( $\eta \rightarrow \gamma\gamma$  only). Having a dedicated software trigger, calorimeter calibration data will be produced at a rate of about 4 kHz. The selection of the events with completely neutral final states makes the calibration independent of any other detectors and thus quickly to perform.

With the available statistics it is expected that a calibration can be performed once a day.

Variations of the calibration for shorter timescales than required for the calibration will be tracked by the monitoring system.

#### 8.1.2 Precalibration with Cosmic Muons and at Test Beams

The absolute geometrical position of the individual calorimeter elements has to be deduced from the mechanical design. The point of impact of the photon relies on the reconstruction of the electromagnetic shower and primarily on the appropriate mathematical algorithm, which will be optimized for the prototype arrays. The optimal position reconstruction algorithm depends on the point of impact and will be evaluated with full size prototypes at test beams.

The precise calibration of the calorimeter by using the constraint on the  $\pi^0$  and  $\eta$  mass relies on a precalibration at a 10% level. Before the final assembly of the calorimeters all submodules will undergo a check and precalibration with cosmic muons. Part of the submodules will be subject to beam tests to verify the precalibration and the position recon-

struction algorithms. The final precalibration of all crystal channels will be performed in situ with cosmic muons. This will be done before the startup with physics beam and at the final and stable temperature. Depending on the position relative to the earth surface different energies are deposited by the minimum ionizing particles. Even for upward pointing crystals enough statistics will be reached within one day of dedicated running. Due to the hardware-trigger-free concept of the  $\overline{\text{PANDA}}$  DAQ system it is easy to set up algorithms to store all relevant events by requiring certain cuts on energy depositions in neighboring crystals. The precision of the calibration will be verified at test beams by comparing the calibration obtained with cosmic muons to the calibration with defined photon energies. The CMS experiment has obtained a precision of 2.5% with the calibration of PWO with muons. It is expected that the resulting precision at  $\overline{\text{PANDA}}$  will be better than 10%, enough for the final calibration with physics events.

### 8.1.3 Online Calibration

The hardware-trigger-free concept of the  $\overline{\text{PANDA}}$  DAQ system requires the availability of calibration data at real time. The trigger decision is taken by software operated on compute nodes where full event information is available. For efficient triggering with the EMC it is therefore essential to have reasonable calibration constants available, to perform a quick analysis of the event.

The calibration constants can be determined once a day by the algorithm described in Sec. 8.1.1. The compute nodes filter the events where only calorimeter information and no charged track is seen. In addition a cut on 5 to 8 clusters and a minimum cut on the total energy are performed. These filtered events are stored for the calibration. Variations on the timescale of minutes and hours are detected by the light monitoring system (Sec. 8.2). Each crystal is flashed 100 times per minute by the light pulser. The data is evaluated on the compute nodes online and variations in the light transmission are measured every minute. These are applied to the calibration constants determined before.

## 8.2 Monitoring

The monitoring system provides a reference to identify and record any changes of the coefficients for the energy calibration of all calorimeter cells. The response can shift due to changes of the lumines-

cence process and the optical quality of the PWO crystals, the quantum efficiency and gain of the APD, and of the preamplifier/ADC conversion gain, for example. These effects can originate from temporary and permanent radiation damages and/or temperature changes. Due to extensive research on the radiation damage of PWO carried out during the last decade it was established that the luminescence yield of PWO crystals is not affected by irradiation, only the optical transmission. Any change of transparency can be monitored by the use of light injection from a constant and stabilized light source. The system will be based on light sources at multiple wavelengths. The monitoring of the radiation damages will be performed at low wavelengths (UV/blue to green, 455 nm and 530 nm). With light in the red region at 660 nm, a wavelength where radiation damages play no role, the chain from the light coupling to the photosensitive detector and the amplifier digitization can be monitored. The wavelengths, which are used for monitoring purposes, are indicated in Fig. 8.1 together with the induced absorption of radiation damaged PWO crystals. The value of 455 nm corresponds to the closest available LED with respect to the peak of the PWO emission. The concept to be used depends on the time scale when these deteriorations appear. As outlined in Sec. 3.2.2.3 the expected dose rate will stay well below the values expected for CMS operation. Therefore, one can assume that the possible degradation of the optical performance will evolve gradually and very slowly in time. In that case, trends and corrections can be deduced from kinematic parameters such as invariant masses calculated off-line. To avoid photon conversion in front of the calorimeter, the overall thickness of dead material has to be minimized. Mechanical structures for support or cooling should be installed as close as possible to the crystal front face. A system of optical fibers for light injection from the front side is excluded due to the space needed to cope with the large bending radius of fibers. Injecting light from the rear with reflection at the front side back to the photosensor is possible. However, the effects due to enhanced multiple scattering must be studied. The temperature gradient of the luminescence yield of PWO, which varies due to temperature quenching between 2 and 3%/K requires a temperature stabilization of the whole system with a precision of  $\sim 0.1^\circ$  including a finely distributed temperature measurement. In addition the intrinsic gain and the noise level of the APD photosensors show similar temperature sensitivity. The thermal contact to the crystals should be sufficiently reliable. Checks of the linearity of the electronics at the sub-percent

level require to cover a dynamic range of 10 000. This will be achieved by neutral density filters.

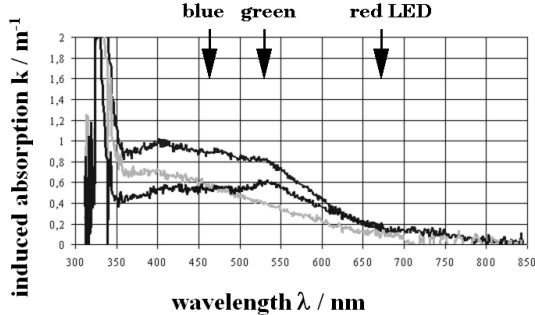


**Figure 8.1:** Induced absorption of various PWO samples after irradiation with a dose of 20 krad ( $^{60}\text{Co}$ ) shown with the indication of the available wavelengths of LEDs, which are used for monitoring purposes.

### 8.2.1 Concept of a Light Source and Light Distribution System

To maintain exact correspondence between observed changes of the measured amplitude of the light monitoring signal and the detector signal initiated by high energy photons, which is influenced by the variation of the optical transmission of PWO crystals, it is necessary to meet two requirements: the optical emission spectrum of the light source should be similar to the radio-luminescence spectrum of PWO; the effective optical path length for monitoring light in the crystal should be identical to the average path length of the scintillation light created by an electromagnetic shower in the crystal. Further technical requirements for the monitoring light source are: the number of photons per pulse should generate the output signal equivalent to about 2 GeV in each cell; the duration of the pulse should be similar to the decay time of the scintillation of PWO; a long-term pulse stability better than 0.1 % has to be achieved; minimal pulse height variation from pulse to pulse (determined only by photon statistics without any additional line broadening to keep the required number of monitoring events at the minimum). Nowadays available ultra-bright LEDs (brightness  $> 10$  cd) emitting at various wavelengths give the opportunity to create a system to meet most of the above requirements. In case of blue-violet LEDs the emission spectrum (centered at 420–430 nm) as well as the spectral

width (approx. 70 nm FWHM) correspond exactly to those for PWO radio-luminescence. The number of photons per 20 ns pulse can be as large as  $10^9$  and can be further increased by more than one order of magnitude by combining optically many LEDs in one emitting block. Moreover, combining LEDs of different color allows fine-tuning to the entire scintillator emission spectrum. Even taking into account the light losses in the distribution system one might illuminate 1 000–1 200 calorimeter cells with one large LED block. Consequently 10 to 15 such stabilized blocks can provide the monitoring of the whole electromagnetic calorimeter. Such a concept allows the selective monitoring of different parts of the calorimeter by electronic triggering of the appropriate LED blocks without the necessity of optical switching. The distribution system should provide the light transfer to each cell with the option to fire selectively only  $\sim 10\%$  of all cells simultaneously to avoid interference problems in the front-end electronics and an overload of the data acquisition system. This can be implemented with optical fibers grouped into 10 bunches attached to the outputs of multi LED blocks. Each fiber bunch will contain additional fibers controlling possible losses in fiber transparency.

### 8.2.2 Concept of the Light Monitoring System

The concept of the system should provide flexible control and redundancy in terms of measured parameters to distinguish between different sources of instability. Each emitting block will be equipped with an optical feedback and a thermo-stabilized PIN-photodiode as reference. Such a device has been successfully implemented for CMS ECAL [3]. A central sequencer will trigger all blocks with maximum frequency up to a few kHz. A separate unit is foreseen to measure the light amplitude of the reference fiber in each bundle. The system does not require regular maintenance. Fig. 8.2 and 8.3 show the schematic layout and the major components of a first functioning prototype.

### 8.2.3 Light Pulser Prototype Studies

#### 8.2.3.1 Experience at Test Beam

A LED-based light pulser system with four LEDs of different wavelengths was made for the test beam studies at Protvino to monitor gain variations of the PMTs and transmission variations of the PWO

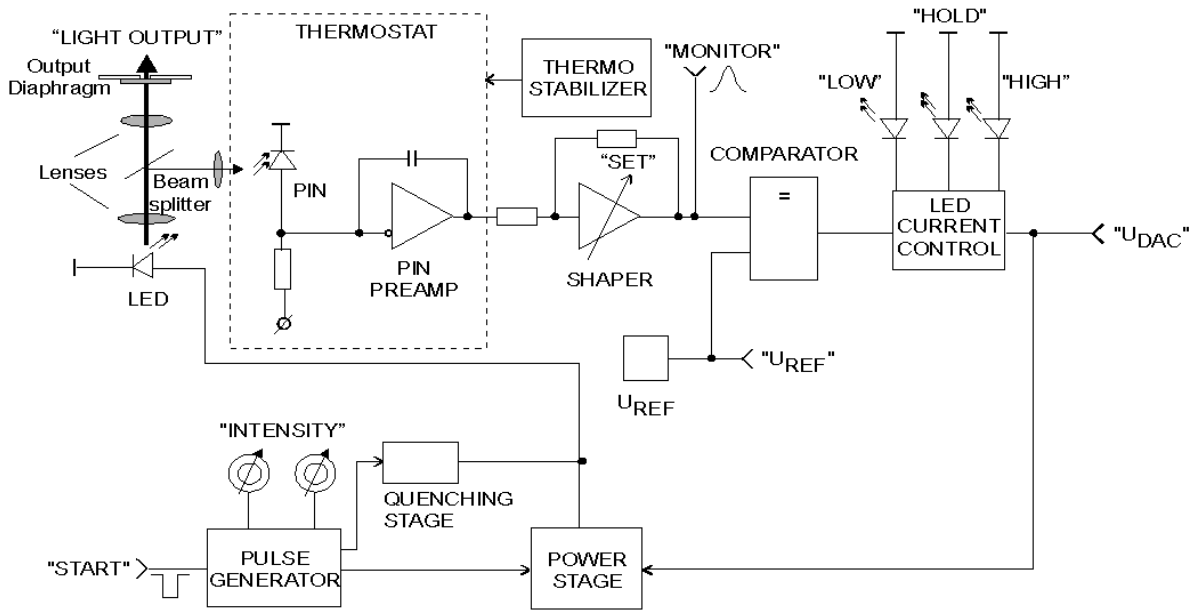


Figure 8.2: Schematic layout of the stabilized light pulser system.

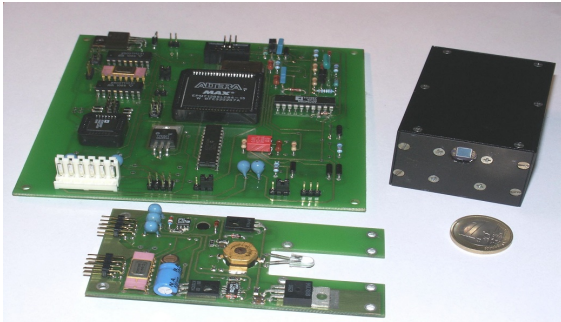


Figure 8.3: Major components of a first prototype of the monitoring system.

crystals. The LEDs emit at red (660 nm), yellow (580 nm), green (530 nm), and blue (470 nm) wavelengths. For the actual analysis of data, the red and the blue LEDs were most useful.

Between two accelerator spills, 10 light pulses of one color were sent to the crystals. Then in the following interval, light pulses of another color were injected in the crystals. This way, four spills were needed to collect data for all four colors. The light from all the LEDs was fed into the same set of optical fibers and they delivered the light to individual crystals.

In the test beam setup, the LED light was injected at the front end of the crystals. So the typical path length of LED light in the crystal approximately

equals the length of the crystal. Since the light comes out of the optical fiber with a characteristic full angle spread of  $25^\circ$ , and this angle is reduced to  $11^\circ$  as the light enters the crystal from air, the path length of light in the crystal should be increased by  $1/\cos 11^\circ$ . As for the scintillation light from incident particles, half of the light travels directly to the PMT while the other half will travel towards the front of the crystal and gets reflected before it is detected by the PMT. Averaging these two cases, the mean path length of scintillation light to the PMT also equals the crystal length in 0th approximation. In order to estimate the 1st order correction, we need to know how much the light zigzags on its way to the PMT. The maximum angle that the light makes with respect to the crystal axis is determined by the reflection angle on the side surfaces due to the total internal reflection angle, which is about  $64^\circ$ . This leads to many more zigzag paths than the paths for LED light. Taking into account that the scintillation light is emitted isotropically, the average  $\langle 1/\cos \theta \rangle$  factor arising from the zigzag paths is about 1.4.

The LED system monitors the transparency of the crystal at a specific wavelength (in our case, 470 nm was chosen partially due to the availability of blue LEDs) and thus does not sample the entire spectrum of scintillation light. The radiation damage effect is less severe at 470 nm than at 430 nm, the center of the PWO scintillation emission peak. From these considerations, we expect that the ratio,

$R$ , of the light loss factors for the LED signal and the particle signal is about  $1/1.4 = 0.7$  to  $1/1.6 = 0.6$ .

One of our goals in the test beam studies of the calibration system is to measure this ratio,  $R$ , experimentally, and to observe how it varies from crystal to crystal. Naively, since this ratio only depends on the geometrical lengths of light paths for the LED and scintillation light, it should not vary from one crystal to the next. If there are variations in the shape of the absorption as a function of wavelength among crystals, the ratio,  $R$ , may vary among crystals. In addition, since the crystals will not be polished to optical flatness, actual reflections of light by the side surfaces do not follow the simple law of geometrical light reflection. This may also lead to variations of the ratio,  $R$ , among crystals. Thus we feel that it is very important to measure the variation of  $R$  values experimentally.

Since it is not practical to measure this ratio for all produced crystals at a test beam facility (it would take too much time), we need to know if the variation, if there is any, is small enough so that we will not spoil the resolution even if we assume and use an average value of the ratio for all crystals.

### 8.2.3.2 Monitoring Systems for the Light Pulser System and Stability of Light Pulser

We built two monitoring systems to check the stability of the magnitude of the light pulses. (*i.e.* monitoring systems of the monitoring system.) One was based on a PIN photodiode, which is considered very stable even when the temperature varies. According to the literature, the temperature variation of PIN photodiodes is less than  $0.01\%/^{\circ}\text{C}$ . However, since we needed an amplifier to detect the PIN photodiode signal, the amplifier gain needed to be stabilized by housing it in the crystal box where the temperature was stable to  $\pm 0.1^{\circ}\text{C}$ .

The second system used a PMT, a scintillation crystal and a radioactive source. The PMT (Hamamatsu R5900) monitored the LED pulser while the PMT was monitored using the stable scintillation light produced when a  $\text{YAlO}_3 : \text{Ce}$  crystal was irradiated with an  $^{238}\text{Pu}$  alpha source (YAP) [4]. The  $\alpha$  energy spectrum measured by the PMT and the peak position of this spectrum as a function of time is presented in Fig. 8.4. The width of the peak is 2.3% r.m.s. as determined by a fit to a Gaussian. The peak position was stable over 85 hours to better than 0.2%.

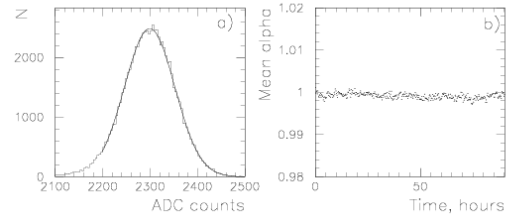


**Figure 8.4:** (a)  $\alpha$  energy spectrum accumulated over 1.5 hours. (b)  $\alpha$  spectrum peak position as a function of time over 85 hours. Each point corresponds to a 15-minute measurement duration.

The measured variations (drifts) of the magnitudes of light pulses (averaged over 120 pulses) over different time periods were measured for the periods of test beam studies. They were:

- 0.1 to 0.2% over a day;
- 0.5% over a week;
- 1% over a few months.

Temperature variations were the main cause for the variations in the size of pulses. When corrections based on the temperature were made in the pulse-height analysis, the long term variation significantly decreased to 0.4% over a few months and down to 0.3% over a week. No LED ageing effects were observed after 3000 hours of operation.

The stability of this system was better than we needed to monitor the gain variations of the PMTs and the transparency variations of the crystals over the relevant time periods. For example, we were able to track the crystal transparency change with an accuracy of better than 1% over a week when we measured how much radiation damage the crystals suffered. Additionally, we were able to track the change in crystal transparency with an accuracy of better than 1% over a few months when we measured the recovery process of the radiation-damaged crystals. Finally, we were able to track the PMT gain variations over a day well enough so that it did not contribute appreciably to the energy resolution. This last accomplishment implies that we already have a good enough system for  $\bar{\text{P}}\text{ANDA}$  except that we need to have a much larger system, and temperature stabilization must be considered.

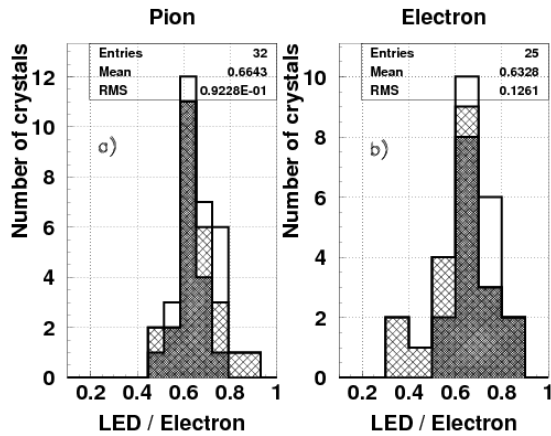


**Figure 8.5:** Linear fit coefficients calculated from the correlation plots of relative changes for the blue LED vs. electron signal under (a) pion and (b) electron irradiation.

### 8.2.3.3 Crystal Light Output Monitoring

As was shown by radiation hardness studies, PWO crystals behave in a similar way in radiation environments of different nature; clear correlations between electron and LED signal changes were observed. The dedicated study has been carried out to confirm that these correlations are not dependent on the type of irradiation using a particular optical monitoring scheme. To be more specific, the same crystals were calibrated with a low intensity electron beam first, then they were exposed to the highly intense electron radiation. The irradiation of crystals continued with a pion beam. Both electron and pion irradiations alternated with calibration runs using a low intensity electron beam. Changes in the crystal transparency were monitored continuously with the use of the LED monitoring system. A linear fit of the distributions of signal change of the relative blue LED signal vs. the electron signal was calculated for both the electron and pion irradiations. Coefficients of the linear fit are presented in Fig. 8.5

As it was expected, on average the measured coefficients are not different and are in a good agreement with the calculations for the current optical scheme. The fact that the linear approximation works well, significantly simplifies the procedure of the EMC intercalibration that will be performed using an LED-based light monitoring system over the time intervals between two subsequent in-situ calibrations.

## 8.2.4 Light Monitoring System for PANDA Calorimeter

The light monitoring system is designed to inject light pulses into each PWO crystal in order to measure optical transmission near the scintillation spectrum peak (430 nm). The red light pulses are used to monitor a photodetector gain stability. The system includes both blue and red LEDs, their driver circuits, and optical fibers to deliver light pulses to each of the PWO crystals.

We plan to use very powerful LEDs, assisted by a reflector and a light mixer so that each light pulsing system produces enough light for  $\sim 3000$  crystals, each receiving light pulses equivalent to scintillation light from 2 GeV photons.

The distribution of light among the 3000 fibers should be very uniform. This is accomplished by designing a good light mixer which will distribute light uniformly across an area of  $38 \times 38 \text{ mm}^2$ . Each bunch of fibers (containing about 3000 fibers, out of which 400 are spares) and two reference PIN silicon photodiodes will be contained in this area. Several light pulsers will serve the whole PANDA calorimeter.

The time dependence of pulse heights from the pulser is monitored by the two reference PIN photodiodes. One of the pulser systems will be activated at any given time to limit the power requirements of the light source, the size of data transfers, as well as high and low voltages current demands.

The principal goal of the system is to monitor short-term variation in the photodetector gains and the light transmission of the crystals. The system will also be used to check out the entire crystal-readout chain during the assembly of the calorimeter. It will also permit a rapid survey of the full calorimeter during the installation or after long shutdowns. Furthermore, the light monitoring system can be used to measure the response linearity of the PWO crystal's photodetector and its readout chain. This should complement measurements with electronic charge injection at the preamplifier level which does not test the photodetector.

Some results obtained with a prototype system are presented in Sec. 8.2.4.3 and in Fig. 8.6. In more detail, the monitoring system prototype design and performance are discussed in [5].

A picture of the whole prototype system is presented in Fig. 8.7. A LED driver is presented in Fig. 8.8.

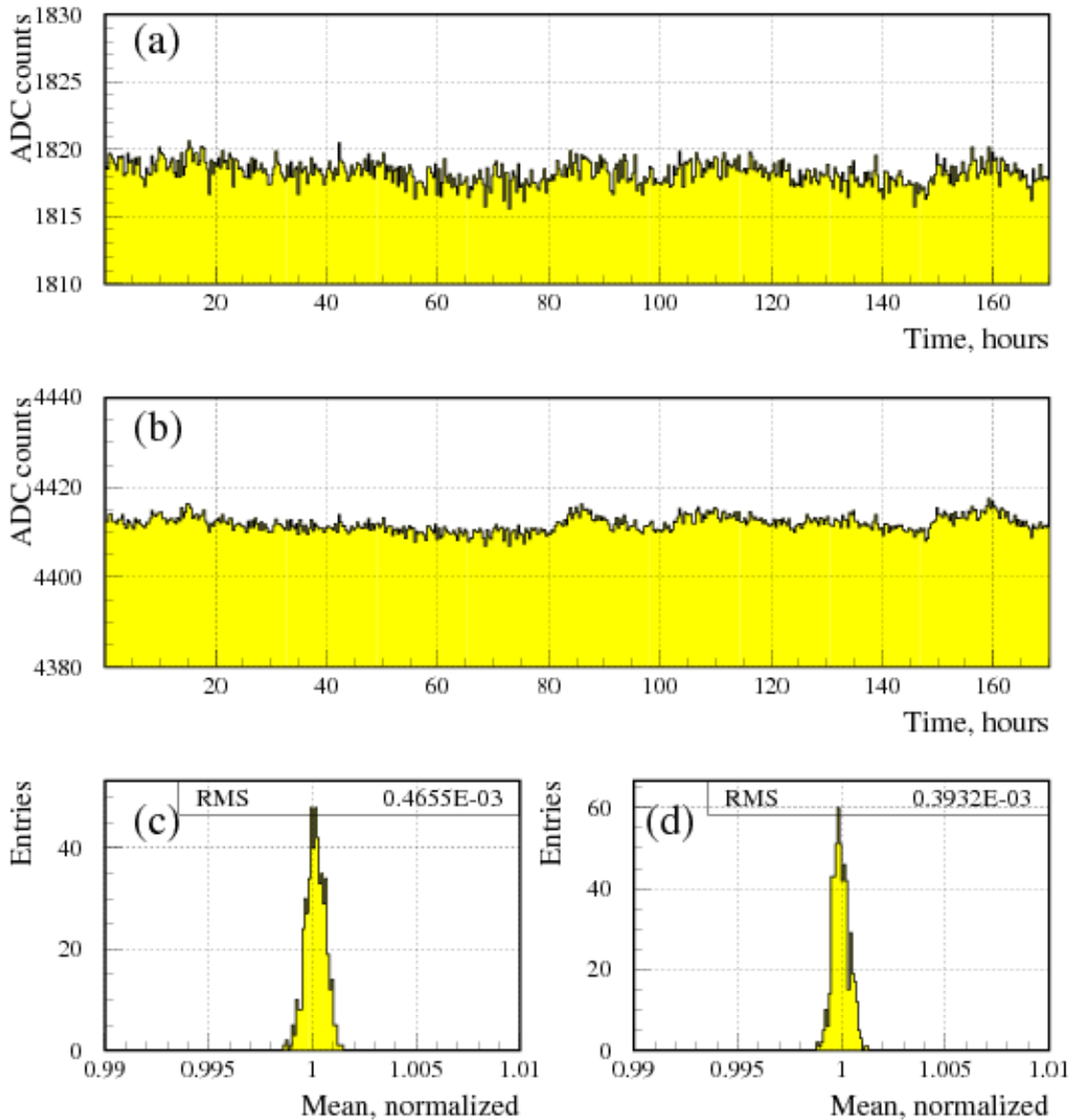


**Figure 8.6:** Stability of the LED pulser prototype: (a),(b) - behaviour in time of blue and red LED signals correspondingly detected by one of the photodiodes over one week of measurements. Each entry is a mean value of amplitude distribution collected over 20 min; (c),(d) - normalized projections on the vertical axis of the diagrams (a) and (b). R.m.s. characterizes instability of the system over the period of measurements.

#### 8.2.4.1 Monitoring System Components

The monitoring system will be located directly at the outer radius of the calorimeter support structure and an optical-fiber light distribution system connects the pulser to the crystals. Since the light pulser is located in a low radiation zone, its components and electronics are not required to be radiation hard. In contrast, many fibers are routed through a high radiation zone and they must be made of radiation-hard materials.

The characteristics of the LEDs we plan to use in the  $\bar{P}$ ANDA calorimeter monitoring system are given in Table 8.2.4.1.

Besides the exceptional luminous fluxes, we find that two additional features of the Luxeon technology are very important for our monitoring system: very long operating lifetime (up to 100,000 hours in DC mode), and small temperature dependence of the light output ( $\approx 0.1\%/^{\circ}\text{C}$ ). The producer is Lumileds Lighting, USA. The reflector which was made at IHEP has a trapezoidal shape and is made

Property	blue (royal blue) LED	red LED
Brand	Luxeon 5-W emitter	Luxeon 1-W emitter
Typical Luminous flux	30 lm (@700 mA)	45 lm (@350 mA)
Radiation Pattern	Lambertian	Lambertian
Viewing Angle	150°	140°
Size of Light Emission Surface	5 × 5 mm <sup>2</sup>	1.5×1.5 mm <sup>2</sup>
Peak Wavelength	470 nm (455 nm)	627 nm
Spectral Half-width	25 nm (20 nm)	20 nm
Average Forward Current	700 mA	350 mA

**Table 8.1:** Properties of LEDs.

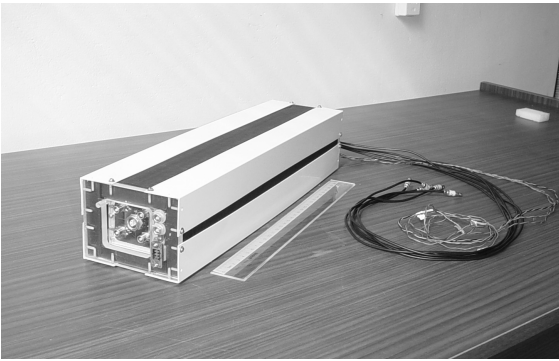


**Figure 8.7:** View of the prototype monitoring system. Inside the box there is a LED driver, blue and red LEDs, a light mixer, a temperature stabilization system, and a referenced PIN-diode system. In use we have a fiber bunch coming out the far side of the box instead of the cables which are pictured; the cables are for tests only and will not go to the calorimeter. The size of the box is 370 mm x 70 mm x 60 mm.

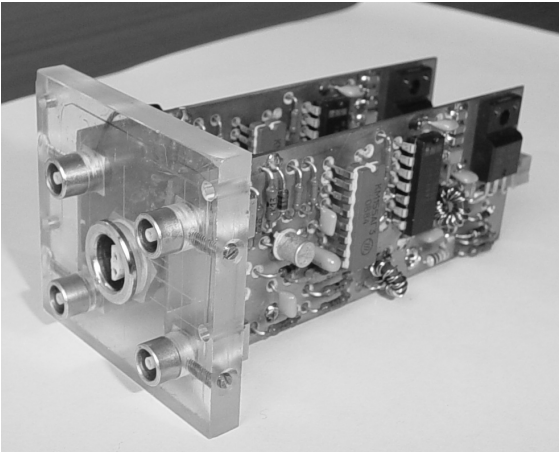


**Figure 8.8:** LED driver of the Prototype of the monitoring system. It will be inside the box (see the previous Figure) near the side opposite to the one with a bunch of fibers.

of aluminum plated Mylar or Tyvek.

The optical fibers we plan to use are produced by Polymicro Technologies, USA. Their properties are:

- Silica / Silica optical fiber
- High - OH Core
- Aluminum Buffer
- Core Diameter 270  $\mu\text{m}$
- Outer Diameter 400  $\mu\text{m}$
- Numerical Aperture 0.22
- Full Acceptance Cone 25.4°

This fiber has very good radiation hardness. According to the tests made by the CMS ECAL group, this fiber has shown no signal degradation under gamma irradiation with an absorbed dose of up to 12 Mrad.

#### 8.2.4.2 Reference PIN Silicon Photodiodes

An essential element of the light monitoring system is a stable reference photodetector with good sensitivity at short wavelengths. PIN silicon photodiodes with a sensitive area of about 6 mm<sup>2</sup> are well suited for this task. In particular, such low leakage currents are achieved with PIN diodes, due to their very narrow depletion zone resulting from heavy (p and n) doping, which is less sensitive to the type inversion than typical PIN diodes. The rather large sensitive area of this photodiode allows us to work without preamplifiers and improve the stability of the reference system itself. A PIN silicon photodiode S1226-5BQ (Hamamatsu) was used in our test measurements. It has an active area of 2.4×2.4 mm<sup>2</sup> and a dark current less than 50 pA (at 5 V reverse-bias voltage).

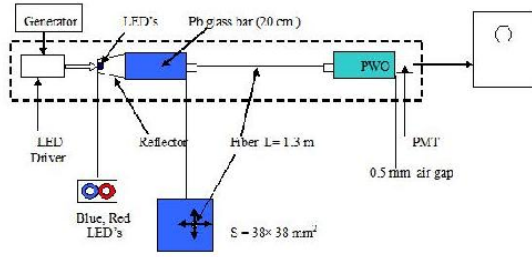


**Figure 8.9:** Schematic view of the light pulser prototype.

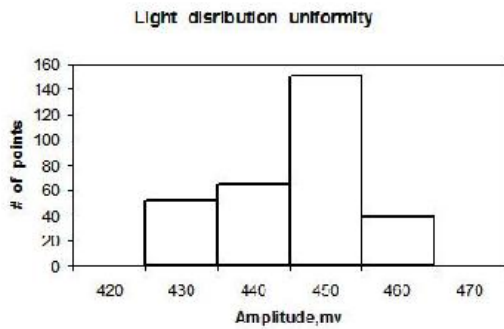


**Figure 8.10:** Distribution of pulse heights (in mV) measured over an area of  $34 \times 34 \text{ mm}^2$  in 2 mm steps.

### 8.2.4.3 Tests of the Light Pulser Prototype

A schematic view of the light pulser prototype is shown in Fig. 8.9. The light distribution uniformity was measured with a single fiber scanner. All the measurements were made with a scope and a manual scan with a step size of 2 mm. The scan area was  $34 \times 34 \text{ mm}^2$ . The results are shown in Fig. 8.10. The FWHM of this pulse height distribution is 2%, and the full width is 8%. The energy equivalent is 20 GeV for the whole scan area. The average forward current in the tests was 20 mA. The maximum forward current is 700 mA. So we have a large safety factor for the amount of light. This light pulser can illuminate more than 3000 fibers.

The short-term stability of light uniformity over the area of  $34 \times 34 \text{ mm}^2$  for a day has been measured to be 0.05% and a long-term stability was 0.1% over 20 days. In spite of these encouraging results, thermostabilisation of the light pulser by means of the Peltier cell is foreseen in the design of the whole system.

## References

- [1] I. Augustin, *Search for Scalar Gluonium in Antiproton-Proton Annihilations at Rest*, PhD thesis, 1992.
- [2] E. Aker et al., Nucl. Instrum. Meth. **A321**, 69 (1992).
- [3] A. Fyodorov, M. Korzhik, A. Lopatik, and O. Missevitch, Nucl. Instrum. Meth. **A413**, 352 (1998).
- [4] V. A. Kachanov et al., Nucl. Instrum. Meth. **A314**, 215 (1992).
- [5] V. A. Batarin et al., Nucl. Instrum. Meth. **A556**, 94 (2006).



## 9 Simulations

---

The simulation of the EMC and the facilitated software is described in this chapter. The goal of the studies described in the following is the expected performance of the planned EMC. We focus here on the energy and spatial resolution of reconstructed photons, the capability of an electron hadron separation, and also the feasibility of the  $\bar{\text{P}}\text{ANDA}$  physics program. A couple of benchmark studies will be presented. These accurate simulations highlight the necessity of the planned EMC. Due to the fact that most of the physics channels have very low cross sections - typically between pb and nb - , a background rejection power up to  $10^9$  has to be achieved. This requires an electromagnetic calorimeter which allows an accurate photon reconstruction within the energy range between 10 MeV and 15 GeV, and an effective and an almost clean electron hadron separation.

### 9.1 Offline Software

The offline software has been devised for detailed design studies of the  $\bar{\text{P}}\text{ANDA}$  detector and for the preparation of the  $\bar{\text{P}}\text{ANDA}$  Physics Book, which will be published by September 2008. It follows an object oriented approach, and most of the code is written in C++. Several proofed software tools and packages have been adapted from other HEP experiments to the  $\bar{\text{P}}\text{ANDA}$  needs. The software contains

- event generators with proper decay models for all particles and resonances involved in the individual physics channels as well as in the relevant background channels,
- particle tracking through the complete  $\bar{\text{P}}\text{ANDA}$  detector by using the GEANT4 transport code [1, 2],
- a digitization which models the signals and the signal processing in the front-end-electronics of the individual detectors,
- the reconstruction of charged and neutral particles, comprising a particle identification that provides lists of particle candidates for the final physics analysis, and
- user friendly high level analysis tools with the purpose to make use of vertex and kinematical fits and to reconstruct even complicate decay trees in an easy way.

The simulations have been done with the complete setup which was already described in detail in Sec. 2.3. The still not finally established Time Of Flight and the Forward RICH detectors have not been considered and the Straw Tube option has been used for the central tracker device.

#### 9.1.1 Photon Reconstruction

##### 9.1.1.1 Reconstruction Algorithm

A photon entering one crystal of the EMC develops an electromagnetic shower which, in general, extends over several crystals. A contiguous area of such crystals is called a cluster.

The energy deposits and the positions of all crystals hit in a cluster allow a determination of the four vector of the initial photon. Most of the EMC reconstruction code used in the offline software is based on the cluster finding and bump splitting algorithms which were developed and successfully applied by the BaBar experiment [3, 4].

The first step of the cluster reconstruction is the finding of a contiguous area of crystals with energy deposit. The algorithm starts at the crystal exhibiting the largest energy deposit. Its neighbors are then added to the list of crystals if the energy deposit is above a certain threshold  $E_{xtl}$ . The same procedure is continued on the neighbors of newly added crystals until no more crystal fulfills the threshold criterion. Finally a cluster gets accepted if the total energy deposit in the contiguous area is above a second threshold  $E_{cl}$ .

A cluster can be formed by more than one particle if the angular distances of the particles are small. In this case the cluster has to be subdivided into regions which can be associated with the individual particles. This procedure is called the *bump splitting*. A bump is defined by a local maximum inside the cluster: The energy deposit of one crystal  $E_{\text{LocalMax}}$  must be above  $E_{max}$ , while all neighbor crystals have smaller energies. In addition the highest energy  $E_{\text{NMax}}$  of any of the  $N$  neighboring crystals must fulfill the following requirement:

$$0.5(N - 2.5) > E_{\text{NMax}} / E_{\text{LocalMax}} \quad (9.1)$$

The total cluster energy is then shared between the bumps, taking into account the shower shape of the cluster. For this step an iterative algorithm is used,

which assigns a weight  $w_i$  to each crystal, so that the bump energy is defined as  $E_{\text{bump}} = \sum_i w_i E_i$ .  $E_i$  represents the energy deposit in the  $i$ th crystal and the sum runs over all crystals within the cluster. The crystal weight for each bump is calculated by

$$w_i = \frac{E_i \exp(-2.5 r_i / r_m)}{\sum_j E_j \exp(-2.5 r_j / r_m)} \quad (9.2)$$

, with

- $r_m$  = Molière radius of the crystal material,
- $r_i, r_j$  = distance of the  $i$ th and  $j$ th crystal to the center of the bump and
- index  $j$  runs over all crystals.

The procedure is iterated until convergence. The center position is always determined from the weights of the previous iteration and convergence is reached when the bump center stays stable within a tolerance of 1 mm.

The spatial position of a bump is calculated via a center-of-gravity method. Due to the fact that the radial energy distribution originating from a photon decreases mainly exponentially, a logarithmic weighting with

$$W_i = \max(0, A(E_{\text{bump}}) + \ln(E_i/E_{\text{bump}})) \quad (9.3)$$

was chosen, where only crystals with positive weights are used. The energy dependent factor  $A(E_{\text{bump}})$  varies between 2.1 for the lowest and 3.6 for the highest photon energies.

### 9.1.1.2 Digitization of the Crystal Readout

Fast FADC will digitize the analog response of the first amplification and shaping stage. Therefore signal waveforms are important to be considered in the simulation. For performance reasons a simplified method has been applied in the simulation studies. It is based on an effective smearing of the extracted Monte Carlo energy deposits. Reasonable properties of  $\text{PbWO}_4$  at the operational temperature of  $-25^\circ\text{C}$  have been considered. A Gaussian distribution of  $\sigma = 1\text{ MeV}$  has been used for the constant electronics noise. The statistical fluctuations were estimated by 80 phe/MeV produced in the LAAPD. An excess noise factor of 1.38 has been used which corresponds to the measurements with the first LAAPD 'normal C' prototype at an internal gain of  $M = 50$  (see Sec. 5.1.2.2). This results in a photo statistic noise term of  $0.41\% / \sqrt{E(\text{GeV})}$ .

#### 9.1.1.2.1 Comparison with $3 \times 3$ Crystal Array Measurements

In order to demonstrate that the digitization is sufficiently described by the simplified method, the simulation was compared with the results of a measurement with a  $3 \times 3$  crystal array at an operational temperature of  $0^\circ\text{C}$  (see Sec. 10.1.1.2). Fig. 10.16 and Fig. 10.17 show the obtained line shapes, and Fig. 10.19 the measured energy resolution as a function of incident photon energy. The simulations have been done for a  $3 \times 3$  array of crystals of  $2 \times 2 \times 20\text{ cm}^3$ . Photons with discrete energies between 40.9 MeV and 1 GeV were shot to the center of the innermost crystal. To consider the crystal temperature of  $0^\circ\text{C}$  the digitization has been done with just 40 phe/MeV instead of 80 phe/MeV produced in the LAAPD. The resulting line shape at the photon energy of 674.5 MeV is illustrated in Fig. 9.1. A fit with a Novosibirsk function defined by

$$f(E) = A_S \exp(-0.5 \ln^2[1 + \Lambda \tau \cdot (E - E_0)] / \tau^2 + \tau^2)$$

, with

- $\Lambda = \sinh(\tau \sqrt{\ln 4}) / (\sigma \tau \sqrt{\ln 4})$ ,
- $E_0$  = peak position,
- $\sigma$  = width, and
- $\tau$  = tail parameter

yields to a resolution of  $\sigma/E = 2.63\%$ , which is in good agreement with the measurements (see Fig. 10.17). Moreover the energy resolution as a function of the photon energy can be reproduced very well. A comparison between the measurements and the simulations are shown in Fig. 9.2, and the results are consistent within a tolerance of 10%. The resolutions obtained with the simulation are systematically better, which may be caused by the uncertainties of the estimated electronic noise term and the number of phe/MeV, as well as by inhomogeneities of the light yield of the crystals, which were not taken into account.

#### 9.1.1.3 Reconstruction Thresholds

In order to detect low energetic photons and to achieve a good energy resolution, the three photon reconstruction thresholds should be set as low as possible. On the other hand the thresholds must be sufficiently high to suppress the misleading reconstruction of photons from the noise of the crystal readout and from statistical fluctuations of the electromagnetic showers. Based on the properties of the  $\bar{P}$ ANDA EMC (see Sec. 9.1.1.2) the following thresholds were chosen:

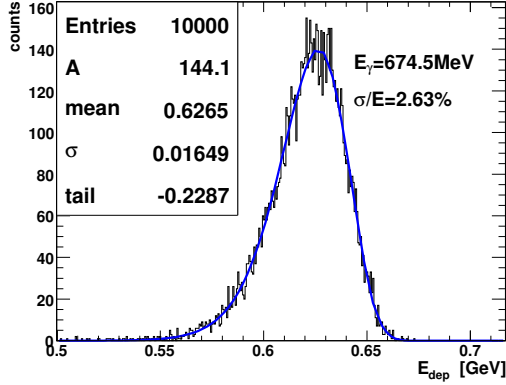


**Figure 9.1:** Simulated line shape of the  $3 \times 3$  crystal matrix at the photon energy of 674.5 MeV. The fit with a Novosibirsk function gives an energy resolution of  $\sigma/E = 2.63\%$

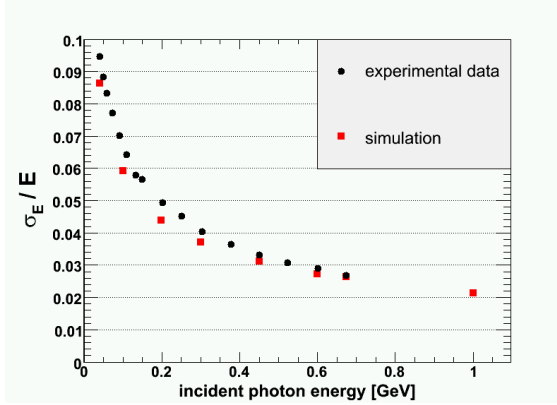


**Figure 9.2:** Energy resolution as a function of incident photon energy between 40.9 MeV and 1 GeV for a  $3 \times 3$  crystal array. The measurements are represented by black circles and the simulation results are illustrated with red rectangles.

- $E_{xtl} = 3 \text{ MeV}$
- $E_{cl} = 10 \text{ MeV}$
- $E_{max} = 20 \text{ MeV}$ .

As already discussed in Sec. 3.1.1.1 the ability to identify photons down to approximately 10 MeV is extremely important for  $\bar{\text{P}}\text{ANDA}$ . A lot of channels – especially in the charmonium sector (exotic and conventional) like  $\bar{\text{p}}\text{p} \rightarrow \eta_c \rightarrow \gamma\gamma$ ,  $\bar{\text{p}}\text{p} \rightarrow h_c \rightarrow \eta_c \gamma$  or  $\bar{\text{p}}\text{p} \rightarrow J/\psi \gamma$  – require an accurate and clean reconstruction of isolated photons. The main background channels here have the same final states with just the isolated photon being replaced by a  $\pi^0$ . If one low energetic photon from a  $\pi^0$  decay

gets lost, the background event will be misidentified. The cross sections for the background channels are expected to be orders of magnitudes higher than for the channels of interest. Therefore an efficient identification of  $\pi^0$  is mandatory for this important part of the physics program of  $\bar{\text{P}}\text{ANDA}$ . Fig. 3.1 in Sec. 3.1.1.1 shows the upper limit for the identification of  $\pi^0$ 's with respect to different photon thresholds. While roughly 1% of the  $\pi^0$ 's get lost for a threshold of 10 MeV, the misidentification increases by one order of magnitude for the scenario where photons below 30 MeV can not be detected.

#### 9.1.1.4 Leakage Corrections

The sum of the energy deposited in the crystals in general is a few percent less than the energy of the incident photon. This is caused by shower leakages particularly in the crystal gaps. The reconstructed energy of the photon is expressed as a product of the total measured energy deposit and a correction function which depends logarithmically on the energy and – due to the layout of the  $\bar{\text{P}}\text{ANDA}$  EMC – also on the polar angle. Single photon Monte Carlo simulations have been carried out to determine the parameters of the correction function  $E_{\gamma, \text{cor}} = E * f(\ln E, \Theta)$  with

$$f(\ln E, \Theta) = \exp(a_0 + a_1 \ln E + a_2 \ln^2 E + a_3 \ln^3 E + a_4 \cos(\Theta) + a_5 \cos^2(\Theta) + a_6 \cos^3(\Theta) + a_7 \cos^4(\Theta) + a_8 \cos^5(\Theta) + a_9 \ln E \cos(\Theta))$$

Fig. 9.3 shows the result for the barrel part in the  $\Theta$  range between  $22^\circ$  and  $90^\circ$ .

#### 9.1.1.5 Energy and Spatial Resolution

The energy resolution of the EMC strongly depends on the length of the crystals. A sufficient containment of the electromagnetic shower within the detector and marginal fluctuations of the shower leakages must be guaranteed for the detection of photons with energies up to 15 GeV. Fig. 9.4 compares the simulation results for the foreseen  $\bar{\text{P}}\text{ANDA}$  EMC equipped with crystals of 15 cm, 17 cm and 20 cm length. While the resolution for low energetic photons – below 300 MeV – is nearly the same for all three scenarios, the performance becomes significantly better for higher energetic photons with an increasing crystal length. The 20 cm setup yields in an energy resolution of 1.5% for 1 GeV photons, and of below 1% for photons above 3 GeV. Another aspect which favors the 20 cm scenario is the toler-

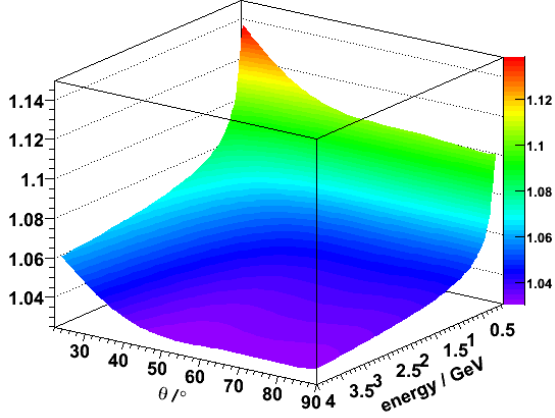


**Figure 9.3:** Leakage correction function for the barrel EMC in the  $\Theta$  range between  $22^\circ$  and  $90^\circ$ .

able level of the nuclear counter effect in the photo sensors (Sec. 2.3).

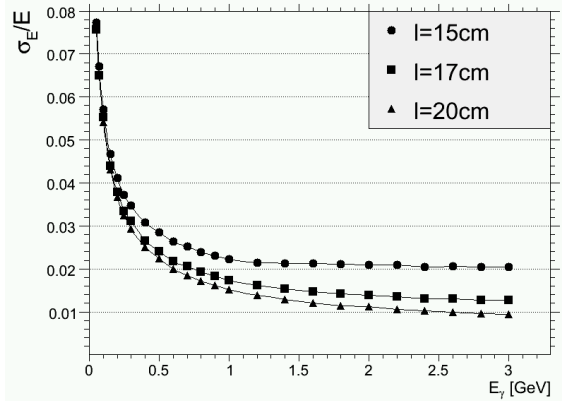


**Figure 9.4:** Comparison of the photon energy resolution for three different crystal lengths. The resolution for 15 cm crystals is illustrated by circles, for 17 cm by rectangles, and the 20 cm scenario is shown with triangles.

As already described in 9.1.1.2 and 9.1.1.3 the choice of the single crystal threshold  $E_{xtl}$ , which is driven by the electronics noise term, strongly effects the resolution. Three different scenarios have been investigated: Fig. 9.5 compares the achievable resolution for the most realistic scenario with a noise term of  $\sigma = 1$  MeV and a single crystal reconstruction threshold of  $E_{xtl} = 3$  MeV with a worse case ( $\sigma = 3$  MeV,  $E_{xtl} = 9$  MeV) and a better case ( $\sigma = 0.5$  MeV,  $E_{xtl} = 1.5$  MeV). While the maximal improvement for the better case is just 20% for the lowest photon energies, the degradation in

the worse case increases by more than a factor of 2. This result demonstrates clearly that the single crystal threshold has a strong influence on the energy resolution.

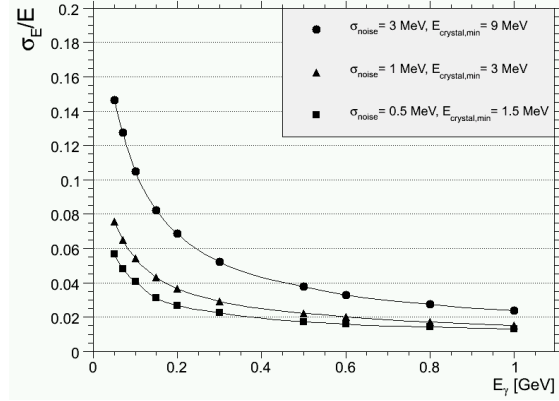


**Figure 9.5:** Comparison of the energy resolutions for three different single crystal reconstruction thresholds. The most realistic scenario with a noise term of  $\sigma = 1$  MeV and a single crystal threshold of  $E_{xtl} = 3$  MeV is illustrated by triangles, a worse case ( $\sigma = 3$  MeV,  $E_{xtl} = 9$  MeV) by circles and the better case ( $\sigma = 0.5$  MeV,  $E_{xtl} = 1.5$  MeV) by rectangles.

The high granularity of the planned EMC provides an excellent position reconstruction of the detected photons. The accuracy of the spatial coordinates is mainly determined by the dimension of the crystal size with respect to the Molière radius. Fig. 9.6 shows the resolution in  $x$  direction for photons up to 3 GeV. A  $\sigma_x$ -resolution of less than 0.3 cm can be obtained for energies above 1 GeV. This corresponds to roughly 10% of the crystal size. For lower energies the position becomes worse due to the fact that the electromagnetic shower is contained in just a few crystals. In the worst case of only one contributing crystal the  $x$ -position can be reconstructed within an imprecision of 0.5 - 0.6 cm.

## 9.1.2 Electron Identification

Electron identification will play an essential role for most of the physics program of PANDA. An accurate and clean measurement of the  $J/\psi$  decay in  $e^+e^-$  is needed for many channels in the charmonium sector as well as for the study of the  $\bar{p}$  annihilation in nuclear matter like the reaction  $\bar{p}A \rightarrow J/\psi X$ . In addition the determination of electromagnetic form factors of the proton via  $\bar{p}p \rightarrow e^+e^-$  requires a suppression of the main background channel  $\bar{p}p \rightarrow \pi^+\pi^-$  in the order of  $10^8$ .

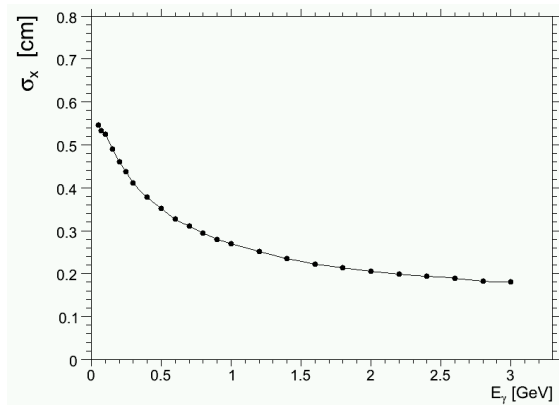


**Figure 9.6:** Position resolution in  $x$ -direction for photons below 3 GeV.

The EMC is designed for the detection of photons. Nevertheless it is also the most powerful detector for an efficient and clean identification of electrons. The character of an electromagnetic shower is distinctive for electrons, muons and hadrons. The most suitable property is the deposited energy in the calorimeter. While muons and hadrons in general lose only a certain fraction of their kinetic energy by ionization processes, electrons deposit their complete energy in an electromagnetic shower. The ratio of the measured energy deposit in the calorimeter to the reconstructed track momentum ( $E/p$ ) will be approximately unity. Due to the fact that hadronic interactions within the crystals can take place, hadrons can also have a higher  $E/p$  ratio than expected from ionization. Figure Fig. 9.7 shows the reconstructed  $E/p$  fraction for electrons and pions as a function of momentum.

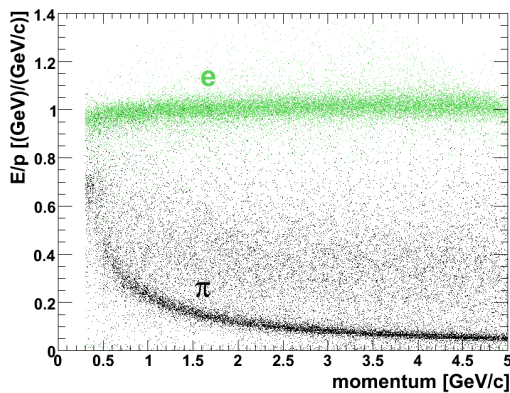


**Figure 9.7:**  $E/p$  versus track momentum for electrons (green) and pions (black) in the momentum range between 0.3 GeV/ $c$  and 5 GeV/ $c$ .

Furthermore the shower shape of a cluster is helpful to distinguish between electrons, muons and hadrons. Since the chosen size of the crystals corresponds to the Molière radius of lead tungstate, the largest fraction of an electromagnetic shower originating from an electron is contained in just a few crystals. Instead, a hadronic shower with a similar energy deposit is less concentrated. These differences are reflected in the shower shape of the cluster, which can be characterized by the following properties:

- $E_1/E_9$  which is the ratio of the energy deposited in the central crystal and in the  $3 \times 3$  crystal array containing the central crystal and the first innermost ring. Also the ratio of  $E_9$  and the energy deposit in the  $5 \times 5$  crystal array  $E_{25}$  is useful for electron identification.
- The lateral moment of the cluster defined by 
$$mom_{\text{LAT}} = \frac{\sum_{i=3}^n E_i r_i^2}{\sum_{i=3}^n E_i r_i^2 + E_1 r_0^2 + E_2 r_0^2}$$
 with
  - $n$ : number of crystals associated to the shower.
  - $E_i$ : deposited energy in the  $i$ -th crystal with  $E_1 \geq E_2 \geq \dots \geq E_n$ .
  - $r_i$ : lateral distance between the central and the  $i$ -th crystal.
  - $r_0$ : the average distance between two crystals.
- A set of zernike moments [5] which describe the energy distribution within a cluster by radial and angular dependent polynomials. An example is given in Fig. 9.8, where the zernike moment  $z_{31}$  is illustrated for all particle types.

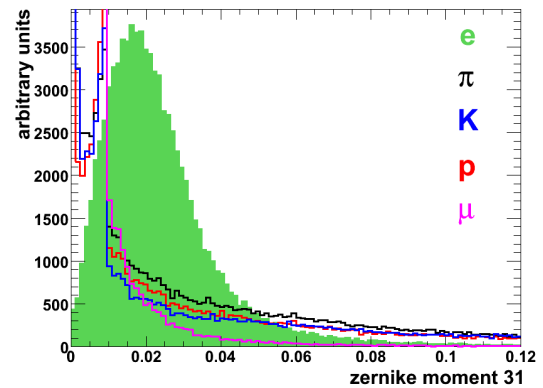


**Figure 9.8:** Zernike moment  $z_{31}$  for electrons, muons and hadrons.

Due to the fact that a lot of partially correlated EMC properties are suitable for electron identification, a Multilayer Perceptron (MLP) has been applied. The advantage of a neural network is that it can provide a correlation between a set of input variables and one or several output variables without any knowledge of how the output formally depends on the input. Such techniques are also successfully used by other HEP experiments [6, 7].

The training of the MLP has been done with a data set of 850.000 single tracks for each particle species ( $e$ ,  $\mu$ ,  $\pi$ ,  $K$  and  $p$ ) in the momentum range between 200 MeV/ $c$  and 10 GeV/ $c$  in such a way that the output values are constrained to be 1 for electrons and -1 for all other particle types. 10 input variables in total have been used, namely  $E/p$ ,  $p$ , the polar angle  $\Theta$  of the cluster, and 7 shower shape parameters ( $E_1/E_9$ ,  $E_9/E_{25}$ , the lateral moment of the shower and 4 zernike moments). The response of the trained network to a test data set of single particles in the momentum range between 300 MeV/ $c$  and 5 GeV/ $c$  is illustrated in Fig. 9.9. The logarithmically scaled histogram shows that an almost clean electron recognition with a quite small contamination of muons and hadrons can be obtained by applying a cut on the network output.

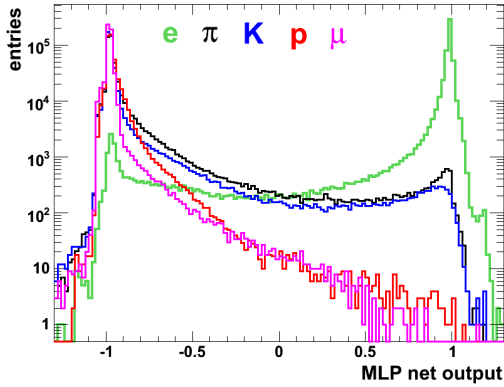


**Figure 9.9:** MLP output for electrons and the other particle species in the momentum range between 300 MeV/ $c$  and 5 GeV/ $c$ .

The global PID, which combines the PID informations of the individual sub-detectors, has been realized with the standard likelihood method. Each sub-detector provides probabilities for the different particle species, and thus a correlation between the network output and the PID likelihood of the EMC has been calculated. Fig. 9.10 shows the electron efficiency and contamination rate as a function of momentum achieved by requiring an electron like-

likelihood fraction of the EMC of more than 95%. For momenta above 1 GeV/ $c$  one can see that the electron efficiency is greater than 98% while the contamination by other particles is substantially less than 1%. For momenta below 1 GeV/ $c$  instead the electron identification obtained with just the EMC is quite bad and not sufficient.

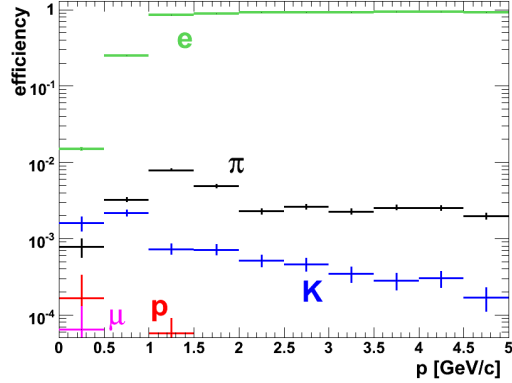


**Figure 9.10:** Electron efficiency and contamination rate for muons, pions, kaons and protons in different momentum ranges by using the EMC information.

A good electron-ID efficiency and small contamination rates can be achieved by taking into consideration additional sub-detectors (MVD, Cherenkov detectors and muon counters) (Fig. 9.11). By applying a 99.5% cut on the combined likelihood fraction, the electron efficiency becomes better than 98% while the pion misidentification is just on the  $10^{-3}$  level over the whole momentum range. The contamination rates for muons, kaons and protons are negligible.

## 9.2 Material Budget in front of the EMC

The reconstruction efficiency as well as the energy and spatial resolution of the EMC are affected by the interaction of particles with material in front of the calorimeter. While the dominant interaction process for photons in the energy range of interest is  $e^+e^-$  pair production, electrons lose energy mainly via Bremsstrahlung ( $e \rightarrow e\gamma$ ). Fig. 9.12 illustrates the material budget in front of the EMC originating from the individual sub-detectors in units of radiation lengths as a function of  $\Theta$ . The largest contribution comes from the Cherenkov detectors, which consist of quartz radiators of 1-2 cm thickness. This

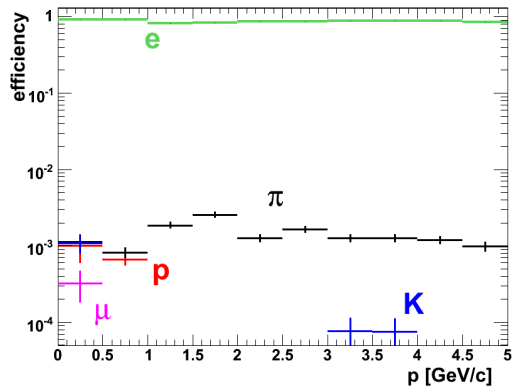


**Figure 9.11:** Electron efficiency and contamination rate for muons, pions, kaons and protons in different momentum ranges by using the combined PID informations.

corresponds to 17% to 50% of a radiation length, depending on the polar angle.

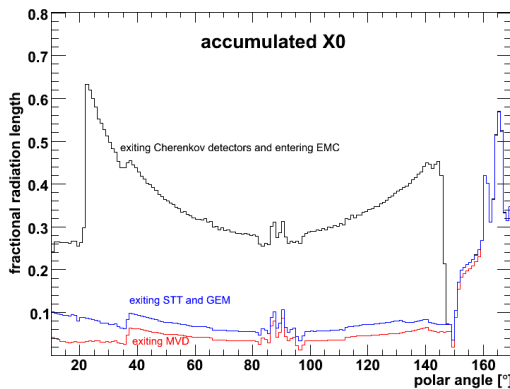


**Figure 9.12:** Material in front of the EMC in units of a radiation length  $X_0$  as a function of the polar angle  $\Theta$ .

## 9.2.1 DIRC Preshower

As Fig. 9.12 shows, the DIRC detector contributes most to the material budget in front of the EMC. Therefore detailed Monte Carlo studies have been done to investigate the impact of this device on the  $\gamma$  reconstruction efficiency and energy resolution. Fig. 9.13 represents the  $\gamma$  conversion probability in the DIRC for 1 GeV photons generated homogeneously in the  $\Theta$  range between  $22^\circ$  and  $145^\circ$ . While 15% of the photons convert at the polar angle of  $90^\circ$ , the DIRC preshower probability increases up to 27% at  $22^\circ$ .

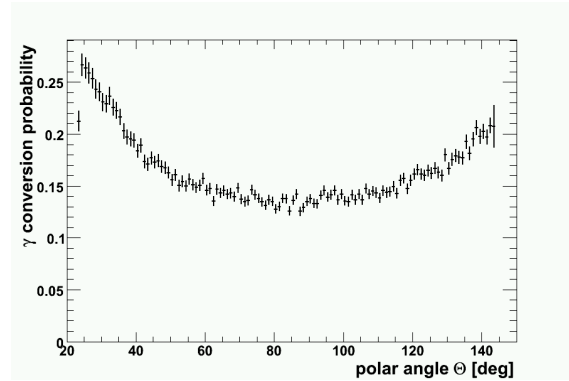


**Figure 9.13:**  $\gamma$  conversion probability in the DIRC as a function of  $\Theta$ .

DIRC preshowers mainly lead to a degradation of the energy resolution. A comparison of the reconstructed energies for 1 GeV photons with and without DIRC preshowers is shown in Fig. 9.14. While the energy distribution for non-preshower photons can be well described by a Gaussian function with  $\sigma(\Delta E/E) < 2\%$ , the distribution for DIRC preshower clusters becomes significantly worse. Due to the fact that a fraction of the photon energy is deposited in the quartz bars, a broad and asymmetric distribution with a huge low energy tail shows up.

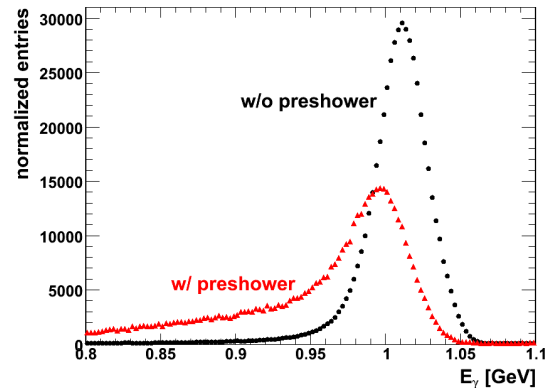


**Figure 9.14:** Reconstructed energy of 1 GeV photons without (black circles) and with (red triangles) DIRC preshowers. For a better comparison the plot with DIRC preshowers is scaled by a factor of 4.87.

### 9.2.1.1 Outlook: Preshower Recognition and Energy Correction.

If the Cherenkov light originating from the produced  $e^+e^-$  pairs gets measured, the number of

detected Cherenkov photons provides a measure for the energy loss, and thus an energy correction of such clusters could be feasible. A DIRC preshower recognition with an additional energy correction would yield in a better performance of the photon reconstruction.

Based upon recent investigations for the BaBar experiment, it is expected to achieve a DIRC preshower detection efficiency of better than 50% and an improvement for the photon energy resolution of more than 1% [8].

## 9.3 Benchmark Studies

As discussed in the introduction of this document, the PANDA physics program covers many fields and the addressed topics range from light and charm hadron spectroscopy over the study of charm in nuclear matter and the measurement of the proton form-factors. To fulfill the requirements defined by the different fields, the EMC is essential in many cases. To demonstrate that the proposed PANDA detector and in particular the EMC is able to reach the defined goals, detailed Monte Carlo studies have been performed. In the following the results of these benchmark studies will be presented, where the EMC plays a major role. These studies cover charmonium spectroscopy as well as the measurement of the time-like electromagnetic form-factors of the proton. In the field of charmonium spectroscopy recent observations of new states [9] falling into the mass range of the charmonium system, underline the importance of the ability to detect these states in as many decay modes as possible to compare the observed decay patterns with theoretical expectations, and thus understand the nature of these states. For the envisaged comprehensive study of the charmonium system at PANDA this implies the detection of hadronic, leptonic and radiative decay modes, where the final states can consist out of charged and neutral particles. Therefore photons have to be detected with precise energy and spatial resolution over a wide energy range and an excellent coverage of the solid angle. For the reconstruction of leptonic decays to  $e^+e^-$  (i.e.,  $J/\psi$  and  $\psi(2S)$  decays) the EMC supplements the PID capabilities of the other detector components and provides together with these a clean identification of electrons. This is also crucial for the measurement of the electromagnetic proton form factors in the time-like region via the process  $\bar{p}p \rightarrow e^+e^-$ , where the rejection of the dominant  $\bar{p}p \rightarrow \pi^+\pi^-$  background requires an excellent separation of electrons and pions.

### 9.3.1 $h_c$ Detection with the $h_c \rightarrow \eta_c \gamma$ Decay and the Role of low Energy $\gamma$ -ray Threshold

#### 9.3.1.1 Description of the Studied Channel

$h_c$  is a singlet state of P wave charmonium ( $1^1P_1$ ) with a mass of  $M=3526 \text{ MeV}/c^2$ . One of its main decay modes is the electromagnetic transition to the ground state,  $\eta_c$ , with the emission of a  $\gamma$  with an energy of  $E_\gamma = 503 \text{ MeV}$ . This decay mode was previously observed by E835 [10] and CLEO [11].  $h_c$  can be observed exclusively in many decay modes of  $\eta_c$ , neutral ( $\eta_c \rightarrow \gamma\gamma$ ) or hadronic. The given analysis is based on the decay modes  $\eta_c \rightarrow \phi\phi$  with a branching fraction of  $BR = 2.6 \cdot 10^{-3}$ , and  $\phi \rightarrow K^+K^-$ ,  $BR = 0.49$ .

#### 9.3.1.2 Background Consideration

The previous observation of  $h_c$  was done in the neutral decay mode of  $\eta_c$  in  $\bar{p}p$  annihilations [10], or in hadronic decay modes of  $\eta_c$  from  $e^+e^- \rightarrow \Psi(2S) \rightarrow \pi^0 h_c, h_c \rightarrow \eta_c \gamma$  [11]. In PANDA, where  $h_c$  is produced in  $\bar{p}p$  annihilations and the detector is capable to detect hadronic final states, the most important aspect of the analysis is the evaluation of signal to background ratios, because the production of the hadronic final states is much more enhanced in  $\bar{p}p$  annihilation in comparison to  $e^+e^-$ . For the exclusive decay mode considered in this study:

$$\bar{p}p \rightarrow h_c \rightarrow \eta_c \gamma \rightarrow \phi\phi\gamma \rightarrow K^+K^-K^+K^-\gamma$$

the following 3 reactions are considered as the main background contributors:

1.  $\bar{p}p \rightarrow K^+K^-K^+K^-\pi^0$ ,
2.  $\bar{p}p \rightarrow \phi K^+K^-\pi^0$ ,
3.  $\bar{p}p \rightarrow \phi\phi\pi^0$ .

With one  $\gamma$ -ray from the  $\pi^0$  decay left undetected, these reactions have the same signature of decay products as the studied  $h_c$  decay.

In Fig. 9.15 the energy distributions of  $\gamma$ s are presented for the signal and one of the background channels.

$\gamma$ s from  $h_c$  decays cover an energy range of [0.15; 2.0] GeV. The corresponding distribution for the background also covers all this range, but increases for small energies. If we want to recover  $\pi^0$ s to separate signal from background, the low energy

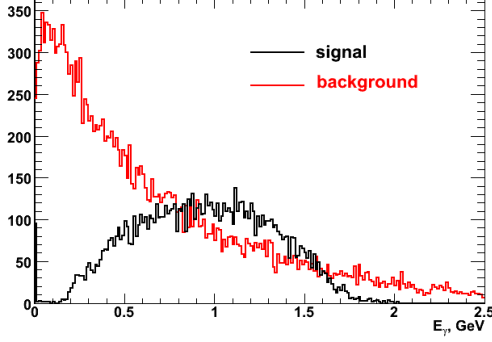


**Figure 9.15:** Energy distribution of  $\gamma$ s from  $\bar{p}p \rightarrow h_c \rightarrow \eta_c \gamma$  and  $\bar{p}p \rightarrow \phi \phi \pi^0$ .

$\gamma$  reconstruction threshold has to be as low as possible, as it was already discussed in section 9.1.1.3. Moreover, if one  $\gamma$  from the  $\pi^0$  is low energetic, the momenta of the other  $\gamma$  and the charged hadrons move closer to the total momentum of the initial  $\bar{p}p$  system. Such events pass cuts on the fit probability of the 4C-fit, and this makes a low energy threshold mandatory for applying anti-cuts on no  $\pi^0$  in the event, and correspondingly to suppress the background.

There are no measurements, to our best knowledge, of the cross-sections of the studied background reactions. The only way to estimate these cross-sections we found was to use the DPM (Dual Parton Model) event generator [12].  $10^7$  events were generated with DPM at a beam momentum of  $p_z = 5.609 \text{ GeV}/c$ , which corresponds to the studied  $h_c$  resonance. The corresponding numbers of events are 60 and 6 for the first two background channels. No event from the  $\bar{p}p \rightarrow \phi \phi \pi^0$  reaction was observed. With a total  $\bar{p}p$  cross-section at this beam momentum of 60 mb, the cross-sections for the corresponding background channels are estimated to 360 nb, 60 nb and below 6 nb, respectively.

### 9.3.1.3 Event Selection

The following selection criteria were applied to select the signal:

1. constraint on a common vertex of  $K^+$  and  $K^-$  with  $\phi$ , pre-fit selection  $\eta_c$  invariant mass window of  $[2.6;3.2] \text{ GeV}/c^2$  and  $\phi$  mass window of  $[0.8; 1.2] \text{ GeV}/c^2$ ,
2. 4C-fit to beam momentum,  $CL > 0.05$ ,
3.  $\eta_c$  invariant mass in  $[2.9;3.06] \text{ GeV}/c^2$ ,

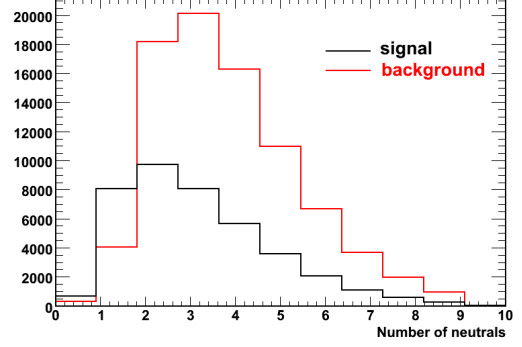


**Figure 9.16:** The number of reconstructed EMC clusters for the  $\bar{p}p \rightarrow h_c \rightarrow \eta_c \gamma$  and  $\bar{p}p \rightarrow \phi \phi \pi^0$  reactions.

4.  $E_\gamma$  within  $[0.4;0.6] \text{ GeV}$ ,
5.  $\phi$  invariant mass in  $[0.97;1.07] \text{ GeV}/c^2$ ,
6. no  $\pi^0$  candidates in the event, i.e. no 2  $\gamma$  invariant mass in the range  $[0.115;0.15] \text{ GeV}/c^2$  with 2 different low energy  $\gamma$  threshold options: 30 MeV and 10 MeV.

Fig. 9.16 presents the multiplicity distribution of reconstructed EMC clusters for the signal and one of the background channels. One may note that the mean numbers of clusters, i.e. neutral candidates, significantly exceed one, expected for the signal, or two expected for the background from  $\pi^0$  decay. This is caused by hadronic split-offs and prevents the use of the number of clusters as a selection criteria. This observation emphasizes the importance of other selection criteria, in particular of the anti-cut on no  $\pi^0$  in an event. The latter strongly depends on the assumed low energy  $\gamma$ -ray threshold.

#### 9.3.1.4 Signal to Background Ratio versus low Energy $\gamma$ -ray Threshold

The efficiencies of the chosen selection criteria are given in Table 9.1 for the signal and the considered background channels.

Assuming an  $h_c$  production cross-section of 40 nb yields in the signal to background ratios given in Table 9.2.

For the  $\bar{p}p \rightarrow \phi \phi \pi^0$  background channel a reduction of the  $\gamma$ -ray threshold from 30 MeV to 10 MeV gives a 20% improvement in the signal to background ratio, for  $\bar{p}p \rightarrow \phi K^+ K^- \pi^0$  the corresponding improvement is 40%.

Selection criteria	signal	$4K\pi^0$	$\phi K^+ K^- \pi^0$	$\phi\phi\pi^0$
pre-selection	0.51	$9.8 \cdot 10^{-3}$	$1.3 \cdot 10^{-2}$	$4.9 \cdot 10^{-2}$
$CL > 0.05$	0.36	$1.6 \cdot 10^{-3}$	$2.0 \cdot 10^{-3}$	$6.8 \cdot 10^{-3}$
$m(\eta_c), E_\gamma$	0.34	$4.2 \cdot 10^{-4}$	$5.2 \cdot 10^{-4}$	$1.7 \cdot 10^{-3}$
$m(\phi)$	0.33	$1.0 \cdot 10^{-5}$	$1.2 \cdot 10^{-4}$	$1.7 \cdot 10^{-3}$
$no \pi^0(30MeV)$	0.27	$1.0 \cdot 10^{-5}$	$4.5 \cdot 10^{-5}$	$8.6 \cdot 10^{-4}$
$no \pi^0(10MeV)$	0.25	$5.0 \cdot 10^{-6}$	$3.0 \cdot 10^{-5}$	$7.0 \cdot 10^{-4}$

**Table 9.1:** Efficiency of different event selection criteria.

channel	signal/backgr. ratio
$\bar{p}p \rightarrow K^+ K^- K^+ K^- \pi^0$	3.5
$\bar{p}p \rightarrow \phi K^+ K^- \pi^0$	10
$\bar{p}p \rightarrow \phi\phi\pi^0$	> 6

**Table 9.2:** Signal to background ratio for different  $h_c$  background channels.

For the final signal selection efficiency of 25% and the assumed luminosity of  $L = 10^{32} \text{cm}^{-2} \text{s}^{-1}$  we expect a signal event rate of 55 events/day.

### 9.3.2 $Y(4260)$ in Formation

The recently discovered vector-state  $Y(4260)$  having a mass and width of  $(4259 \pm 8_{-6}^{+2}) \text{MeV}/c^2$  and  $(88 \pm 23_{-4}^{+6}) \text{MeV}$  [13], is observed in radiative return events from  $e^+e^-$  collisions [14] and direct formation in  $e^+e^-$  annihilation [15]. Evidence is also reported in  $B \rightarrow J/\psi \pi^+ \pi^- K$  decays [16]. The  $Y(4260)$  is found in the  $J/\psi \pi \pi$  and  $J/\psi K^+ K^-$  decay modes. Here the reaction  $Y(4260) \rightarrow J/\psi \pi^0 \pi^0$  is studied in  $\bar{p}p$ -formation and the decay chain is exclusively reconstructed via  $J/\psi \rightarrow e^+e^-$  and  $\pi^0 \rightarrow \gamma\gamma$ .

Electron candidates are identified by the global likelihood selection algorithm described in Sec. 9.1.2. For the reconstruction of  $J/\psi \rightarrow e^+e^-$  decays at least one of the lepton candidates must have a likelihood value  $L > 0.99$  while the other candidate should fulfill  $L > 0.85$ . The corresponding tracks of the  $e^+e^-$  candidates are fitted to a common vertex and an accepted candidate should have a confidence level of  $CL > 0.1\%$ . Photon candidates are formed from the clusters found in the EMC applying the reconstruction algorithm discussed in Sec. 9.1.1.1, must have an energy  $> 20 \text{MeV}$  and are combined to  $\pi^0 \rightarrow \gamma\gamma$  candidates.

Accepted  $J/\psi$  and  $\pi^0$  candidates are combined to  $J/\psi \pi^0 \pi^0$  candidates, where the  $\pi^0$  candidates should not share the same photon candidate. The

final state lepton and photon candidates are kinematically fitted by constraining the sums of their spatial momentum components and energies to the corresponding values of the initial  $\bar{p}p$  system. An accepted  $J/\psi \pi^0 \pi^0$  candidate must have a confidence level of  $CL > 0.1\%$  and the invariant mass of the  $e^+e^-$  and  $\gamma\gamma$  subsystems should be within  $[3.07; 3.12] \text{GeV}/c^2$  and  $[120; 150] \text{MeV}/c^2$ , respectively. A FWHM of  $\approx 14 \text{MeV}/c^2$  ( $\approx 7 \text{MeV}/c^2$ ) is obtained for the  $J/\psi$  ( $\pi^0$ ) signal after the kinematic fit (Fig. 9.17, Fig. 9.17). For the final event selection  $J/\psi \pi^0 \pi^0$  candidates are refitted kinematically by constraining the invariant  $e^+e^-$  mass to the  $J/\psi$  mass and the invariant  $\gamma\gamma$  mass to the  $\pi^0$  mass on top of the constraints applied to the initial  $\bar{p}p$  four-vector. Only events where exactly one valid  $J/\psi \pi^0 \pi^0$  candidate with  $CL > 0.1\%$  is found are accepted for further analysis.

To reject background from the reactions  $\bar{p}p \rightarrow J/\psi \eta \eta$  ( $\bar{p}p \rightarrow J/\psi \eta \pi^0$ ) with  $\eta \rightarrow \gamma\gamma$  the events are reconstructed and kinematically fitted similar to the fit with the  $J/\psi \pi^0 \pi^0$  signal hypothesis described above but assuming the  $J/\psi \eta \eta$  ( $J/\psi \eta \pi^0$ ) hypothesis, where  $\eta$  candidates should have an invariant mass within  $[500; 600] \text{MeV}/c^2$ . Events where at least one valid  $J/\psi \eta \pi^0$  or  $J/\psi \eta \eta$  candidate with  $CL > 0.01\%$  is found are rejected.

The reconstruction efficiency after all selection criteria is found to be 13.8%. For  $\bar{p}p \rightarrow J/\psi \eta \eta$  and  $\bar{p}p \rightarrow J/\psi \eta \pi^0$  events the suppression rate is better than  $10^4$  and the contamination of the  $J/\psi \pi^0 \pi^0$  signal with events from these reactions is expected to be negligible unless the cross sections for  $\bar{p}p \rightarrow J/\psi \eta \eta$  and  $\bar{p}p \rightarrow J/\psi \eta \pi^0$  are enhanced by more than an order of magnitude compared to the signal cross section. Another source of background which has been investigated are non-resonant  $\bar{p}p \rightarrow \pi^+ \pi^- \pi^0 \pi^0$  events. For this reaction an upper limit of  $132 \mu\text{b}$  at 90% CL can be derived from the measurement at  $\sqrt{s} = 4.351 \text{GeV}/c^2$  [17],  $92 \text{MeV}/c^2$  above the  $Y(4260)$  resonance. The cross section for the signal reaction is estimated from Ref. [18] to be in the order of 50 pb. This

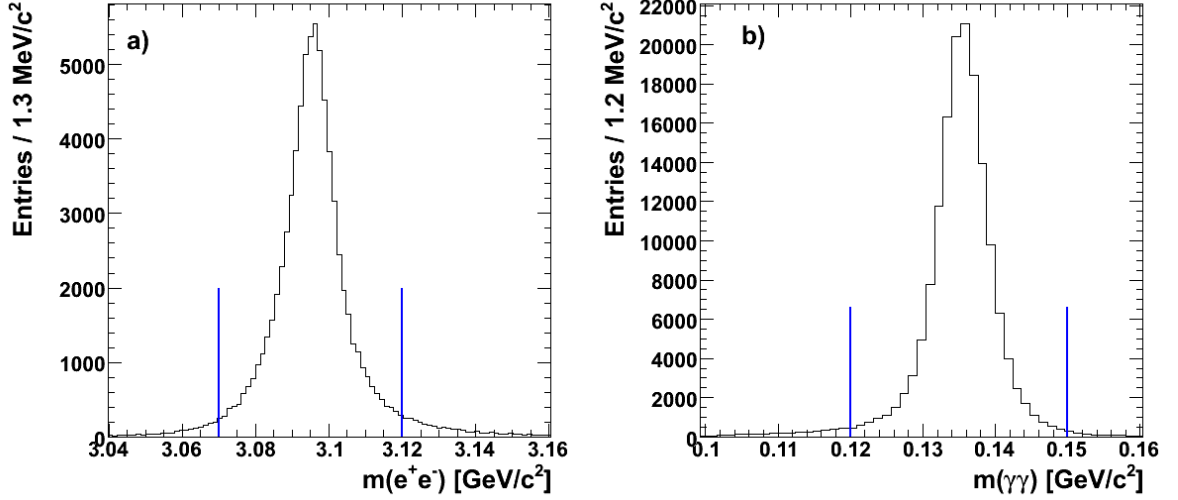


**Figure 9.17:** Invariant a)  $J/\psi \rightarrow e^+e^-$  and b)  $\pi^0 \rightarrow \gamma\gamma$  mass after the kinematic fit with constraints on the initial  $\bar{p}p$  system as described in the text. The vertical lines indicate the mass windows chosen for further selection.

requires a suppression for  $\bar{p}p \rightarrow \pi^+\pi^-\pi^0\pi^0$  of at least  $10^7$ , whereas with the currently available amount of MC events a suppression better than  $10^8$  is obtained.

In summary the reconstruction of the  $Y(4260) \rightarrow J/\psi\pi^0\pi^0$  decay mode with one  $e^+e^-$  pair and four photons in the final state yields a good detection efficiency and suppression of the dominant  $\bar{p}p \rightarrow \pi^+\pi^-\pi^0\pi^0$  background.

### 9.3.3 Charmonium Hybrid in Production

Closely connected with charmonium spectroscopy is the search for predicted exotic hadrons with hidden charm, such as charmonium molecule, tetra-quark or hybrid states. For the latter the ground state is generally expected to be a spin-exotic  $J^{PC} = 1^{-+}$  state and lattice QCD calculations predict its mass in the range between 4100 and 4400 MeV/ $c^2$  [19, 20, 21]. In  $\bar{p}p$  annihilation this state can be produced only in association with one or more recoiling particles. Here the results of a study assuming the production of a state having a mass 4290 MeV/ $c^2$  and a width of 20 MeV together with a  $\eta$  meson are reported.

Flux-tube model calculations predict for a hybrid state of this mass suppressed decays to open charm with respect to hidden charm decays [22]. An OZI-allowed decay to hidden charm would be the tran-

sition to  $\chi_{c1}$  with emission of light hadrons, preferable scalar particles [23]. The lightest scalar system is composed out of two neutral pions in a relative  $s$ -wave.

In the study the decay of the charmonium hybrid (labeled as  $\psi_g$  in the following) to  $\chi_{c1}\pi^0\pi^0$  with the subsequent radiative  $\chi_{c1} \rightarrow J/\psi\gamma$  decay with  $J/\psi$  decaying to a lepton pair  $e^+e^-$  is considered. The recoiling meson is reconstructed from the decay  $\eta \rightarrow \gamma\gamma$ . The total branching fraction for the subsequent  $\psi_g$  and  $\eta$  decays is given by  $\mathcal{B}(\psi_g \rightarrow \chi_{c1}\pi^0\pi^0) \times 0.81\%$ , where  $\mathcal{B}(\psi_g \rightarrow \chi_{c1}\pi^0\pi^0)$  is the unknown branching fraction of the  $\psi_g$  decay.

Photon candidates are selected from the clusters found in the EMC with the reconstruction algorithm explained in Sec. 9.1.1.1. Two photon candidates are combined and accepted as  $\pi^0$  and  $\eta$  candidates if their invariant mass is within the interval [115;150] MeV/ $c^2$  and [470;610] MeV/ $c^2$ , respectively.

For the reconstruction of  $J/\psi$  decays two candidates of opposite charge, both identified as electrons applying the likelihood selection algorithm described in Sec. 9.1.2, where one of the candidates should have a likelihood value  $L > 0.2$  and the other a value  $L > 0.85$ , are combined and accepted as  $J/\psi$  candidates if their invariant mass is within the interval [2.98; 3.16] GeV/ $c^2$ . The corresponding tracks of the two lepton candidates are kinematically and geometrically fitted to a common vertex and their

invariant mass is constrained to the nominal  $J/\psi$  mass.

Afterwards  $\chi_{c1} \rightarrow J/\psi \gamma$  candidates are formed by combining accepted  $J/\psi$  and photon candidates, whose invariant mass is within the range 3.3–3.7 GeV/ $c^2$ . From these  $\chi_{c1} \pi^0 \pi^0 \eta$  candidates are created, where the same photon candidate does not occur more than once in the final state. The corresponding tracks and photon candidates of the final state are kinematically fitted by constraining their momentum and energy sum to the initial  $\bar{p}p$  system and the invariant lepton candidates mass to the  $J/\psi$  mass. Accepted candidates must have a confidence level of  $CL > 0.1\%$  and the invariant mass of the  $J/\psi \gamma$  subsystem should be within the range [3.49; 3.53] GeV/ $c^2$ , whereas the invariant mass of the  $\eta$  candidates must be within the interval [530; 565] MeV/ $c^2$ . A FWHM of  $\approx 13$  MeV/ $c^2$  is observed for the  $\chi_{c1}$  and  $\eta$  signals (Fig. 9.18) after the kinematic fit.

For the final event selection the same kinematic fit is repeated with additionally constraining the invariant  $\chi_{c1}$ ,  $\pi^0$  and  $\eta$  invariant mass to the corresponding nominal mass values. Candidates having a confidence level less than 0.1% are rejected. If more than one candidate is found in an event, the candidate with the biggest confidence level is chosen for further analysis.

The reconstruction efficiency after all selection criteria is 3.1%. The invariant  $\chi_{c1} \pi^0 \pi^0$  mass is shown in Fig. 9.19. The  $\psi_g$  signal has a FWHM of 27 MeV/ $c^2$ .

The final state with 7 photons and an  $e^+e^-$  lepton pair originating from  $J/\psi$  decays has a distinctive signature and the separation from light hadron background should be feasible. Another source of background are events with hidden charm, in particular events including a  $J/\psi$  meson. This type of background has been studied by analyzing  $\bar{p}p \rightarrow \chi_{c0} \pi^0 \pi^0 \eta$ ,  $\bar{p}p \rightarrow \chi_{c1} \pi^0 \eta \eta$ ,  $\bar{p}p \rightarrow \chi_{c1} \pi^0 \pi^0 \pi^0 \eta$  and  $\bar{p}p \rightarrow J/\psi \pi^0 \pi^0 \pi^0 \eta$ . The hypothetical hybrid state is absent in these reactions, but the  $\chi_{c0}$  and  $\chi_{c1}$  mesons decay via the same decay path as for signal. Therefore these events have a similar topology as signal events and could potentially pollute the  $\psi_g$  signal. The suppression after application of all selection criteria is found to be  $4 \cdot 10^3$  ( $\bar{p}p \rightarrow \chi_{c0} \pi^0 \pi^0 \eta$ ),  $2 \cdot 10^4$  ( $\bar{p}p \rightarrow \chi_{c1} \pi^0 \eta \eta$ ),  $> 1 \cdot 10^5$  ( $\bar{p}p \rightarrow \chi_{c1} \pi^0 \pi^0 \pi^0 \eta$ ) and  $9 \cdot 10^4$  ( $\bar{p}p \rightarrow J/\psi \pi^0 \pi^0 \pi^0 \eta$ ). Therefore only low contamination of the  $\psi_g$  signal from this background reactions is expected.

### 9.3.4 Time-like Electromagnetic Form-Factors

The electric ( $G_E$ ) and magnetic ( $G_M$ ) form factors of the proton parameterize the hadronic current in the matrix element for elastic electron scattering  $e^+e^- \rightarrow \bar{p}p$  and in its crossed process  $\bar{p}p \rightarrow e^+e^-$  annihilation. The form-factors are analytic functions of the four momentum transfer  $q^2$  ranging from  $q^2 = -\infty$  to  $q^2 = +\infty$ . The annihilation process allows to access the formfactors in the time-like region ( $q^2 > 0$ ) starting from the threshold of  $q^2 = 4m_p^2c^4$ . Measurements are concentrated to the region near threshold and few data points in the  $q^2$  range between 8.8 (GeV/ $c$ ) $^2$  and 14.4 (GeV/ $c$ ) $^2$  [24]. Thus the determination for low to intermediate momentum transfer remains an open question. This region can be accessed at PANDA between  $q^2 = 5$  (GeV/ $c$ ) $^2$  and  $q^2 = 22$  (GeV/ $c$ ) $^2$ . The differential cross section for the reaction  $\bar{p}p \rightarrow e^+e^-$  is given by [25]

$$\frac{d\sigma}{d\cos\theta} = \frac{\pi\alpha^2(\hbar c)^2}{8m_p^2\sqrt{\tau}(\tau-1)} \left( |G_M|^2 (1 + \cos^2\theta) + \frac{|G_E|^2}{\tau} (1 - \cos^2\theta) \right) \quad (9.4)$$

with  $\tau = s/4m_p^2c^4$ , where  $\theta$  is the angle between the electron and the antiproton beam in the center of mass system. The factors  $|G_E|$  and  $|G_M|$  can be determined from the angular distribution of  $\bar{p}p \rightarrow e^+e^-$  events in dependence of the beam momentum. A measurement of the luminosity will provide a measurement of both factors  $|G_E|$  and  $|G_M|$ , otherwise the absolute height of the cross section remains unknown and only the ratio  $|G_E|/|G_M|$  is accessible. However, for a precise determination of the form factors a suppression better than  $10^8$  of the dominant background from  $\bar{p}p \rightarrow \pi^+\pi^-$ , having a cross section about  $10^6$  times higher than the signal reaction is mandatory. For the simulations, a model lagrangian for the process  $\bar{p}p \rightarrow \pi^+\pi^-$  has been created and fitted to the data [26, 27, 28, 29, 30] in order to get cross section predictions at angular regions, where no data exist.

To achieve the required background suppression a good separation of electrons and pions over a wide momentum range up to  $\approx 15$  GeV/ $c$  is mandatory, where the PID information from the individual detector components has to be exploited. In particular information from the EMC is important in the high momentum range where PID measurements from the tracking, Cherenkov and muon detectors do not allow to distinguish between the two species.

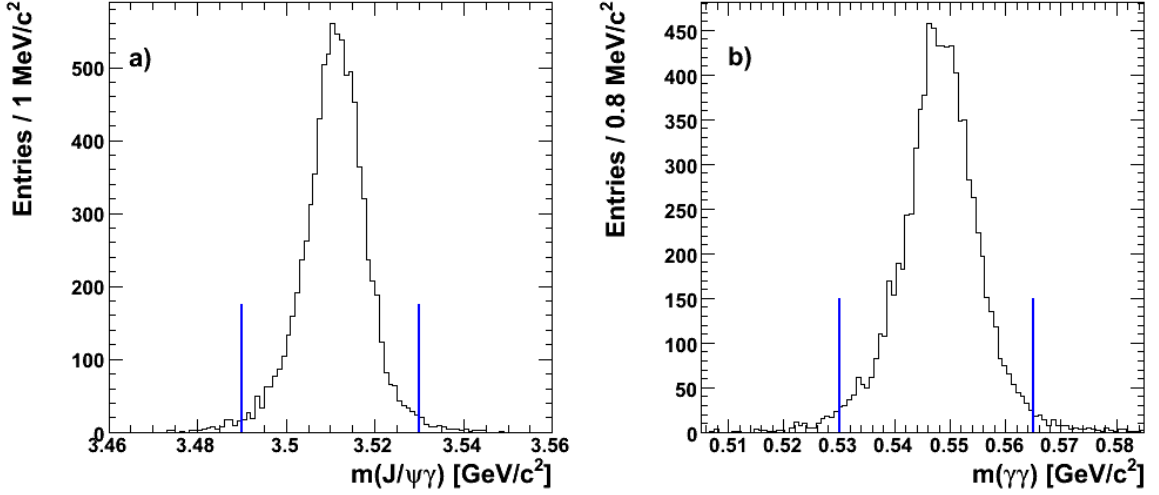


**Figure 9.18:** Invariant a)  $\chi_{c1} \rightarrow J/\psi \gamma$  and b)  $\eta \rightarrow \gamma \gamma$  mass after the kinematic fit with constraints on the initial  $\bar{p}p$  system as described in the text. The vertical lines indicate the mass windows chosen for further selection.

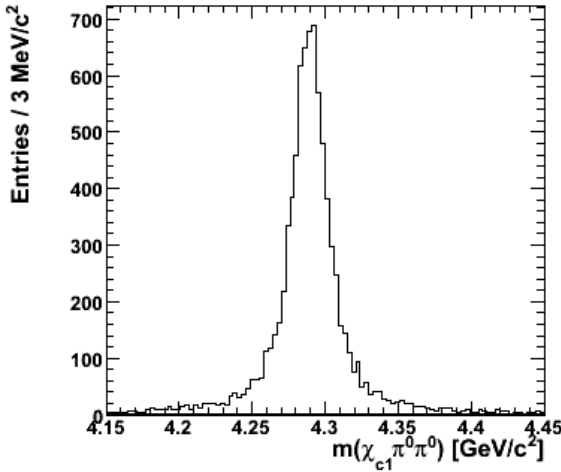


**Figure 9.19:** Invariant  $\chi_{c1} \pi^0 \pi^0$  mass after the kinematic fit with constraints on the initial  $\bar{p}p$  system and resonances as described in the text.

For the reconstruction of  $\bar{p}p \rightarrow e^+e^-$  two candidates identified as electrons (see Sec. 9.1.2) having a likelihood value  $> 0.998$  are combined. The two tracks are kinematically fitted by constraining the sum of the four-momenta to the four-momentum of the initial  $\bar{p}p$  system and are accepted as a  $e^+e^-$  candidate if the fit converges. The same fit is repeated but assuming pion hypothesis for the two tracks. For events where more than one valid  $e^+e^-$  candidate is found, only the candidate with the biggest confidence level is considered for further

analysis.

For the measurement of  $|G_E|$  and  $|G_M|$  the angle  $\theta$  between the  $e^+$  candidate's direction of flight and the beam axis is computed in the center of mass system. The obtained  $\cos(\theta)$  distribution is corrected by the  $\cos(\theta)$ -dependent reconstruction efficiency. In lack of an absolute luminosity measurement for MC data only the ratio  $|G_E|/|G_M|$  can be determined from a fit to the corrected  $\cos(\theta)$  distribution. In Fig. 9.20 the corrected distribution for  $\sqrt{s} = 3.3 \text{ GeV}/c$  is shown exemplarily, whereas a ratio  $|G_E|/|G_M|$  of 0, 1 and 3 has been assumed in the simulation. The values  $-0.14 \pm 0.07$ ,  $1.04 \pm 0.02$  and  $2.98 \pm 0.03$  derived from a fit to these distributions are in good agreement with the input values of the simulation.

Currently,  $10^8$  MC events are available for the background process  $\bar{p}p \rightarrow \pi^+\pi^-$  at a beam momentum of  $3.3 \text{ GeV}/c$  and additionally the same amount for the same process at a beam momentum of  $7.9 \text{ GeV}/c$ . Figure Fig. 9.21 shows the rejection of  $\bar{p}p \rightarrow \pi^+\pi^-$  when we apply different cuts based on PID and kinematical fits. We find 2 out of  $10^8$  events misinterpreted as electron positron pairs at a beam momentum of  $3.3 \text{ GeV}/c$  based on PID only and 0 events out of  $10^8$  events misinterpreted if we add kinematical constraints. The respective numbers for a beam momentum of  $7.9 \text{ GeV}/c$  are 8 events misinterpreted out of  $10^8$  from PID only, and 0 events out of  $10^8$  when adding kinematical constraints.

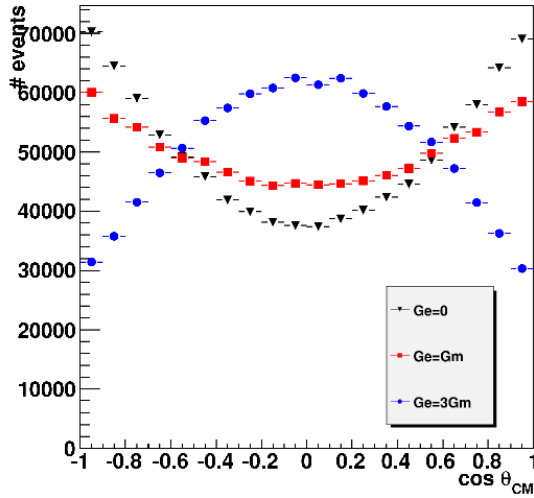


**Figure 9.20:** Angular distribution for reconstructed  $\bar{p}p \rightarrow e^+e^-$  events at an incident beam momentum of 3.3 GeV/c after efficiency correction. For the ratio of the form-factors  $|G_E|/|G_M|$  a value of 0 (black), 1 (red) and 3 (blue) has been assumed in the simulation.

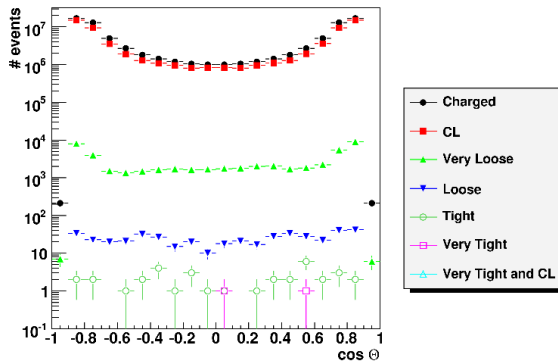


**Figure 9.21:** Angular distribution for reconstructed  $\bar{p}p \rightarrow \pi^+\pi^-$  events at an incident beam momentum of 3.3 GeV/c. Different colors represent different cuts. When requiring a probability to be an electron greater than 99.8 % (from a combined PID analysis of EMC, DIRC, MVD and STT), we have only two out of  $10^8$  simulated and reconstructed  $\bar{p}p \rightarrow \pi^+\pi^-$  events which are misinterpreted as an electron positron pair. If we add the constraints from the kinematical fit, there are no misidentified  $\bar{p}p \rightarrow \pi^+\pi^-$  events left over out of the  $10^8$  simulated  $\bar{p}p \rightarrow \pi^+\pi^-$  events. In the case of 7.9 GeV/c beam momentum 8 events out of  $10^8$   $\bar{p}p \rightarrow \pi^+\pi^-$  events are left over after PID cuts. Those 8 events are also rejected by adding the constraints from the kinematical fit.

## References

[1] J. Allison et al., IEEE Transactions on Nuclear Science **53**, 270 (2006).

- [2] S. Agostinelli et al., Nucl. Instrum. Meth. **A506**, 250 (2003).
- [3] B. Aubert et al., Nucl. Instrum. Meth. **A479**, 1 (2002).
- [4] P. Strother, *Design and application of the reconstruction software for the BaBar calorimeter*, PhD thesis, 1998, University of London and Imperial College, UK.
- [5] F. Zernike, Physica 1, 689 (1934).
- [6] H. Abramowicz, A. Caldwell, and R. Sinkus, Nucl. Instrum. Meth. **A365**, 508 (1995).
- [7] V. Breton et al., Nucl. Instrum. Meth. **A362**, 478 (1995).
- [8] A. Adametz, Preshower Measurement with the Cherenkov Detector of the BaBar Experiment, 2005, Diploma Thesis, University of Heidelberg, Germany.
- [9] E. S. Swanson, Phys. Rept. **429**, 243 (2006), and references therein.
- [10] M. Andreotti et al., Phys. Rev. **D72** (2005).
- [11] J. Rosner et al., Phys. Rev. Lett. **95** (2005).
- [12] A. Capella et al., Phys. Rept. **236** (1994).
- [13] W.-M. Yao et al., J. Phys. **G33**, 1 (2006).
- [14] B. Aubert et al., Phys. Rev. Lett. **95**, 142001 (2005).
- [15] T. E. Coan et al., Phys. Rev. Lett. **96**, 162003 (2006).
- [16] B. Aubert et al., Phys. Rev. **D73**, 011101 (2006).
- [17] E. J. Flaminio, D. J. Hansen, D. R. O. Morrison, and N. Tovey, Compilation of Cross Section, 1970, CERN/HERA 70-5.
- [18] M. Negrini, *Measurement of the branching ratios  $\psi' \rightarrow J/\psi X$  in the experiment E835 at FNAL*, PhD thesis, 2003, FERMILAB-THESIS-2003-12.
- [19] C. W. Bernard et al., Phys. Rev. **D56**, 7039 (1997).
- [20] F. E. Close et al., Phys. Rev. **D57**, 5653 (1998).
- [21] P. R. Page, Acta Phys. Polon. **B29**, 3387 (1998).

- [22] P. R. Page, Phys. Lett. **B402**, 183 (1997).
- [23] C. Michael, Beyond the quark model of hadrons from lattice QCD, 2002, International Conference On Quark Nuclear Physics.
- [24] M. Ambrogiani et al., Phys. Rev. **D60**, 032002 (1999), and references therein.
- [25] A. Zichichi et al., Nuovo Cim. **24**, 170 (1962).
- [26] E. Eisenhandler et al., Nucl. Phys. B **96**, 109 (1975).
- [27] T. Buran et al., Nucl. Phys. B **116**, 51 (1976).
- [28] T. Berglund et al., Nucl. Phys. B **137**, 276 (1978).
- [29] R. Dulude et al., Phys. Lett **79B**, 329 (1978).
- [30] T. Armstrong et al., Phys. Rev. D **56**, 2509 (1997).



## 10 Performance

---

As documented by the intrinsic performance of individual crystals of the present quality of PWO-II, such as luminescence yield, decay kinetics and radiation hardness and the additional gain in light yield due to cooling down to  $T=-25^{\circ}\text{C}$ , there is presently no alternative scintillator material for the electromagnetic calorimeter of  $\overline{\text{PANDA}}$  besides lead tungstate. The general applicability of PWO for calorimetry in High-Energy Physics has been promoted and finally proven by the successful realization of the CMS/ECAL detector as well as the photon spectrometer ALICE/PHOS, both installed at LHC.

The necessary mass production of high-quality crystals has been achieved primarily at BTCP and North Crystals in Russia and SICCAS in China. However, driven by the much more stringent requirements to perform the Physics program of  $\overline{\text{PANDA}}$ , from the beginning it became mandatory to search for a significantly higher scintillation yield in order to extend photon detection down to the MeV energy range. Beyond the realization of a nearly perfect crystal the operation at temperatures well below room temperature will reduce the effect of the thermal quenching of the scintillation process and improve the photon statistics. The spectrometer PHOS is following the same line. Our requirements are even more stringent, since the target spectrometer EMC of  $\overline{\text{PANDA}}$  has to cover nearly the full solid angle and stresses even more the concept of thermal insulation and cooling.

The test experiments to prove the concept and applicability of PWO have concentrated on the response to photons and charged particles at energies below 1 GeV, since those results are limited by the photon statistics of the scintillator, the sensitivity and efficiency of the photo sensor and the noise contributions of the front-end electronics. The conclusions are drawn based on crystal arrays comprising up to 25 modules. The individual crystals have a final length of 200 mm and a rectangular cross section of  $20 \times 20 \text{ mm}^2$ . Only the most recently assembled array PROTO60 consists of 60 crystals in  $\overline{\text{PANDA}}$  geometry. The tapered shape will improve the light collection due to the focusing effect of the geometry as known from detailed simulations at CMS/ECAL.

The performance tests completed up to now have been aiming at two complementary aspects. On one hand, the quality of full size PWO-II crystals has to be verified by in-beam measurements with en-

ergy marked photons covering the most critical energy range up to 1 GeV. Therefore, the scintillator modules were readout with standard photomultiplier tubes (Philips XP1911) with a bi-alkali photocathode, which covers  $\sim 35\%$  of the crystal endface with a typical quantum efficiency of  $\text{QE}=18\%$ . The noise contribution of the sensor can be neglected and the fast response allows an estimate of the time response. All achieved resolutions, which have been deduced at various operating temperatures, can be considered as benchmark limits for further studies including simulations and electronics development.

The second R&D activity was aiming to come close to the final readout concept with large area avalanche photodiodes (LAAPD), which are mandatory for the operation within the magnetic field. The new developments of the sensor as well as the parallel design of an extremely low-noise and low-power preamplifier, based on either discrete components or customized ASIC technology, are described in detail in separate chapters. All the reported results are performed by collecting and converting the scintillation light with a single quadratic LAAPD of  $10 \times 10 \text{ mm}^2$  active area with a quantum efficiency above  $60\%$ . The final readout considers two LAAPDs of identical surface but rectangular shape to fit on the crystal endface, which is presently prevented by the dead space of the ceramic support. The reported experiments are using in addition individual low-noise preamplifiers and commercial electronics for the digitization. Again, the present data deliver a lower limit of the final performance, which will be achieved with twice the sensor surface.

In order to simulate the operation of large arrays, the mechanical support structures, cooling and temperature stabilization concepts and long term stabilities, a large prototype comprising 60 tapered crystals in  $\overline{\text{PANDA}}$ -geometry has been designed and brought into operation. First in-beam tests are scheduled in summer 2008. In a next iteration, a mechanical prototype for housing 200 crystals is presently under construction. This device is primarily meant for studying stable operation and cooling simulating two adjacent detector slices of the barrel section of the EMC.

In spite of some compromises compared to the final concept, the achieved resolutions represent excellent lower limits of the performance to be expected. Operation at  $T=-25^{\circ}\text{C}$  using a photomulti-

plier readout delivers an energy resolution of  $\sigma/E = 0.95\%/\sqrt{E} + 0.91\%$  ( $E$  given in GeV) for a  $3\times 3$  sub-array accompanied with time resolutions below  $\sigma=130$  ps. The complementary test using a single LAAPD for readout reaches even at  $T=0^\circ\text{C}$  a fully sufficient resolution of  $\sigma/E = 1.86\%/\sqrt{E} + 0.65\%$  ( $E$  given in GeV). Timing information can be expected with an accuracy well below 1 ns for energy depositions above 100 MeV. Summarizing, according to the detailed simulations and the selected test results, operation of the calorimeter at  $T=-25^\circ\text{C}$  will allow to perform the very ambitious research program, even if radiation damage at most forward directions might reduce asymptotically the light output by up to 30%.

## 10.1 Results from Prototype Tests

### 10.1.1 Energy Resolution of PWO arrays

Almost in parallel to the research project for CMS/ECAL, investigations have been started to explore the applicability of PWO in the low and medium energy regime. Beside the response to low energy  $\gamma$ -rays of radioactive sources the initial pilot experiments used electrons as well as energy marked photons at the tagging facility of MAMI at Mainz [1] between 50 and 850 MeV energy [2, 3]. The crystals were rectangular of 150 mm length and with a quadratic cross section of  $20\times 20\text{mm}^2$  with all sides optically polished. The quality was similar to CMS samples of the pre-production runs and contained slow decay components on the percent level due to Mo-contamination. The readout of the scintillation light was achieved with photomultiplier tubes and commercial electronics of NIM and CAMAC standard. In most of the cases the anode signals were carried via RG58 coaxial cables over a distance of 30 – 50 m outside the experimental area to the DAQ system. For practical reasons, energy and time information were deduced and digitized after long passive delays, causing a significant signal attenuation and loss of the high-frequency response. The compact detector arrays were operated at a stabilized temperature, always above  $T=0^\circ\text{C}$  but slightly below room temperature. Keeping the crystals at a fixed temperature had to guarantee stable operation, not with the intention to increase the luminescence yield.

The response to monoenergetic photons showed for the first time an excellent energy resolution

even for photons well below the expected range for CMS/ECAL. Resolution values of  $\sigma/E = 1.54\%/\sqrt{E} + 0.30\%$  ( $E$  given in GeV) were achieved for a matrix of  $5\times 5$  elements and in addition time resolutions of  $\sigma_t \leq 130$  ps for photon energies above 25 MeV [4].

Besides the studies using low and high-energy photons exploratory experiments at KVI, Groningen, and COSY, FZ Jülich, have delivered results for low and high energy protons and pions [5]. However, in all these cases PWO of standard quality according to the CMS specifications was used. For protons, which are completely stopped in a crystal of 150 mm length, an energy resolution of  $\sigma/E = 1.44\%/\sqrt{E} + 1.97\%$  ( $E$  given in GeV) has been extracted as an upper limit, since the proton energy had to be deduced from the time of flight measured using a fast plastic start counter. For 90 MeV protons typical resolutions between 4% and 5% were obtained.

In the following chapters, the obtained experimental results are based on scintillator crystals, which correspond to the performance parameters of PWO-II [6].

#### 10.1.1.1 Energy Response Measured with Photomultiplier Readout

As outlined in the previous chapters on PWO (Sec. 4.1) the specifications of the calorimeter can be further optimized by the reduction of the thermal quenching of the relevant scintillation process by cooling the crystals down to temperatures as low as  $T=-25^\circ\text{C}$ , which leads to a significant increase of the light yield by a factor 4 compared to  $T=+25^\circ\text{C}$ . For a typical PWO-II crystal 500 photons can be collected at the endface of a 200 mm long crystal for an energy deposition of 1 MeV at 100% quantum efficiency.

The reported experiments [7] are based on large size crystals of 200 mm length grouped in arrays composed of  $3\times 3$  up to  $5\times 5$  crystals manufactured at BTCF or comparable in quality grown at SICCAS. All crystals were rectangular parallelepipeds to allow in addition a direct comparison to initial pilot experiments with limited quality as stated in the previous chapter.

The temperature stabilization and the operation at significantly lower temperatures in an atmosphere free of moisture required the installation of a new experimental setup, which comprises an insulated container of large volume to house the different detector arrays with high flexibility. A computer con-



**Figure 10.1:** The experimental setup at the tagged photon facility at MAMI comprising the cooling unit (right), the connection pipe to circulate cold dry air and the insulated container for the test detectors (left).

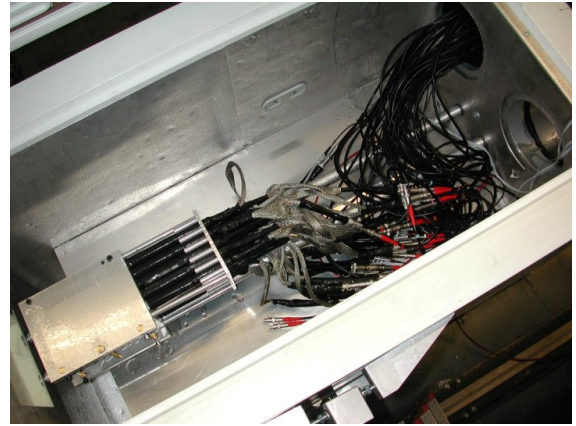


**Figure 10.3:** A typical 5x5 PWO matrix shown inside the insulated box including photomultiplier readout, signal and high voltage cables.

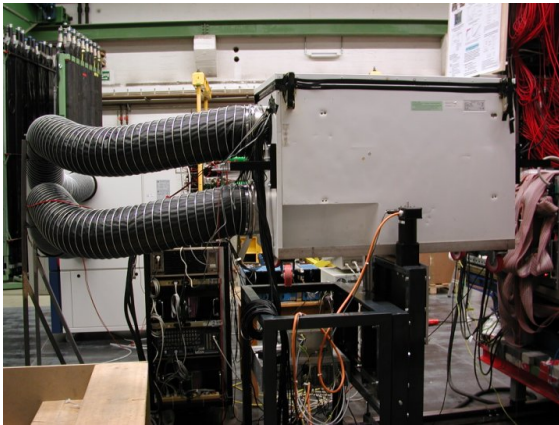


**Figure 10.2:** The insulated container to house the various test arrays. The cold air is circulated via the two black pipes.

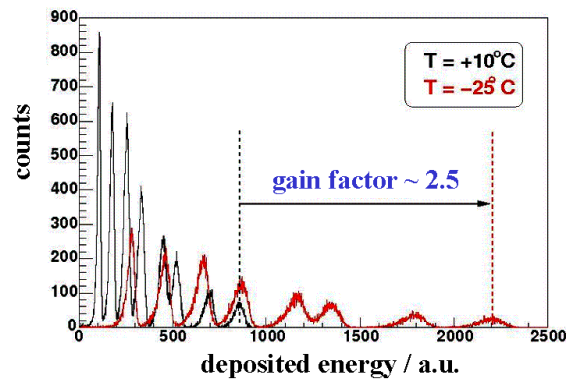


**Figure 10.4:** Lineshape of the central detector module measured at eight different photon energies and two operating temperatures. The change of the light yield due to the difference in the thermal quenching of the scintillation light can be deduced directly.

trolled cooling machine circulates cold and dry air of constant temperature via thermally insulated 5 m long pipes of large diameter to the detector container. Fig. 10.1, Fig. 10.2 and Fig. 10.3 show the experimental installation as well as details of a typical detector matrix mounted in the A2 hall at Mainz behind the CB/TAPS experiment.

The setup shown particularly in Fig. 10.3 was used to test the inner 3x3 section of a 5x5 matrix of 200 mm long crystals from BTCP, individually readout via photomultiplier tubes (Philips XP 1911). The measurement was performed at  $T=+10^{\circ}\text{C}$  and  $T=-25^{\circ}\text{C}$ , respectively, to illustrate the effect of cooling. The advantage of reduced temperatures becomes immediately obvious in Fig. 10.4 in the overlay of the response of the central de-

detector to eight different photon energies between 64 MeV and 520 MeV, respectively, measured at the two operating temperatures. The light-output was measured under identical experimental conditions of the photomultiplier bias and electronics settings and documents a gain factor of 2.6 of the overall luminescence yield.

Figure 10.5 and Fig. 10.6 show for the low temperature of  $T=-25^{\circ}\text{C}$  with reduced statistics the lineshape of the central detector, the total energy deposition in the surrounding ring of eight crystals and the integral of the full array for the two extreme photon energies. In particular at the highest energy, the persisting low energy tail indicates the significant lateral shower leakage, which lim-

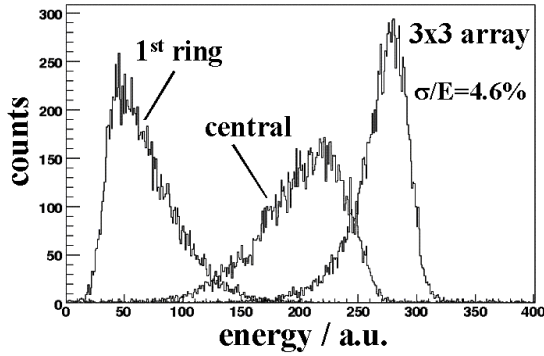


**Figure 10.5:** Response function of the  $3 \times 3$  matrix to photons of 63.8 MeV energy measured at  $T = -25^\circ\text{C}$ .

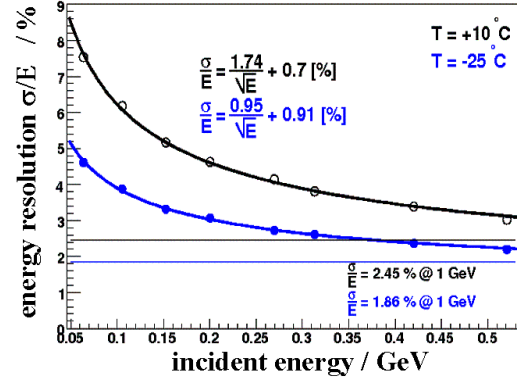


**Figure 10.7:** Comparison of the energy resolution of a  $3 \times 3$  PWO-II matrix of 200 mm long crystals measured at two different operating temperatures of  $T = -25^\circ\text{C}$  and  $T = +10^\circ\text{C}$ , respectively. The crystal responses were readout individually with photomultiplier tubes.

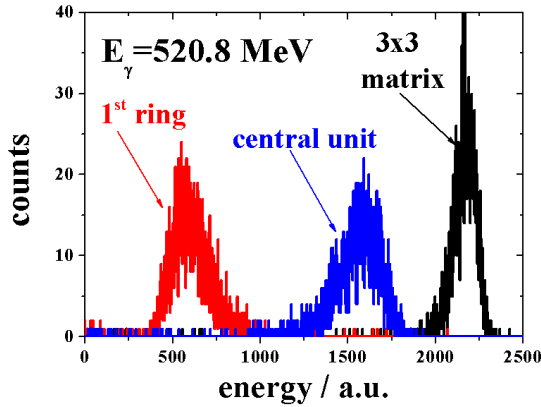


**Figure 10.6:** Response function of the  $3 \times 3$  matrix to photons of 520.8 MeV energy measured at  $T = -25^\circ\text{C}$ .

its the obtainable resolution. To parameterize the achieved energy resolution the reconstructed lineshapes of the electromagnetic showers have been fitted with an appropriate function to determine the FWHM. Finally, an excellent energy resolution of  $\sigma/E = 0.95\%/\sqrt{E} + 0.91\%$  ( $E$  given in GeV) was deduced, which represents the best resolution ever measured for PWO (see Fig. 10.7). A value well below 2% extrapolating to an incident photon energy of 1 GeV is very similar to the performance of several operating EM calorimeters, which are based on well known bright scintillator materials such as CsI(Tl), NaI(Tl) or BGO, respectively.

In comparison, the reduced energy resolution of  $\sigma/E = 1.74\%/\sqrt{E} + 0.70\%$  ( $E$  given in GeV) deduced at  $T = +10^\circ\text{C}$  is consistent with the lower light output due to thermal quenching and is quantitatively expressed by the higher statistical term in the

parametrization of the resolution [8].

In order to extend and quantify experimentally the response function to even lower energies, tests were performed at the MAX-Lab laboratory at Lund, Sweden. The tagging facility delivers low-energy photons in the energy range between 19 MeV and 50 MeV with an intrinsic photon resolution far below 1 MeV. The rectangular crystals of  $20 \times 20 \times 200 \text{ mm}^3$  were individually wrapped in Teflon and coupled to a photomultiplier tube (Philips XP 1911). The detector array was mounted in a climate chamber and cooled down to a temperature of  $T = -25^\circ\text{C}$ . The assembled detector matrix as well as the cooling unit accommodating the setup are shown in Fig. 10.8.

The individual modules have been calibrated using the energy loss of minimum ionizing muons in order to reconstruct the electromagnetic shower within the matrix. Fig. 10.9 illustrates the energy distribution within the array for an incident photon energy of 35 MeV. Nearly Gaussian-like lineshapes have been deduced for energies as low as 20 MeV as illustrated in Fig. 10.10.

Fig. 10.11 summarizes the obtained energy resolutions over the investigated range of low incident photon energies and documents the excellent performance even at the lowest energies to be studied with the target spectrometer EMC. One should consider that the readout with a standard photomultiplier represents only a lower limit compared to the future readout with two LAAPDs. They will convert a significantly higher percentage of the scintillation light, which should have a strong impact on photon

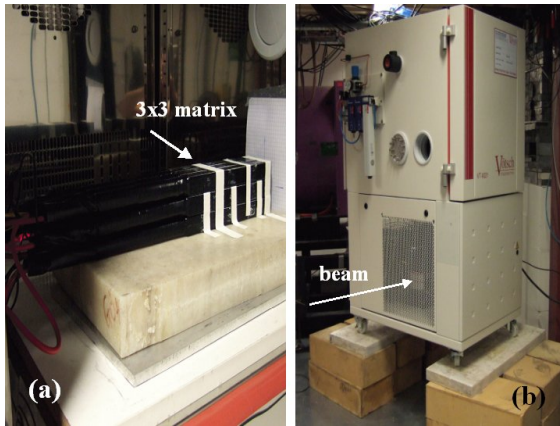


**Figure 10.8:** The 3×3 PWO-II matrix (left) and the climate chamber (right) for detector operation at low temperatures as installed for response measurements at MAX-Lab.

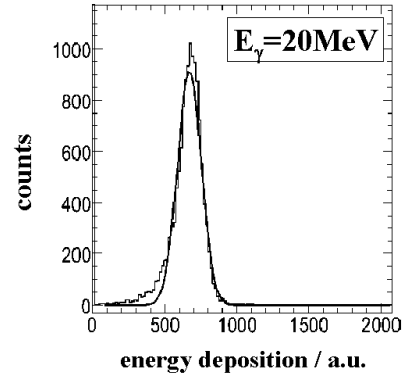


**Figure 10.10:** Response of a 3×3 PWO-II matrix to incident photons of 20 MeV energy measured at a temperature of  $T=-25^{\circ}\text{C}$  at MAX-Lab. A Gaussian-like lineshape is shown for comparison.

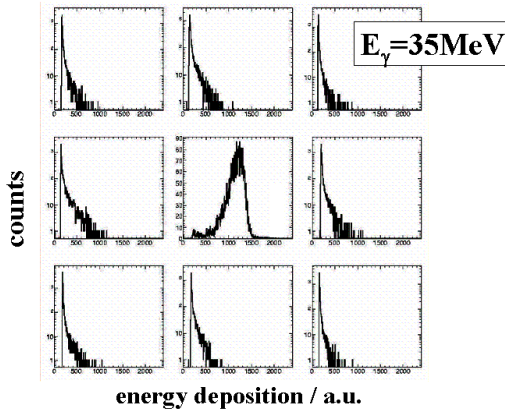


**Figure 10.9:** Energy deposition of a 35 MeV incident photon in a 3×3 PWO-II matrix measured at a temperature of  $T=-25^{\circ}\text{C}$  at MAX-Lab.

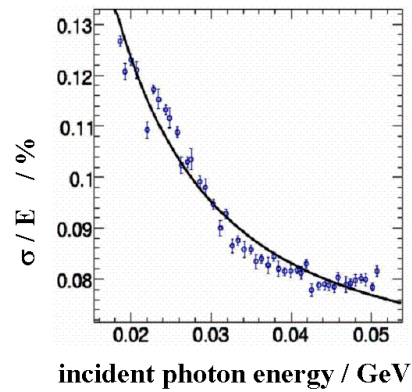


**Figure 10.11:** Experimental energy resolution of a 3×3 PWO-II matrix in the energy range between 19 MeV and 50 MeV, respectively, measured at a temperature of  $T=-25^{\circ}\text{C}$  at MAX-Lab.

detection in particular at very low energies.

#### 10.1.1.2 Energy Response Measured with LAAPD Readout

The operation of the calorimeter inside the solenoid will require a readout with LAAPD or equivalent sensors, which are not affected by strong magnetic fields. As outlined in more detail in the relevant chapters, a new low-noise and compact charge sensitive preamplifier was developed and used in prototype tests. As a test of principle, with low energy  $\gamma$ -sources and small PWO-II crystals, cooled down to  $T=-25^{\circ}\text{C}$ , a clean identification of the photopeak of  $\gamma$ -rays as low as 511 keV was demonstrated, thus indicating the low level of noise contributions.

In a first in-beam test [9] in 2004 at the tagged photon facility of MAMI at Mainz, a 3×3 matrix of 150 mm long crystals of PWO-II quality was operated at  $T=-25^{\circ}\text{C}$ . All modules were read out with  $10\times 10\text{mm}^2$  LAAPD manufactured by Hamamatsu [10]. The charge output was collected in the new charge sensitive preamplifier and passively split afterwards to integrate the signals in a spectroscopy amplifier as well as to deduce a timing information from a constant fraction discriminator after shaping in a timing filter amplifier ( $\text{INT}=50\text{ ns}$ ,  $\text{DIFF}=50\text{ ns}$ ). Both signals were transferred via 50 m coaxial cables to the DAQ system for digitization.

In spite of the long transfer lines and the miss-

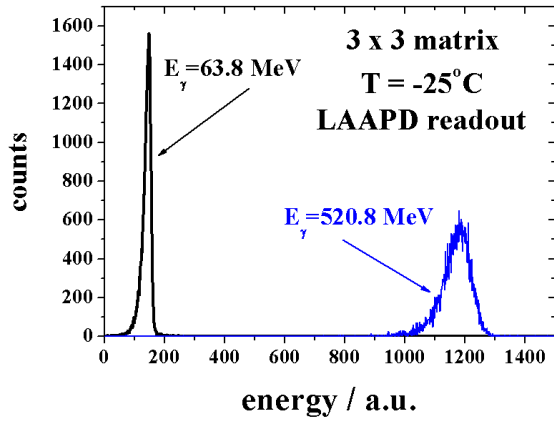


**Figure 10.12:** Response function of the  $3 \times 3$  PWO-II matrix to photons of 63.8 MeV and 520.8 MeV energy measured at  $T = -25^\circ\text{C}$ . The 150 mm long crystals are readout with LAAPDs.

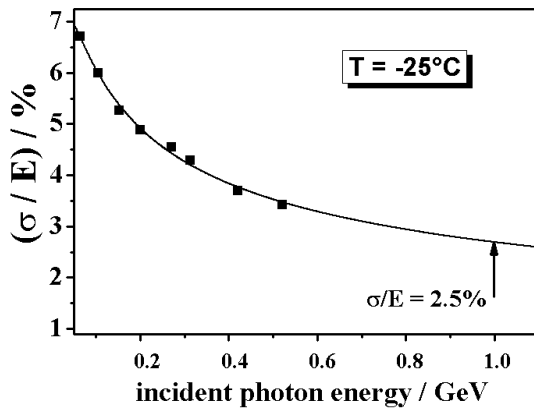


**Figure 10.13:** Energy resolution of a  $3 \times 3$  PWO-II matrix of 150 mm long crystals measured at  $T = -25^\circ\text{C}$  readout with LAAPDs.

ing option to optimize the adjustments of the electronics an excellent result has been achieved. Fig. 10.12 shows the obtained lineshape at 64 MeV and 520 MeV incident photon energy, respectively, after reconstruction of the electromagnetic shower deposited within the array. It should be mentioned that even one of the detector modules was not functioning at all. The deduced energy resolution is summarized in Fig. 10.13 and can be parameterized as  $\sigma/E = 0.90\%/\sqrt{E} \oplus 2.13\%$  ( $E$  given in GeV). The low value of the statistical factor reflects the high electron/hole statistics due to the significantly larger quantum efficiency of the avalanche diode compared to a standard alkali photocathode. The large constant term can be related to the missing detector, reduced signal/noise ratio due to

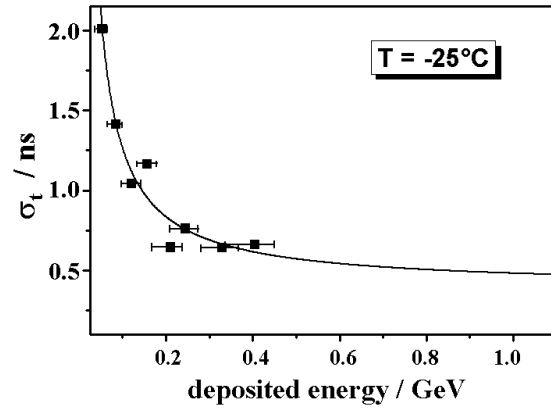


**Figure 10.14:** Time resolution of a  $3 \times 3$  PWO-II matrix of 150 mm long crystals measured at  $T = -25^\circ\text{C}$  readout with LAAPDs.

passive splitting and the not yet optimized adjustments of the used commercial electronics.

The used readout represents a first attempt to deduce as well timing information. In order to identify off-line the selected photon energies the trigger signal of the responding scintillators of the tagger ladder had to be in coincidence. The recorded time information serves as a reference with an intrinsic resolution of approximately 1.2 ns (FWHM). In spite of the by far not optimized timing measurement, a resolution of  $\sigma_t \ll 1$  ns can be reached already above the typical energy deposition in the central crystal for an incident photon energy of  $\geq 200$  MeV. The result emphasizes the excellent timing capabilities of PWO even for a readout via LAAPDs. The achieved time resolutions are summarized in Fig. 10.14.

In order to investigate a larger range of operational temperature a  $3 \times 3$  matrix of 200 mm long PWO-II crystals, produced in 2007 under more stringent specification limits, was tested at a temperature of  $T = 0^\circ\text{C}$  [11]. In addition, the rectangular crystals were covered for the first time with one layer of a thermally molded reflector foil consisting of the 3M radiant mirror film VM2000<sup>TM</sup> and mounted in a container made of carbon fibre, similar to the alveole-structure to be foreseen for the final assembly of the EMC. Detailed tests with respect to the properties of VM2000 show an increase of the collected light of 10–15% compared to a wrapping with several layers of Teflon. The matrix was mounted in an insulated container, which could be cooled down to a low temperature well stabilized ( $\Delta T < 0.1^\circ\text{C}$ ) by circulating cold and dry air similar to the setup as shown in Fig. 10.1 and

Fig. 10.2. A thin plastic scintillator covering the total front of the prototype served as a charged particle veto to reject electrons and/or positrons due to converted photons upstream of the detector. The crystal matrix could be moved remote controlled in two dimensions perpendicular to the axis of the collimated photon beam by stepping-motors to perform a relative calibration of each detector element under beam conditions. Each of the optically polished crystals was coupled to a single LAAPD using optical grease (BAYSILONE 300.000). The used prototype-2 version (S8664-1010SPL) has an active area of  $10 \times 10 \text{ mm}^2$ , a quantum efficiency of 70 % (at 420nm), a dark current of 10 nA at a gain of 50 and a capacitance of 270 pF at a gain of 50 and at a frequency of 100 kHz. The charge signal of the LAAPD was amplified with a low-noise and low-power charge sensitive preamplifier with a sensitivity of 0.5 V/pC and a small feedback time constant of 25  $\mu\text{s}$ .

The output signal of the preamplifier was fed into a 16-fold multi-functional NIM module (MESYTEC, MSCF-16), which provided a remote controllable multi-channel spectroscopic amplifier (1  $\mu\text{s}$  Gaussian shaping), timing filter amplifier (INT=DIFF=50 ns), and constant fraction discriminator to serve both the analog and logic circuit in parallel. The energy response was digitized in a peak-sensing ADC (CAEN V785N). Time information of the individual modules was deduced relative to the central module. The coincidence timing of the central crystal with one of the timing signals of the chosen tagger channels selected the event type. The energy and time information of each module together with the timing response of the relevant tagger channels were recorded event-by-event for an off-line analysis. The response function of the crystal matrix was measured for the first time at an intermediate temperature of  $T=0^\circ\text{C}$ .

The distribution of the electromagnetic shower within the  $3 \times 3$  crystal matrix has been obtained after a carefully prepared relative calibration of the individual modules. The readout concept of a common integration gate did not impose any hardware energy threshold. The absolute calibration was deduced from the simulation of the total energy deposition in the array based on a GEANT4 simulation, taking into account all instrumental details. Fig. 10.15 illustrates the measured energy distribution within the crystal matrix at an incident photon energy of 674.5 MeV. Since the cross section of the used crystals is comparable to the Molière radius, approximately 70 % of the shower energy are contained in the central module.

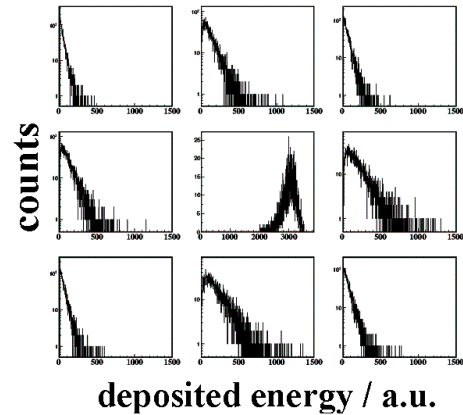


**Figure 10.15:** Distribution of the electromagnetic shower into the  $3 \times 3$  PWO-II matrix at an incident photon energy of 674.5 MeV readout with single LAAPDs as photo sensors at a temperature of  $T=0^\circ\text{C}$ .

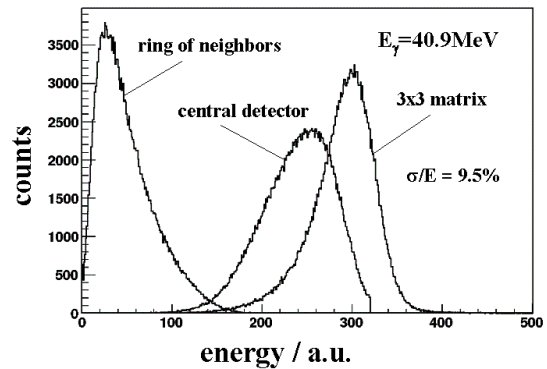


**Figure 10.16:** Experimental line shape of the  $3 \times 3$  PWO-II matrix measured at the lowest photon energy of 40.9 MeV at a temperature of  $T=0^\circ\text{C}$ . The figure shows the individual energy depositions into the central module and the surrounding ring. Each crystal was readout with a single LAAPD.

The line shape and the resulting energy resolution of the sub-array are obtained by summing event-wise the responding modules. All contributions above the pedestal were taken into account corresponding to a minimum energy threshold of approximately 1 MeV. Fig. 10.16 shows the excellent resolution of  $\sigma/E=9.5\%$  for the lowest photon energy measured in such a configuration. The corresponding distributions for the highest investigated incident energy are reproduced in Fig. 10.17.

The response of the matrix over the entire energy range follows a linear relation, both for the central module as well as the whole detector block. The

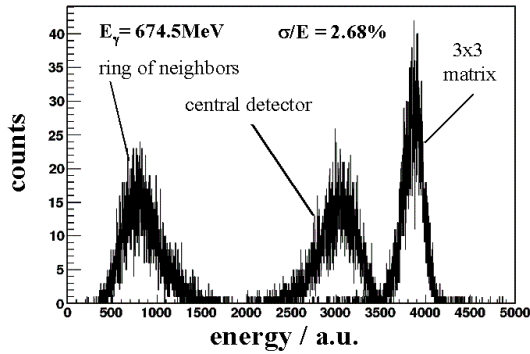


**Figure 10.17:** Experimental line shape of a 3×3 PWO-II matrix measured at the highest photon energy of 674.5 MeV at a temperature of  $T=0^\circ\text{C}$ . The figure shows the individual energy depositions into the central module and the surrounding ring. The crystal was readout with a single LAAPD.

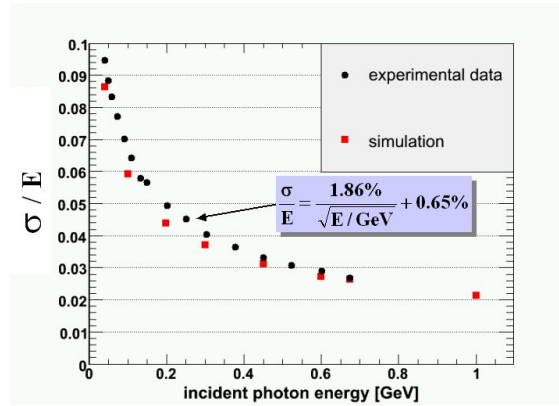


**Figure 10.19:** Experimental energy resolution as a function of incident photon energy measured for a 3×3 PWO-II matrix readout with LAAPDs at a temperature of  $T=0^\circ\text{C}$ . The result of a GEANT4 simulation is shown for comparison.

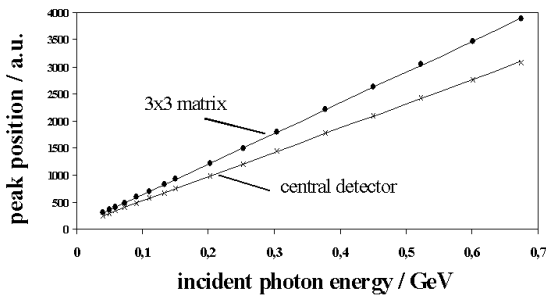


**Figure 10.18:** The linearity of the response of a 3×3 matrix over the entire range of photon energies measured at a temperature of  $T=0^\circ\text{C}$ . The most probable energy deposition into the central module is shown separately.

correlation is shown in Fig. 10.18. The overall performance is summarized in Fig. 10.19. From the experimental data one can extrapolate an energy resolution of 2.5 % at 1 GeV photon energy in spite of the fact, that the lateral dimensions of the detector array are not sufficient at that energy. The figure contains for comparison the expected resolution based on the Monte-Carlo simulation using the code GEANT4 including the concept of digitization as used in the overall simulation of the PANDA detector. It confirms that the simulations discussed in chapter 9 are close to the present experimental

performance.

The results show the excellent performance even at operating conditions well above the envisaged temperature of  $T=-25^\circ\text{C}$  and with a limited collection efficiency of the LAAPD compared to the final coverage with two sensors, which will lead to an improvement in resolution at least in the order of  $\geq 1.4$  and will be significant at lower photon energies, when the resolution is dominated by the photon statistics. However, the final gain factor will strongly depend on the read-out concept and noise imposed by the front-end electronics [12].

## 10.1.2 Position Resolution

The point of impact of the impinging photon can be reconstructed from the center of gravity of the electromagnetic shower distributed over the cluster of responding detector modules. Such an analysis can be performed in a straight forward fashion using data from previously described measurements, independent of the used readout of the scintillation response. However, reconstructions and optimizations adapted to the crystal geometry of the target spectrometer EMC have been performed so far only based on Monte-Carlo simulations.

Experimental studies in the past with detector arrays of identical geometry but inferior crystal quality have delivered a position resolution of  $\sigma < 2$  mm, slightly depending on the reconstruction algorithm but typical for crystal cross sections close to the Molière radius.

### 10.1.3 Particle Identification

The capabilities of particle identification, such as the different cluster size of detector modules responding to hadron or photon/electron induced events, have not been investigated so far experimentally but will be a major task using the PROTO60 device within the next months. In previous experiments with 2.1 GeV proton induced reactions at COSY [5, 13] a clean separation of hadrons and photons was possible even in a sub-array of  $5 \times 5$  units. More specific aspects are studied in simulations discussed in the next section on simulations.

The high quality of the timing information of the calorimeter elements was documented in several experiments and will be further exploited strongly depending on the final concept of the front-end electronics and final digitization. Exploratory measurements were previously discussed in the context of the electronics, see Sec. 6.4. Time resolutions even below 1 ns will allow selective and precise correlations between different inner detector components, in particular the tracking as well as the particle identification in the barrel DIRC. In addition, the calorimeter allows the extension of muon detection and identification down to low energies. Finally, the expected fast response can become a selective tool to discard random coincidences and events initiated by background such as due to residual gases in the beamline near the target region or secondary interactions at beamline components up- and downstream from the central target.

### 10.1.4 Construction and Basic Performance of the Barrel Prototype Comprising 60 Modules

Several prototypes have been constructed in order to validate the concepts of performance with respect to physics, mechanics, thermics and integration. The last one and the most complete is the real-size PROTO60, composed of 60 crystals of PWO-II. The setup is representative for the center part of a slice, assembled of type 6 crystals in their realistic positions. The design principle is similar to the final one except that the crystals, LAAPDs and preamplifiers are easily accessible for reasons of maintenance or controls as needed for a prototype. The crystals are resting on a thick support plate made of aluminum and the inserts into the carbon fiber alveoles are not permanently glued. The insulation box has a removable back cover.

Fig. 10.20 shows a group of 2 pairs of left and

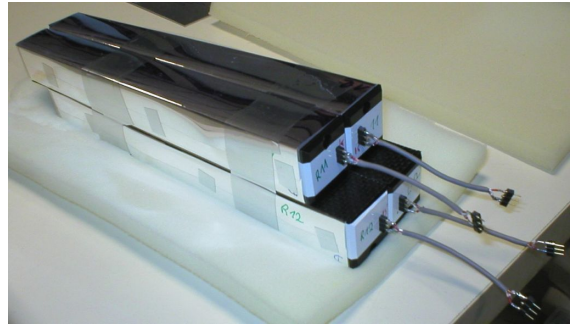


**Figure 10.20:** Pack of 4 crystals wrapped with reflector and coupled to a LAAPD as part of the PROTO60.

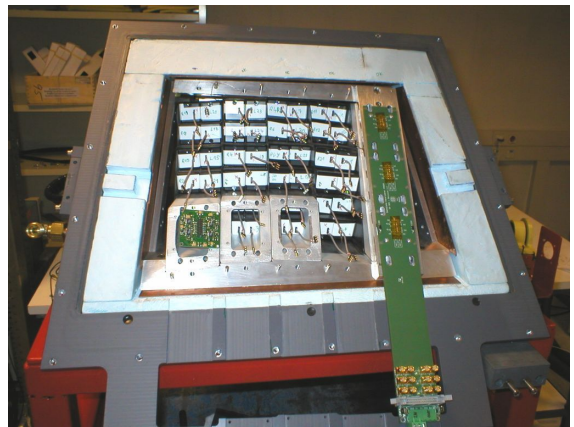


**Figure 10.21:** Back view of PROTO60 before installing the fiber system for monitoring.

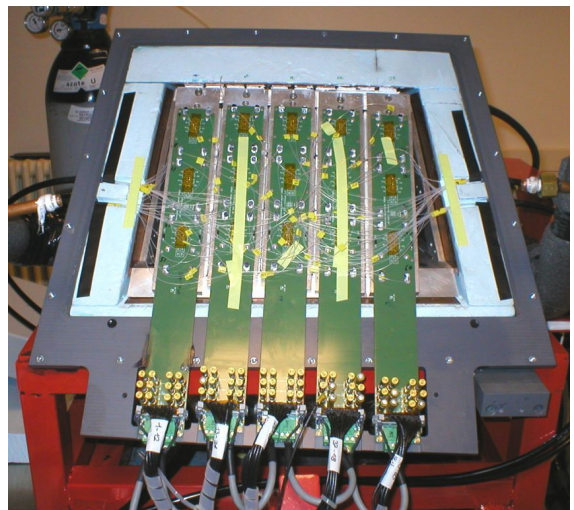


**Figure 10.22:** Back view of the fully assembled PROTO60 including the optical fibers.

right crystals, wrapped with the ESR reflector. The

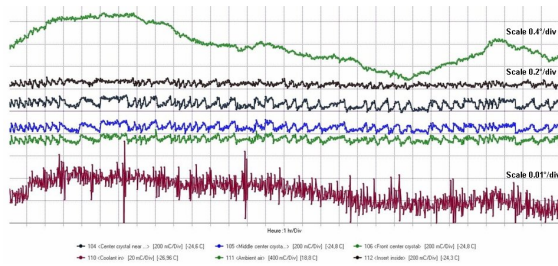


**Figure 10.23:** Temperature stability of the PROTO60. The temperature variation of the inlet coolant, the crystals and the ambient air stay within  $\pm 0.01^\circ\text{C}$ ,  $\pm 0.05^\circ\text{C}$ , and  $\pm 0.6^\circ\text{C}$ , respectively.

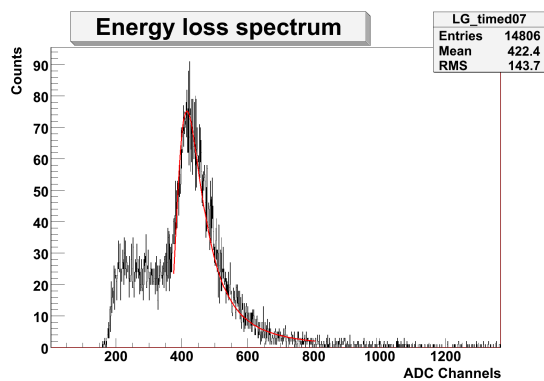


**Figure 10.24:** Measured response of a single module of the PROTO60 to the energy deposition of penetrating minimum ionizing cosmic muons.

large LAAPDs (hidden behind their black capsules) are coupled with optical grease for easy removal and connected to the preamplifiers by twisted and shielded wires. They are arranged in groups of 4 precisely positioned with a thin mylar tape before being inserted into the alveoles. The Fig. 10.21 shows a back view with all alveoles being already filled, with some inserts and one printed circuit board in place for signal readout. This multilayer board connects the preamplifiers and transfers the signals to the data acquisition across the thermal shield. The next Fig. 10.22 shows the back view before mounting the cover plate. Besides the printed boards one can notice the distribution of the optical fibers, which inject light pulses from a LED-pulsar individually into each crystal. The fibers are just contacting the rear surface without grease for better optical coupling. The light is provided by a pulsed LED with a variable frequency up to several kHz and distributed and homogenized via an optical system to serve the 60 optical fibers made of fused silica.

The insulation is achieved by thermal screens composed of copper plates with serpentines, confined in an insulated plastic box filled with dry nitrogen to avoid ice formation. In front of the calorimeter, a prototype of the vacuum panel with coolant carbon channels is successfully running with a temperature variation of up to  $3^\circ\text{C}$  between both crystal end faces. It means that the front side is well above the dew point and avoids any risk of moisture close to the DIRC. The set of crystals is operating at a temperature of  $T = -25^\circ\text{C}$  stabilized to  $\pm 0.1^\circ\text{C}$  with a Julabo chiller recirculating Syltherm coolant at a flow rate of 3.5 liters/minute. A set of 13 thermocouples measures the temperatures at different locations and is recorded with an Agilent data acquisition. The Fig. 10.23 shows one cooling cycle over a period of 30 hours. The temperature variation of the inlet coolant, selected crystals and the ambient air inside the prototype stay within  $\pm 0.01^\circ\text{C}$ ,  $\pm 0.05^\circ\text{C}$ , and  $\pm 0.6^\circ\text{C}$ , respectively, and verify the required thermal stability.

In order to prepare the in-beam tests, the functionality of the calorimeter prototype has been investigated using the response to cosmic muons. From the known high-voltage settings of the LAAPDs for a gain of 50, given by the manufacturer for a temperature at  $T = +20^\circ\text{C}$ , the corresponding lower bias voltages at the final working temperature of  $T = -25^\circ\text{C}$  have been adjusted exploiting the light pulser as a reference. The fine-tuning of the gain including the amplification settings in the spectroscopy amplifiers have been performed using the energy deposition of cosmic muons into the crystals. The individual spectra can be used as a relative calibration of the calorimeter elements for later reconstruction of an electromagnetic shower. The linearity of the assembled module including the electronics chain is checked with the LED light, which can be diminished in intensity by a set of gray-filters. Presently the PROTO60 is ready for beam tests in the summer of 2008 including a DAQ system based on commercial VME-modules for event-wise recording of the responding detectors. Fig. 10.24 shows for a single module a typical spectrum initiated by penetrating muons. The prominent peak corresponds to the most probable path-length of minimum ionizing muons, equivalent to an energy deposition of 24 MeV. The prototype has been running for weeks under stable conditions.

## 10.2 Expected performance of the EMC

Summarizing, the experimental data as well as the detailed design concepts and simulations, respectively, show that the ambitious physics program can be fully explored with respect to the measurement of the electromagnetic probes, such as photons, electrons/positrons or the reconstruction of the invariant mass of neutral mesons.

The calorimeter design in the target region is in full accordance with the constraints imposed by a fixed target experiment with the strong focusing of the momenta in forward direction. It is composed of a barrel and two endcaps comprising in total 15,552 tapered crystal modules of 11 + 2 different shapes. A nearly full coverage of  $\sim 99\%$  solid angle in the center-of-mass system is guaranteed in combination with the forward electromagnetic calorimeter, which is not part of the present TDR but is based on well known technology of a sampling calorimeter and is located downstream beyond the dipole magnet. The granularity is adapted to the tolerable maximum count rate of the individual modules and the optimum shower distribution for energy and position reconstruction by minimizing energy losses due to dead material. The front faces of the crystal elements cover a nearly identical solid angle and have lateral dimensions close to the Molière radius. All crystals are pointing off the target center.

PWO has been chosen as the most appropriate scintillator material, which allows a compact design within the solenoidal magnet, a fast response and high-rate capability due to the short decay time of the dominating scintillation process concentrated on the blue emission. All crystals have a common length of 200 mm corresponding to 22 radiation lengths, which allows optimum shower containment up to 15 GeV photon energy and limits the nuclear counter effect in the subsequent photo sensor to a tolerable level. The luminescence yield, which was sufficient for the high-energy regime at LHC, has been significantly improved by nearly a factor of two due to the optimization of the production technology, such as raw material selection, pre-fabrication processing and optimized co-doping with a minimum concentration of La- and Y-ions. To cope with the need for low energy photon detection in the tens of MeV range, the calorimeter will be operated at  $T=-25^\circ\text{C}$  in order to gain another factor of 4 due to the lower thermal quenching of the scintillation light.

The radiation level will be well below typical LHC

values by at least two orders of magnitude at the most forward direction and even further below at larger angles. However, the interplay between radiation damage and recovery processes is almost negligible at the envisaged temperatures [14, 15]. Therefore, the change of the optical transparency of the crystals is degrading asymptotically to a value, which is given by the absolute concentration of defect centers in the crystal. As a consequence, the present quality of PWO, characterized as PWO-II, provides an induced absorption coefficient, which is almost a factor two below the quality limits of CMS/ECAL. The light loss, asymptotically reached in a typical running period of 6-8 months, stays below 30%, which reduces the optimum gain factor to a value of 3 compared to an operation at  $T=+25^\circ\text{C}$ . It should be noted, that these effects have to be considered only in the very forward region of the forward endcap EMC. When the calorimeter is brought up to room temperature after a typical experimental period of 6-8 months, there will be a full recovery of the optical transmission within a few weeks. In Y-, La-doped crystals shorter the dominant relaxation times are on the level 20 to 25 hours. There are only very small contributions due to tunneling processes, with recovery constants near 75 hours.

The operation at low temperatures imposes a technological challenge on the mechanical design, the cooling concept and thermal insulation under the constraints of a minimum material budget of dead material in particular in front and in between substructures. Detailed simulations and prototyping have confirmed the concept and high accuracy has been achieved in temperature stabilization taking into account also realistic scenarios of the power consumption of the front-end electronics.

The direct readout of the scintillation crystals has been significantly improved by the development of a large size avalanche photodiode, similar to the intrinsic structure of the CMS/ECAL version, in collaboration with Hamamatsu. In total, two LAAPDs of  $100\text{ mm}^2$  active surface each will be used to convert the scintillation light with high efficiency, since almost 30% of the crystal endface are covered. Irradiation studies with electromagnetic and hadronic probes have confirmed the radiation hardness. The operation at low temperatures is even in favor and leads to a significantly slower increase of the dark current due to radiation damage. In order to cope with a substantially higher count rate of the individual crystal modules in the forward endcap EMC, vacuum photo triodes are foreseen as photo sensors for the forward endcap. Besides the

design used at CMS, the development and testing of prototypes continues in parallel at both the manufacturers Hamamatsu and Photonis, which focus in addition on the implementation of photocathodes with higher quantum efficiency compared to standard alkali versions.

The concept of the readout electronics has been elaborated. As the most sensitive element, a prototype of a custom designed ASIC implementing preamplification and shaping stages has been successfully brought into operation and will provide a large dynamic range of 12,000 with a typical noise level corresponding to  $\sim 1$  MeV. Again, the operation at low temperatures reduces further any noise contributions. Presently most of the experimental tests were based on low-noise preamplifiers assembled of discrete components. A similar version might be used for the VPTs after some modifications.

The expected overall performance of the calorimeter is presently based on a series of test experiments with detector arrays comprising up to 60 full size crystals. The basic quality parameters of PWO-II are confirmed in many tests including a first pre-production run of 710 crystals which are sufficient in shape and quantity to complete one out of the 16 slices of the barrel part. The results establish the readiness for mass production, at least at the manufacturer plant BTCP in Russia. Parallel developments of full size samples from SICCAS, China, are expected soon for comparison.

The experimental tests, mostly performed at the tagged photon facility at MAMI at Mainz and MAXLab at LUND have delivered values for energy and time resolutions, which should be considered as safety limits. They have been performed at various temperatures and were read out via photomultiplier tubes or just with a single LAAPD [11]. Therefore, only a significantly lower percentage of the scintillation light was converted into an analogue signal. From these results one can extrapolate and confirm at an operating temperature of  $T=-25^\circ\text{C}$  an energy resolution, which will be well below 2.5% at 1 GeV photon energy. At the lowest investigated shower energy of 20 MeV a resolution of 13% has even been obtained, which reflects the excellent statistical term due to the overall improved and enhanced light yield. Relevant for the efficient detection and reconstruction of multi-photon events, an effective energy threshold of 10 MeV can be considered for the whole calorimeter as a starting value for cluster identification along with a single crystal threshold of 3 MeV for adjacent channels which will enable us to disentangle physics channels with extremely low

cross section.

The fast timing performance will allow a time resolution close to 1 ns even based on the readout with LAAPDs and provide a very efficient tool to correlate the calorimeter with other devices for tracking and particle identification or an efficient reduction of background caused by residual gas in the beam pipe or interactions at accelerator components acting as secondary targets. In a series of tests the detection of hadronic probes such as low energy protons or minimum ionizing particles has been proven and will provide complementary information to the particle tracking or even identification of muons based on the energy deposition or different cluster multiplicity of trespassing hadrons.

The overall performance of the calorimeter will be carefully controlled by injecting light from LED-sources distributed via optical fibers via the rear face of the crystal. The change of optical transmission will be monitored near the emission wavelength at 420 nm, at a dominant defect center due to Molybdenum at 530 nm, and far in the red spectral region to control independently the readout chain including the photo sensor. Radiation damage is not expected to appear in the red. A first prototype is already implemented into the PROTO60 array and operating.

Based on the ongoing developments of PWO-II crystals and LAAPDs, a detailed program has been elaborated for quality assurance of the crystals and screening of the photo sensors. The crystal studies include the preparation of various facilities for irradiation studies at Protvino and Giessen. In addition, the quality control is planned to be performed at CERN, taking advantage of the existing infrastructure and experience developed for CMS. One of the two ACCOS machines, semi-automatic robots, is presently getting modified for the different specification limits and geometrical dimensions of the  $\overline{\text{PANDA}}$  crystals.

Similar infrastructure has been developed for the final certification of the LAAPDs in rectangular shape. The intrinsic layout is identical to the quadratic version, which has been tested in great detail. The new geometry allows to fit two sensors on each crystal irrespective of its individual shape.

The general layout of the mechanical structure is completed including first estimates of the integration into the  $\overline{\text{PANDA}}$  detector. The concepts for signal- and HV-cables, cooling, slow control, monitoring as well as the stepwise assembly are worked out to guarantee that the crystal geometries could be finalized. Prototypes of the individual crys-

tal containers, based on carbon fiber alveoles, have been fabricated and tested and are already implemented in the PROTO60 device.

## References

- [1] I. Anthony et al., Nucl. Instrum. Meth. **A301**, 230 (1991).
- [2] R. Novotny et al., IEEE Trans. on Nucl. Sci. **44**, 477 (1997).
- [3] K. Mengel et al., IEEE Trans. on Nucl. Sci. **45**, 681 (1998).
- [4] R. Novotny et al., IEEE Trans. on Nucl. Sci. **47**, 1499 (2000).
- [5] M. Hoek et al., Nucl. Instrum. Meth. **A486**, 136 (2002).
- [6] A. Fedorov et al., Proceedings of SCINT05, Alushta, Ukraine, 2005 , 389 (2006).
- [7] K. Makonyi et al., Proceedings of SCINT05, Alushta, Ukraine, 2005 , 338 (2006).
- [8] R. Novotny et al., IEEE Trans. on Nucl. Sci. **51**, 3076 (2004).
- [9] M. Thiel et al., Proceedings of SCINT05, Alushta, Ukraine, 2005 , 342 (2006).
- [10] B. Lewandowski et al., Proceedings of SCINT05, Alushta, Ukraine, 2005 , 391 (2006).
- [11] R. W. Novotny et al., IEEE Trans. on Nucl. Sci. **55**, 1207 (2008).
- [12] R. Novotny, IEEE NSS2007, Conference Record , 161 (2007).
- [13] M. Hoek et al., IEEE Trans. on Nucl. Sci. **49**, 946 (2002).
- [14] R. W. Novotny et al., IEEE Trans. on Nucl. Sci. **55**, 401 (2008).
- [15] P. A. Semenov et al., Nucl. Instrum. Meth. **A582**, 575 (2007).



# 11 Organisation

## 11.1 Quality Control and Assembly

### 11.1.1 Production Logistics

The realization of the two major components of the target spectrometer EMC, the barrel part and the two endcaps of different size, is split into several parts, which also require significantly different logistics. The mechanical parts, such as the basic detector modules including their housing as well as the support structure, the thermal insulation and cooling as well as the container for the readout electronics, are presently under development and first design studies have been realized in prototype development. The detector components comprise basically the nearly 16,000 PWO-II crystals and the two types of photo sensors, LAAPDs and vacuum triodes. Both require a sophisticated program of production by manufacturers, the quality control and assurance and screening and pre-radiation in particular of the avalanche photo diodes. The concept and the procedures of the latter components are outlined in great detail in the chapter about photo sensors.

The major steps in realization are defined on one hand by the optimum logistics but also by the capabilities and interests of the participating institutions as well as the supporting funding profile. The present layout assumes the sufficient funding and a timing profile to be available when necessary. The logistics is based on a practicable concept to achieve an optimum realization and to guarantee the envisaged performance of the calorimeter and is schematically illustrated in Fig. 11.1.

### 11.1.2 The PWO-II Crystals

Presently, the production of high-quality PWO crystals delivering the specifications of PWO-II can be expected to be performed only by the two manufacturers BTCP and SICCAS, respectively, which have been successfully involved in the realization of the CMS EM calorimeter. There is foreseen to have prepared at both companies an infrastructure to measure the specifications primarily to have a fast response to instabilities of the production line and to deliver crystals according to the very selective specification parameters. There will be a major

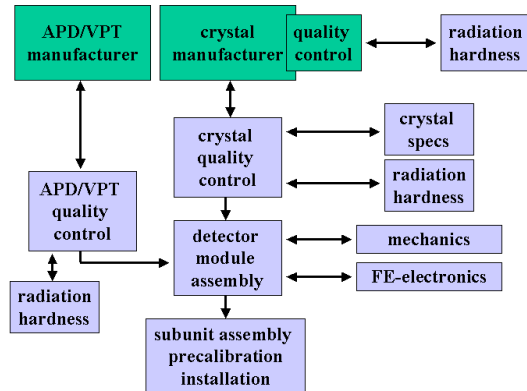


**Figure 11.1:** Schematic layout for the realization of the target spectrometer EMC of PANDA.

center for the crystal inspection and assembly of the detector modules. As an option, it could be located at Giessen, which is in addition advantageous due to the very close distance to FAIR. Already confirmed by an official offer of the CMS collaboration, the quality tests will be performed at CERN using the semi-automatic ACCOS machine. It guarantees a well accepted and adapted procedure and allows to exploit more than 10 years of experience. Preparations have been initiated already, to adapt the installations to the geometry and more selective specifications of the PANDA crystals. Afterwards, the crystals will be shipped back to control for each crystal its radiation hardness and the wavelength dependence, which is very crucial for the operation at low temperatures and has to be performed for a very high percentage of the crystals. These measurements could be handled at the irradiation facility at Giessen, as characterized in chapter 4.

### 11.1.3 Detector Module Assembly

In a second line, to be performed at an appropriate regional center, the crystals will be equipped with a reflector foil, photo and temperature sensors, and the front-end electronics. All latter components are delivered tested and screened from the responsible laboratories at GSI (LAAPD, front-end electronics) and Bochum/KVI (VPT), most probably.

### 11.1.4 Final Assembly, Pre-calibration and Implementation into $\bar{P}$ ANDA

The final assembly of the barrel slices or the two endcaps will be completed by the implementation of the optical fibers for the monitoring system, the electronics for digitization, the cables for signal transfer and low- and high voltage support, the sensors and lines for slow control as well as the installations for cooling. This task including the intermediate storage have to be performed at or at least close to FAIR in a dedicated laboratory space. The basic functionality of the assembled units will be tested using on one hand the monitoring system to check the electronics chain including the photo sensors. A first hint of the expected sensitivity of each detector module is given by the measured light yield of the crystal, the absolute value of optical transmission at the absorption edge and the known gain of the photo sensor. These parameters will allow a first step towards a pre-calibration with an accuracy on the order of 5%. On the other hand, a more sensitive relative and absolute calibration of the calorimeter modules will be obtained by using minimum ionizing cosmic muons. The submodules have to be mounted on a mechanical support structure, which allows to rotate most of the detector modules into vertical positions. Requiring anti-coincidence with all neighboring modules selects the full path length of 200 mm of the particle, which corresponds to an energy deposition of  $\sim 240$  MeV. This procedure will deliver calibration parameters with an intended accuracy of 2.5%, values which base on the experience of CMS. In order to obtain a more accurate calibration, a cross check with the calibration steps explained above and to determine finally the response function a substantial part of the units will be exposed to a direct beam of energy marked photons, which can be provided at the two tagging facilities at MAMI (Mainz) and ELSA (Bonn), respectively, covering the complete energy range up to  $\sim 3.2$  GeV. At both places experimental set-ups are under consideration.

### 11.1.5 Other Calorimeter Components

Besides the basic calorimeter components, crystals, photo sensors and pre-amplifier/shaper, all other parts including mechanical structure, cooling, thermal insulation, electronics and DAQ are under development. In case of the most critical tasks prototypes have been designed and realized and confirm

the proposed concept. The responsibility for the final design and realization are distributed among those groups within the collaboration, which have the infrastructure and experience with large scale experimental installations.

### 11.1.6 Integration in $\bar{P}$ ANDA

The design of the target spectrometer EMC is in full agreement to the overall layout of the whole  $\bar{P}$ ANDA detector. The components including service connections and mounting spaces fit within the fiducial volume defined by the magnet and the other detector components. It is foreseen, that the fully assembled and tested submodules are stored in an air-conditioned area with stabilized temperature and low humidity. The sealed components should be kept in a nitrogen atmosphere. The necessary steps for mounting and integrating the calorimeter into  $\bar{P}$ ANDA have been described already in great detail in the chapter on mechanics for both major parts and will be the final task performed by the whole collaboration.

## 11.2 Safety

The design details and construction of the calorimeter including the infrastructure for operation will be done according to the safety requirements of FAIR and the European and German safety regulations. Design aspects for which the CMS calorimeters are taken as examples take into consideration the detailed guidelines given by CERN, which are most appropriate to the case of large scientific installations.

### 11.2.1 Mechanics

The strength of the EMC support structures has been computed with physical models in the course of the design process. Details of finite element analysis are shown in Sec. 7.1.2. Each mechanical component will undergo a quality acceptance examination including stress and loading tests for weight bearing parts. Spare samples may also be tested up to the breaking point. A detailed material map of the entire apparatus showing location and abundance of all materials used in the construction will be created. For structural components radiation resistance levels will be taken into account in the selection process and quoted in the material map. For the calorimeter crystals themselves precautions will be taken to rule out exposure of persons to toxic

material due to exhaustion in case of fire or due to mechanical operations. In normal conditions lead tungstate is stable, non-hygroscopic, and hardly soluble in water, oils, acids and basis.

### 11.2.2 Electrical Equipment and Cooling

All electrical equipment in  $\bar{P}$ ANDA will comply to the legally required safety code and concur to standards for large scientific installations following guidelines worked out at CERN to ensure the protection of all personnel working at or close to the components of the  $\bar{P}$ ANDA system. Power supplies will have safe mountings independent of large mechanical loads. Hazardous voltage supplies and lines will be marked visibly and protected from damage by near-by forces, like pulling or squeezing. All supplies will be protected against overcurrent and overvoltage and have appropriate safety circuits and fuses against shorts. All cabling and optical fibre connections will be executed with non-flammable halogen-free materials according to up-to-date standards and will be dimensioned with proper safety margins to prevent overheating. A safe ground scheme will be employed throughout all electrical installations of the experiment. Smoke detectors will be mounted in all appropriate locations.

Lasers or high output LEDs will be employed in the monitoring system and their light is distributed throughout the calorimeter systems. For these devices all necessary precautions like safe housings, color coded protection pipes, interlocks, proper warnings and instructions as well as training of the personnel with access to these components will be taken.

The operation of the PWO EMC at temperature down to  $-25^{\circ}\text{C}$  requires a powerful and stable cooling system for the crystals and sensors. It consists of a system of cooling pipes, pumps and heat exchangers and employs a liquid silicone polymer as coolant. This material is highly inert and non-toxic. Its flow will be in the order of 4 l/s for the full EMC. A control system is employed to detect any malfunctioning of the cooling system and include interlocks for electronics and high-voltage supplies. In the case of coolant loss or in case of abnormal temperature gradients between coolant input and output the control system enacts the appropriate safety procedures. A highly redundant system of temperature sensors allows the continuous monitoring of the effectiveness of the system.

### 11.2.3 Radiation Aspects

The PWO crystals can be activated by low energy protons and neutrons leading to low-energy radioactivity of the activated nuclei. However, simulations based on the computer code MARS deliver in case of the maximum luminosity of  $2 \times 10^{32}/\text{s}$  and for an operation period of 30 days a dose rate of  $20 \mu\text{Sv}/\text{h}$  at the crystal surface of the forward endcap EMC closest to the beam axis, where the rate is expected to be the highest in the entire EMC by several orders of magnitude. The estimated rate is one order of magnitude lower than in case of CMS at LHC. Shielding, operation and maintenance will be planned according to European and German safety regulations to ensure the proper protection of all personnel.

## 11.3 Schedule

Fig. 11.2 shows in some detail the estimated timelines including the main tasks for the design phase, prototyping, production, pre-calibration and implementation of the target spectrometer EMC into the  $\bar{P}$ ANDA detector. The schedule is based on the experience gathered during the R&D and prototyping phase, the close collaboration with optional manufacturers and the fruitful exchange of experience in particular the CMS/ECAL project at CERN. The timelines assume sufficient funding, which should become available when necessary.

After an initial phase of research and development of the target spectrometer EMC concentrating on the basic performance of the essential components, i.e. the optimal scintillator material and the photo sensors of choice, the collaboration has completed the design phase. The integration of the mechanical components into the  $\bar{P}$ ANDA detector has been clarified, prototype crystals, sensors, discrete and ASIC preamplifiers, and digitization modules are at hand, and a prototype detector has been set up and is ready for beam experiments. A number of institutions, who have gained specific expertise in past and ongoing research programme at large-scale experiments such as BaBar, TAPS/Crystal Ball/Crystal Barrel at several accelerator facilities, are engaged in the remaining tasks leading to the completion of the target spectrometer EMC. The responsibilities for the various work packages and tasks are listed in Fig. 11.3 and show the participating institutions. The coordination of the work packages is performed by those groups marked in bold-face. However, the responsibility is not automatically linked to the availability of future funding.

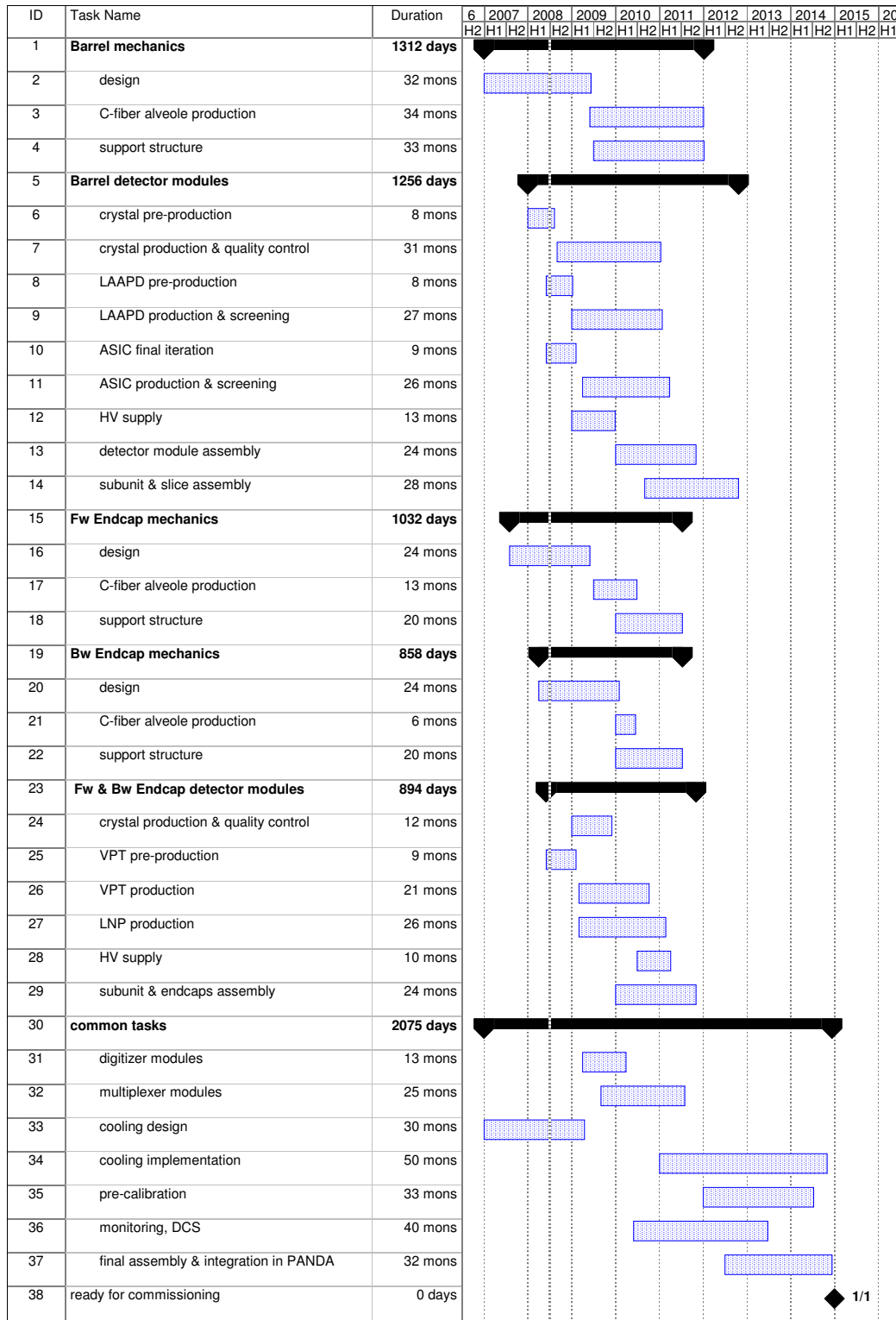


Figure 11.2: Timeline for the realization of the target spectrometer EMC.

work package	task	participating (coordinating) institute
<b>Barrel mechanics</b>	design	Giessen, <b>Orsay</b> , Protvino
	C-fiber alveole production	<b>Orsay</b> , <b>Protvino</b>
	support structure	<b>Orsay</b> , Protvino
<b>Barrel detector modules</b>	crystal pre-production	<b>Giessen</b> , Protvino
	crystal production & quality control	<b>Giessen</b> , GSI, Minsk, Protvino
	LAAPD pre-production	<b>GSI</b>
	LAAPD production & screening	<b>GSI</b>
	ASIC final iteration & production	<b>GSI</b> , KVI
	ASIC screening	<b>GSI</b> , KVI
	HV supply	<b>Basel</b> , Giessen
	detector module assembly	Giessen, GSI, Orsay, <b>Protvino</b> , Valencia, Warsaw
subunit & slice assembly	Giessen, <b>Orsay</b> , Protvino	
<b>Fw endcap mechanics</b>	design	Bochum, <b>KVI</b> , Orsay
	C-fiber alveole production	Bochum, <b>KVI</b> , Lund, Stockholm, Uppsala
	support structure	<b>KVI</b>
<b>Bw endcap mechanics</b>	design	GSI, KVI, <b>Mainz</b>
	C-fiber alveole production	<b>KVI</b>
	support structure	<b>GSI</b> , KVI, Mainz
<b>Endcap detector modules</b>	crystal production & quality control	Bochum, <b>Giessen</b> , GSI, Lund, Minsk, Stockholm, Uppsala
	VPT pre-production	<b>Bochum</b> , KVI, Stockholm, Uppsala
	VPT production	<b>Bochum</b> , KVI, Lund, Stockholm, Uppsala
	LNP production	<b>Basel</b> , Giessen
	HV supply	<b>Basel</b> , Uppsala
	subunit & endcaps assembly	Bochum, Giessen, GSI, <b>KVI</b> , <b>Mainz</b> , Stockholm, Uppsala
<b>Common tasks</b>	digitizer modules	GSI, KVI, Munich, <b>Uppsala</b>
	multiplexer modules	KVI, <b>Munich</b>
	cooling design & implementation	Bochum, KVI, <b>Orsay</b> , Protvino
	pre-calibration	Basel, Bochum, <b>Giessen</b> , GSI, <b>KVI</b> , Lund, <b>Mainz</b> , Protvino, Stockholm, Uppsala, Valencia, Warsaw
	monitoring, DCS	<b>Bochum</b> , KVI, Protvino, Warsaw
	Final assembly & integration in PANDA	Basel, Bochum, Giessen, <b>GSI</b> , KVI, Lund, Mainz, Minsk, Orsay, Protvino, Stockholm, Uppsala, Valencia, Warsaw

**Figure 11.3:** Tasks and responsibilities for the realization of the target spectrometer EMC.

Since the table documents as well the capabilities of the collaboration members, the different institutions are shortly described and characterized by

their expertise gathered in previous or ongoing research activities.

- **Basel** (B. Krusche, M. Steinacher): The group

is conducting experiments at tagged photon facilities and has expertise in analogue electronics.

- **Bochum**(F.-H. Heinsius, U. Wiedner): The Bochum group is engaged in the design and operation of calorimeters for BaBar (SLAC), Crystal Barrel (CERN and Bonn/ELSA) and the WASA detector (Uppsala and Jülich).
- **Giessen** (V. Metag, R. Novotny): The Giessen group has a longstanding experience in crystal calorimetry. It has been the leading institution in building the TAPS detector including electronics. The group has played a leading role in the development of the PWO-II.
- **GSI** (B. Lewandowski, F. Mass, K. Peters, A. Wilms): The GSI group has long experience in crystal calorimetry (BaBar (SLAC), Crystal Barrel (CERN), Mami A4 (Mainz)) and ASIC design. Particular fields of expertise include design and construction of sensors and electronics as well as calibration, monitoring and front-end software. The APD-LAB branch is a renowned R&D center for LAAPDs channeling the developments for PANDA and R3B. In addition technical and infrastructure coordination for PANDA is performed by GSI.
- **KVI** (H. Löhner, J. Messchendorp): The Groningen group participated in the construction and exploitation of the TAPS calorimeter. They have major experience in applications of scintillation detectors, photo sensors, light pulser systems for monitoring crystals, developing FPGA electronics and DSP networks.
- **Lund** (B. Schröder): The Lund group performs research at the MAX-Laboratory with monoenergetic photons in the 15 to 200 MeV range with an energy resolution of 250 keV at best.
- **Mainz** (F. Maas): The group has a long standing experience in fast EM calorimetry, trigger systems and operation of a facility for energy marked photons up to 1.5 GeV energy.
- **Minsk** (M. Korzhik, O. Missevitch): The group has long year expertise in solid state physics of scintillation materials and has been the coordinator for PWO production for CMS at CERN.
- **München** (I. Konorov, S. Paul): The group has expertise in design and development of digital electronics for large scale experiments (COMPASS) and has developed ADC systems for physics and medical applications.
- **Orsay** (T. Hennino, P. Rosier): Long year experience in mechanical and electronics engineering and construction of large scale detector systems.
- **Protvino** (V. A. Kachanov, A. N. Vasiliev): The group has been strongly involved in the design and construction of the endcap of CMS/ECAL and R&D for the proposed BTeV experiment.
- **Stockholm** (P. E. Tegner): The Stockholm University group has a major experience in operating detectors in high magnetic fields at the former CELSIUS machine in Uppsala.
- **Uppsala** (P. Marciniewski, T. Johansson): The Uppsala group has been involved in experiments at CERN, Uppsala and Jülich. Their experience covers many aspects of calorimeters (WASA), electronic signal digitization and readout systems.
- **Valencia** (J. Diaz): The group is involved in scintillator systems of large scale detectors such as TAPS and HADES.
- **Warsaw** (B. Zwieglinski): The SINS Warsaw group has experience in response studies of scintillators exploiting proton accelerators.

## Acknowledgments

We acknowledge financial support from the Bundesministerium für Bildung und Forschung (bmbf), the Deutsche Forschungsgemeinschaft (DFG), the University of Groningen, Netherlands, the Gesellschaft für Schwerionenforschung mbH (GSI), Darmstadt, the Helmholtz-Gemeinschaft Deutscher Forschungszentren (HGF), the Schweizerischer Nationalfonds zur Förderung der wissenschaftlichen Forschung (SNF), the Russian funding agency “State Corporation for Atomic Energy Rosatom”, the CNRS/IN2P3 and the Université Paris-sud, the British funding agency “Science and Technology Facilities Council” (STFC), the Istituto Nazionale di Fisica Nucleare (INFN), the Swedish Research Council, the Polish Ministry of Science and Higher Education, the European Community FP6 FAIR Design Study: DIRACsecondary-Beams, contract number 515873, the European Community FP6 Integrated Infrastructure Initiative: HadronPhysics, contract number RII3-CT-2004-506078, the INTAS, and the Deutscher Akademischer Austauschdienst (DAAD).

We also would like to thank the CMS Collaboration at CERN for their support.



<b>ADC</b> Analog to Digital Converter	<b>GEM</b> Gas Electron Multiplier
<b>ALICE</b> A Large Ion Collider Experiment at CERN LHC	<b>GLAST</b> Gamma ray Large Area Space Telescope
<b>ALICE/PHOS</b> ALICE Photon Spectrometer	<b>GSI</b> Gesellschaft für Schwerionenforschung
<b>APD</b> Avalanche Photo Diode	<b>HEP</b> High Energy Physics
<b>APFEL</b> ASIC for Panda Front End Electronics	<b>HESR</b> High Energy Storage Ring
<b>ASIC</b> Application Specific Integrated Circuit	<b>HV</b> High Voltage
<b>AWG</b> Arbitrary waveform generator	<b>IHEP</b> Institute for High Energy Physics
<b>BGO</b> Bismuth Germanate	<b>J-FET</b> Junction Field-Effect Transistor
<b>BTCP</b> Bogoroditsk Techno-Chemical Plant	<b>KVI</b> Kernfysisch Versneller Instituut
<b>C</b> Capacitance	<b>LAAPD</b> Large Area APD
<b>CAD</b> Computer Aided Design	<b>LEAR</b> Low Energy Antiproton Ring
<b>CERN</b> Conseil European pour la Recherche Nucléaire	<b>LED</b> Light Emitting Diode
<b>CLAS</b> CEBAF Large Acceptance Spectrometer	<b>LHC</b> Large Hadron Collider
<b>CMOS</b> Complementary Metal Oxide Semiconductor	<b>LNP</b> Low Noise Preamplifier
<b>CMS</b> Compact Muon Solenoid	<b>LOI</b> Letter of Intent
<b>CMS/ECAL</b> CMS electromagnetic calorimeter	<b>LY</b> Light Yield
<b>COMPASS</b> Common Muon Proton Apparatus for Structure and Spectroscopy	<b>M</b> Gain of APD
<b>COSY</b> Cooler Synchrotron	<b>MAMI</b> Mainz Microtron
<b>DAQ</b> Data Acquisition	<b>MIP</b> Minimum Ionizing Particle
<b>DCS</b> Detector Control System	<b>MLP</b> Multi Layer Perceptron
<b>DIRC</b> Detector for Internally Reflected Cherenkov Light	<b>MVD</b> Micro Vertex Detector
<b>DPM</b> Dual Parton Model	<b>NCE</b> Nuclear counter effect
<b>DSP</b> Digital Signal Processor	<b>NIEL</b> Non-Ionizing Energy Loss
<b>DVCS</b> Deeply Virtual Compton Scattering	<b>PANDA</b> Pbar ANihilation at Darmstadt
<b>EMC</b> Electromagnetic Calorimeter	<b>PCB</b> Printed Circuit Board
<b>ENC</b> Equivalent Noise Charge	<b>PEEK</b> Polyetheretherketone
<b>EPR</b> Electron Paramagnetic Resonance	<b>phe</b> photo electrons
<b>FADC</b> Flash ADC	<b>PID</b> Particle Identification
<b>FAIR</b> Facility for Antiproton and Ion Research	<b>PMT</b> Photomultiplier
<b>FINUDA</b> Fisica Nucleare a DAFNE	<b>PSI</b> Paul Scherrer Institute
<b>FPGA</b> Field Programmable Gate Array	<b>PWO</b> Lead Tungstate
	<b>QCD</b> Quantum Chromo Dynamics
	<b>QE</b> Quantum efficiency
	<b>RICH</b> Ring Imaging Cherenkov Counter

**RT** Room Temperature

**SCADA** Supervisory Control And Data Acquisition

**SICCAS** Shanghai Institute of Ceramics, Chinese Academy of Sciences

**SIS** Heavy ion synchrotron

**SMD** Surface Mount Device

**STT** Straw Tube Tracker

**TDC** Time to Digital Converter

**TSL** The Svedberg Laboratory

**TSL** Thermo stimulated luminescence

**UrQMD** Ultra-relativistic Quantum Molecular Dynamic

**VME** Versa Module Eurocard

**VPT** Vacuum Photo Triode

# List of Figures

---

1.1	Overview of the $\bar{P}$ ANDA spectrometer.	2	4.8	Integral dependence of the radioluminescence.	45
2.1	Schematic view of the HESR.	16	4.9	The measured induced absorption of various PWO-II samples.	47
2.2	Average luminosity vs. cycle time.	17	4.10	Schematic layout of the irradiation facility at IHEP.	48
2.3	Artistic view of the $\bar{P}$ ANDA Detector.	18	4.11	Photograph of the major components of the irradiation setup at IHEP.	48
2.4	Side view of the target spectrometer.	19	4.12	The experimental setup for irradiation studies at Giessen.	49
2.5	Schematic of the target and beam pipe setup with pumps.	20	4.13	The irradiation facility operating at BTCP in Russia.	49
2.6	The Microvertex detector of $\bar{P}$ ANDA	21	4.14	Schematic layout of the spectrometric setup at BTCP.	49
2.7	Straw Tube Tracker in the Target Spectrometer	23	4.15	Schematic layout of a single spectrometric channel of the setup at BTCP.	50
2.8	GEM Time Projection Chamber in the Target Spectrometer	23	4.16	Light yield of full size polished scintillation crystals.	52
2.9	Top view of the experimental area.	29	4.17	Pulse height spectra measured for a PWO-II crystal.	53
3.1	$\pi^0$ loss rate as a function of energy threshold.	31	4.18	Temperature dependence of the yield of PWO-II scintillation light.	53
3.2	Photon energy distribution vs. lab. angle.	33	4.19	Average PWO-II light yield vs. integration gate.	54
3.3	Energy resolutions for different single crystal reconstruction thresholds.	34	4.20	Correlation of light yield at low and high temperature.	55
3.4	$\pi^0$ and $\eta$ energy spectrum.	35	4.21	Variation of the light output measured for different crystal geometries and reflector materials when a collimated $\gamma$ -source is moved relative to the sensor position along the crystal axis.	55
3.5	Minimum $\pi^0$ opening angle.	36	4.22	Relative change of the light yield of two PWO-II samples.	55
3.6	Mass resolution for $\pi^0$ (spatial resolution).	36	4.23	Relative change of the monitoring signal.	56
3.7	Hit rate in the barrel part.	36	4.24	The absolute loss in transmission due to irradiation.	56
3.8	Hit rate in the forward part.	36	4.25	The induced absorption due to irradiation.	56
4.1	Integrated single crystal rate for the barrel section.	41	4.26	The decay kinetics of an absorption region after irradiation.	56
4.2	Integrated single crystal rate for the forward endcap.	41	4.27	The decay kinetics of an absorption region after irradiation.	57
4.3	Single crystal energy differential rate spectrum.	41			
4.4	Relative energy dose as function of the radial depth.	41			
4.5	Selected PWO-II ingots.	43			
4.6	The optical transmission and radioluminescence spectra.	43			
4.7	The scintillation kinetics of PWO measured at room temperature.	43			

4.28	EPR signal measured after irradiation.	57	5.15	Dark current increase of 'low C' diode caused by proton irradiation.	75
4.29	Change of the scintillation response due to a continuous irradiation.	57	5.16	$M(\lambda)$ of 'normal C' type after proton exposure.	75
4.30	Maximum change of the scintillation response vs. induced absorption.	57	5.17	$M(\lambda)$ of 'low C' type after proton exposure.	75
4.31	Change of the scintillation response before and after irradiation.	58	5.18	Gain $M$ of 'normal C' type after and before photon irradiation.	76
4.32	Machined and optically polished barrel type PWO-II crystals.	58	5.19	Dark current $I_d$ of 'normal C' type after and before photon irradiation.	76
4.33	Distribution of the light yield of barrel type PWO-II crystals.	58	5.20	$M(\lambda)$ of 'normal C' type after $\gamma$ exposure.	76
4.34	Radiation induced absorption spectra.	59	5.21	Apparatus used for neutron irradiation.	77
4.35	Distribution of the induced absorption after an absorbed dose of 50 Gy.	59	5.22	Gain $M$ of 'normal C' type after and before neutron irradiation.	77
4.36	The ACCOS machine installed at the CMS regional center at CERN.	60	5.23	Dark current $I_d$ of 'normal C' type after and before neutron irradiation.	77
4.37	Optical transmission of crystal samples from BTCP and SICCAS.	63	5.24	Dark current $I_d$ of 'low C' type after and before neutron irradiation.	77
4.38	Absolute light yield.	63	5.25	$M(\lambda)$ of 'normal C' type after neutron exposure.	77
4.39	Longitudinal optical transmission of two 200 mm long crystals.	64	5.26	$M(\lambda)$ of 'low C' type after neutron exposure.	78
4.40	Inhomogeneity in the transversal optical transmission.	64	5.27	PEEK APD capsule.	79
5.1	APD reverse structure.	67	5.28	Schematic of VPT.	79
5.2	Technical drawing of the rectangular APD type.	69	5.29	VPT gain vs. cathode HV for R2148.	80
5.3	Gain and dark current of 'normal C' version LAAPD.	70	5.30	VPT gain vs. cathode HV for FEU-188.	80
5.4	Gain and dark current of 'low C' version LAAPD.	70	5.31	Quantum efficiency VPT.	82
5.5	Ratio $I_d/M$ for different APD types.	71	5.32	VPT response to magnetic field vs. angle.	82
5.6	Excess noise factor of CMS-APDs.	71	5.33	Light transmission of VPT window after gamma irradiation.	82
5.7	Excess noise factor of 'normal C' version LAAPD from Hamamatsu.	71	5.34	Light transmission of VPT window as function of gamma irradiation.	82
5.8	NCE of the investigated LAAPD versions.	72	5.35	Relative anode response of VPT versus the neutron fluence.	83
5.9	QE of a PANDA-LAAPD.	72	6.1	The readout chain of the Electromagnetic Calorimeter.	86
5.10	Absorption coefficient $\alpha(\lambda, T)$ of Si.	73	6.2	Schematic diagram of the folded cascade front end.	88
5.11	Normalized gain of 'normal C' type APD.	73	6.3	Principle diagram of the self biasing feedback network.	89
5.12	Normalized gain of 'low C' type APD.	74	6.4	Block diagram and photograph of the preamplifier and shaper ASIC.	90
5.13	Gain $M$ of 'normal C' type after and before proton irradiation.	74			
5.14	Dark current rise of 'normal C' diode caused by proton irradiation.	74			

6.5	Test PCB with glued and bonded preamplifier ASIC. . . . .	90	7.8	Summary of the expected dead space between calorimeter elements. . . . .	111
6.6	Measured noise values of the preamplifier prototype. . . . .	91	7.9	Schematic view of the concept and of the major components of a slice. . . . .	113
6.7	Amplification characteristics of the preamplifier at $-20^{\circ}\text{C}$ . . . . .	91	7.10	CAD integration of the insert with the preamplifier and optical fiber. . . . .	113
6.8	Power consumption for one chip in dependence of temperature. . . . .	91	7.11	Exploded view of a slice. . . . .	114
6.9	Power dissipation as function of continuous event rate. . . . .	93	7.12	Deformation of the support beam. . . . .	114
6.10	Circuit diagram of the LNP-P prototype for the VPT readout. . . . .	96	7.13	Barrel supported on the magnet. . . . .	115
6.11	The measured noise performance of the LNP-P. . . . .	96	7.14	Integration of the services in the support beam. . . . .	115
6.12	PSPICE simulation of ENC versus the detector capacitance. . . . .	97	7.15	Front thermal screen. . . . .	116
6.13	Time resolution as function of the corresponding pulse energy. . . . .	97	7.16	Equivalent chain for the analytical analysis of the LAAPD temperature. . . . .	117
6.14	The functional diagram of the digitizer module. . . . .	97	7.17	Thermal simulation. . . . .	117
6.15	The layout of the prototype ADC module. . . . .	99	7.18	Cooling power summary. . . . .	118
6.16	The layout of the Layer Stack Back-PCB. . . . .	101	7.19	Dimensions of a slice. . . . .	119
6.17	Scheme of the layer stack of flat cables. . . . .	101	7.20	Next thermal prototype 480. . . . .	119
6.18	The various functions of the Detector Control System. . . . .	102	7.21	Services out of barrel. . . . .	120
6.19	The DCS network structure. . . . .	102	7.22	Barrel final mounting. . . . .	121
6.20	Microchip wafer. . . . .	104	7.23	The position of the forward endcap EMC with respect to the target. . . . .	123
6.21	An integrated circuit connected by needles during a wafertest. . . . .	104	7.24	The geometry of a single forward endcap EMC crystal. . . . .	123
6.22	The top- and the bottom side of the single-channel LNP-P prototype. . . . .	105	7.25	The geometry of a C-fiber alveole for 16 crystals. . . . .	124
7.1	The components of the $\bar{\text{P}}\text{ANDA}$ electromagnetic calorimeter. . . . .	108	7.26	Photograph of three produced C-fiber alveoles for 16 crystals each. . . . .	124
7.2	Overall view of the target spectrometer. . . . .	108	7.27	The explosion view of a 16-crystal subunit. . . . .	125
7.3	The shape of the scintillator crystal. . . . .	109	7.28	The attachment of the C-fiber alveoles in front of the mounting plate. . . . .	125
7.4	Segmentation of the calorimeter along the circumference of the barrel. . . . .	109	7.29	One quadrant of the $\bar{\text{P}}\text{ANDA}$ forward endcap calorimeter. . . . .	126
7.5	Geometrical arrangement of the crystals of the barrel. . . . .	110	7.30	The complete endcap. . . . .	127
7.6	View of the barrel of 11360 crystals with a separated slice. . . . .	110	7.31	Impedance of laminate cable. . . . .	127
7.7	Deformation test of carbon alveoles. . . . .	110	7.32	Arrangement of digitizer modules for the forward endcap EMC. . . . .	128
			7.33	Acceptance of the backward endcap EMC . . . . .	128
			7.34	The position of the backward endcap EMC with respect to the target. . . . .	130
			7.35	The dimensions of a single crystal of the backward endcap EMC. . . . .	130

7.36	The geometry of one quadrant of the backward endcap EMC. . . . .	130	9.14	Reconstructed photon energy with/without DIRC preshowers. . . .	147
8.1	Induced absorption of various PWO samples after irradiation. . . . .	133	9.15	Energy distributions of $\gamma$ s from $\bar{p}p \rightarrow h_c \rightarrow \eta_c \gamma$ and $\bar{p}p \rightarrow \phi \phi \pi^0$ . . . .	149
8.2	Schematic layout of the stabilized light pulser system. . . . .	134	9.16	The number of reconstructed EMC clusters. . . . .	149
8.3	Major components of a first prototype of the monitoring system. . . .	134	9.17	Invariant mass for $J/\psi \rightarrow e^+e^-$ and $\pi^0 \rightarrow \gamma\gamma$ . . . . .	151
8.4	$\alpha$ signal stability. . . . .	135	9.18	Invariant $\chi_{c1} \rightarrow J/\psi \gamma$ and $\eta \rightarrow \gamma\gamma$ mass for the process $\bar{p}p \rightarrow \psi_g \eta$ . . .	153
8.5	Linear fit coefficients for pion and electron irradiation. . . . .	136	9.19	Invariant $\chi_{c1} \pi^0 \pi^0$ mass for the reaction $\bar{p}p \rightarrow \psi_g \eta$ . . . . .	153
8.6	Stability of the LED pulser prototype. . . . .	137	9.20	Angular distribution of reconstructed $\bar{p}p \rightarrow e^+e^-$ events. . . . .	154
8.7	Monitoring system prototype. . . . .	138	9.21	Angular distribution of reconstructed $\bar{p}p \rightarrow \pi^+\pi^-$ events. . . . .	154
8.8	Prototype LED driver. . . . .	138	10.1	The experimental setup at the tagged photon facility at MAMI. . .	159
8.9	Schematic view of the light pulser prototype. . . . .	139	10.2	The insulated container to house the various test arrays. . . . .	159
8.10	Light distribution uniformity. . . . .	139	10.3	A typical $5 \times 5$ PWO matrix. . . . .	159
9.1	Simulated line shape at the photon energy of 674.5 MeV. . . . .	143	10.4	Lineshape of the central detector module. . . . .	159
9.2	Measured and simulated energy resolution vs. incident photon energy. .	143	10.5	Response function of the $3 \times 3$ matrix to photons. . . . .	160
9.3	Leakage correction function for the barrel EMC. . . . .	144	10.6	Response function of the $3 \times 3$ matrix to photons. . . . .	160
9.4	Energy resolution for three different crystal length scenarios. . . . .	144	10.7	Comparison of the energy resolution. . . . .	160
9.5	Energy resolutions for different single crystal reconstruction thresholds. . . . .	144	10.8	Detector operation at low temperatures at MAX-Lab. . . . .	161
9.6	Position resolution in $x$ -direction for photons below 3 GeV. . . . .	145	10.9	Energy deposition of a 35 MeV incident photon. . . . .	161
9.7	E/p versus track momentum for electrons and pions. . . . .	145	10.10	Response of a $3 \times 3$ PWO-II matrix to incident photons. . . . .	161
9.8	Zernike moment $z_{31}$ for electrons, muons and hadrons. . . . .	145	10.11	Experimental energy resolution of a $3 \times 3$ PWO-II matrix. . . . .	161
9.9	MLP output for electrons and other particle species. . . . .	146	10.12	Response function of the $3 \times 3$ PWO-II matrix to photons. . . . .	162
9.10	Electron efficiency and contamination rate using EMC information. . .	146	10.13	Energy resolution of a $3 \times 3$ PWO-II matrix. . . . .	162
9.11	Electron efficiency and contamination rate using combined PID information. . . . .	147	10.14	Time resolution of a $3 \times 3$ PWO-II matrix. . . . .	162
9.12	Amount of material in front of the EMC. . . . .	147	10.15	Distribution of the electromagnetic shower into the $3 \times 3$ PWO-II matrix. . . . .	163
9.13	$\gamma$ conversion probability in the DIRC as a function of $\Theta$ . . . . .	147	10.16	Experimental line shape of the $3 \times 3$ PWO-II matrix. . . . .	163

10.17	Experimental line shape of a $3 \times 3$ PWO-II matrix. . . . .	164
10.18	The linearity of the response of a $3 \times 3$ matrix. . . . .	164
10.19	Experimental energy resolution as a function of incident photon energy. .	164
10.20	Pack of 4 crystals wrapped with reflector. . . . .	165
10.21	Back view of PROTO60. . . . .	165
10.22	Back view of the fully assembled PROTO60. . . . .	165
10.23	Temperature stability of the PROTO60. . . . .	166
10.24	Measured response of a single module of the PROTO60. . . . .	166
11.1	Schematic layout for the realization of the target spectrometer EMC of PANDA. . . . .	171
11.2	Timeline for the realization of the target spectrometer EMC. . . . .	174
11.3	Tasks and responsibilities for the realization of the target spectrometer EMC. . . . .	175



# List of Tables

---

1.1	Main requirements for the $\bar{\text{P}}\text{ANDA}$ EMC. . . . .	4
2.1	Injection parameters, experimental requirements and operation modes. .	16
3.1	Main requirements for the $\bar{\text{P}}\text{ANDA}$ EMC. . . . .	38
4.1	Properties of various scintillation crystals. . . . .	40
4.2	Distribution of the crystal properties of accepted PWO crystals. . . . .	45
4.3	Selected parameters of the electron capturing centers in PWO crystals. .	47
4.4	Comparison of the induced absorption.	56
5.1	Properties of tested APDs. . . . .	73
5.2	Conversion layer thicknesses of the tested APD types. . . . .	73
5.3	Dark current parameters after proton irradiation of the tested APDs. .	75
5.4	Specification for $\bar{\text{P}}\text{ANDA}$ VPT. . . . .	81
5.5	Parameters of the RIE FEU-189 VPT.	81
6.1	Measured preamplifier parameters. . . . .	91
7.1	Geometrical parameters of the EMC.	107
7.2	Thermal properties of PWO. . . . .	116
7.3	List of services in the backward area.	120
8.1	Properties of LEDs. . . . .	138
9.1	Efficiency of different event selection criteria. . . . .	150
9.2	Signal to background ratio for different $h_c$ background channels. . . . .	150